The University of Sheffield

Analysis of Fractional Slot and Vernier Permanent Magnet Synchronous Machines

Yinzhao Zheng

A thesis submitted for the degree of Doctor of Philosophy

Department of Electronic and Electrical Engineering

The University of Sheffield

Mappin Street, Sheffield, S1 3JD, UK

June 2024

ABSTRACT

Fractional slot (FS) vernier permanent magnet (PM) synchronous machines (VPMSMs) offer higher torque/power output capability under rated-load conditions. In particular, a compact structure and high torque/power density can be achieved when combined with concentrated winding (CW), consequent pole (CP) rotor, and multi-tooth stator structures. This thesis systematically investigates the effects of end windings, rotor topologies (north-south pole (NSP) and CP), and multi-tooth stator structures on the electromagnetic performance, unipolar end leakage flux caused by the CP structure, asymmetric PM loss and temperature distributions, and corresponding hotspot locations in conventional FS PMSMs and FS VPMSMs.

The electromagnetic performance, e.g., torque, torque density, power factor, etc. under various machine design optimization scenarios have been investigated and compared for SPMSMs with different slot/pole number combinations and rotor topologies (NSP and CP), accounting for the effects of end windings, coil pitches, and iron loss under different speeds.

Since unbalanced magnetic circuits in the north and south poles of the CP structure lead to unipolar end leakage flux, a simple and effective composite rotor, consisting of a non-magnetic shaft and a non-magnetic ring inside the rotor core (which could be integrated into a single shaft), is proposed to reduce the end leakage without sacrificing torque capability. The proposed structure can significantly mitigate the adverse effects of end leakage.

To further enhance torque and power densities, the FSCW is combined with the multi-tooth stator. The effect of multi-tooth numbers on the electromagnetic performances of NSP and CP VPMSMs is investigated and compared. The optimal multi-tooth number, in terms of torque characteristics, PM utilization, efficiency, and unipolar end leakage, is determined.

A finite element analysis (FEA) based harmonic restoration method is utilized to evaluate and quantify the asymmetric PM eddy current loss density and temperature distributions in SPMSMs which are found to be caused by the interaction between the armature reaction and PM fields. The resultant PM local hotspots are also investigated. Furthermore, the effect of armature reaction on asymmetric PM eddy current loss and temperature distributions in IPMSMs is also investigated and compared with SPMSMs.

All investigations have been carried out by electromagnetic and thermal FEA simulations and experimental verification.

ACKNOWLEDGMENTS

I would like to express my heartfelt gratitude to my supervisor, Professor Zi-Qiang Zhu, for his invaluable guidance, constructive feedback, and sincere encouragement throughout my PhD project. I am privileged to have the opportunity, provided by Prof. Zhu, to study and conduct research in one of the foremost Electrical Machines and Drives Research Groups globally. His exceptional guidance and the resources provided have greatly facilitated my academic and scientific pursuits through numerous meetings and discussions. These experiences and lessons will accompany me throughout my lifetime.

I would like to thank the Midea Group, an enterprise renowned for leadership in technological innovation, brand reputation, and global expansion, for the sponsorship and technical support. I would like to thank Dr. Peilin Xu, Dr. Hai Lan, Dr. Liren Huang, Dr. Huayang Li, Dr. Yanjian Zhou, Dr. Liang Chen, and Mr. Hailong Liu for their helpful supervision, support, and advice.

I would like to express my gratitude to Professor Libing Zhou for encouraging and recommending me to pursue my PhD degree. As the initiator of my academic research, his meticulous guidance and rigorous research attitude have been immensely beneficial to me.

I would like to thank Dr. Bo Shao, Dr. Ji Qi, Dr. Luocheng Yan, Mr. Jun Yan, Mr. Hai Xu, Mr. Qiang Wei, Dr. Yafeng Zhang, Dr. Fangrui Wei, Dr. Ximeng Wu, Dr. Wei Zhang, Dr. Dong Xiang, Mr. Zhitong Ran, and Mr. Milad Kazemi. You are the most cherished friendships I've gained in Sheffield, accompanying me through the toughest time. I would like to thank Dr. Yang Xiao, Dr. Shun Cai, Dr. Dawei Liang, Dr. Zeting Mei, Dr. Yue Liu, Dr. Yu Wang, Dr. Bo Shuang, Dr. Huan Qu, Mr. Guanbo Zhang, Dr. Yan Jia, Mr. Yang Chen, Mr. Peng Wang, Mr. Jialu He, Mr. Tianzheng Xiao, Mr. Henghui Li, Mr. Kejing Lu, Mr. Ankan Dey, and all my colleagues in the Electrical Machines and Drives Research Group for your support.

I would like to extend my sincere thanks to my trusted friends, Dr. Yuhang Zhang, Dr. Runquan Xiao, and Mr. Linghui Ruan. We had joy, we had fun, we had seasons in the sun. Every time that I was down, you would always come around. I would like to thank my beloved girlfriend, Ke Xu, for your thoughtfulness and understanding. I am fortunate to have your companionship. Thank you for being willing to accompany me through wind and rain without retreat.

Special thanks to my parents, Ms. Qihua Zheng and Mr. Chuanyi Zheng, sisters, Ms. Zhenzhen Zheng and Ms. Yanping Zheng, and brother, Mr. Guibin Zheng, for your unconditional love and support from birth until now and into the future. I would not have been able to achieve this milestone without your constant encouragement. I hope you stay healthy and happy forever.

CONTENTS

NOMENCLATURES

Symbol	Description	Units
A_{PMi}	Magnitude of i^{th} order harmonic	-
B_{δ}	Air-gap flux density	T
B_r	Remanence of rotor PM	T
b_{so}	Stator slot opening width	mm
D_H	Hydraulic diameter of channel	mm
d_{sh}	Shaft diameter	mm
d_{si}	Stator inner diameter	mm
d_{so}	Stator outer diameter	mm
F_{PM}	PM magnetomotive force	AT
Gr	Grashof number	-
H/W	Ratio of channel height to width	-
h_{mt}	Depth of dummy slot	mm
h_{pm}	Thickness of rotor PM	mm
h_y	Thickness of stator yoke	mm
i_d	*D*-axis current	A
I_{dc}	DC current	A
I_{peak}	Amplitude of phase current	A
i_q	*Q*-axis current	A
i_s	Stator armature current	A
K_{ec}	Eddy current core loss coefficient	-
K_{ex}	Excess core loss coefficient	-

K_h	Hysteresis core loss coefficient	-
L_{Ch}	Length of each cooling channel	mm
L_d	*D*-axis inductance	mH
l_{ef}	Effective axial length of stator lamination	mm
l_{fe}	Lamination stack length	mm
n	Speed	r/min
n_c	Number of turns per coil	-
N_s	Stator slot number	-
n_{st}	Multi-tooth number per stator-tooth	-
Nu	Nusselt number	-
p_a	Pole-pair number of armature winding	-
P_{cu}	Copper loss	W
p_r	Rotor pole pair number	-
Pr	Prandtl number	-
p_{rPM}	Pole arc to pole pitch ratio	-
q	Number of slots per pole per phase	-
Re	Reynolds number	-
R_{ER}	Equivalent reluctance of end region	H^{-1}
r_g	Average airgap radius	mm
R_{PM}	Equivalent reluctance of PM	H^{-1}
R_{RT}	Equivalent reluctance of rotor tooth	H^{-1}
R_{RY}	Equivalent reluctance of rotor yoke	H^{-1}
R_S	Equivalent reluctance of stator	H^{-1}
R_{SH}	Equivalent reluctance of rotor shaft	H^{-1}

r_δ	Air-gap radius	mm
R_σ	Equivalent reluctance of airgap	H^{-1}
S	Area	mm^2
T	Torque	Nm
Ta_m	Modified Taylor number	-
T_{av}	Average torque	Nm
T_{ripple}	Torque ripple	%
v	Rotor peripheral velocity	m/s
v_{pm}	PM volume	cm^3
V_{dc}	DC voltage	V
w_{mt1}, w_{mt2}	Width of multi-tooth	mm
w_t	Width of stator tooth	mm
β	Current advancing angle	°
δ	Air-gap length	mm
θ	Mechanical angle	°
θ_{PM}	Pole arc of rotor PM	°
λ	Thermal conductivity	W/(mK)
μ_A	Air kinematic viscosity	m^2/s
μ_r	Relative permeability of rotor PM	-
ρ_{MG}	Ratio of torque produced by magnetic gearing effect	-
Ψ_{PM}	PM flux linkage	Wb
ω	Electrical velocity	rad/s

ABBREVIATIONS

1-D	One-dimensional
2-D	Two-dimensional
3-D	Three-dimensional
6s/2mt/20p	6-slot/2 multi-teeth/20-pole
12s/20p	12-slot/20-pole
AC	Alternating current
Alnico	Aluminium nickel cobalt
AR	Armature reaction
CP	Consequent pole
CW	Concentrated winding
DC	Direct current
DW	Distributed winding
ECS	Equivalent current sheet
EV	Electric vehicle
EW	End winding
FEA	Finite element analysis
FS	Fractional slot
FSCW	Fractional slot concentrated winding
HRM	Harmonic restoration method
HTC	Heat transfer coefficient
IPM	Interior permanent magnet
IS	Integral slot

ISDW	Integral slot distributed winding
LPTM	Lumped-parameter thermal model
MMF	Magnetomotive force
MT	Multi-teeth
NdFeB	Neodymium boron iron
NSP	North-south pole
PM	Permanent magnet
PMSM	Permanent magnet synchronous machine
SmCo	Samarium Cobalt
SPM	Surface-mounted permanent magnet
SPMSM	Surface-mounted permanent magnet synchronous machine
VPMSM	Vernier permanent magnet synchronous machine

CHAPTER 1
GENERAL INTRODUCTION

1.1. Introduction

The development of Alnico magnets in the 1930s and ferrite magnets in the 1950s promoted the industrial applications of PM machines. The invention of SmCo magnets in the late 1960s and NdFeB magnets in the early 1980s accelerated the development of PM machines and improved machine performance significantly. The development of high-performance PMs is still ongoing, aiming to improve the remanence, resistance to demagnetization, and resistance to corrosion and temperature.

In general, electrical machines can be divided into brushed and brushless machines. The major difference between them is that brushed machines have the commutator and brushes, while these mechanical contacted components are replaced by electronically controlled inverters in brushless machines with the development of semiconductor technology.

Table 1.1 compares the main advantages and disadvantages of brushed and brushless machines. Brushless machines can be divided into synchronous and asynchronous machines depending on whether the rotational speed of the rotor is synchronized with the rotating magnetic field of the stator as shown in Fig. 1.1.

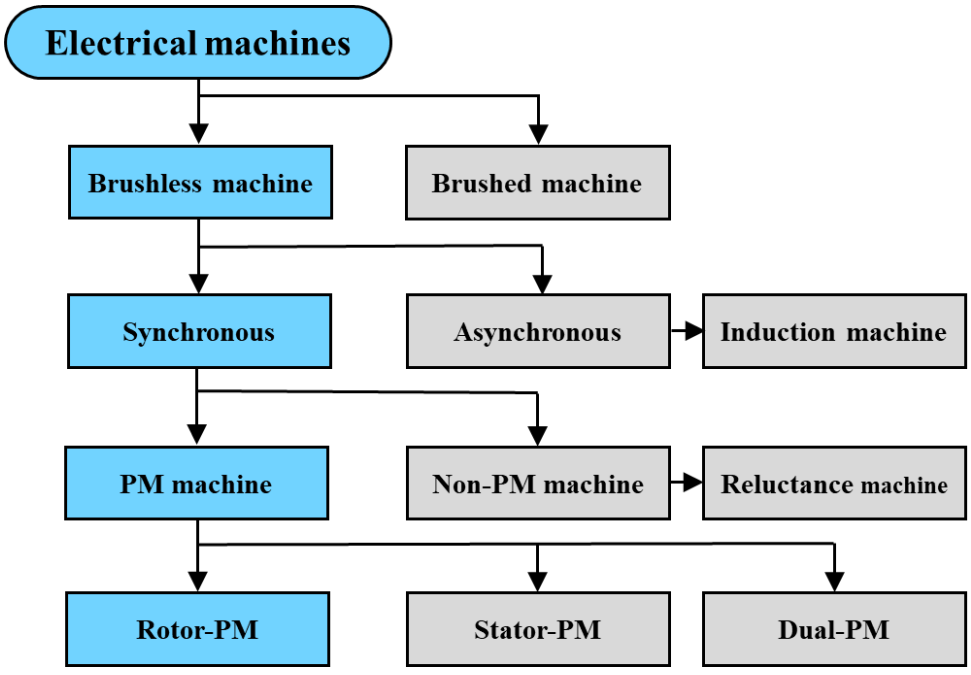

Fig. 1.1. Classification of electrical machines.

Table 1.1 Advantages and Disadvantages of Brushed and Brushless Machines

	Brushed machines	Brushless machines
Lifetime	Short (brushes and commutator)	Long
Maintenance	High	Low
Speed	Medium	High
Torque	Medium	High
Efficiency	Medium	High
Electrical noise	High	Low
Acoustic noise	High	Medium
Weight and size	Large	More compact
Cost	Low	High

The induction machine in Fig. 1.2 (a) is an asynchronous machine and has the advantages of high reliability, low cost, and self-starting characteristics [DEP88]. Even though the induction machine can achieve flux weakening easily, it is difficult to control due to asynchronous rotating magnetic fields between the stator and rotor.

Synchronous machines can be divided into two categories: non-PM machines and PM machines. The reluctance machine shown in Fig. 1.2 (b) is a typical type of non-PM synchronous machine with the feature of high robustness and simple structure, making it suitable for harsh operation environments. However, this kind of machine has common drawbacks of low torque density, low power factor, and high torque ripple [BIA09a].

To improve torque output capability and increase torque/power density, PM machines are widely investigated. PM machines can be divided into rotor-PM machines, stator-PM machines, and dual-PM machines according to PM locations. According to PM configurations, rotor-PM machines can be further divided into SPM and IPM machines as shown in Fig. 1.2 (c) and Fig. 1.2 (d) [CHA08].

Owing to high torque density, high efficiency, simple structure, and easy control, PM machines have been extensively employed in various applications, e.g., aerospace, domestic appliances, electric or hybrid electric vehicles, wind power generation, etc. [ZHU07] [PEL12] [POL13] [HE22]. Due to climate change, governments are paying more attention to EVs because they emit fewer greenhouse gases over their lifetime than conventional gasoline-powered vehicles.

PM machines are one of the most preferred motor types in EVs and have attracted significant attention in recent years.

To save the overall cost of machines, reduce PM volume, and increase PM utilization, CP PM machines, as shown in Fig. 1.2 (e), also attract significant attention [AME05].

The flux reversal PM machine [WAN01] and switched flux PM machine [HOA97], illustrated in Fig. 1.2 (f) and Fig. 1.2 (g), are typical types of stator-PM machines. Moving the rotor-PM to the stator side makes the thermal management of the machine system easier since both PMs and armature winding are placed on the stator side [CHE11] [WU15a] [WU15b].

Fig. 1.2 (h) shows the dual-PM machine. The dual PM and bidirectional field modulation effect effectively improve torque output capability and torque density [NIU14]. However, the dual-PM machine has a complex structure, costs a large amount of PMs, and has poorer overload capability.

This chapter will review the state of the art of rotor-PM synchronous machines, especially the FS PMSMs and VPMSMs, which will be the primary focus of this thesis. Section 1.2 will introduce the machine topologies in terms of winding configurations, rotor topologies, and stator structures. Afterward, Section 1.3 will review the challenges of FS PMSMs and VPMSMs, including torque enhancement, unipolar end leakage flux in CP structure, thermal management of PMs, etc. Finally, the research scope and major contributions of this thesis will be illustrated in Section 1.4.

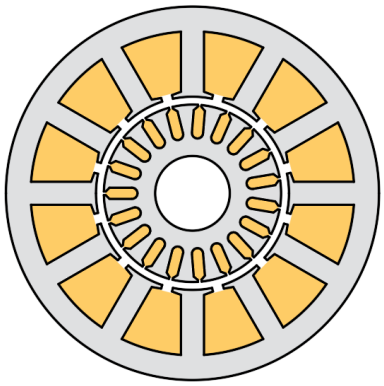

(a) Induction machine.

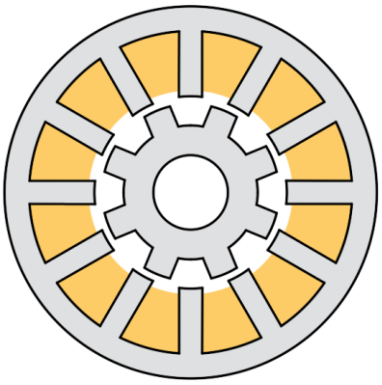

(b) Reluctance machine.

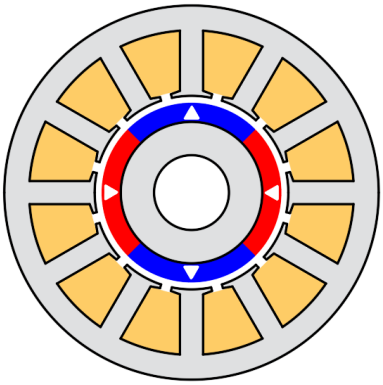

(c) SPM machine.

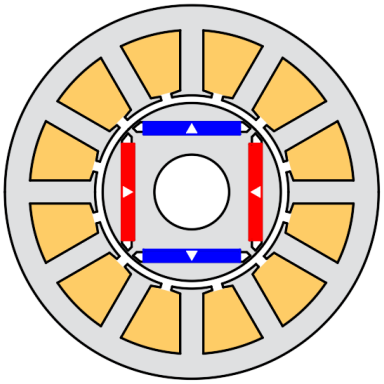

(d) IPM machine.

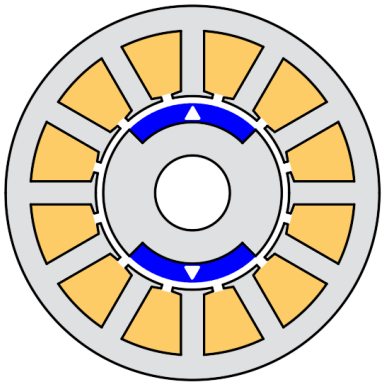

(e) Consequent pole PM machine.

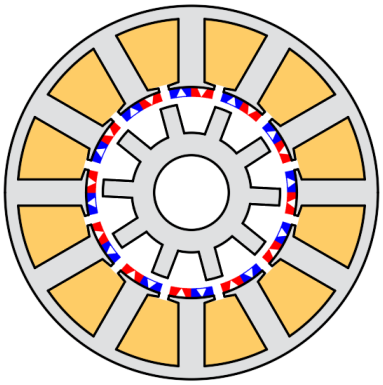

(f) Flux reversal PM machine.

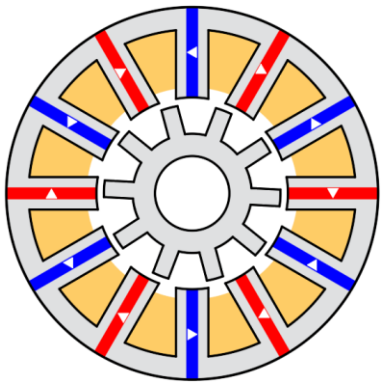

(g) Switched flux PM machine.

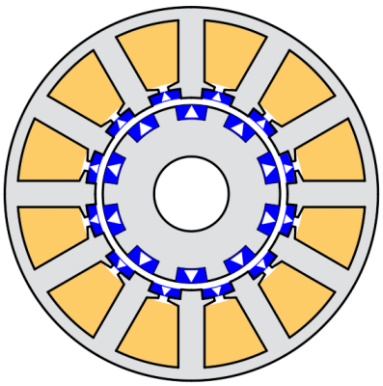

(h) Dual-PM machine.

Fig. 1.2. Topologies of brushless electrical machines.

1.2. Permanent Magnet Synchronous Machines

This section will introduce the topologies of rotor-PM synchronous machines in terms of rotor topologies, winding configurations, and stator structures, as shown in Fig. 1.3.

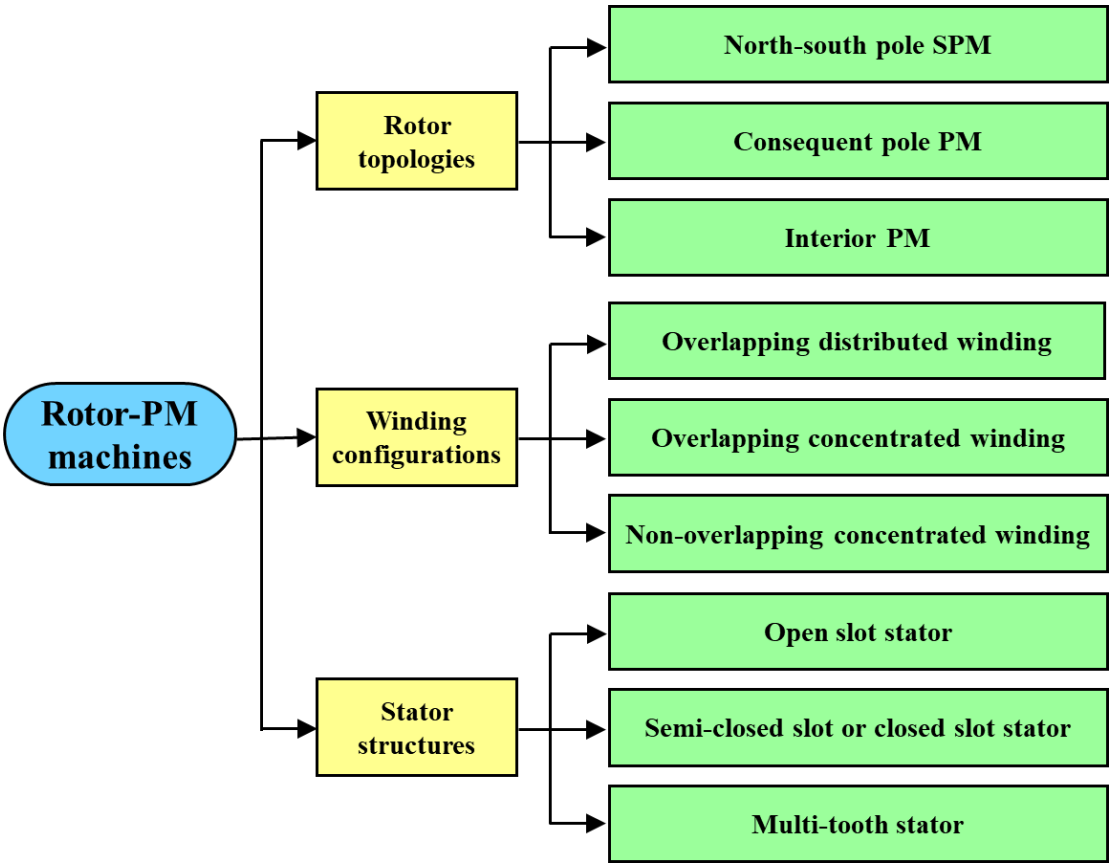

Fig. 1.3. Classification of rotor-PM synchronous machines in terms of rotor topologies, winding configurations, and stator structures.

1.2.1. Rotor topologies

From the perspective of PM positions of rotor-PM machines, the PMs can be placed on the surface of the rotor iron core or embedded into the core.

1.2.1.1. Surface-mounted PM

There are three common structures when the PMs are placed on the rotor surface as shown in Fig. 1.4, including SPM, surface inset PM, and Halbach PM. The SPM rotor has a simple structure for design and manufacture, as well as high efficiency. However, it has no reluctance torque and requires a retaining sleeve when used in high speed applications [PIL91] [BIA04]. The drawbacks of SPM can be improved by using the surface inset PM rotor as the salient iron

core helps to generate reluctance torque and fix the PMs, but the flux leakage will increase and sacrifice the torque output capability. Halbach PM rotor has inherently sinusoidal air-gap field distribution, leading to negligible cogging torque, essentially sinusoidal back EMF, and lower iron loss [HAL80] [ZHU01]. However, the Halbach structure leads to complex magnetization and assembling processes.

1.2.1.2. **Interior PM**

The IPM structure [BRA52] [STR52] can utilize the reluctance torque component to improve the ratio of torque per PM volume, eliminate the need to retain PMs, and achieve high withstand to demagnetization. Fig. 1.5 illustrates typical IPM rotor structures, including I-type in Fig. 1.5 (a), V-type in Fig. 1.5 (b), U-type in Fig. 1.5 (c), delta-type in Fig. 1.5 (d), spoke-type in Fig. 1.5 (e), and multi-layer-type in Fig. 1.5 (f). Compared with the I-type, other structures, especially the spoke-type, have better flux-concentrated effects, which can enhance the air-gap flux density and improve the torque output capability [BIN75]. Generally, the V-type has a higher salient rate and generates higher saliency torque, which offers a wider constant power region [BIN78]. The multi-layer-type can provide higher reluctance torque and has the potential to generate higher torque [HON97].

1.2.1.3. **Consequent pole PM**

The CP structure is attractive and has been employed in SPM and IPM machines to reduce the PM volume and increase the PM utilization [CHU12] [WU14b] [CHU15] [LI18a] [ZHA19] compared with conventional NSP structures illustrated in the previous section. Meanwhile, iron poles in CP structures act as modulators, enhancing the field modulation and magnetic gearing effects, thereby increasing the torque density. The CP structure can be applied to almost every SPM and IPM topology as shown in Fig. 1.6.

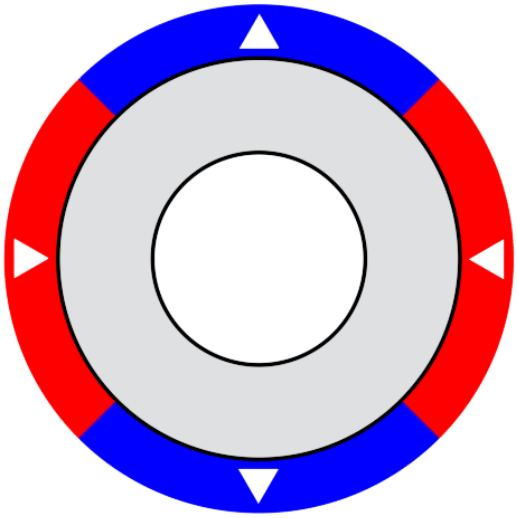

(a) SPM.

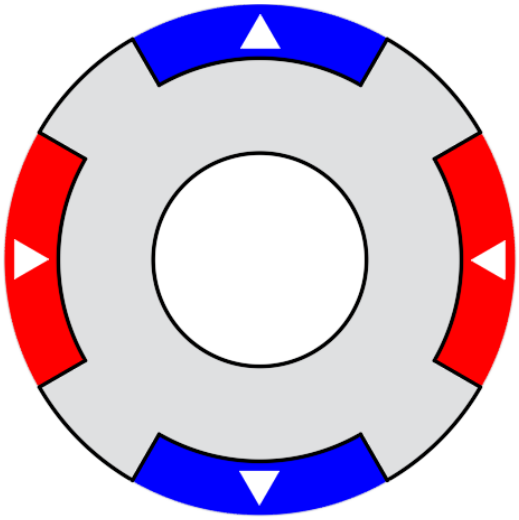

(b) Surface inset PM.

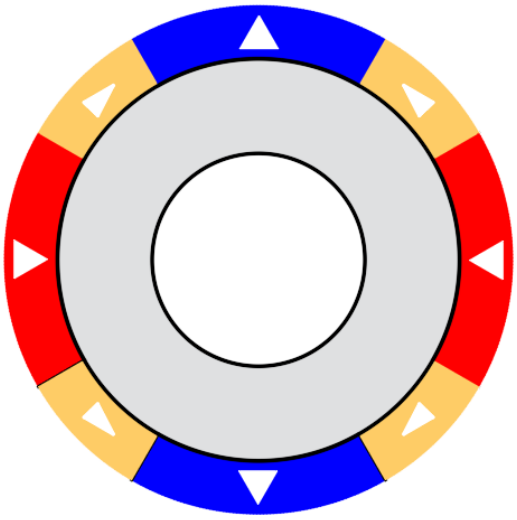

(c) Halbach PM.

Fig. 1.4. Common surface PM rotor structures.

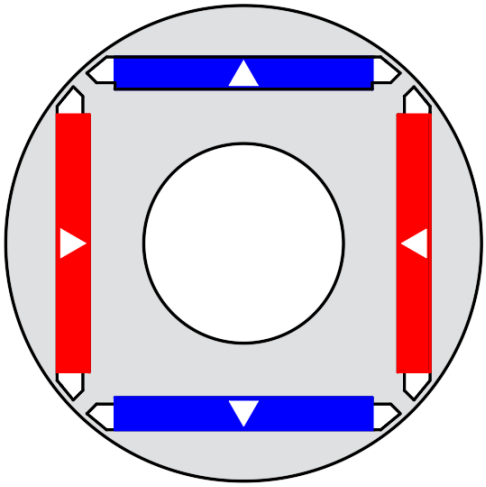

(a) I-type.

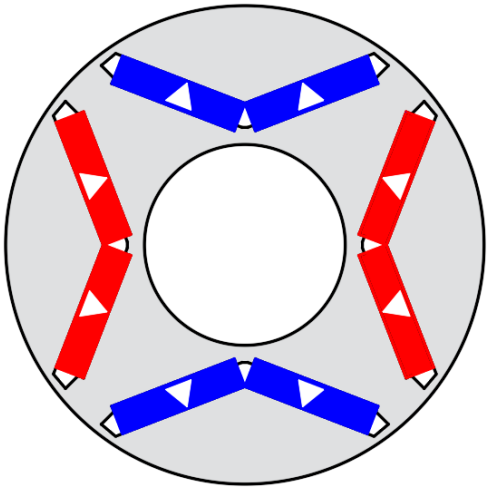

(b) V-type.

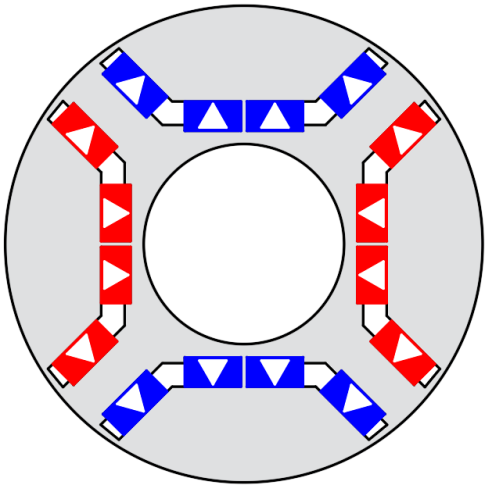

(c) U-type.

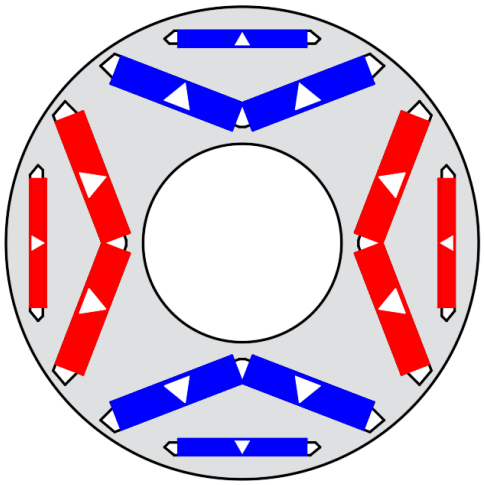

(d) Delta-type.

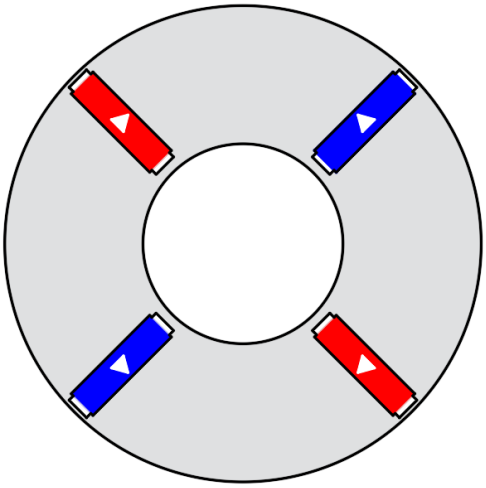

(e) Spoke-type.

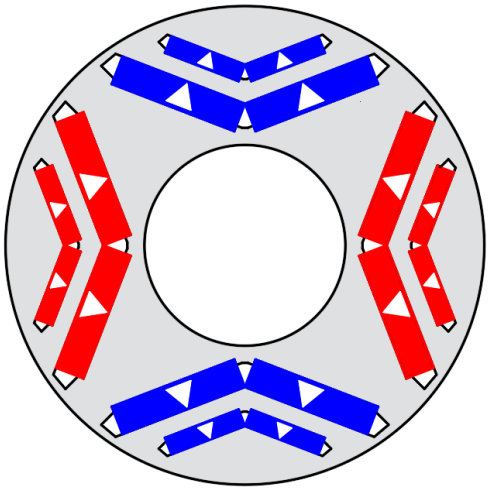

(f) Multi-layer-type.

Fig. 1.5. Common interior PM rotor structures.

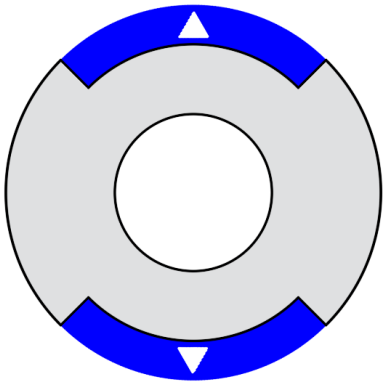

(a) SPM CP.

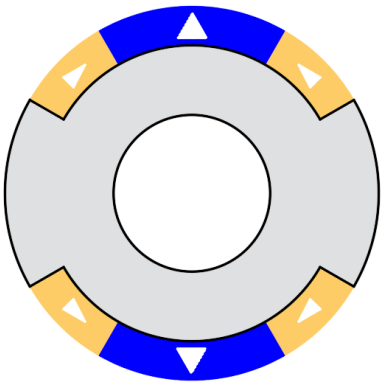

(b) Halbach CP.

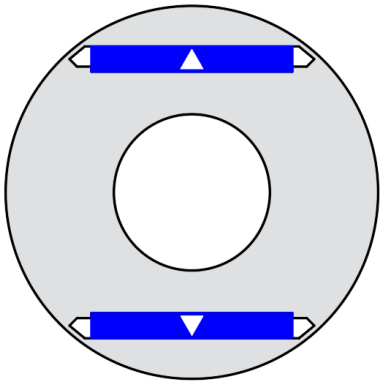

(c) I-type CP.

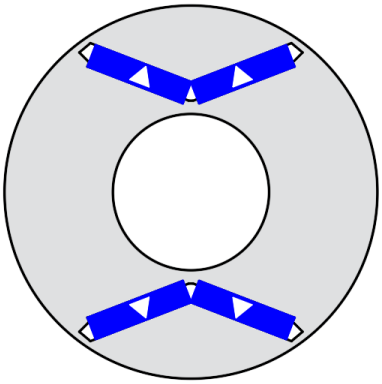

(d) V-type CP.

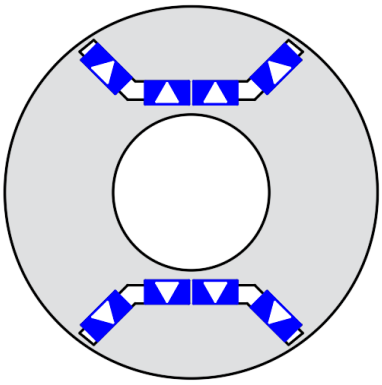

(e) U-type CP.

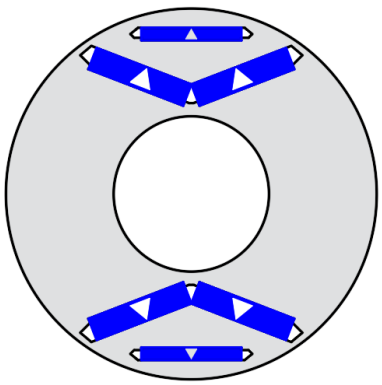

(f) Delta-type CP.

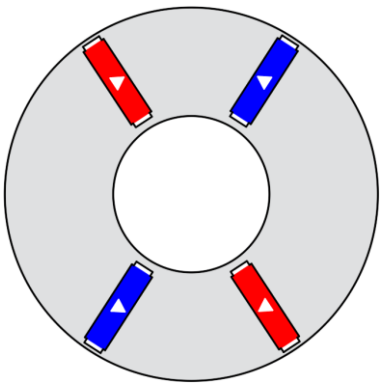

(g) Spoke-type CP.

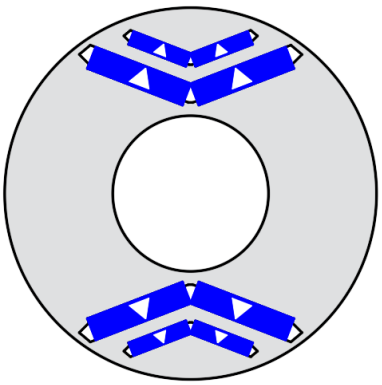

(h) Multi-layer-type CP.

Fig. 1.6. Common CP rotor structures.

1.2.2. Winding configurations

From the perspective of winding configurations, PM machines can be configured with overlapping winding and non-overlapping winding. On the one hand, overlapping ISDW, as shown in Fig. 1.7(a), having integral slot numbers per pole per phase, can achieve high winding factors by using the DW configurations. This allows them to achieve the largest fundamental harmonic winding factor for maximum average output torque. Since ISDW machines have more sinusoidal winding MMF waveforms with fewer higher order harmonics, they are beneficial for reducing iron and PM eddy current losses [RED12] [REF10]. Most importantly, ISDW can utilize the reluctance torque to achieve high torque per PM volume and thus reduce the usage of PMs. On the other hand, non-overlapping FSCW PM machines, as shown in Fig. 1.7 (b), which have FS numbers per pole per phase have been extensively investigated recently. Compared to ISDW PMSMs, due to shorter end windings and lower copper usage, FSCW PMSMs have the advantages of high power and torque densities, high efficiency, lower torque ripple, and enhanced flux weakening capability [ZHU07] [REF10]. However, FSCW PMSMs result in significantly reduced reluctance torque and abundant sub-harmonic field contents, leading to higher iron and PM losses [BIA09b] [WU14a]. The two coil pitches winding, as shown in Fig. 1.7 (c), can achieve a trade-off between ISDW and FSCW.

1.2.3. Stator structures

From the perspective of stator tooth structures, stators can be divided into closed-slot stator, semi-closed-slot stator, open-slot stator, and multi-tooth stator as shown in Fig. 1.8. Different stator structures have their advantages and disadvantages [TOB99] [LIB06] [WU12] [VU13] [ZIV13] [ZOU17a] [LI18a] [LI18b] [LI19a] [TAN20].

The closed-slot stator has a higher equivalent air-gap permeance but also produces higher slot leakages. It reduces the permeance pulsation which is beneficial to reduce the airgap harmonics. The closed-slot structure also has better mechanical support for coils but it creates difficulties in manufacturing and putting coils into slots. On the contrary, the open-slot stator, with the slot fully exposed to the air-gap, is easier to manufacture and put coils into slots. However, it will reduce the equivalent air-gap permeance and cause more difficulties for supporting coils. The semi-closed-slot stator, as a compromise between the closed-slot and open-slot structures, offers some mechanical support for coils and provides slightly higher equivalent air-gap permeance compared with the open-slot stator. The stator teeth of the multi-tooth stator are split into several dummy slots to produce the multipole effect. Therefore, the multi-tooth stator

is widely used in vernier machines together with non-overlapping FSCW, offering the advantages of short axial end winding and high torque/power density. However, the slots between the teeth create large dead spaces, leading to less area available for the armature winding [TOB99].

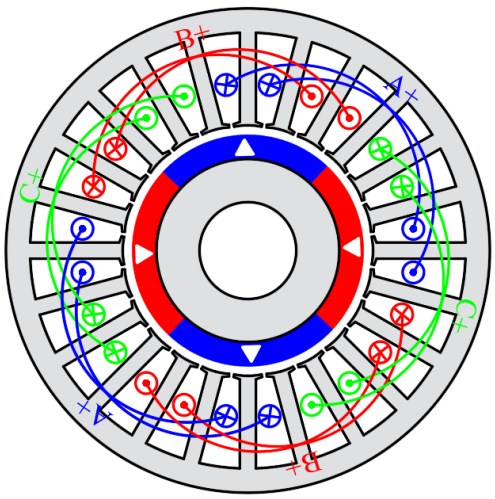

(a) Overlapping distributed winding.

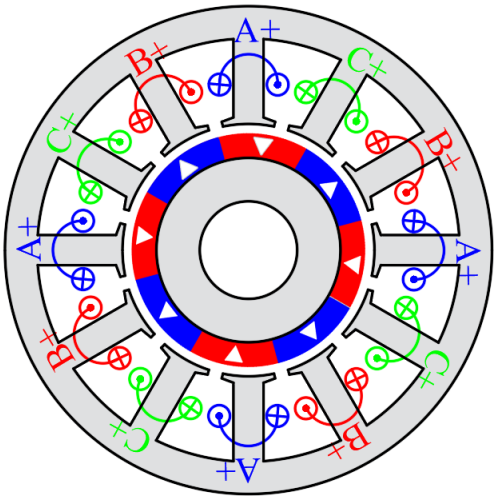

(b) Non-overlapping concentrated winding.

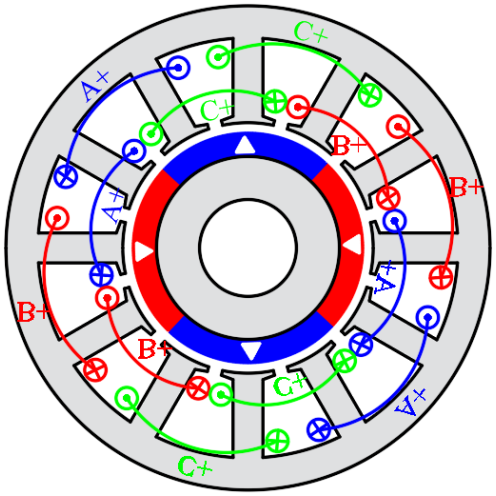

(c) Two coil pitches winding.

Fig. 1.7. Illustration of different winding configurations.

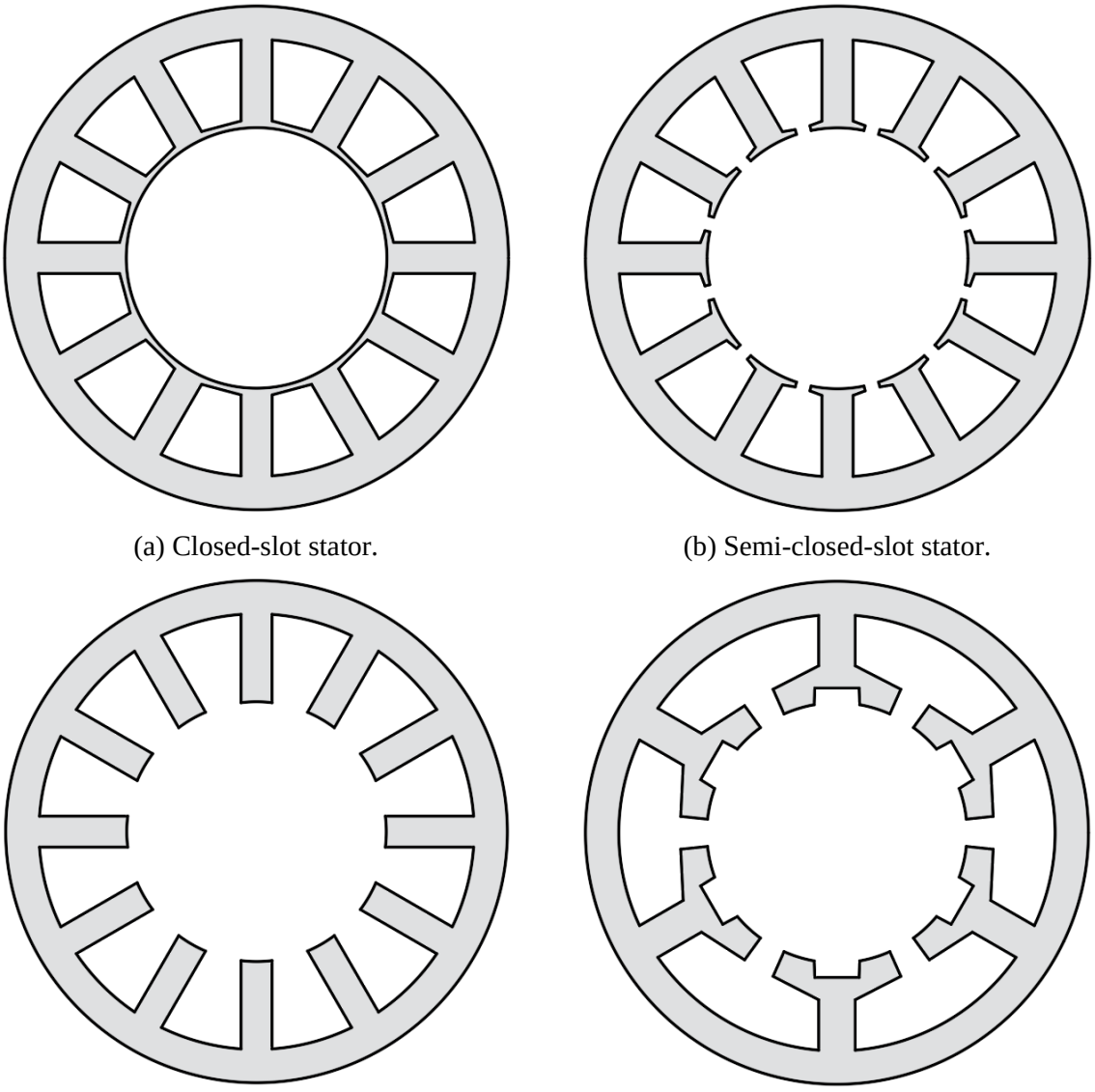

(a) Closed-slot stator. (b) Semi-closed-slot stator.

(c) Open-slot stator. (d) Multi-tooth stator.

Fig. 1.8. Common stator structures.

1.2.4. Fractional slot and vernier PM synchronous machines

Although there are various machine topologies, this thesis focuses on conventional FS PMSMs and FS VPMSMs with NSP and CP rotor structures. For convenience, the conventional FS PMSMs will be designated as FS PMSMs, while FS VPMSMs will be simply designated as VPMSMs. Fig. 1.9 shows typical machine topologies of FS PMSMs and VPMSMs analyzed in this thesis, including VPMSMs with ISDW/FSCW, single-tooth/multi-tooth stators, and NSP/CP rotors. The state of the art for FS PMSMs and VPMSMs will be reviewed in the next section.

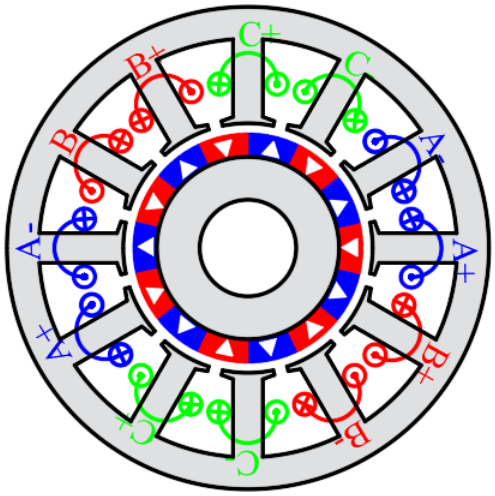

(a) FSCW and single-tooth stator NSP PMSMs.

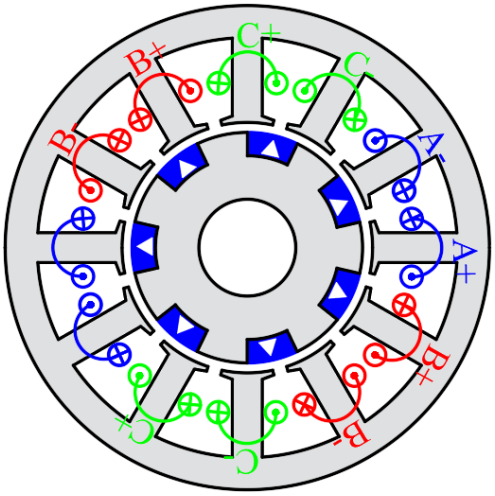

(b) FSCW and single-tooth stator CP PMSMs.

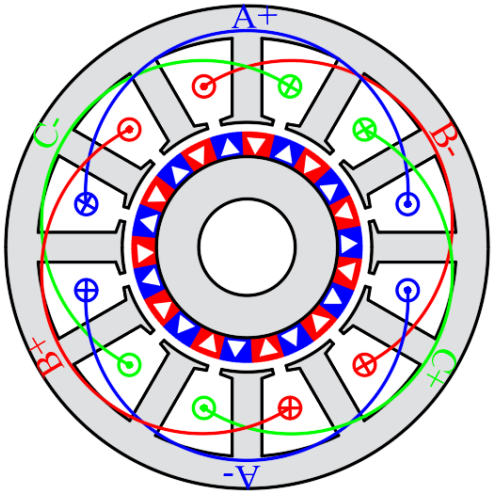

(c) ISDW and single-tooth stator NSP VPMSMs.

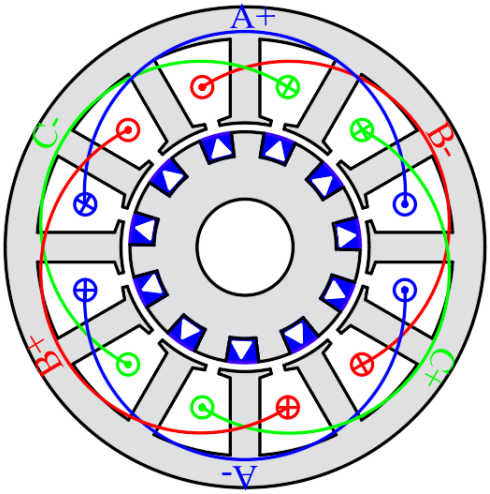

(d) ISDW and single-tooth stator CP VPMSMs

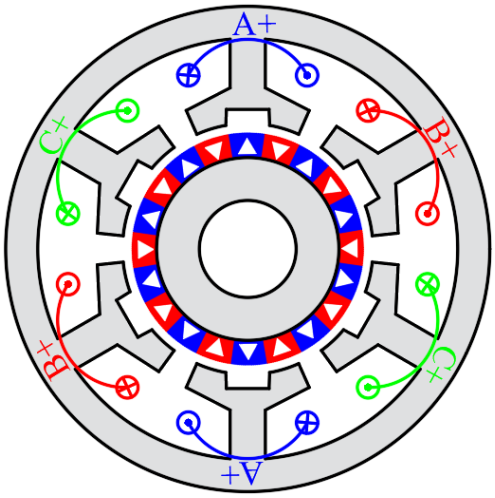

(e) FSCW and multi-tooth stator NSP VPMSMs.

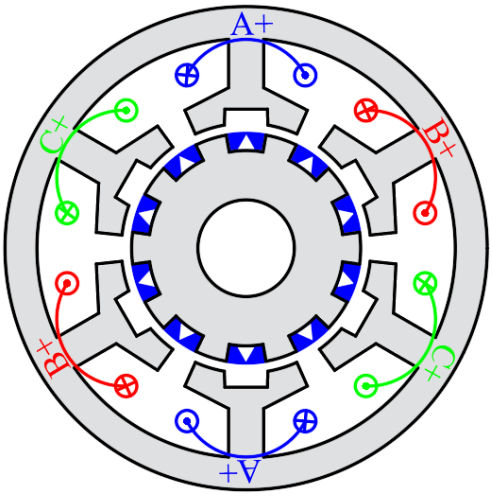

(f) FSCW and multi-tooth stator CP VPMSMs.

Fig. 1.9. Typical machine topologies of FS PMSMs and VPMSMs analyzed in this thesis.

1.3. Challenges of Fractional Slot and Vernier PM Synchronous Machines

1.3.1. Machine topologies

Vernier motors are first proposed in [LEE63] with a reluctance-type rotor as shown in Fig. 1.10. The concept of the modulated field is also introduced into cageless induction machines in [BRO71]. The advancement of PM materials and PM machines has driven research on PM vernier machines and further enhanced the torque density [ISH95] [TOB99] [TOB00]. Fig. 1.11 shows the PMVM proposed in [ISH95]. Due to their low-speed and high-torque characteristics, VMs are promising candidates for direct-drive applications such as wind turbines and in-wheel motors.

The working principle of VPMSMs, i.e., the field modulation effect, is illustrated in [KIM14] [LI18b]. The magnetic gearing effect and the gear ratio in FSCW PMSMs with different phases and slot/pole number combinations are revealed in [ZHU18a] [LIU19]. Conventional VPMSMs are open-slot ISDW as shown in Fig. 1.12, which have high average torque but low torque density due to long axial end winding length [TOB99] [XU15]. Various machine topologies are proposed to improve the performance of VPMSMs.

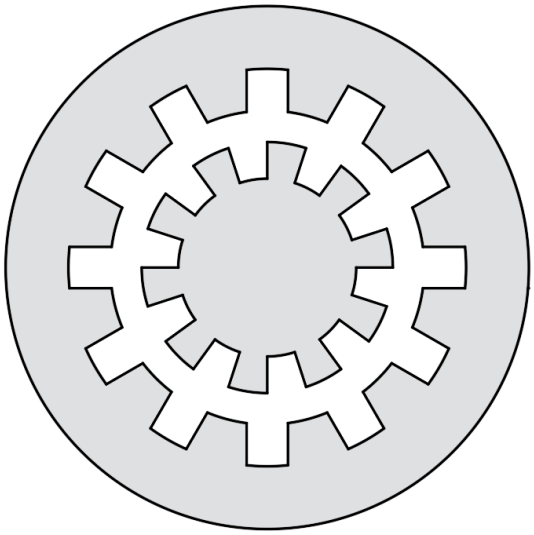

Fig. 1.10. Vernier motor proposed in [LEE63].

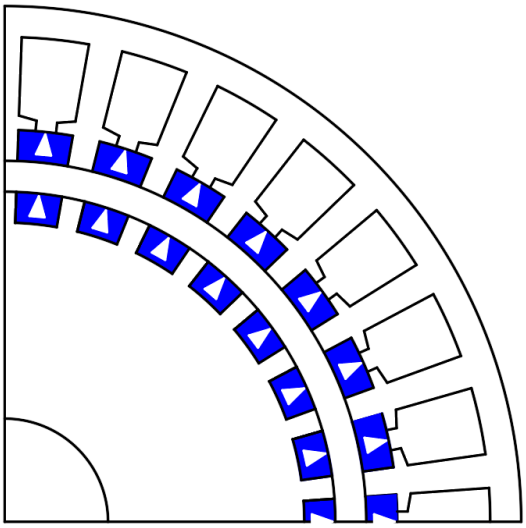

Fig. 1.11. PMVM proposed in [ISH95].

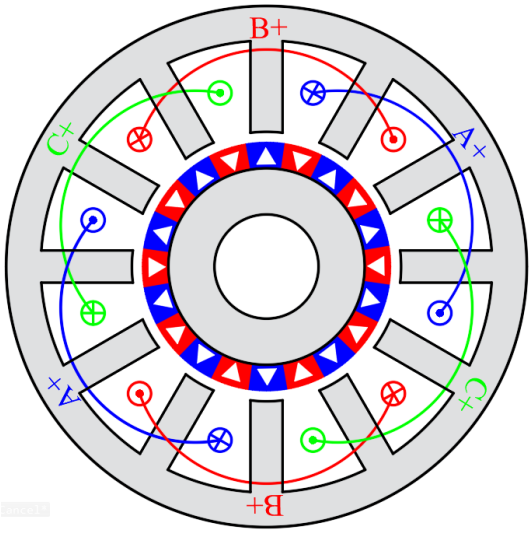

Fig. 1.12. Conventional open-slot 12-slot/20-pole overlapping winding VPMSMs.

FSCW is introduced to achieve higher torque density and optimal flux-weakening capability due to its short axial end winding length and increasing phase inductance [REF05] [REF06]. The toroidal-winding is also used to improve the torque density of a dual-rotor axial-flux VPMSM [ZOU17b]. The hybrid excitation VPMSMs with DC current or DC-biased sinusoidal current excitation are proposed with the flexibly adjusted exciting field, flux-weakening capability, enhanced torque output capability, and improved power factor [CHI16] [WAN17b] [LI17] [JIA17] [JIA18]. Fig. 1.13 shows the FSCW VM in [REF05], toroidal-winding VM in [LI15a], hybrid excitation VM with DC current excitation in [WAN17b], and VM with DC-biased sinusoidal current excitation in [JIA17].

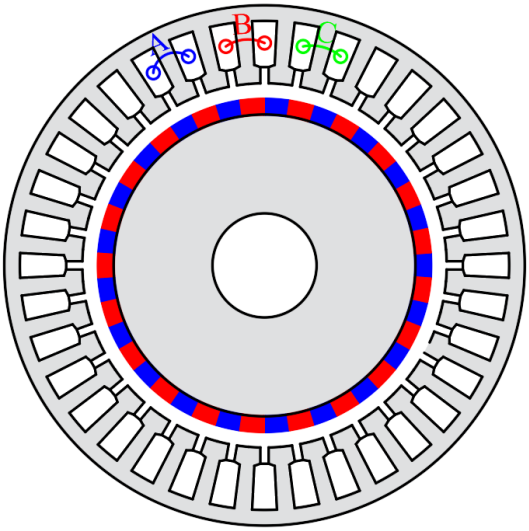

(a) FSCW VM in [REF05].

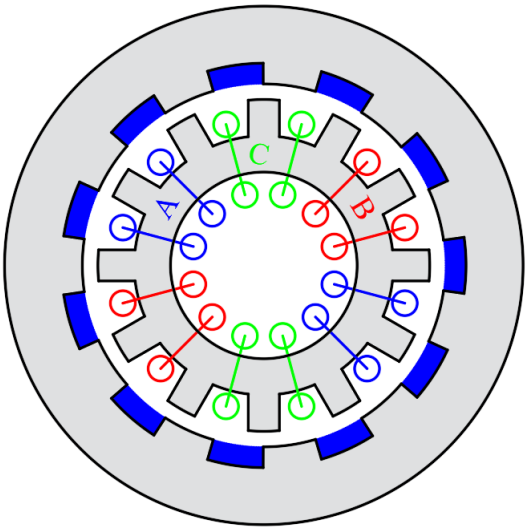

(b) Toroidal-winding VM in [LI15a].

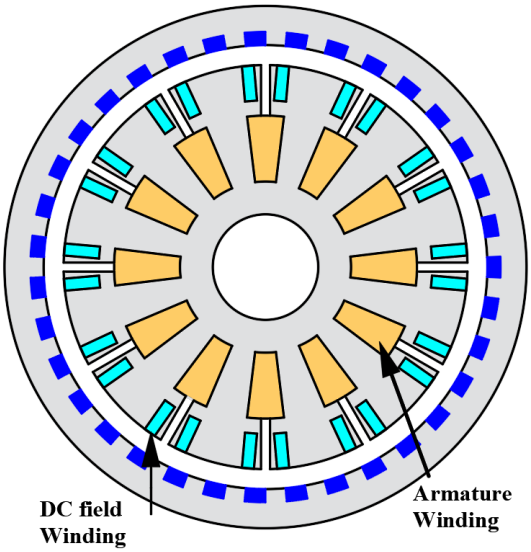

(c) Hybrid excitation VM with DC current excitation in [WAN17b].

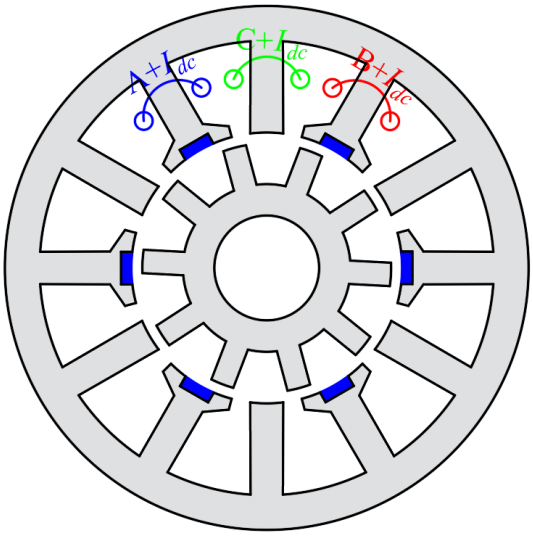

(d) VM with DC-biased sinusoidal current excitation in [JIA17].

Fig. 1.13. VMs with different winding configurations.

Multi-tooth stator structures are investigated in [LI10] [YAN13] [OKA13] [ZOU17a] [LI18c]. Combined with FSCW, multi-tooth stator VPMSMs can have the advantages of short end winding and high-modulation pole numbers simultaneously. Some special stator tooth structures are proposed in [FAN22] [DU22] [FAN23], which could introduce specific permeance harmonics for achieving better field modulation effect. Fig. 1.14 shows the multi-tooth stator VM in [LI10] and the coding-shaped tooth stator in [FAN22].

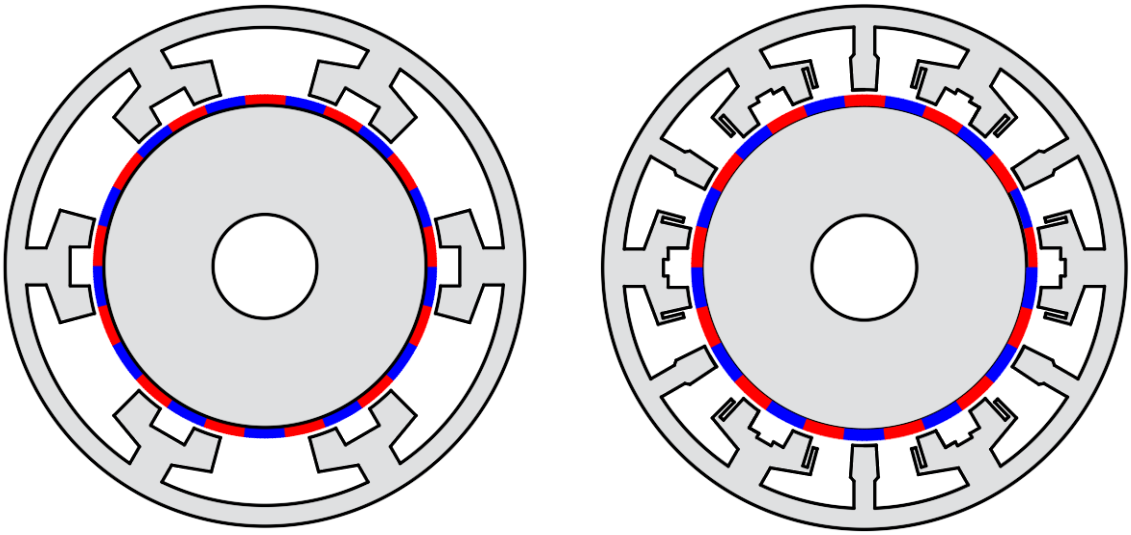

(a) Multi-tooth stator VM in [ZOU17a]. (b) Coding-shaped tooth stator in [FAN22].

Fig. 1.14. Multi-tooth stator and coding-shaped tooth stator VMs.

Various rotor topologies are proposed and investigated for VPMSMs apart from conventional NSP rotor VPMSMs [REF05] [REF06] [LI10] [YAN13] [OKA13]. The CP rotor can be used to save PM volume and improve the field modulation effect [CHU11] [LI15a] [YAN20a]. The flux-memoizable concept and vernier structure are combined in vernier memory machines to achieve flexible flux-controllability and expand high-speed constant-power region [LIU14] [YAN14]. In addition, the Halbach array PM, with the advantages of enhancing main flux and reducing flux leakage, is used to improve torque capability, power factor, and efficiency [XU16] [YAN21] [JIN22]. Moreover, the V-type and spoke-type PM rotors are used to achieve better flux-concentrated effect [KIM16] [LI15b] [LIU18a] [XIA22]. Furthermore, the claw-pole rotor can be used to enhance the field modulation effects and increase the torque density [ZHA22] [LIU23]. Fig. 1.15 shows the NSP rotor VM in [REF05], CP rotor VM in [CHU11], vernier memory machine in [LIU14], Halbach array VM in [XU16], spoke-type VM in [KIM16], and claw-pole rotor VM in [ZHA22].

The PMs can be moved to the stator side to form flux reversal or switched flux VPMSMs, which can utilize the simple salient rotor structure for easy thermal management. Meanwhile, higher magnet utilization and torque density can be achieved [WU15a] [EVA15] [GAO16] [YAN20a]. The PMs can be placed on both stator and rotor sides to form the dual-PM structure and improve torque density and power factor [ISH95] [TOB99] [NIU14] [JAN14] [XIE17] [ZHA16]. Fig. 1.16 shows the stator-PM VM in [GAO16] and dual-PM VM in [ISH95].

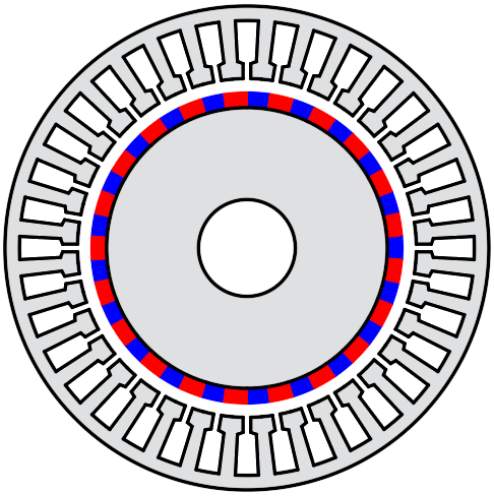

(a) NSP rotor VM in [REF05].

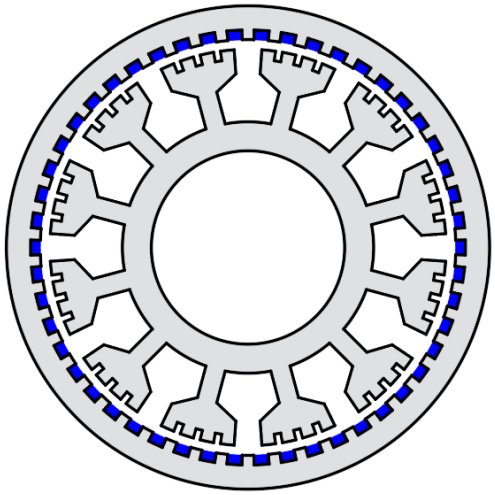

(b) CP rotor VM in [CHU11].

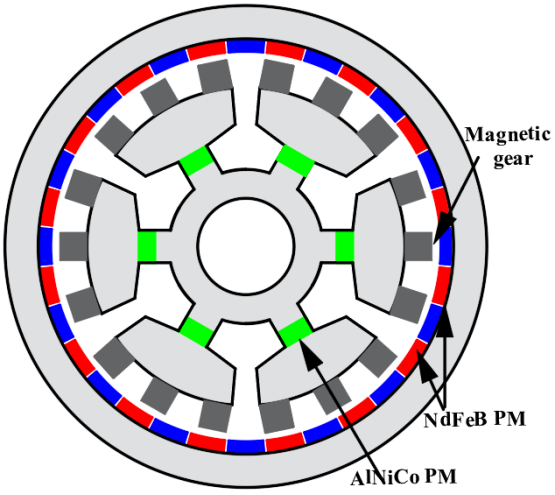

(c) Vernier memory machine in [LIU14].

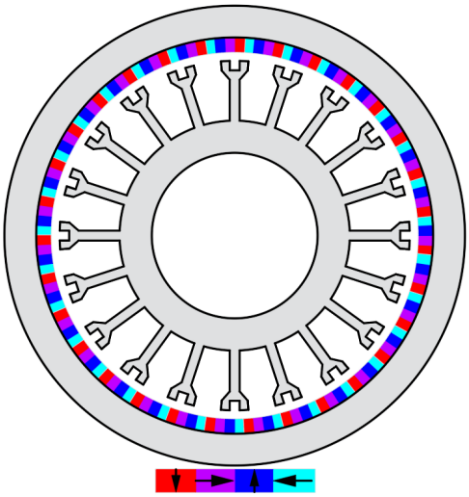

(d) Halbach array VM in [XU16].

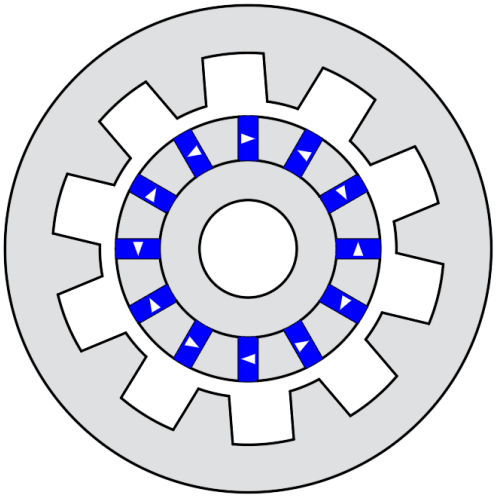

(e) Spoke-type VM in [KIM16].

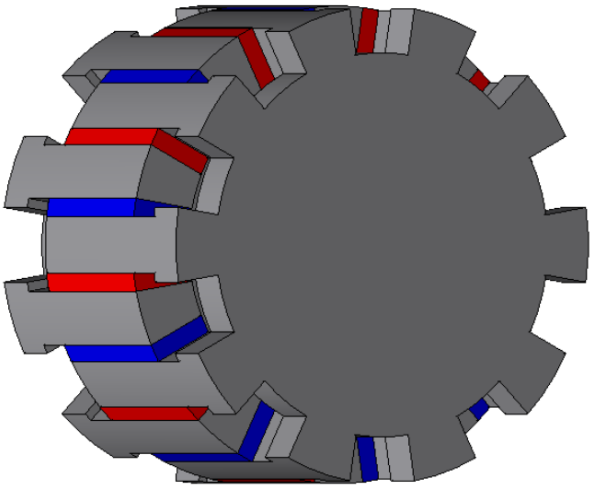

(f) Claw-pole rotor VM in [ZHA22].

Fig. 1.15. VMs with different rotor topologies.

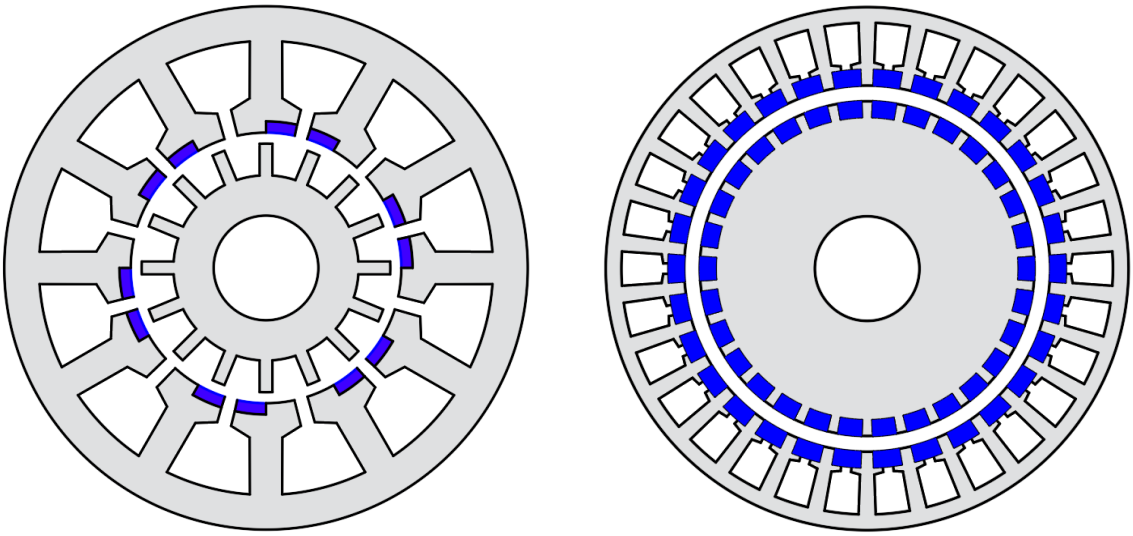

(a) Stator-PM VM in [GAO16]. (b) Dual-PM VM in [ISH95].

Fig. 1.16. Stator-PM and dual-PM VMs.

Dual stator structures are also used to improve the power factor and torque density [TOB99] [ZHA14a] [LI14a] [LI14b] [LI15b] [WAN17a] [HUA24], as well as dual rotor structures [NIU10] [ZOU17b]. Fig. 1.17 shows the dual stator VM in [LI15b] and the dual rotor VM in [NIU10].

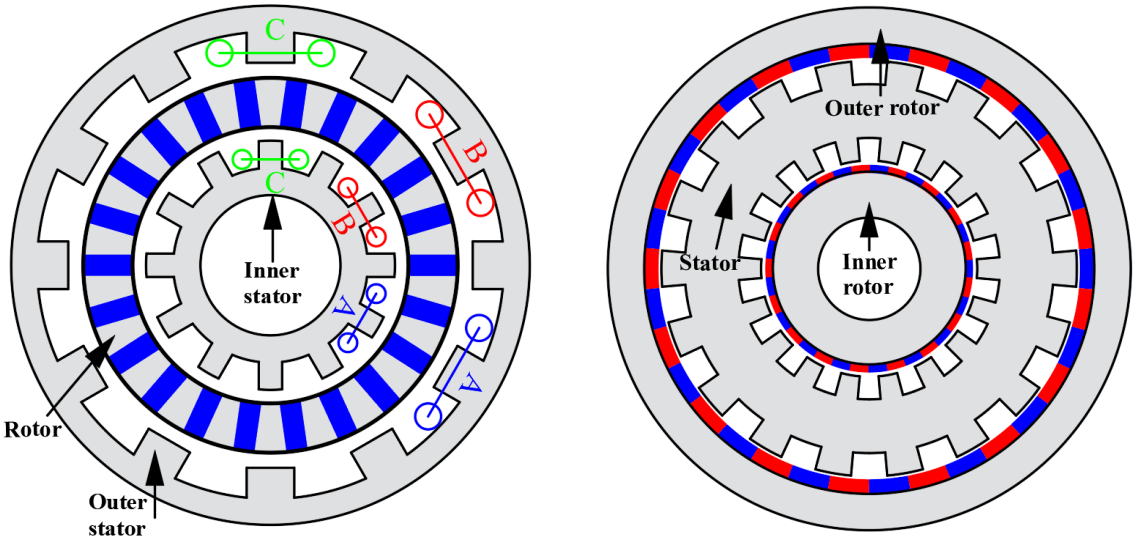

(a) Dual stator VM in [LI15b]. (b) Dual rotor VM in [NIU10].

Fig. 1.17. Dual stator and dual rotor VMs.

Fig. 1.18 shows the machine structure and arrangement of PMs in VMs. Various VPMSM topologies are presented. There are still many issues that require further investigation, including torque output and torque density enhancement, unipolar end leakage flux in CP rotor structures, thermal management of PMs, etc. The arrangement of the research topics of this thesis is illustrated in Fig. 1.19.

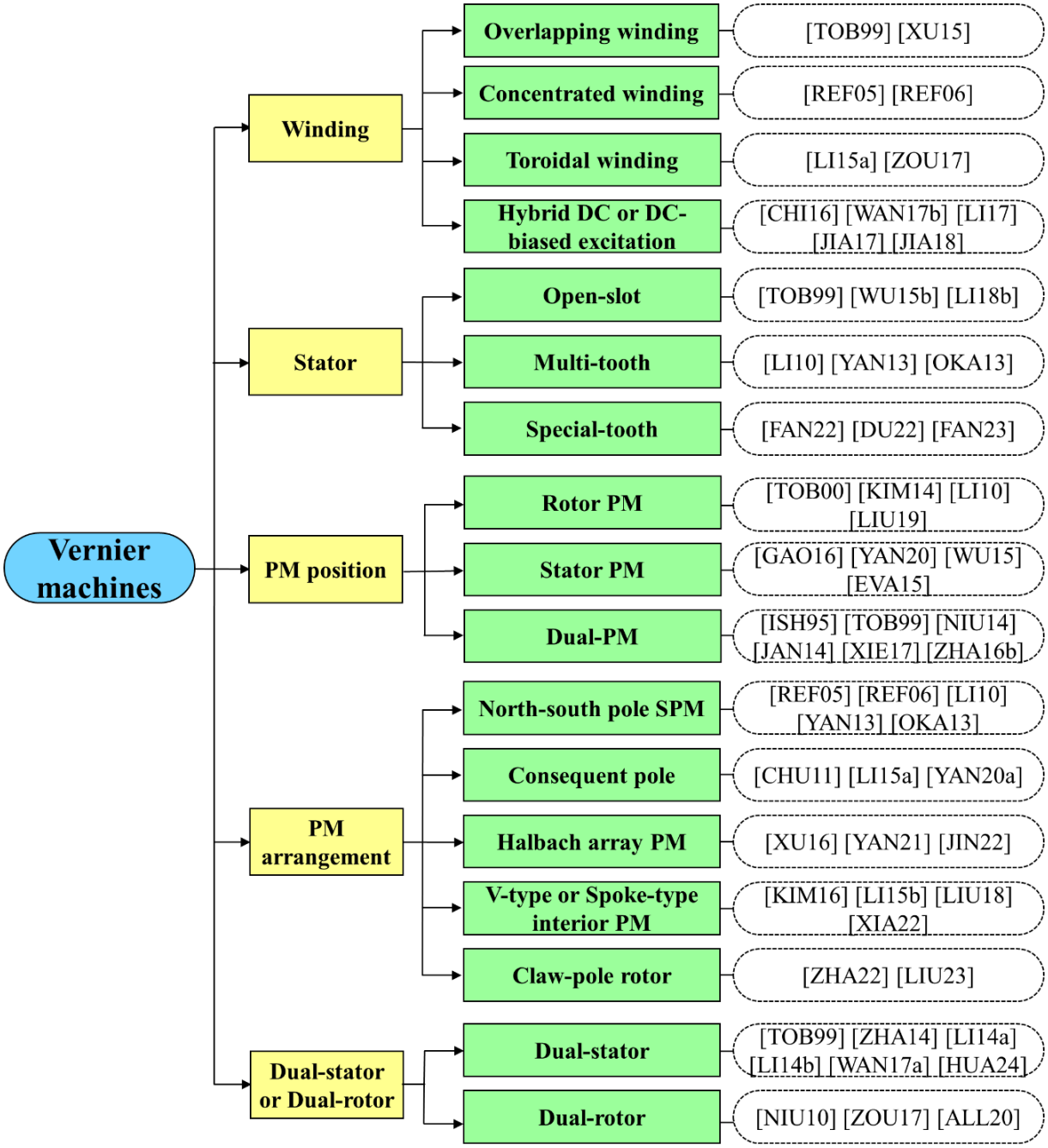

Fig. 1.18. Structures of VMs.

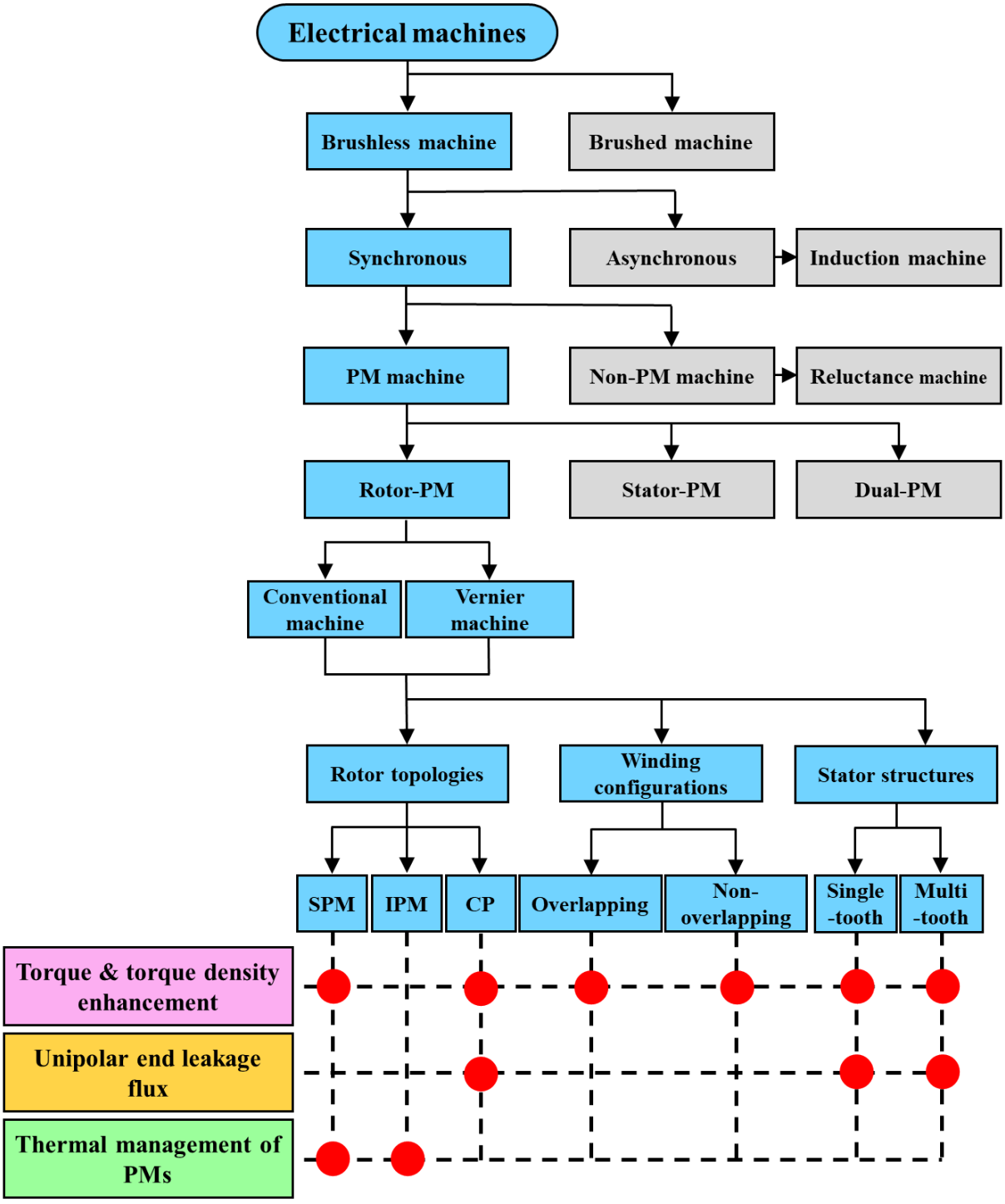

Fig. 1.19. Research topics in this thesis.

1.3.2. Torque output and torque density enhancement

The torque and torque density can be improved by carefully choosing proper winding configurations, rotor topologies, and stator structures.

1.3.2.1. **Rotor topologies**

From the perspective of rotor topologies, the CP rotor is attractive and has been employed in PMSMs, such as CP VPMSMs and CP FS PMSMs, to reduce the PM volume and increase the utilization of PMs [TOB00] [HEN94] [CHU12] [ZHU18a] [LI18a]. Especially for CP VPMSMs, the CP structure can increase the torque density as the iron poles, acting as modulators, can enhance the armature reaction field, large winding inductance, field modulation and magnetic gearing effects. The field modulation effects between NSP and CP structures are compared in [GAO16] [LI20] [LI21], which shows that the CP structure can generate higher modulated torque. The field modulation effect and torque component of CP VPMSMs with 2 multi-teeth are investigated in [XU17] [JAN19] [ZHO19a] [ZHA20] [LI22], which shows that the torque output capacity can be enhanced compared with conventional NSP VMs and single-tooth stator VMs.

For FSCW PMSMs, the CP rotor structure can reduce around 30-40% of PM volume, but the average torque will be slightly reduced [CHU15] [LI18a]. Fig. 1.20 shows the NSP and CP PMSMs in [CHU15].

For VPMSMs with higher rotor pole numbers, the CP rotor structure can generate higher modulated torque, enhance torque output capacity, and have the potential to generate higher torque than the NSP rotor [JAN19] [ZHO19a]. Fig. 1.21 shows the NSP and CP VPMSMs in [JAN19].

For IPMSMs, the CP rotor structure helps to reduce PM volume and increase the average torque simultaneously, resulting in higher efficiency at lower speed conditions [WU14b] [ZHA19] [ONS18]. The CP rotor IPMSM has better demagnetization withstand capability compared with their SPM counterparts [ZHO19b]. An asymmetric modular CP rotor is proposed to improve the flux-weakening capability and wide constant power operation in spoke-type IPMSM [LI19b]. The hybrid excited machines with CP rotor PM and stator DC field winding are proposed to achieve an extended operation range with flux-weakening field excitation [CAI21].

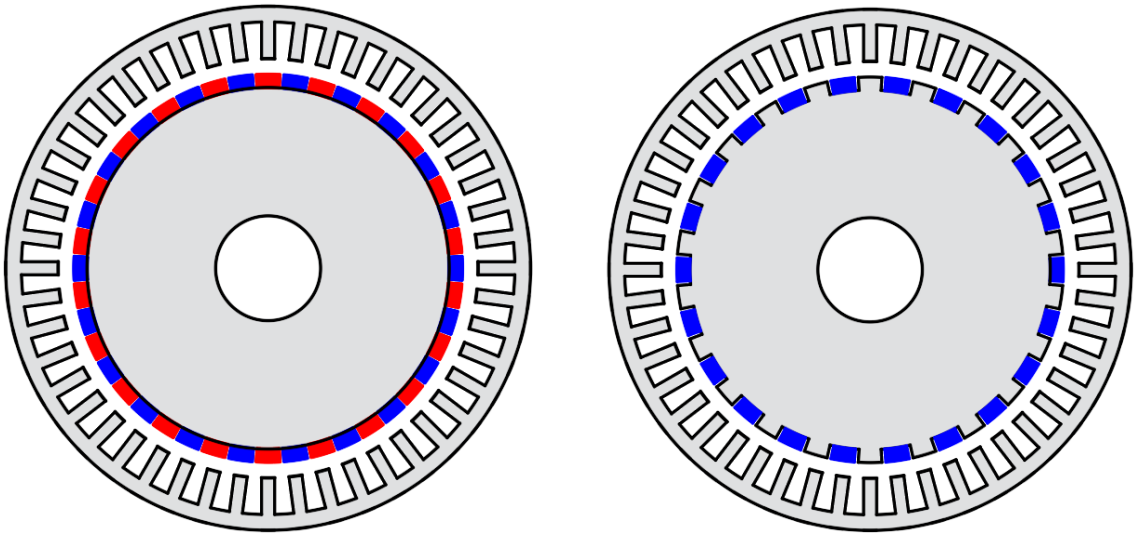

(a) NSP. (b) CP.

Fig. 1.20. NSP and CP PMSMs in [CHU15].

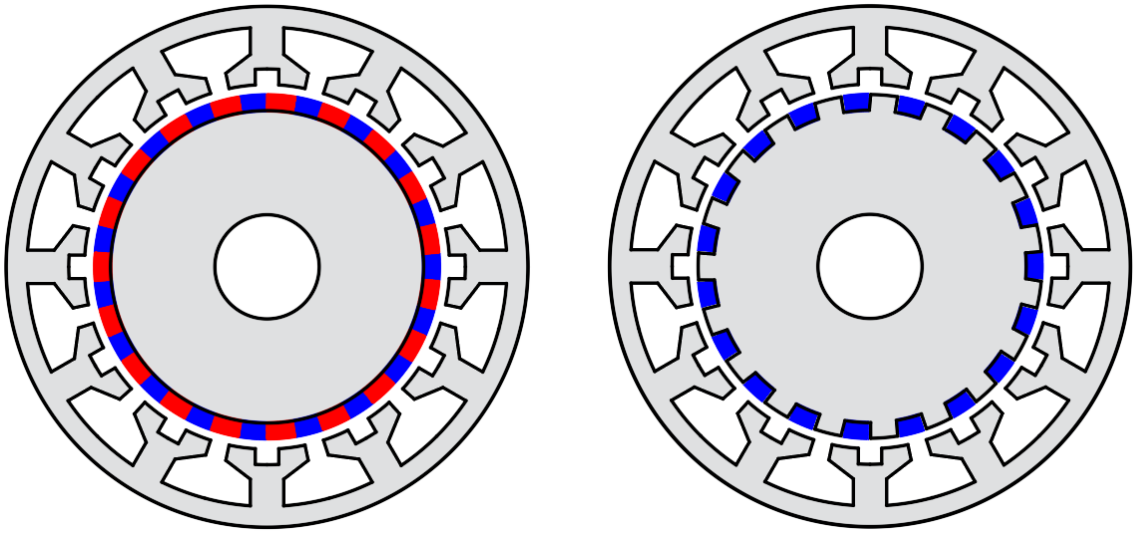

(a) NSP. (b) CP.

Fig. 1.21. NSP and CP VPMSMs in [JAN19].

1.3.2.2. **Winding configurations**

From the perspective of winding configurations, PMSMs are normally configured by overlapping DW or non-overlapping CW. On the one hand, IS PMSMs, having integral slot numbers per pole per phase, could achieve high winding factors by using the DW configurations, i.e., they could achieve the largest fundamental harmonic winding factor for maximum average output torque. Since an ISDW PMSM has more sinusoidal winding MMF waveform with fewer higher order harmonics, it is beneficial for reducing iron and PM eddy current losses [RED12] [REF10]. On the other hand, FS PMSMs which have FS numbers per pole per phase have been extensively investigated. In comparison to ISDW PMSMs, FSCW

PMSMs have the advantages of high power and torque densities, high efficiency, lower torque ripple, and enhanced flux weakening capability [ZHU07] [REF10]. Meanwhile, it has shorter end winding and lower copper usage. However, FSCW PMSMs result in abundant sub-harmonic field contents, which lead to higher iron and PM losses [BIA09b] [WU14a]. Fig. 1.22 shows the 2-pole ISDW and 10-pole FSCW, as well as the corresponding MMF waveforms (I_b=I_c= - 0.5I_a) and spectra.

Furthermore, to tradeoff between the winding factor and the end winding length, PMSMs with different coil pitches have also been investigated [WAN14a] [WAN14b] [SUN19] [HUA18]. Fig. 1.23 illustrates the winding configurations with different coil pitches. In [WAN14a], windings with two slot coil pitches are used for PMSMs to eliminate and/or reduce undesirable space harmonics resulting from nonoverlapping FSCW. [WAN14b] [SUN19] investigate the feasible slot/pole number combinations of PMSMs with two slot-pitches. The influences of windings with different coil pitches for flux reversal PMSMs are compared in [HUA18]. Meanwhile, [HE21] compares the small-size 6-slot/2-pole high-speed PMSMs with one, two, and three coil-pitch windings, and underpins that the two coil-pitch winding is the promising candidate for high-speed PMSMs.

Besides, VPMSMs are one of the FS PMSMs with special slot/pole number combinations, typically with pole numbers higher than slot numbers. VPMSMs have been gaining more attention recently due to their high torque as a result of field modulation and magnetic gearing effect [ZHU18a] [LI18a] [LI18b] [LIU18b] [LIU19]. In [LIU18b], the FS VPMSMs having two slot-pitch coils are developed to improve the power factor and achieve a compromise between axial end winding length and torque capacity. [LI16] proposes a general instantaneous torque equation of VPMSMs based on a 12-slot/22-pole ISDW VPMSMs, which further compares with a 12-slot/10-pole FSCW PMSM in terms of torque and torque density. In [WU15c], the variations of the optimized geometric parameters for VPMSMs with different pole ratios and winding pole numbers are presented. The torque production mechanism of VPMSMs with different pole ratios and winding pole numbers are investigated and analyzed in [ZOU16] [LI18b], but the influences of the end winding on torque density, efficiency, and power factor are not analyzed. Likewise, it has been demonstrated in [XU15] that the ISDW VPMSMs have higher torque per machine volume than the FSCW VPMSMs, while the volume of end winding is also not considered.

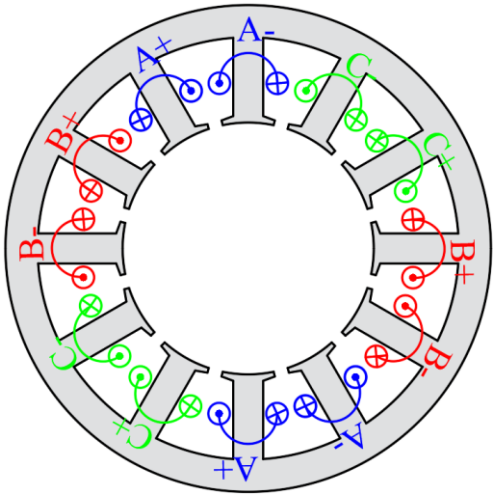

(a) 10-pole FSCW.

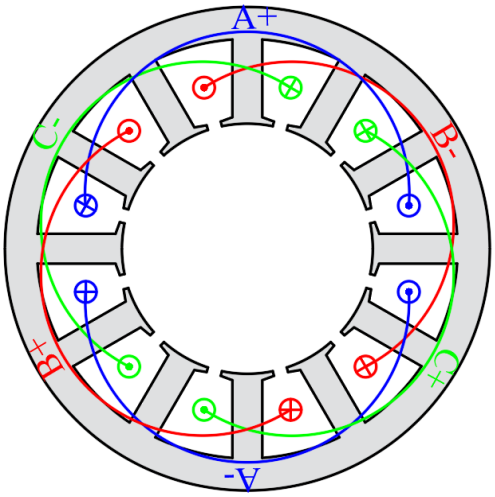

(b) 2-pole ISDW.

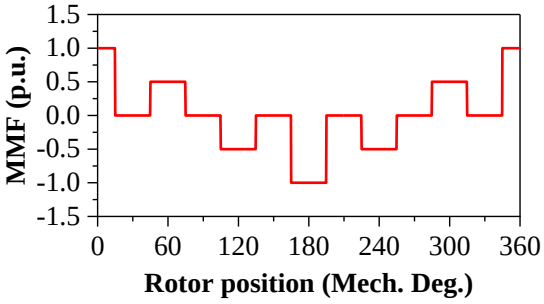

(c) MMF of 10-pole FSCW.

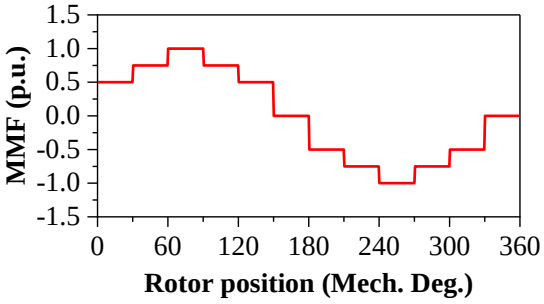

(d) MMF of 2-pole ISDW.

(e) Spectrum for MMF of 10-pole FSCW.

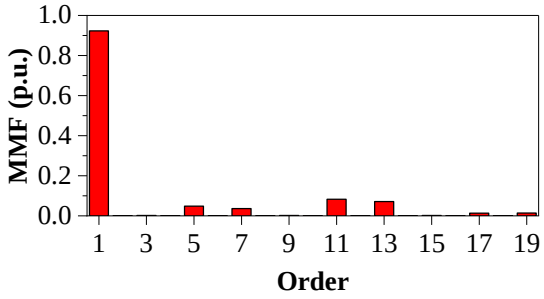

(f) Spectrum for MMF of 2-pole ISDW.

Fig. 1.22. 2-pole ISDW and 10-pole FSCW, as well as corresponding MMF waveforms (I_b=I_c= -0.5I_a) and spectra.

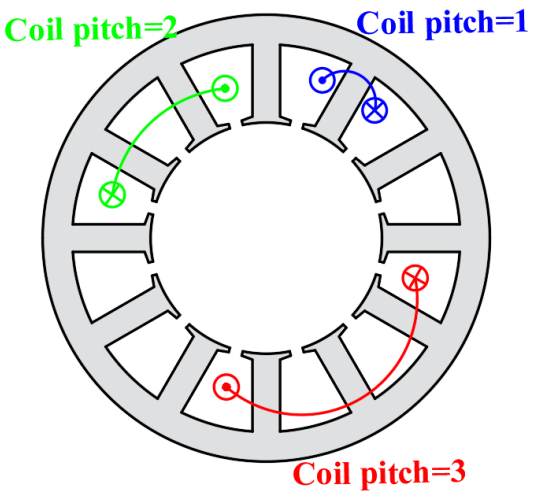

Fig. 1.23. Illustration of winding configurations with different coil pitches.

The electromagnetic performances of PMSMs considering the influences of end winding in terms of machine optimization, machine volume, end winding flux leakage, and power factor simultaneously have not been evaluated systematically. Furthermore, in some applications with limited space, torque density is one of the most critical machine design parameters, which is strongly affected by the axial end winding length.

1.3.2.3. **Stator structures**

From the perspective of stator structures, stators can be divided into the closed-slot stator, the semi-closed-slot stator, the open-slot stator, and the multi-tooth stator.

The field modulation effect of different stator slot structures on NSP and/or CP PM machines is investigated [ZHU18a] [LI18a] [LI18b] [LI23a], and the results show that the slot-opening ratio has a great influence on the field modulation effect. Fig. 1.24 shows the CP PM machines with different stator slot structures in [ZHU18a].

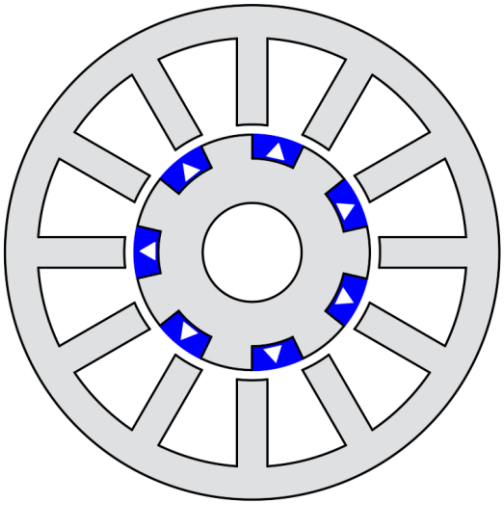

(a) Open-slot.

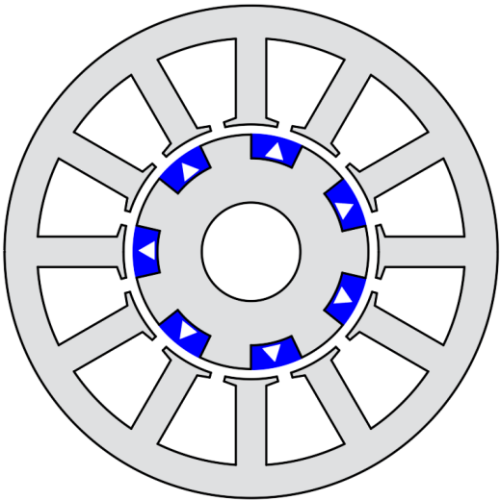

(b) Semi-closed-slot.

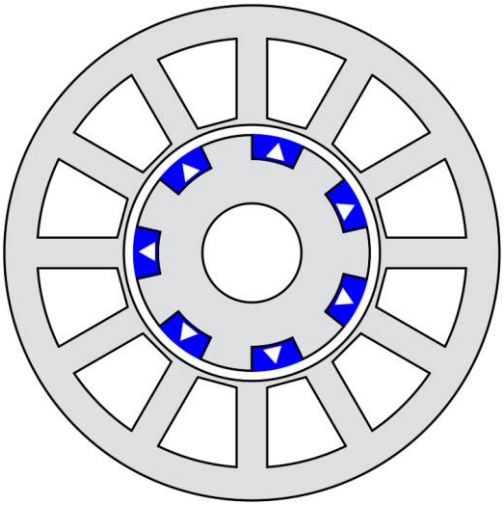

(c) Closed-slot.

Fig. 1.24. CP PM machines with different stator slot structures in [ZHU18a].

For the multi-tooth stator, the stator tooth is split into several dummy slots to produce the multipole effect. Together with non-overlapping FSCW, VMs with multi-tooth stator structures

have the advantages of short axial end winding, high torque/power density, high efficiency, and enhanced flux weakening capability compared with their overlapping winding counterparts [LI10] [HO11] [XU15] [ZOU17a] [LI19c]. Furthermore, PM utilization and torque output capability can be enhanced when combined with a CP rotor structure [CHU15] [JAN19].

The torque characteristics of NSP SPM VMs with different stator slot and multi-tooth numbers are investigated and the optimal multi-tooth number is determined [OKA13] [ZOU17a] [LI19c] [XIE19] [YU19]. Fig. 1.25 shows the NSP VPMSMs different multi-tooth numbers.

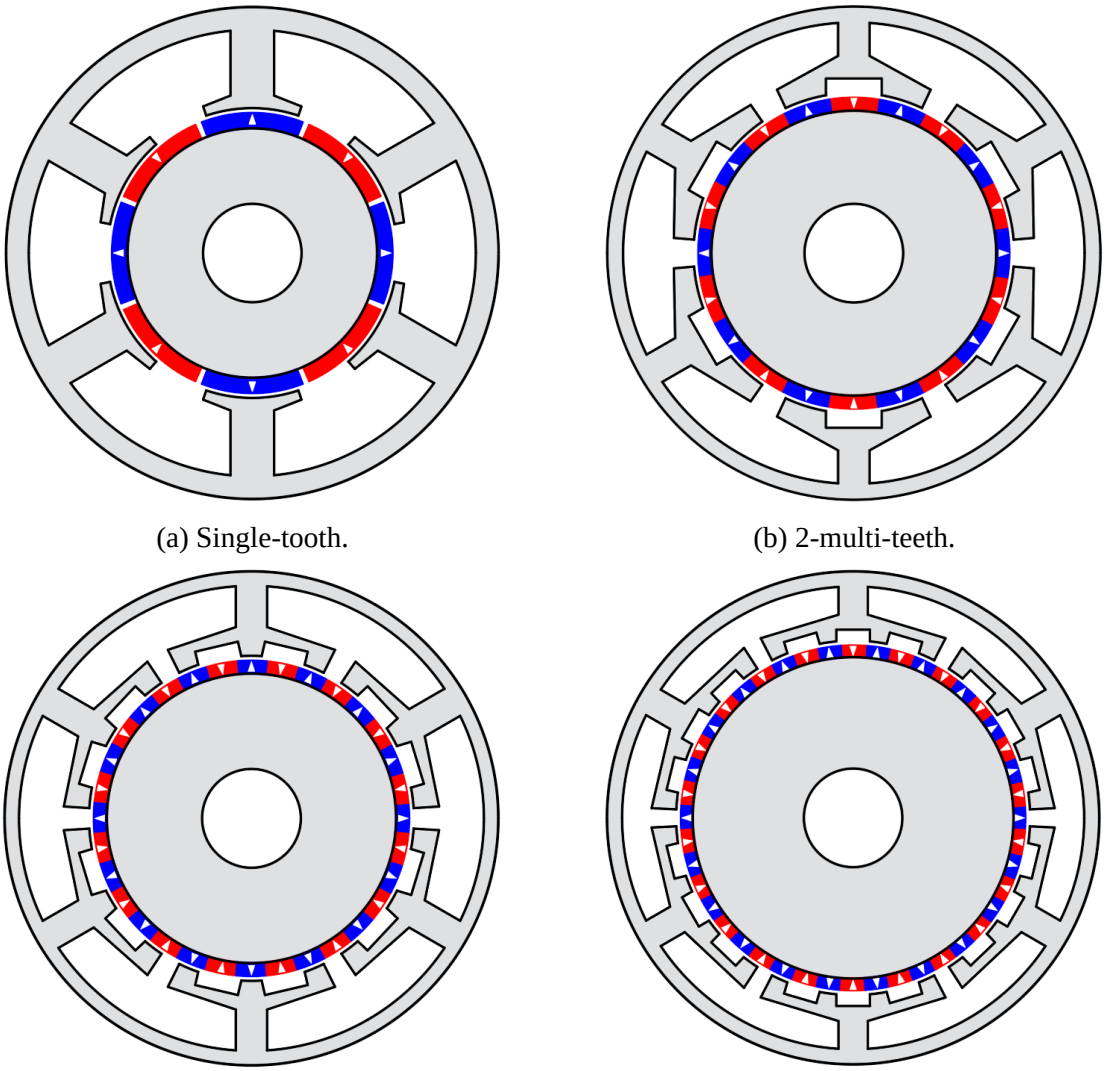

(a) Single-tooth. (b) 2-multi-teeth.

(c) 3-multi-teeth. (d) 4-multi-teeth.

Fig. 1.25. NSP VPMSMs with different multi-tooth numbers.

Some special stator tooth structures are proposed. The coding-shaped tooth can introduce specific permeance harmonics to improve torque density, cogging torque, and torque ripple [FAN22]. The uniform distributed split-teeth can generate multiple working harmonics and improve power factor, torque, and fault-tolerant performance[DU22]. The unequal element coil

and stator teeth unit better exploit multiple flux density harmonics to enhance back EMF as well as torque output capability [FAN23].

Field modulation effects and torque components of CP VPMSMs with 2 multi-teeth are investigated in [XU17] [JAN19] [ZHO19a] [ZHA20] [LI22] which shows that the torque output capacity can be enhanced compared with conventional NSP VMs and single-tooth stator VMs. The stator with 4-multi-teeth is proposed to suppress the magnetic unbalance caused by the CP rotor structure [CHU11]. Fig. 1.26 shows the VPMSMs with the multi-tooth stator and CP rotor proposed in [CHU11] and [JAN19].

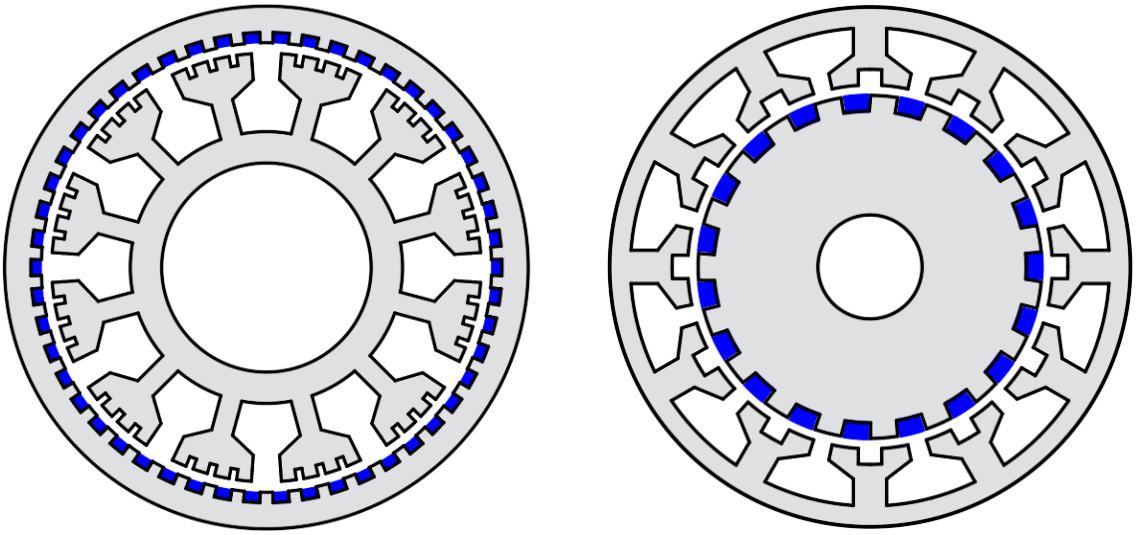

(a) 4-multi-tooth [CHU11]. (b) 2-multi-tooth [JAN19].

Fig. 1.26. CP VPMSMs with multi-tooth stator.

In conclusion, the torque output and torque density of VPMSMs can be enhanced by using FSCW, CP rotor, and multi-tooth stator. The detailed description of the literature review in this section is summarized in Table 1.2.

Table 1.2 Literature Review on FS VPMSMs

Reference	Feature	Remark
Rotor topologies		
[TAP03] [CHU12] [CHU15] [LI18a] [WU14b] [ONS17] [LI21] [XU17] [JAN19] [ZHO19a] [LI22]	CP in SPM	• CP: reduce around 30-40% of PM volume but average torque will be slightly reduced in FS PMSMs. • Wider constant power range under rated load. • CP structure can generate higher modulated torque and enhance torque output capacity for VMs with higher rotor pole numbers.
[WU14b] [ZHA19] [LI20] [LI23b] [ZHA20] [ZHO19b] [CAI21] [ONS18] [LI19b] [LIU18c] [REN18] [LI20]	CP in IPM	• Reduce PM volume and increase torque simultaneously. • Higher efficiency. • Lower cogging torque. • Better demagnetization withstand capability. • Wider constant power region. • Better flux-weakening capability.
[ISH95] [LI15a] [ALL20] [ZHO22] [WAN19] [LI19a] [DAJ20] [BAB20] [XU21] [WU15b] [GAO16] [LI18c] [LI15b] [LIU14] [XU16]	CP in other topologies	• CP in outer rotor, stator-PM, Halbach-array, dual rotor, dual stator, dual-PM, hybrid-pole, and memory machines.
Winding configurations		
[XU15] [LIU17] [LI16]	ISDW	• Offers potential higher torque. • Fewer higher order harmonics. • Better utilize reluctance torque. • Better field modulation effect.

[WU14a] [REF05] [REF06] [BIA09b] [REF10] [RED12]	FSCW	• High-power and torque density and high efficiency. • Short end turns and high slot fill factor. • Better flux weakening capability. • Easy for modularity.
[WAN14a] [SUN19] [LIU18b] [LI18b]	Two-slot coil pitches	• Compromise between end winding and torque capacity. • Eliminate and/or reduce undesirable space harmonics for FSCW.
[WU15c] [ZOU16] [HUA18] [HE21]	Different coil pitches	• Effects of different coil pitches.
Stator structures		
[ZHU18a] [LI18a] [LI18b] [LI23a]	Different slot opening	• Slot opening has a great influence on field modulation effect.
[LI10] [HO11] [XU15] [ZOU17a] [LI19c] [OKA13] [XIE19] [YU19]	Multi-tooth stator and NSP rotor	• Enhanced torque output capability and torque density. • Enhanced flux weakening capability. • Reduce torque ripple.
[CHU11] [JAN19] [XU17] [ZHO19a] [ZHA20] [LI22]	Multi-tooth stator and CP rotor	• Enhanced torque output capability and torque density. • Save PM volume and higher PM utilization.
[FAN22] [DU22] [FAN23]	Special stator tooth	• Coding-shaped tooth, uniformly distributed split-teeth, and unequal element coil and stator teeth unit to introduce specific permeance harmonics. • Larger torque density, and smaller cogging torque and torque ripple. • Improve power factor, torque, and fault-tolerant performance.

1.3.3. Unipolar end leakage flux

Unbalanced magnetic circuits, i.e., unbalanced equivalent north and south poles, exist in the CP structure and will cause unipolar end leakage flux, resulting in magnetization of end region components and threaten the safety of the system [WU16] [GE16] [ZHU17] [WAN19] [LI19d] [LI19e] [QI22a] [QI22b]. By way of example, both shaft and bearing will be magnetized by unipolar end leakage flux and attract screws and nuts in the end region. Meanwhile, this issue will be more severe for machines with short stack lengths and high magnetic saturation levels [WU16] [WAN19]. Up to date, unipolar end leakage fluxes in various CP PMSMs have been investigated, including spoke-type IPM [GE16], CP partitioned stator flux reversal PMSM [WU16], CP FS concentrated winding PMSM [WAN19] [LI19d] [LI19e] [QI22a], and CP VPMSM [CHU11] [XU23].

To mitigate unipolar end leakage fluxes in conventional CP PMSMs, several methods have been developed, e.g., step-staggered rotor structure [GE16] and special magnetic pole sequences [WAN19] [LI19d] [LI19e]. In [GE16], two spoke-type CP rotors with equal stack length are step-staggered where iron ribs in two rotors are circumferentially staggered by one pole pitch as shown in Fig. 1.27. Staggered iron ribs provide inward and outward paths for end leakage flux, which is supposed to travel through the end shaft, effectively reducing unipolar leakage flux in the end region. However, staggered rotors increase the manufacturing complexity of the machine. Novel pole sequences are employed in CP FS concentrated winding PMSMs, including N-Iron-N-Iron-N-S-Iron-S-Iron-S, Iron-S-Iron-S-Iron-Iron-N-Iron-N-Iron, and N-S-N-Iron sequences [WAN19] [LI19d] [LI19e] as shown in Fig. 1.28. The end leakage flux generated by the north and south consequent poles are opposite in polarity and canceled each other. However, the new pole sequences may also cause large subharmonics of air-gap flux density and reduced torque. The higher PM volume will also reduce the PM utilization (average torque per PM volume) compared with its conventional CP counterpart.

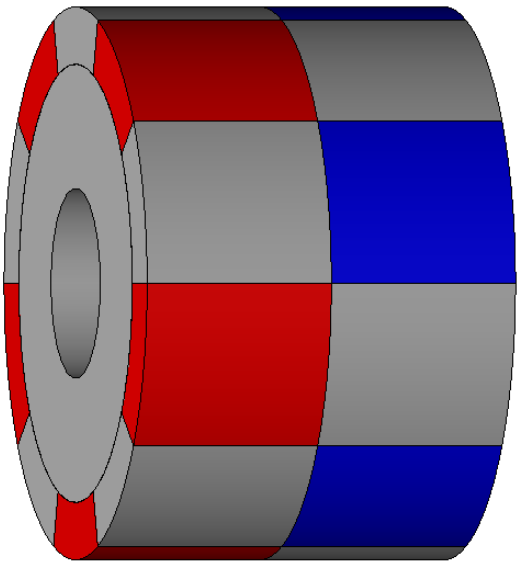

Fig. 1.27. Step-staggered rotor structure [GE16].

Unipolar end leakage flux in CP VPMSMs has also been investigated [CHU11] [XU23]. It has been reported in [CHU11] that unipolar end leakage flux becomes much more serious for external rotor CP VPMSMs, using non-magnetic material to replace the magnetic rotor end-cap is suggested but without any further investigation. For internal rotor CP VPMSM in [XU23], by combining two conventional CP structures with opposite polarities as shown in Fig. 1.29, half of the circumferential rotor with north-pole PMs, while the other part with south-pole PMs, unipolar end leakage flux in CP VPMSM can be reduced. The PMs with opposite excitation directions improve the unbalanced magnetic circuits, leading to fewer leakage flux in the end region. However, the iron loss, cogging torque, and torque ripple are deteriorated compared with its conventional counterpart.

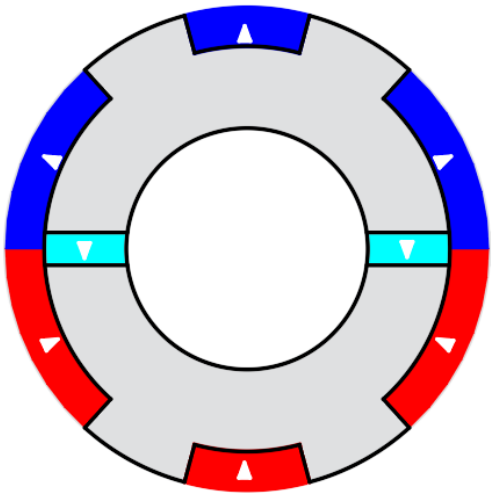

(a) [WAN19].

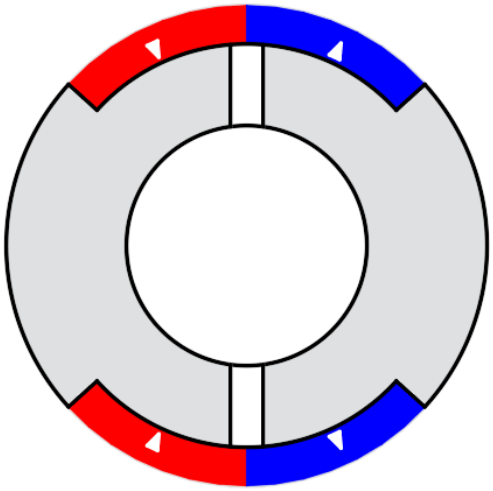

(b) [LI19d].

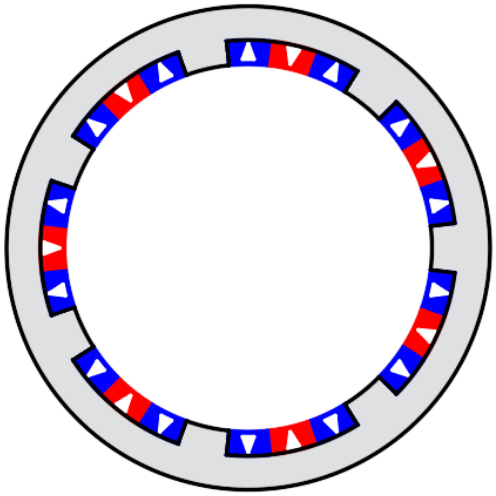

(c) [LI19e].

Fig. 1.28. Special magnetic pole sequences.

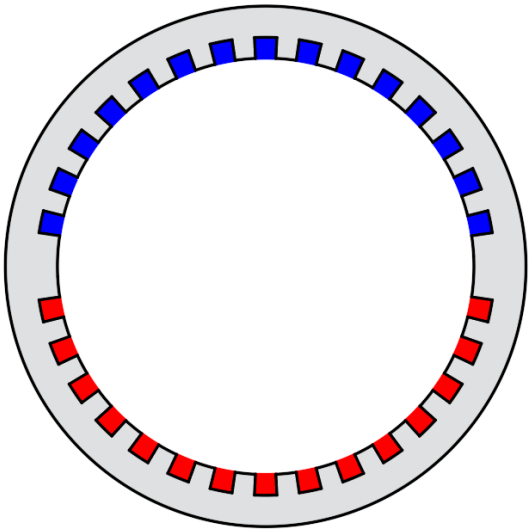

Fig. 1.29. Combining two conventional CP structures with opposite polarities [XU23].

The detailed description of the literature review in this section about suppressing unipolar end leakage is summarized in Table 1.3.

1.3.4. Thermal management of PMs

The SPMSM is one of the most preferred choices due to its simple structure, where PMs are mounted on the surface of the rotor and adjacent to the air-gap.

However, the PM eddy current loss in SPMSMs may be significant since PMs are directly exposed to the ARMF, particularly in high-speed and high pole-pair SPMSMs [MA19] [CHE17]. Furthermore, the rotor in SPMSMs usually has limited heat dissipation capability, and thus, the induced PM loss more easily causes the risk of over-temperature. Besides, the widely employed NdFeB PM has a high electrical conductivity and a negative temperature coefficient of the coercive field strength, which further aggravates the thermal effect and demagnetization risk [ZHA18].

Therefore, accurate information on PM temperature distribution and PM local hotspots is always important to prevent unexpected demagnetization and improve machine reliability. To date, it has been widely investigated from the perspective of thermal analysis [KRA14] [GRO15] [LIA22a] [LIA22b] [LIA22c]. The early study [KRA14] usually assumes that PM temperature is evenly distributed. However, the subsequent research [GRO15] highlights that the SPM has a highly non-uniform PM temperature distribution in the radial direction due to the skin effect, while it still assumes the temperature is identical in the circumferential direction. More recently, it has been demonstrated in [LIA22a] [LIA22b] [LIA22c] that the 12-slot/10-

pole PMSM has asymmetric PM temperature distributions in both radial and circumferential directions, and the local PM hotspot temperature is concentrated on one side of the PM outer edge. Moreover, it has also been reported in [ZHE22] that this asymmetric distribution is also affected by the current advancing angle. However, the mechanism for the asymmetric PM temperature distributions and locations of PM hotspots have not been fully revealed so far.

To elucidate the underlying reason for this phenomenon, the investigation should focus on the PM eddy current loss, which is the primary reason for PM temperature rises. There are two mainstreams to calculate the PM eddy current loss, i.e., the FEA method and the analytical method. As is well known, the FEA method is a common tool and exhibits high accuracy [CHE17] [ZHA18], while it cannot reveal the physical mechanism of asymmetric PM loss. On the other hand, the analytical method is an alternative approach [ZHU04] [ATA00] [DUB14] [OU19] [LIU16] [MAR08] [TON22] [ARU13], which can separate contributions of different spatial field harmonics and/or temporal current harmonics. Generally, the PM eddy current loss can be calculated analytically based on the Poynting theorem [ZHU04] or the Maxwell theorem [ATA00] [DUB14] [OU19] [LIU16] [MAR08] [TON22] [ARU13].

Firstly, the power dissipated due to the PM loss can be simply calculated by the real part of the Poynting vector [ZHU04], which is defined as the cross-product of vectors of electric and magnetic fields. However, the Poynting theorem is based on the average power flow, and thus, it cannot predict the distribution of eddy currents within PMs. In comparison, based on the Maxwell theorem, spatial eddy current distributions can be calculated by temporal derivations of the magnetic potential vector, which is solved by the Laplace equation [ATA00] [DUB14] [OU19] [LIU16]. Moreover, when the diffusion effect is considered, the Laplace equation needs to be replaced by Helmholtz's equation [MAR08] [TON22] [ARU13]. However, it is worth noting that analytical methods usually focus on the PM loss caused by the ARMF, while the PM remanence is usually neglected. Consequently, the interaction between ARMF and PM field and the resultant asymmetric PM eddy current loss distribution still cannot be obtained by analytical methods.

The detailed description of the literature review in this section about thermal management of PMs is summarized in Table 1.4.

Although there are various machine topologies, the scope of this thesis focuses on rotor-PM FS PMSMs and VPMSMs. Some challenges could be summarised as follows.

- The torque and torque density improvement through investigating rotor topologies, winding configurations, and stator structures.
- Unipolar end leakage suppression for CP rotor structure.
- Asymmetric PM eddy current loss density distribution and local hotspot.

Table 1.3 Literature Review on Suppressing Unipolar End Leakage

Reference	Feature	Remark
[GE16]	Step-staggered rotor	• Increase manufacturing complexity.
[WAN19] [LI19d] [LI19e]	Novel pole sequences	• Cause large subharmonics of air-gap flux density and reduced torque. • Higher PM volume and reduced PM utilization ratio.
[CHU11]	Multi-tooth inner stator	• Non-magnetic material for rotor end-cap is suggested.
[XU23]	Combining two CP structures with opposite polarities	• Iron loss, cogging torque, and torque ripple are deteriorated.

Table 1.4 Literature Review on Thermal Management of PMs

Reference	Feature	Remark
[CHE17] [ZHA18]	FEA for PM loss	• High accuracy but cannot reveal physical mechanism of asymmetric PM loss.
[ZHU04] [ATA00] [DUB14] [OU19] [LIU16] [MAR08] [TON22] [ARU13]	Analytical method for PM loss	• Based on Poynting theorem or Maxwell theorem. • Poynting theorem cannot predict distribution of eddy currents within PMs. • Analytical methods usually focus on PM loss caused by ARMF, while PM remanence is usually neglected. Cannot obtain asymmetric PM eddy current loss distribution caused by interaction between ARMF and PM field.
[KRA14]	Simplified LPTM	• Assume PM temperature is evenly distributed.
[GRO15]	Analytic thermal model	• Highly non-uniform PM temperature distribution in radial direction. • Assume PM temperature is identical in circumferential direction.
[LIA22a] [LIA22b] [LIA22c]	Hybrid analytical and LPTM	• Asymmetric PM temperature distributions in both radial and circumferential directions. • Local PM hotspot temperature is concentrated on one side of PM outer edge.
[ZHE22]	LPTM and FEA	• Asymmetric distribution is affected by current advancing angle.

1.4. Research Scope and Major Contributions

1.4.1. Research scope

This thesis focuses on rotor-PM FS PMSMs and VPMSMs with NSP and CP rotor structures, including torque and torque density enhancement, unipolar end leakage suppression, asymmetric PM eddy current loss distribution calculation, and PM local hotspot investigation. The arrangements of all chapters are illustrated in Fig. 1.30. The analyzed machine topologies of this thesis are summarized in Fig. 1.31.

Chapter 1

Various machine topologies of PMSMs in terms of winding configurations, stator structures, and rotor topologies are introduced. The challenges and corresponding research of FS PMSMs and VPMSMs are reviewed for further investigation.

Chapter 2

This chapter attempts to present a complete procedure from various machine optimization scenarios to electromagnetic performance analysis and provides a comprehensive and informative investigation regarding end winding effects on SPMSMs. The influences of different slot/pole number combinations, winding configurations, rotor PM topologies, as well as iron loss at different speeds, on the electromagnetic performances of SPMSMs are evaluated systematically. The analyses have been validated by experiments on the prototype NSP and CP PMSMs with different slot-pole number combinations.

Chapter 3

This chapter investigates the unipolar end leakage flux of CP PMSMs with different slot-pole number combinations and winding configurations. A simple and effective composite rotor structure, consisting of a non-magnetic shaft and/or a non-magnetic ring inside the rotor core (which could be integrated into a single shaft), is proposed to reduce the unipolar end leakage flux without sacrificing the torque capability. The analyses have been validated by experiments on the prototype CP PMSMs with different slot-pole number combinations, magnetic/non-magnetic shafts, and conventional/composite rotors. The analyses are validated experimentally based on two existing prototypes.

Chapter 4

This chapter systematically investigates the effect of multi-tooth numbers on electromagnetic performances of NSP and CP VPMSMs, including average torque, overload torque capability, PM utilization, loss, efficiency, and power factor, etc. In particular, the influence of multi-tooth numbers on the unipolar end leakage flux of CP VPMSMs is investigated. The prototypes with 2 and 3 multi-tooth numbers are manufactured and tested to verify the analyses.

Chapter 5

This chapter investigates the mechanism of asymmetric PM eddy current loss and temperature distributions of SPMSMs with different slot/pole number combinations. An FEA based harmonic restoration method is utilized to evaluate and quantify the contributions of individual armature reaction spatial harmonics to asymmetric PM eddy current loss and temperature distributions caused by the interaction between the armature reaction and PM field. Consequently, the resultant PM local hotspot temperature has been calculated through the 3-D thermal finite element method. Two prototypes are manufactured, and the corresponding electromagnetic and thermal tests are carried out to verify the validity of the analyses.

Chapter 6

This chapter investigates the effect of armature reaction on asymmetric distributions of PM eddy current loss and temperature in a double-layer V-shape IPMSM for electric vehicles. The LPTM and analytical method are established to predict the average temperature distribution and identify the hotspots in the windings. 2-D FEA is used to calculate PM eddy current loss distributions and other loss density distributions, which are coupled into the 3-D thermal FEA model to investigate the PM temperature distribution.

Chapter 7

The general conclusions will be drawn and potential future work will be proposed.

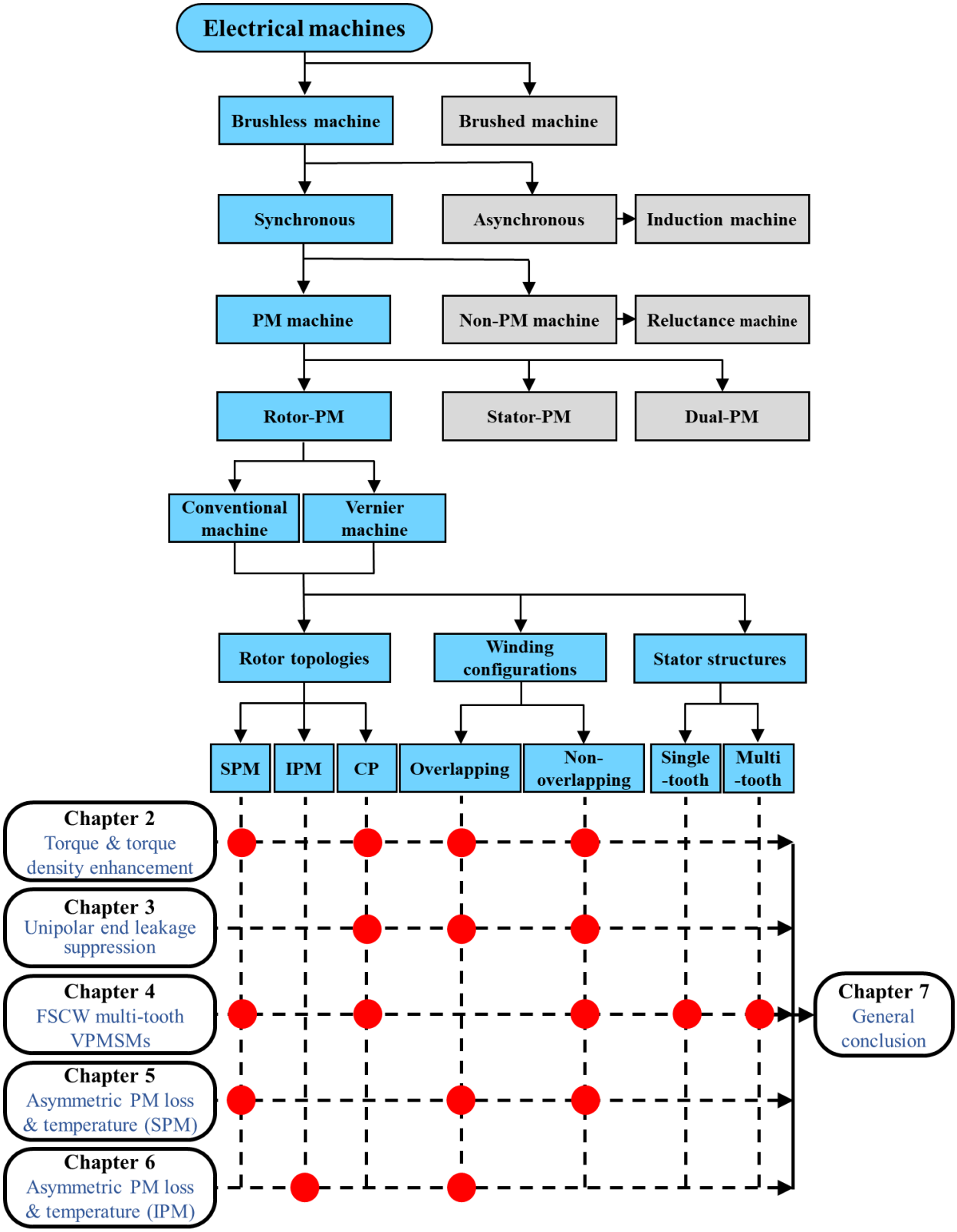

Fig. 1.30. Arrangement of thesis.

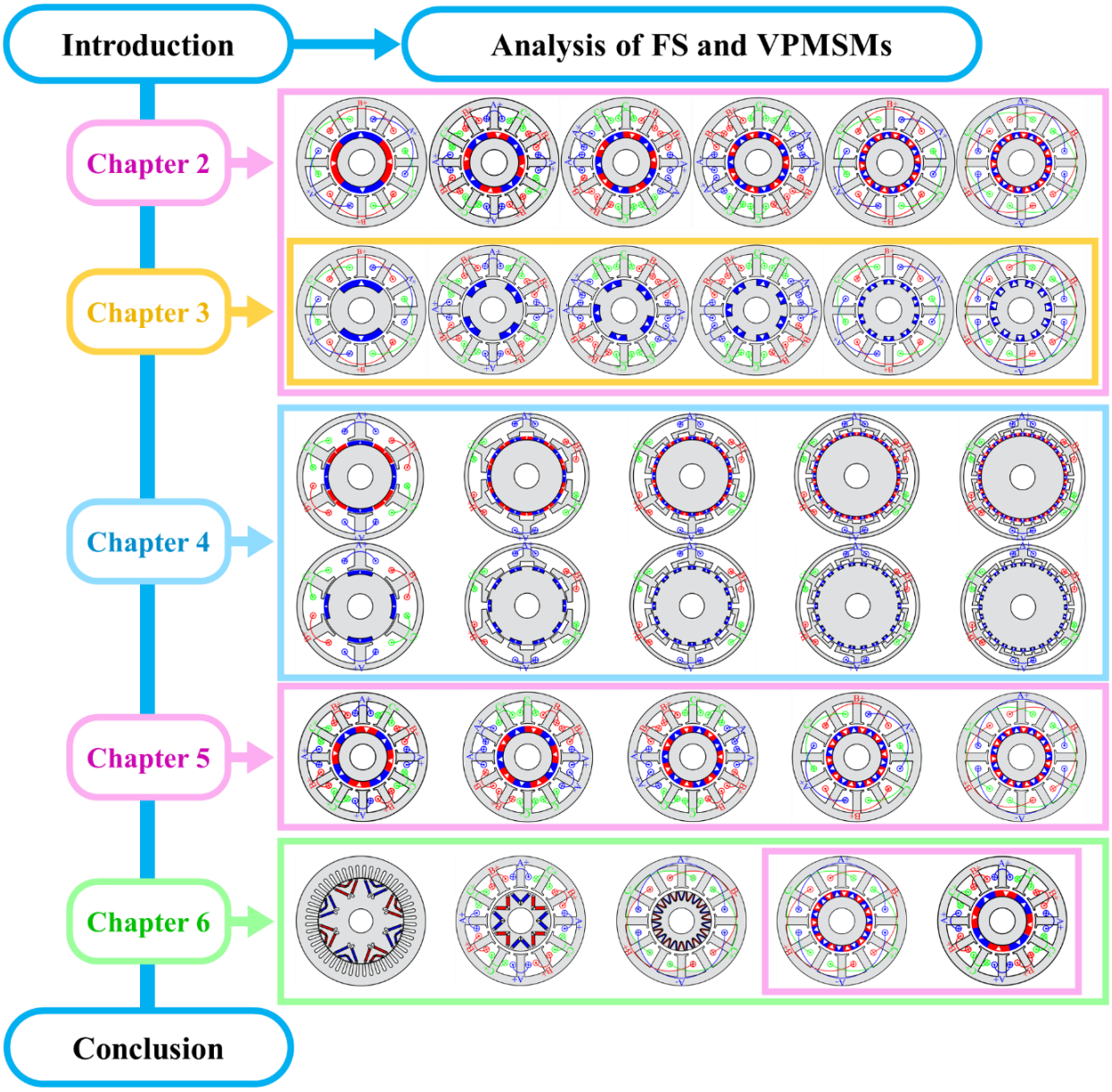

Fig. 1.31. Summary of analyzed machine topologies in thesis.

1.4.2. Major contributions

The main contributions of this thesis can be summarized as follows:

1. A complete procedure from various machine optimization scenarios (considering/neglecting end winding, different coil pitches, and considering/neglecting iron loss under different speeds) to electromagnetic performance analysis is provided for SPMSMs with different slot/pole number combinations and rotor topologies (NSP and CP).
2. A simple and effective composite rotor structure, consisting of a non-magnetic shaft and/or a non-magnetic ring inside the rotor core (which could be integrated into a single shaft), is proposed to reduce the unipolar end leakage flux of CP PMSMs without sacrificing the torque capability.
3. The effects of multi-tooth numbers on the electromagnetic performances of NSP and CP VPMSMs are investigated, as well as the influence of multi-tooth numbers on the unipolar end leakage flux of CP VPMSMs.
4. An FEA based harmonic restoration method is utilized to evaluate and quantify the asymmetric PM eddy current loss caused by the interaction between the armature reaction and PM field. The resultant PM local hotspot temperature is also calculated.
5. The effect of armature reaction on asymmetric PM eddy current loss and temperature distributions in a double-layer V-shape IPMSM for electric vehicles is investigated.

Published and submitted journal papers

[1] Z. Q. Zhu, **Y. Zheng**, Y. Liu, F. Wei, D. Liang, L. Huang, and H. Liu, "Effect of end-winding on electromagnetic performance of fractional slot and vernier PM machines with different slot/pole number combinations and winding configurations," *IEEE Access*, vol. 10, pp. 49934-49955, 2022. **(Chapter 2)**

[2] **Y. Zheng**, Z. Q. Zhu, D. Liang, H. Xu, Y. Zhou, H. Liu, and L. Chen, "Analysis and reduction of unipolar end leakage flux in consequent-pole PM machines," *IEEE Trans. Ind. Appl.* Accepted. **(Chapter 3)**

[3] **Y. Zheng**, Z. Q. Zhu, H. Xu, J. Yan, and D. Liang, "Optimal multi-tooth numbers for vernier PM synchronous machines," *IEEE Access*, vol. 12, pp. 89599-89612, 2024. **(Chapter 4)**

[4] **Y. Zheng**, D. Liang, Z. Q. Zhu, J. Yan, Y. Zhou, H. Liu, and H. Xu, "Asymmetric PM eddy current loss and temperature distributions of SPMSMs," *IEEE Trans. Ind. Appl.* Under review. **(Chapter 5)**

Conference papers

[5] **Y. Zheng**, D. Liang, Z. Q. Zhu, H. Liu, and Y. Zhou, "Effect of armature reaction on asymmetric PM loss and temperature distributions in V-shape interior permanent magnet synchronous machines," in 2022 *2nd Int. Conf. Sustain. Mobility Appl., Renew. Tech.*, 2022, pp. 1-10. **(Chapter 6)**

[6] **Y. Zheng**, Z. Q. Zhu, D. Liang, Y. Zhou, H. Liu, and L. Chen, "Analysis and reduction of unipolar end leakage flux in consequent-pole Vernier and fractional slot PM machines," *Proc. IEEE Int. Electric Mach. Drives Conf.*, 15-18 May 2023, pp. 1-7.

[7] **Y. Zheng**, D. Liang, Z. Q. Zhu, Y. Zhou, H. Liu, and H. Xu, "Effect of armature reaction on asymmetric PM eddy current loss and temperature distributions of SPMSMs accounting for slot/pole number combinations," in *Proc. IEEE Energy Convers. Congr. Expo. Conf.*, Nov. 2023, pp. 4008-4015.

[8] F. Wei, Z. Q. Zhu, **Y. Zheng**, and H. Xu, "Comparative study of statorPM and dual-PM consequent-pole hybrid excited flux-reversal machines," in 2022 *Int. Conf. Electr. Mach. Syst.*, 2022, pp. 1-5.

[9] D. Liang, Z.Q. Zhu, A. Dey, Z. Ran, and **Y. Zheng**, "Comparison of surface-mounted and switched-flux PM machines accounting for thermal characteristics and limits," in 2023 *Int. Conf. Electr. Mach. Syst.*, 5-8 Nov. 2023.

[10] A. Dey, D. Liang, Z. Q. Zhu, Y. Zhou, and **Y. Zheng**, "Effect of Cooling Strategies on Performance of Rotor PM and Stator PM Machines," in 2023 *Int. Conf. Electr. Mach. Syst.*, 2023, pp. 3117-3122

CHAPTER 2
EFFECTS OF END WINDING AND ROTOR PM TOPOLOGIES ON FRACTIONAL SLOT AND VERNIER PM SYNCHRONOUS MACHINES

Owing to high torque density and high efficiency, PM machines have been extensively employed in various applications, e.g. aerospace, domestic appliances, electric and hybrid electric vehicles, wind power generation, etc. [ZHU07] [PEL12] [POL13] [HE22]. Amongst different types of PM machines, radial-field rotor PM machines are the most common topology in terms of electromagnetic performance, manufacturability, cost, etc. For radial-field rotor PM machines, PMs could be located either on the surface or the interior of the rotor. To date, SPMSMs are widely used due to their simple structure since the PMs are mounted on the rotor surface and adjacent to the air-gap. Meanwhile, SPMSMs are also preferred in ultra high-speed applications although a rotor sleeve is required to withstand the centrifugal force [HE22] [OU21]. In industrial applications with limited space, torque density is one of the most critical machine design parameters, which is strongly affected by the axial end winding length.

In this chapter, the effects of end winding on the electromagnetic performance of SPMSMs (including vernier machines) with different slot/pole number combinations and winding configurations are analyzed and compared, attempting to present a complete procedure from various machine optimization scenarios to electromagnetic performance analysis and provide a comprehensive and informative reference regarding end winding effects on SPMSMs. Moreover, the electromagnetic performances of the conventional NSP and CP SPMSMs are compared.

This chapter has been published by IEEE ACCESS [ZHU22]:

[ZHU22] Z. Q. Zhu, Y. Zheng, Y. Liu, F. Wei, D. Liang, L. Huang, and H. Liu, “Effect of end-winding on electromagnetic performance of fractional slot and vernier PM machines with different slot/pole number combinations and winding configurations,” *IEEE Access*, vol. 10, pp. 49934-49955, 2022.

2.1. Introduction

From perspective of winding configurations, the SPMSMs can be configured by either overlapping DW or overlapping/non-overlapping CW, as introduced in Chapter 1. On the one hand, IS SPMSMs, having integral slot numbers per pole per phase, could achieve high winding factors by using the DW configurations, i.e., they could achieve the largest fundamental harmonic winding factor for maximum average output torque. Since an ISDW SPMSM has more sinusoidal MMF waveform with fewer higher order harmonics, it is beneficial for reducing iron and PM eddy current losses [RED12] [REF10]. On the other hand, FS PMSMs which have fractional slot numbers per pole per phase have been extensively investigated so far. In comparison to ISDW SPMSMs, FSCW SPMSMs have the advantages of high power and torque densities, high efficiency, lower torque ripple, and enhanced flux weakening capability [ZHU07] [REF10]. Meanwhile, it has shorter end winding and lower copper usage. However, FSCW SPMSMs result in abundant sub-harmonic field contents, which lead to higher iron and PM losses [BIA09] [WU14].

Furthermore, to tradeoff between the winding factor and the end winding length, SPMSMs with different coil pitches have also been investigated [WAN14a] [WAN14b] [SUN19] [HUA18]. In [WAN14a], windings with two slot coil pitches are used for PMSMs to eliminate and/or reduce undesirable space harmonics resulting from nonoverlapping FSCW. [WAN14b] [SUN19] investigate the feasible slot/pole number combinations of SPMSMs with two slot-pitch. The influences of windings with different coil pitches for flux reversal PMSMs are compared in [HUA18]. Meanwhile, [HE21] compares the small-size 6-slot/2-pole high-speed SPMSMs with one, two, and three coil-pitch windings and underpins that the two coil-pitch winding is the promising candidate for high-speed PMSMs.

Besides, VPMSMs are one of the FSCW SPMSMs with special slot/pole number combinations, typically with pole numbers higher than slot numbers. VPMSMs have been gaining more attention recently due to their high torque resulting from field modulation and magnetic gearing effects [ZHU18a] [LI18a] [LIU19] [LIU18a]. In [LIU18b], the FS VPMSMs having two slot-pitch coils are developed to improve the power factor and achieve a compromise between axial end winding length and torque capacity. [LI16] proposes a general instantaneous torque equation of VPMSMs based on a 12-slot/22-pole ISDW VPMSMs, which further compares with a 12-slot/10-pole FSCW SPMSM in terms of torque and torque density. In [WU15], the variations of the optimized geometric parameters for VPMSMs with different pole ratios and

winding pole numbers are presented. The torque production mechanism of VPMSMs with different pole ratios and winding pole numbers is investigated and analyzed in [ZOU16] [LI18b], but the influences of the end winding on torque density, efficiency, and power factor are not analyzed. Likewise, it has been demonstrated in [XU15] that the ISDW VPMSMs have higher torque per machine volume than the FSCW VPMSMs, while the volume of end winding is also not considered.

The electromagnetic performances of SPMSMs considering the influences of end winding in terms of machine optimization, machine volume, end winding flux leakage, and power factor simultaneously have not been evaluated systematically. Furthermore, in some applications with limited space, torque density is one of the most critical machine design parameters, which is strongly affected by the axial end winding length. To address this issue, based on the common 12-slot ISDW and FSCW SPMSMs (including VPMSMs), this chapter comprehensively evaluates the influences of different slot/pole number combinations, winding configurations, rotor PM topologies, as well as iron loss at different speeds, on their electromagnetic performances, with particular concerns on the effects of end winding on torque, torque density, efficiency, inductance, and power factor. Overall, this chapter attempts to present a complete procedure from various machine optimization scenarios to electromagnetic performance analysis and provides a comprehensive and informative reference regarding end winding effects on SPMSMs.

The main contributions of this chapter can be summarized as follows:

1. This chapter attempts to present a complete procedure from various machine optimization scenarios to electromagnetic performance analysis and provides a comprehensive and informative reference regarding end winding effects on SPMSMs with different slot/pole number combinations.
2. The electromagnetic performances of SPMSMs considering the influences of end winding in terms of optimal coil pitch, machine optimization, machine volume, end winding flux leakage, and power factor simultaneously, are systematically evaluated.
3. The iron loss is taken into consideration during the machine optimization under different speeds, and corresponding electromagnetic performances are compared with those neglecting iron loss.
4. The electromagnetic performances, advantages, and disadvantages of SPMSMs with north-south pole and consequent pole rotors are compared.

This chapter is organized as follows. Firstly, machine topologies, corresponding EMF phasor diagrams, and winding connections of six SPMSMs with 12-slot and different pole numbers, i.e., 12-slot/8-pole (12s/8p), 12-slot/10-pole (12s/10p), and 12-slot/14-pole (12s/14p) FSCW SPMSMs, and 12-slot/4-pole (12s/4p), 12-slot/20-pole (12s/20p), and 12-slot/22-pole (12s/22p) ISDW SPMSMs, are presented in section 2.2. Then, six machines are optimized for maximum average torque with the same active lamination stack length and different coil pitches under fixed 40 W copper loss neglecting/considering end winding by using GA in 2-D FEA, as well as considering iron loss under different speeds during optimization in section 2.3. Afterward, the electromagnetic performances, including efficiencies, power factors, inductances, etc., of optimized SPMSMs are compared, as well as the effect of stack length on torque and torque density. Moreover, the consequent pole SPMSMs with 12-slot and different pole numbers are optimized and their electromagnetic performances are compared with their north-south pole counterparts in section 2.4. The analyses have been validated by experiments on the prototype in section 2.5 and this chapter is concluded in section 2.6.

2.2. Machine Topologies

FSCW and ISDW can be implemented in SPMSMs. Typical examples of cross-sections of the SPMSMs with different slot/pole number combinations and winding configurations are illustrated in Fig. 2.1. The SPMSMs with different coil pitches, i.e., 1, 2, and 3 slot pitches, will be investigated in section III.

The number of slots per pole per phase (q) is an integer in ISDW machines while a fraction in FSCW machines according to (2.1).

$$q=\frac{N_s}{2mp} \tag{2.1}$$

where N_s is the slot number, p is the number of pole pairs, and m is the phase number.

It should be noted that for 12s/20p and 12s/22p, the number of pole pairs in (2.1) is 2 and 1, respectively, which are the numbers of pole pairs of the armature windings. Therefore, for 12s/8p, 12s/10p, and 12s/14p FSCW SPMSMs, the corresponding q equals 1/2, 2/5, and 2/7, respectively. For 12s/4p, 12s/20p, and 12s/22p ISDW SPMSMs, the corresponding q equals 1, 1, and 2, respectively.

The star-of-slot theory [ALB13] can be used to obtain the winding layout by the phasors of coil EMFs. The coil EMF phasors of the six SPMSMs are shown in Fig. 2.2. For 12s/8p, the coils of one phase are located in separate slots. For 12s/10p, the phase consists of two adjacent coils with different directions and two opposite coils while the phase sequence for 12s/14p swaps compared with that for 12s/10p. The coil locations of 12s/4p and 12s/20p are the same because their pole numbers of stator armature windings are 4. For 12s/22p, the phase consists of two adjacent coils with the same direction and two opposite coils.

2.3. Machine Optimization

2.3.1. Neglecting end winding

Typical winding connections of six SPMSMs have been presented in Section 2.2. Furthermore, the winding connections for machines can be varied with different coil pitches, leading to different winding factors. In this Section, six SPMSMs are optimized for maximum average torque with the same active lamination stack length and different coil pitches to investigate the influence of coil pitch and winding factor on the performance of SPMSMs by using GA in FEA.

During the optimization, the stator outer diameter (d_{so}), lamination stack length (l_{fe}), air-gap length (δ), shaft diameter (d_{sh}), PM volume(v_{pm}), and pole arc to pole pitch ratio (p_{rPM}) are fixed, as listed in Table 2.1, while the stator inner diameter (d_{si}), the thickness of stator yoke (h_y), the width of stator tooth (w_t), and the stator slot opening width (b_{so}) will be globally optimized under fixed 40 W copper loss in the active part of winding by using GA in FEA. In general, the iron loss can be neglected in optimization if the machines operate at low speed. Therefore, the total copper loss is set as a constraint considering the thermal limitation of maximum winding temperature. For the analyzed small size machine with natural cooling condition, 40 W copper loss is selected. The thickness of the PM (h_{pm}) is determined by the stator inner diameter since the volume of PMs is fixed during the optimization. Geometric variables during the optimization are shown in Fig. 2.3.

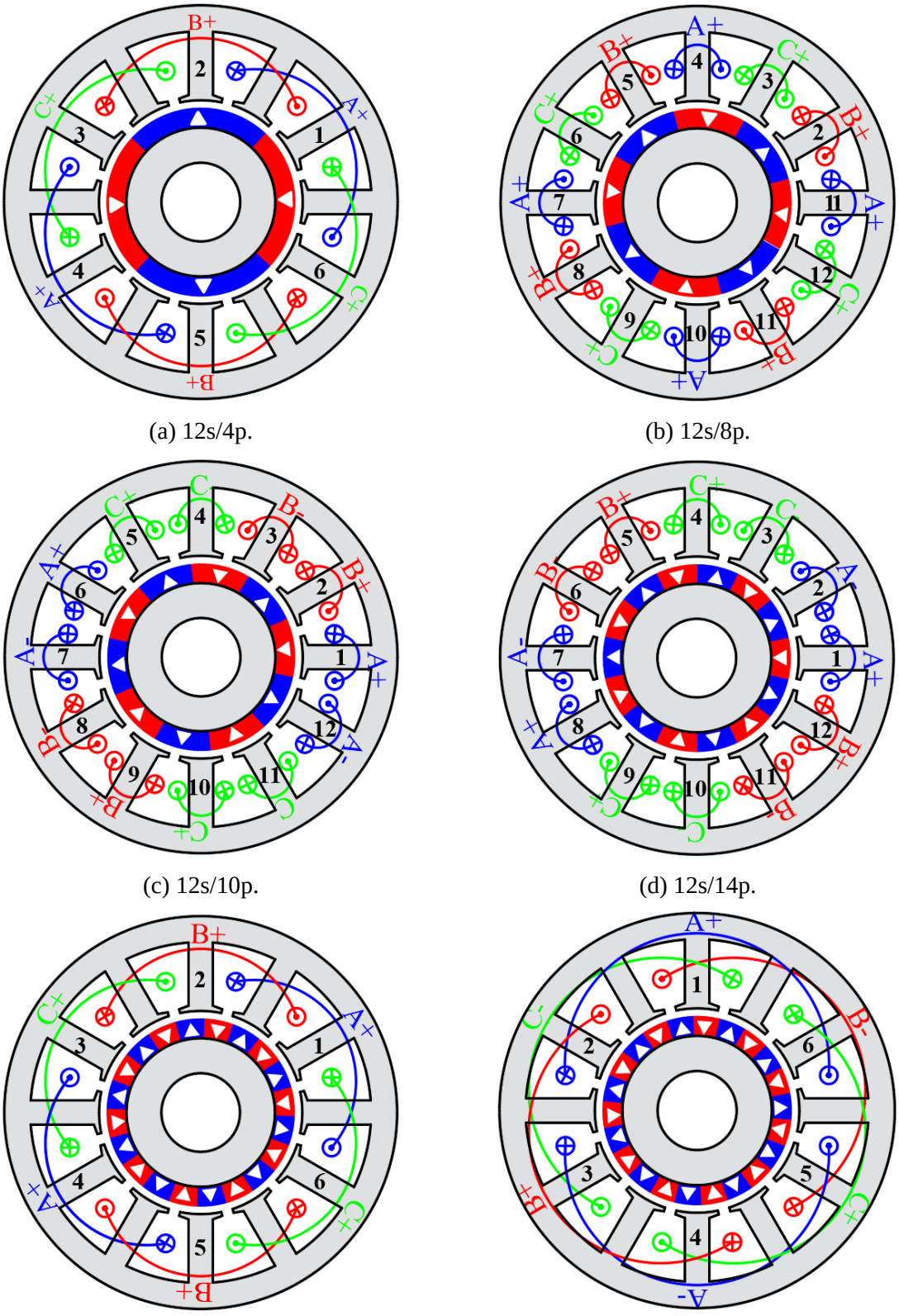

(a) 12s/4p. (b) 12s/8p.

(c) 12s/10p. (d) 12s/14p.

(e) 12s/20p. (f) 12s/22p.

Fig. 2.1. Machine topologies and winding connections of SPMSMs with different slot/pole number combinations.

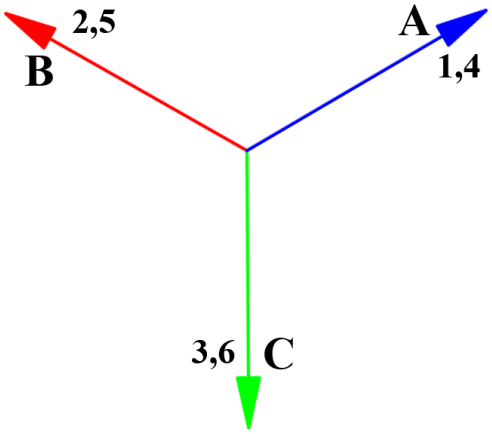

(a) 12s/4p.

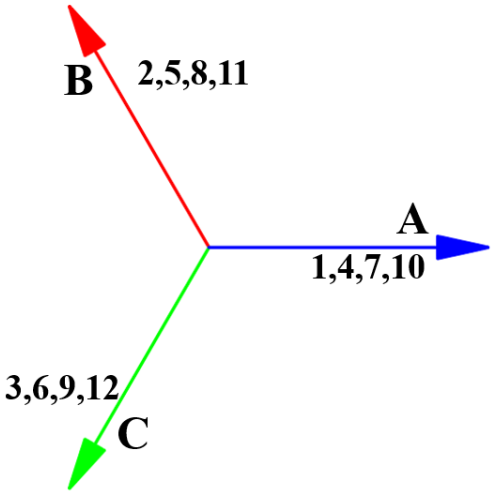

(b) 12s/8p.

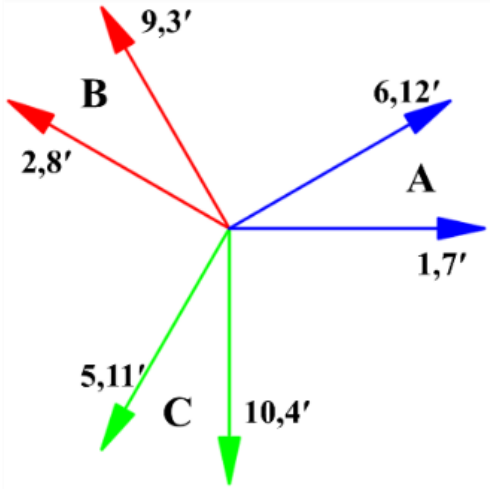

(c) 12s/10p.

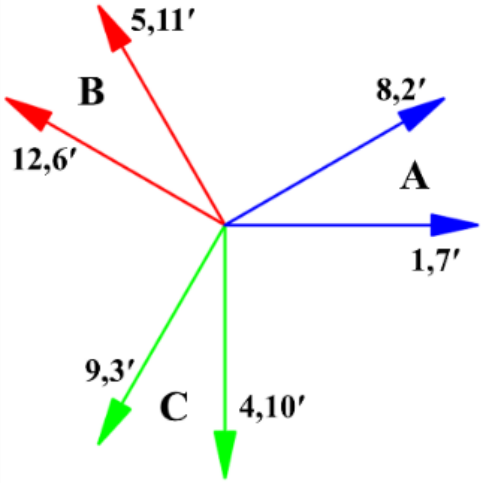

(d) 12s/14p.

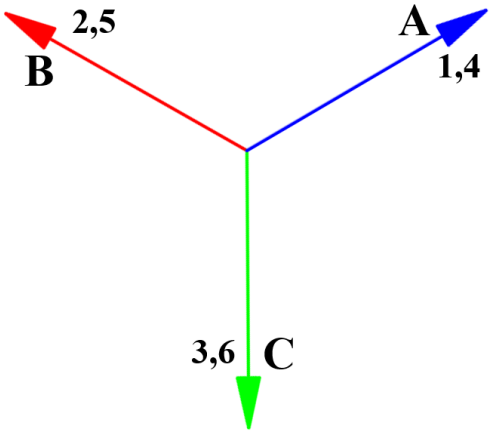

(e) 12s/20p.

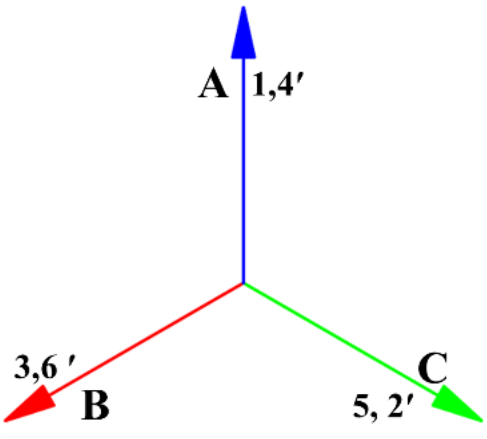

(f) 12s/22p.

Fig. 2.2. Coil EMF phasors of SPMSMs with different slot/pole number combinations.

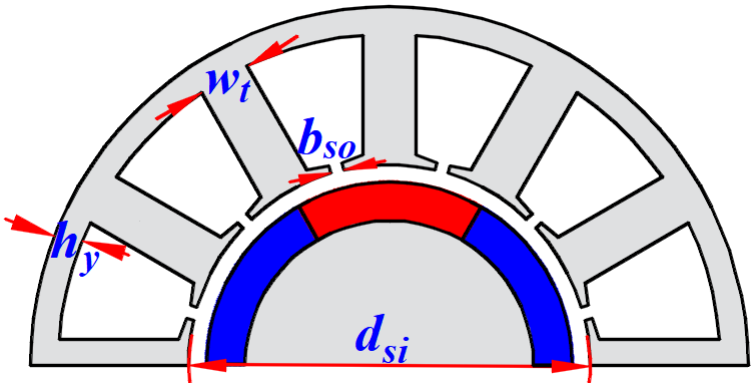

Fig. 2.3. Geometric variables for NSP SPMSM optimization.

Table 2.1 Fixed Geometric and Design Parameters During Optimization

Symbol	Parameters	Unit	Value
N_s	Number of stator slots	-	12
$2p$	Number of rotor poles	-	4/8/10/14/20/22
d_{so}	Stator outer diameter	mm	100
l_{fe}	Lamination stack length	mm	50
N_{ph}	Number of turns per phase	-	184
s_f	Slot filling factor	-	0.28
δ	Air-gap length	mm	1
d_{sh}	Shaft diameter	mm	20
v_{pm}	PM volume	cm^3	24.5
p_{rPM}	Pole arc to pole pitch ratio	-	1
B_r	PM remanence	T	1.20
μ_r	PM relative permeability	-	1.05

Windings with different coil pitches are illustrated in Fig. 2.4. When coil pitch equals 1, coils of one phase are concentrated and wound on one tooth, and thus, there is no overlapping end winding part. Otherwise, there may be overlapping parts when the coil pitch is larger than 1. It is obvious that the end winding of non-overlapping FSCW is much shorter than that of overlapping winding.

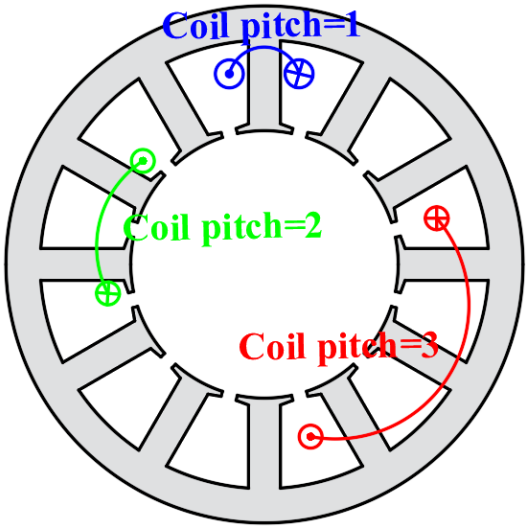

Fig. 2.4. Illustration of winding configurations with different coil pitches.

Taking 12s/4p SPMSM as an example, windings with different coil pitches are shown in Fig. 2.5.

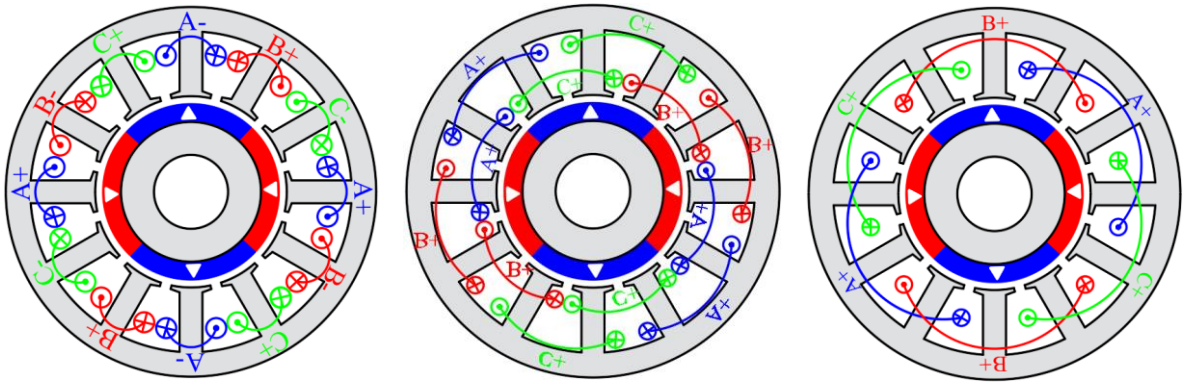

(a) Coil pitch = 1. (b) Coil pitch = 2. (c) Coil pitch = 3.

Fig. 2.5. Winding configurations with different coil pitches.

The torques of all optimized six SPMSMs with different coil pitches are shown in Fig. 2.6 (a) and the corresponding winding factors are shown in Fig. 2.6 (b). When the SPMSMs are optimized for maximum average torque under fixed 40 W copper loss neglecting end winding, the optimized average torques almost show the same trend with winding factors.

1. For 12s/4p SPMSM, the optimal coil pitch is 3 due to its highest winding factor.
2. For 12s/8p/10p/14p SPMSMs, the optimal coil pitch is 1.
3. For 12s/20p and 12s/22p vernier machines, the optimal coil pitch is 3 and 6, respectively, due to their highest winding factors and field modulation effect [LIU18a].

Fig. 2.6 (c) shows the ratio between average torque and winding factor. The ratio increases significantly with pole number because the magnetic gearing effect increases with the pole number [LIU18a], as shown in Fig. 2.7, where T_U is the torque component produced by the principle of the conventional electrical machine while T_M is the torque component produced by the principle of the magnetic gearing effect. The torque components are separated by the ECS method, which consists of several steps [LIU18a].

1. The armature reaction field harmonics without being modulated by stator slots are obtained by using ECS without PM excitations (replaced by air space). The stator is replaced by a slotless magnetic steel cylinder and the ECS is placed over the surface of the slot opening with a 0.05mm radial thickness. The total magnetomotive force in ECS is the same as that when the carrying current is in the slots.
2. For convenience, for each obtained armature reaction field harmonic component to be investigated, an FEA model is built with an equivalent thin sinusoidally magnetized PM layer (0.05mm radial thickness) with the same pole number of armature reaction field harmonic component, whose amplitude and phase of magnetization are adjusted to mimic the same effect of each armature reaction field harmonic component without stator slot modulation.
3. To calculate unmodulated torque, T_U, the equivalent PM layer, obtained by the above method and associated with the armature reaction field harmonic, is applied on the stator bore surface of an actual machine with PM excitation and slots. It is worth noting that (a) this armature reaction field harmonic has the same pole number as the rotor PM pole number; (b) the slots are introduced in the FEA model only to account for the equivalent air-gap increase due to slotting and will not introduce field modulation effect.
4. Similarly, to calculate modulated torque, T_M, the same procedure as above step 3 is employed, except that the armature reaction field harmonic is different. In this case, the slots are critical for field modulation effect and torque production since the armature reaction field harmonic has different pole numbers from the rotor PM pole numbers. It is worth mentioning that there may be other dominant armature reaction field harmonics that could contribute to the torque production, and should be similarly calculated and finally summed up.

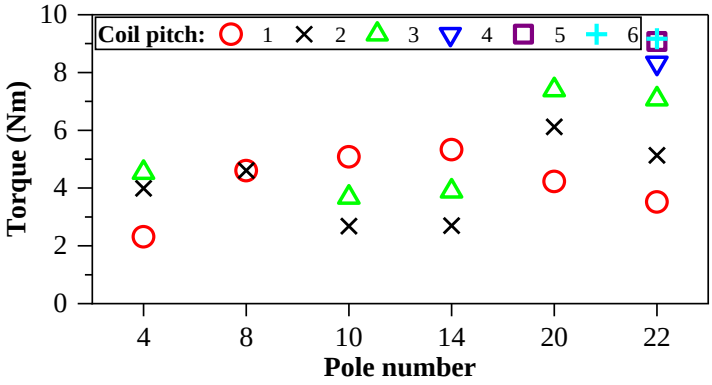

(a) Average torques.

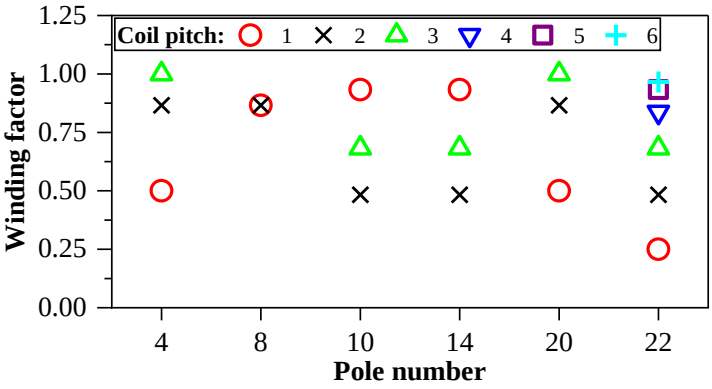

(b) Winding factors.

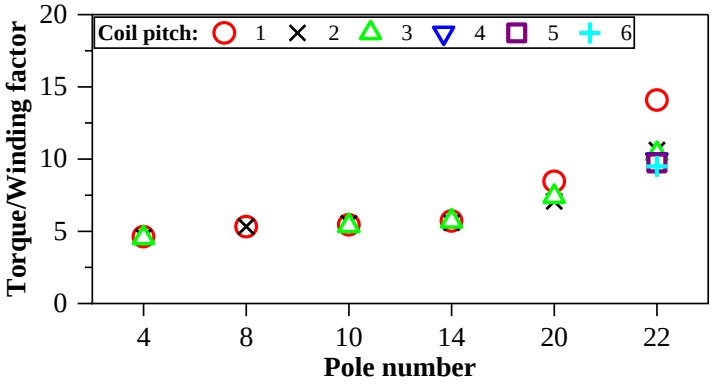

(c) Ratios between torque and winding factor.

Fig. 2.6. Optimized average torques, winding factors, and ratios between torque and winding factor of SPMSMs with the same active lamination stack length under fixed 40 W copper loss neglecting end winding with different coil pitches.

Meanwhile, the ratio of torque produced by the magnetic gearing effect to the total torque is defined by:

$$\rho_{MG} = \frac{T_M}{T_M + T_U} \tag{2.2}$$

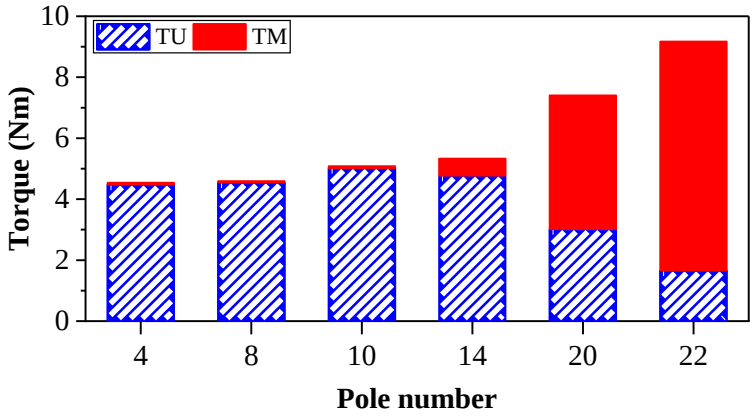

(a) Torque components of SPMSMs with different slot/pole number combinations.

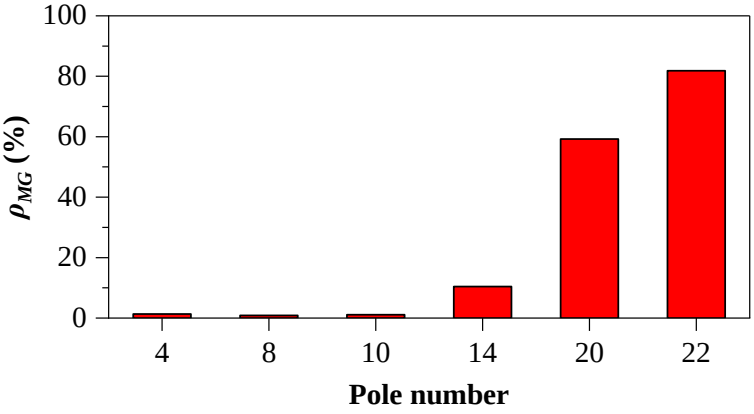

(b) Ratios of torque produced by magnetic gearing effect.

Fig. 2.7. Torque components of SPMSMs with different slot/pole number combinations and ratios of torque produced by magnetic gearing effect.

Optimal torques and coil pitches for all SPMSMs are shown in Fig. 2.8. According to the optimization results, the optimal coil pitches for 12s/8p, 12s/10p, and 12s/14p SPMSMs for maximum average torque are 1 due to the largest winding factor. For 12s/4p, 12s/20p, and 12s/22p SPMSMs, optimal coil pitches are 3, 3, and 6, respectively.

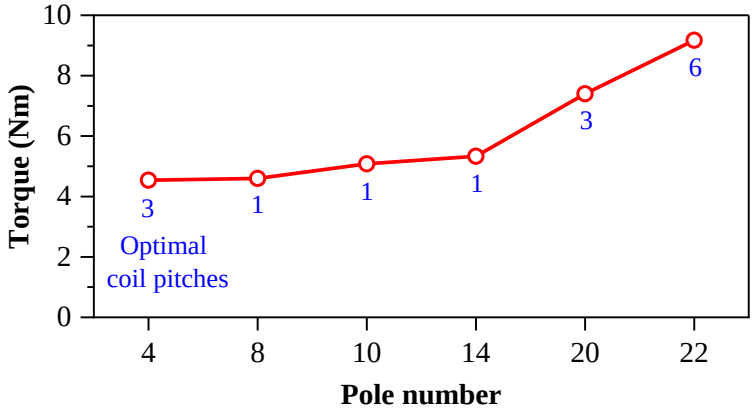

Fig. 2.8. Optimized average torques of 12-slot SPMSMs with the same active lamination stack length and corresponding optimal coil pitches under fixed 40 W copper loss neglecting end winding.

2.3.2. Considering end winding

2.3.2.1. Optimal coil pitch considering end winding

The coil pitch not only affects the winding factor but also leads to different end winding lengths. The end winding length of ISDW is much longer than that of FSCW, and thus, for fair comparison, the copper loss of end winding should be taken into consideration during optimization. The end winding will increase the phase resistance and axial length of the machine, which will decrease the torque density. In this Section, the SPMSMs are optimized for maximum average torque under fixed 40 W copper loss considering end winding. Other constraints are the same as in Section 2.3.1. The modeling of end winding and calculation of end winding length are shown in Appendix A.

At first, the six machines with different coil pitches are optimized for maximum average torque under fixed 40 W copper loss considering end winding. The optimization results are shown in Fig. 2.9. Compared with Fig. 2.6 (a), the optimized average torques considering end winding decrease, especially for overlapping windings. When coil pitch equals 1, the end winding length of FSCW is relatively short, and thus, the torque decreases slightly. The torques reduce more obviously as the coil pitches increase.

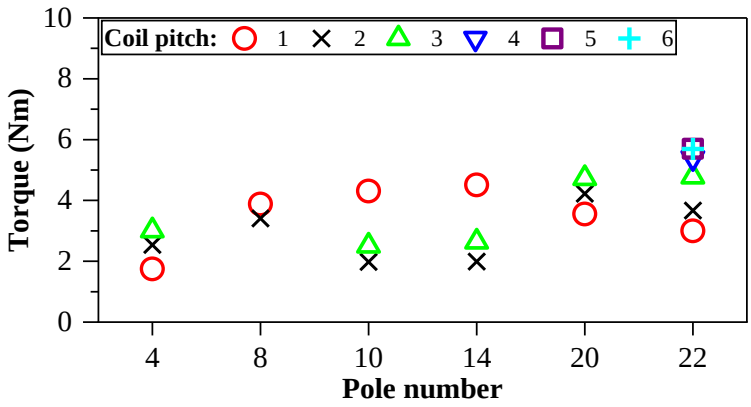

Fig. 2.9. Optimized average torques of SPMSMs with the same active lamination stack length under 40 W copper loss considering end winding with different coil pitches.

According to the optimization results, the optimal coil pitches for the six SPMSMs with fixed 40 W copper loss and 50 mm stack length are selected according to the maximum average torque. For 12s/4p SPMSM, the optimal coil pitch for maximum average torque under fixed 40 W copper loss considering end winding is 3, due to its highest winding factor even though it has the longest end winding. When the coil pitch is 2, the end winding length will be shorter,

but the lower winding factor (0.866) cannot guarantee higher torque. For 12s/8p, 12s/10p, and 12s/14p SPMSMs, the optimal coil pitch is 1, due to their shorter end winding length and high winding factor. For the 12s/20p SPM vernier machine, the optimal coil pitch is 3, due to its highest winding factor and field modulation effect. For the 12s/22p SPM vernier machine, when coil pitch equals 4, 5, and 6, the winding factors are 0.837, 0.933, and 0.966, respectively. The corresponding average torques are 5.40 Nm, 5.70 Nm, and 5.69 Nm. Thus, the optimal can be either 5 or 6. In this chapter, 5 is selected for 12s/22p.

The optimized average torques of all SPMSMs with respective optimal coil pitches considering end winding and those neglecting end winding are compared in Fig. 2.10.

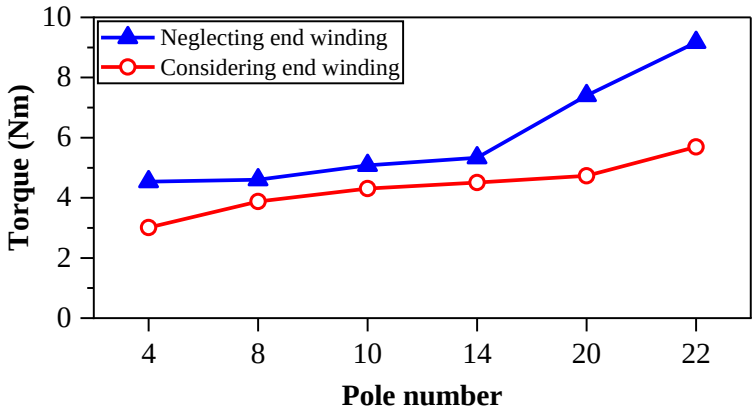

(a) Optimized torques considering end winding and neglecting end winding.

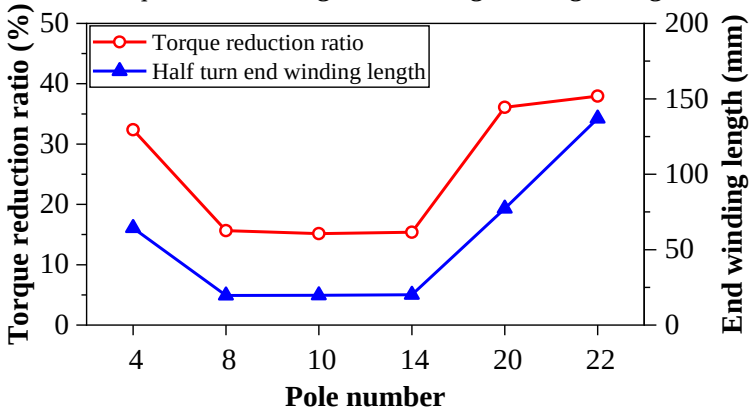

(b) Torque reduction ratios between optimization considering end winding and neglecting end winding.

Fig. 2.10. Optimized average torques comparison between SPMSMs considering and neglecting end winding with optimal coil pitch.

The optimized torque reduction ratio increases with the increase of end winding length. The optimized torques of 12s/8p/10p/14p considering end winding are 3.88 Nm, 4.31 Nm, and 4.51 Nm, respectively, decreasing about 15% compared with that of neglecting end winding. However, the torques of 12s/4p, 12s/20p, and 12s/22p decrease significantly because ISDW

has longer end winding length. For 12s/4p SPMSM, the torque is 3.07 Nm and decreased by 32%. For 12s/20p and 12s/22p vernier machines, the torques are 4.73 Nm and 5.69 Nm and decreased by 36% and 38%, respectively.

2.3.2.2. **Comparison of optimization results**

The optimized parameters of all SPMSMs with the same active lamination stack length under fixed 40 W copper loss considering end winding with optimal coil pitch are shown in Table 2.2, while the corresponding geometries, on-load flux lines, and magnetic field distributions are shown in Fig. 2.11.

Table 2.2 Results of Global Optimization under Fixed 40 W Copper Loss Considering End Winding

Rotor pole number	4	8	10	14	20	22
Coil pitch	3	1	1	1	3	6
d_{si} (mm)	50.7	54.4	56.6	61.5	69.0	67.1
h_y (mm)	6.6	3.8	3.4	2.7	3.0	4.6
w_t (mm)	6.3	7.2	7.0	5.7	3.5	2.7
b_{so} (mm)	2.5	1.9	2.7	5.0	10.4	11.5
h_{pm} (mm)	3.4	3.1	3.0	2.7	2.4	2.5
Torque (Nm)	3.07	3.88	4.31	4.51	4.90	5.69
I_{peak} (A)	4.80	6.34	6.37	6.50	4.53	3.63

Fig. 2.12 and Fig. 2.13 show the flux lines and magnetic fields caused by PMs or armature reactions only by using frozen permeability. It shows that the magnetic fields of 12-slot SPMSMs caused by armature reaction increase with the rotor pole number. For 12s/20p and 12s/22p vernier machines, armature reaction has a significant influence on on-load flux lines and magnetic field distributions. For other 12-slot SPMSMs, armature reaction has a relatively smaller influence on on-load flux lines and magnetic field distributions.

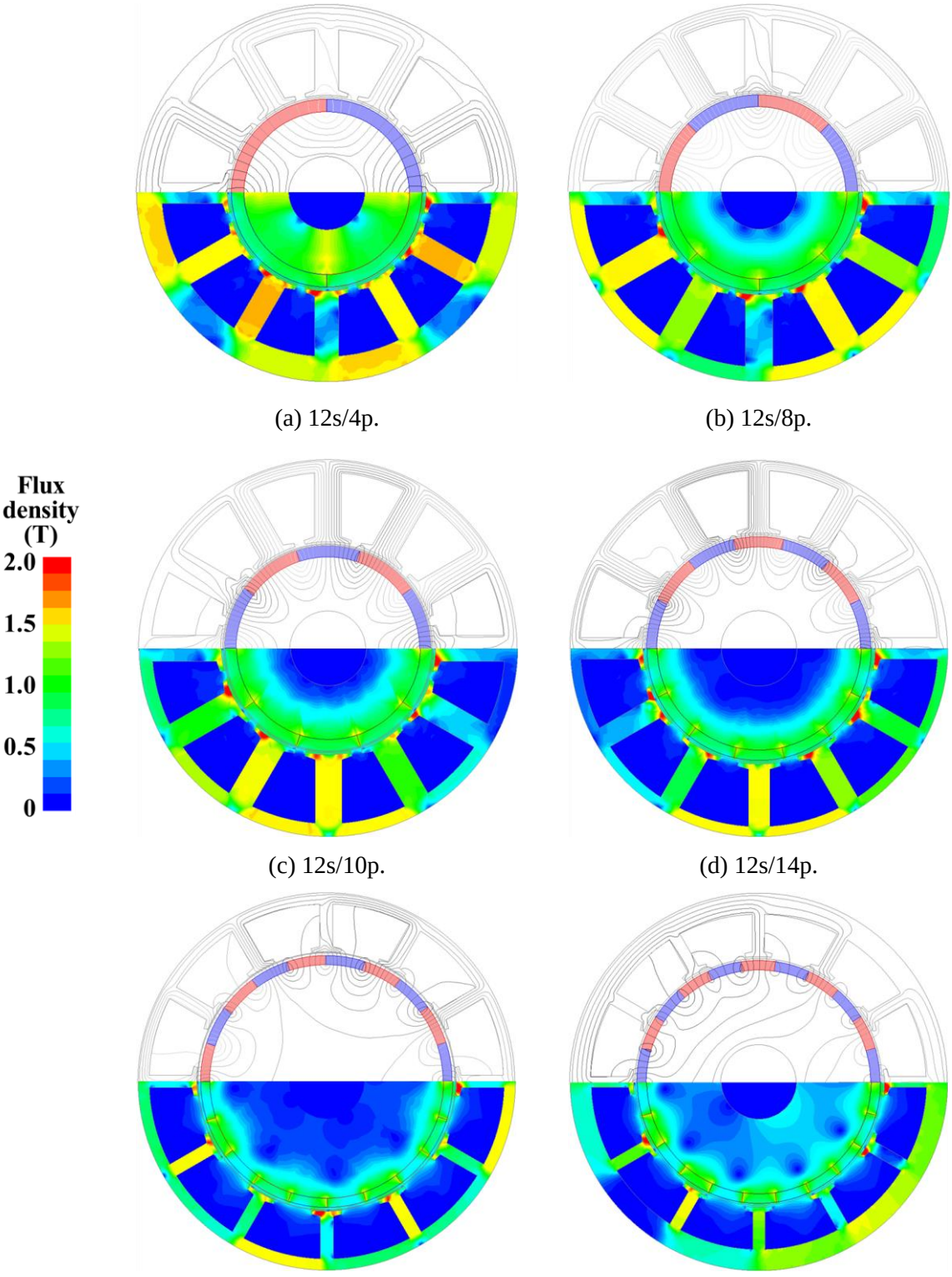

(a) 12s/4p. (b) 12s/8p.

(c) 12s/10p. (d) 12s/14p.

(e) 12s/20p. (f) 12s/22p.

Fig. 2.11. Load flux contour distributions of optimized SPMSMs under 40 W copper loss.

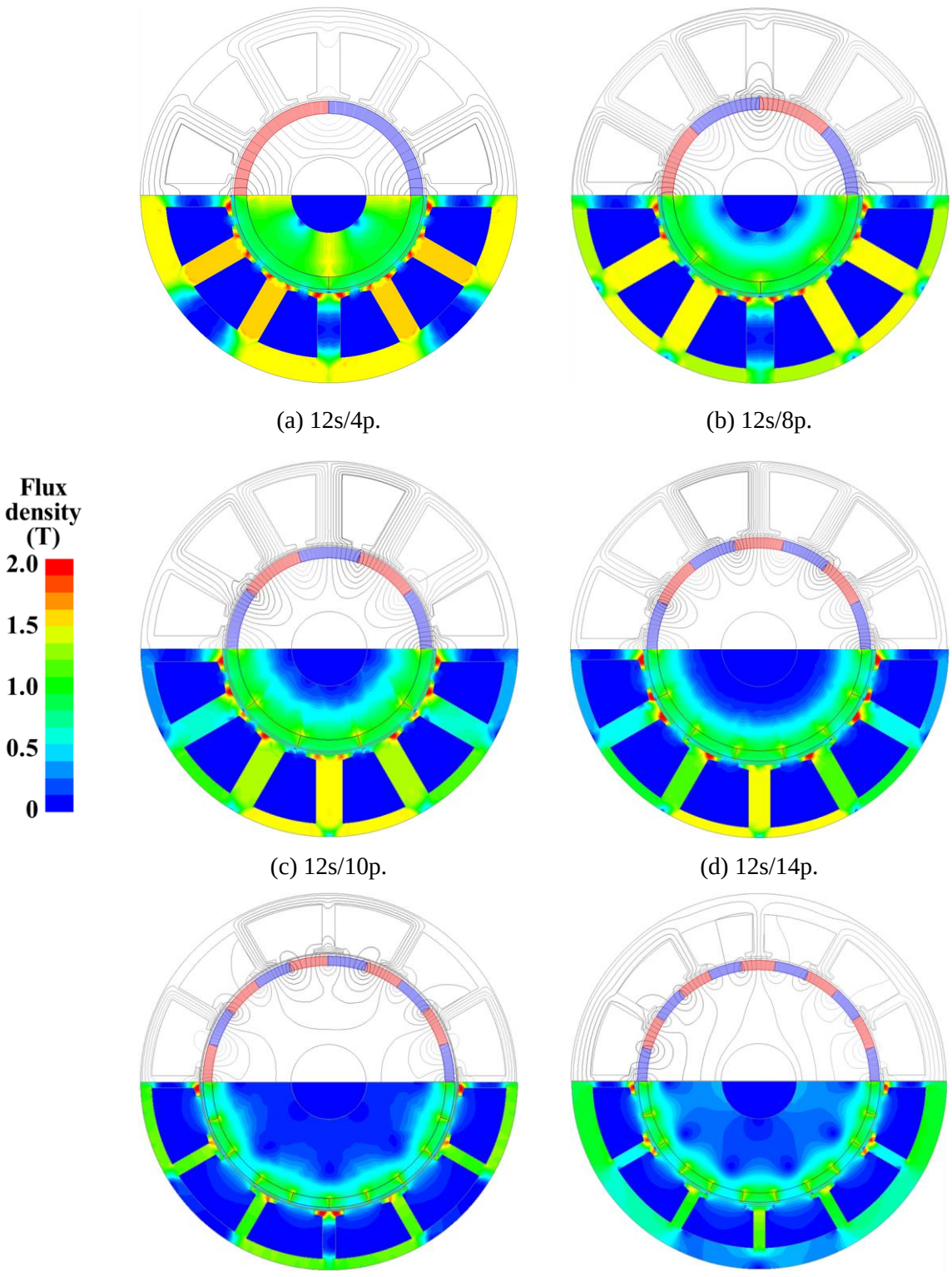

(a) 12s/4p. (b) 12s/8p.

(c) 12s/10p. (d) 12s/14p.

(e) 12s/20p. (f) 12s/22p.

Fig. 2.12. Flux contour distributions of optimized SPMSMs under 40 W copper loss caused by PMs only.

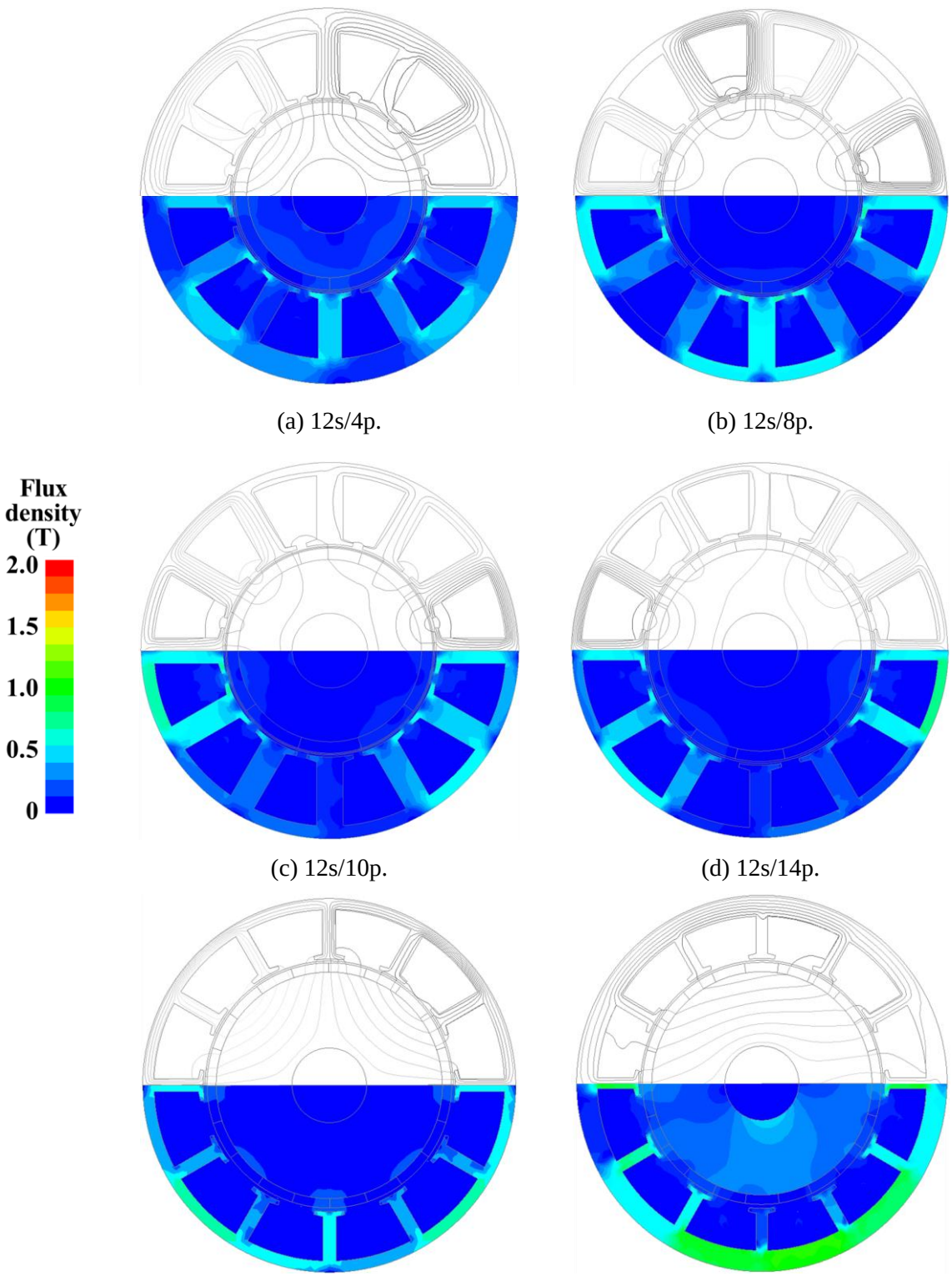

(a) 12s/4p. (b) 12s/8p.

(c) 12s/10p. (d) 12s/14p.

(e) 12s/20p. (f) 12s/22p.

Fig. 2.13. Flux contour distributions of optimized SPMSMs under 40 W copper loss caused by armature reaction only.

Fig. 2.14 compares the optimized average torques, torque densities, and dimensional parameters. The optimized average torques under 40 W copper loss considering end winding increase with pole number. However, for ISDW vernier machines, the axial length of the end

winding is much longer than FSCW SPMSMs, the axial end winding length and torque density are compared in Fig. 2.14 (b). The torque densities of 12s/8p, 12s/10p, and 12s/14p FSCW SPMSMs are larger than those of 12s/20p and 12s/22p vernier machines, which have relatively longer axial end windings even though vernier machines can generate higher torque for the same lamination stack length. Fig. 2.14 (e) presents the influence of slot-opening width on the output torque in all SPMSMs, where other parameters remain constant. The values with the black frame marks are the optimized slot-opening widths. As can be seen, there is an optimal slot opening width for maximum average torque for each SPMSM.

The split ratio almost increases with pole number, while the PM thickness is inversely proportional to the split ratio as the PM volumes of all SPMSMs are fixed during optimization. For 12s/8p, 12s/10p, and 12s/14p FSCW SPMSMs, the yoke thickness and tooth width decrease with the pole numbers. Therefore, the slot area and current amplitude increase with pole numbers, and the torque increases with pole numbers under fixed copper loss. The yoke thickness of 12s/22p vernier machine is larger than that of 12s/20p vernier machine. When the vernier machines operate on on-load condition, the armature reactions will affect the magnetic field distribution. For the 12s/22p vernier machine, the stator pole number is 2 while the stator pole number is 4 for the 12s/20p vernier machine, and thus, the yoke thickness of 12s/22p needs to be larger than that of 12s/20p vernier machine. The optimal slot opening width increases with the rotor pole numbers except for 12s/4p SPMSM. The ratio of tooth tip width and PM pole pitch increases when the pole number smaller than the slot number, while decreasing when the pole number larger than the slot number, as shown in Fig. 2.14 (d).

Fig. 2.15 compares the variations of average torque with copper loss to illustrate the overload capability of SPMSMs optimized under fixed 40 W copper loss with different slot/pole number combinations. The average torques of VPMSMs (12s/20p and 12s/22p) are higher at light load conditions, but VPMSMs cannot maintain the advantage in high torque output capacity at heavy load conditions, especially 12s/22p VPMSM due to more severe magnetic saturation. In contrast, FSCW SPMSMs, especially 12s/10p and 12s/14p SPMSMs, have better torque output capacity at heavy load conditions.

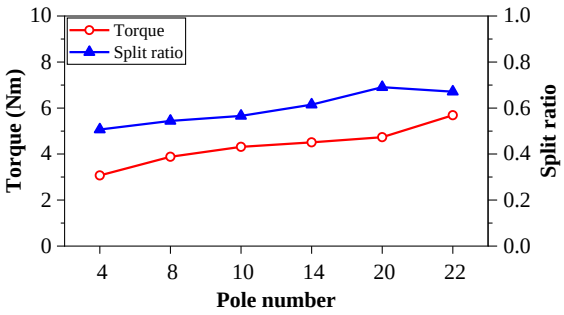

(a) Average torque and split ratio.

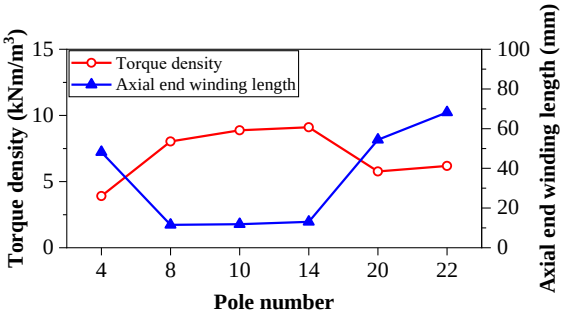

(b) Torque density.

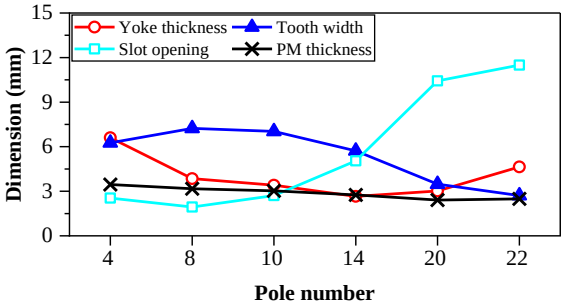

(c) Dimensional parameters.

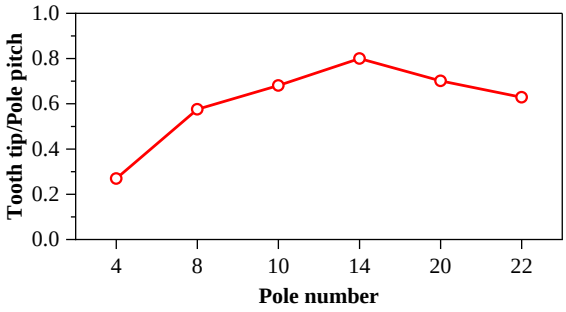

(d) Ratio of tooth tip width and PM pole pitch.

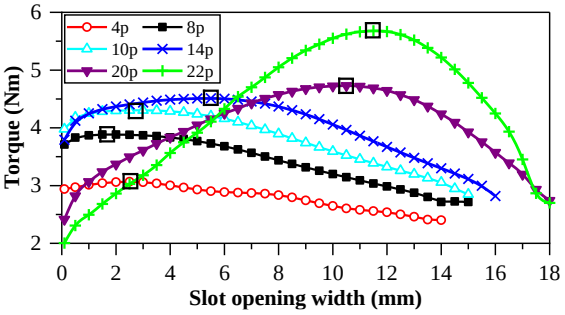

(e) Variation of slot opening width and torque.

Fig. 2.14. Optimization results under fixed 40 W copper loss considering end winding.

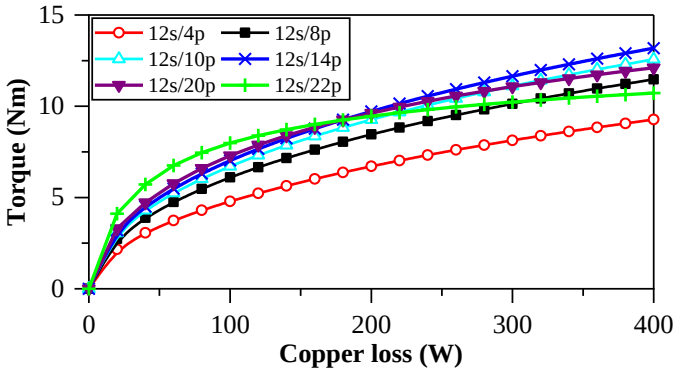

Fig. 2.15. Comparison of average torques with copper loss among SPMSMs optimized under fixed 40 W copper loss with different slot/pole number combinations.

2.3.2.3. **Effect of axial stack length**

As mentioned in the previous section, due to the axial end winding length differences between ISDW and FSCW, the torque densities of 12s/20p and 12s/22p ISDW vernier machines are lower than those of 12s/8p, 12s/10p, and 12s/14p FSCW SPMSMs even they have higher average torque. The effect of the stack axial length on the torque and torque density of SPMSMs with different slot/pole number combinations will be investigated in this Section.

The torques and torque densities of the optimized SPMSMs under fixed currents (provided in Table 2.2) and different lamination stack lengths are shown in Fig. 2.16.

As can be seen, the average torque shows a linear relationship with lamination stack lengths under fixed current. The torque density increases with the lamination stack length but eventually levels off as the lamination stack length continues to increase. This is because the axial end winding length of FSCW is relatively short compared with the stack length, whereas the end winding length of ISDW is relatively long when the lamination stack length of the machine is short. Increasing the lamination stack length will mitigate the adverse effect of axial end winding length on torque density, especially for ISDW. Therefore, the torque densities of 12s/8p, 12s/10p, and 12s/14p FSCW SPMSMs are higher than those of 12s/20p and 12s/22p ISDW vernier machines when the lamination stack length is short. While increasing the lamination stack length, the torque density of vernier machines will be higher.

In general, the torque densities of ISDW vernier machines are lower compared with FSCW SPMSMs due to the long axial end winding length. However, the vernier machines with long lamination stack lengths can maintain high average torque and torque density simultaneously.

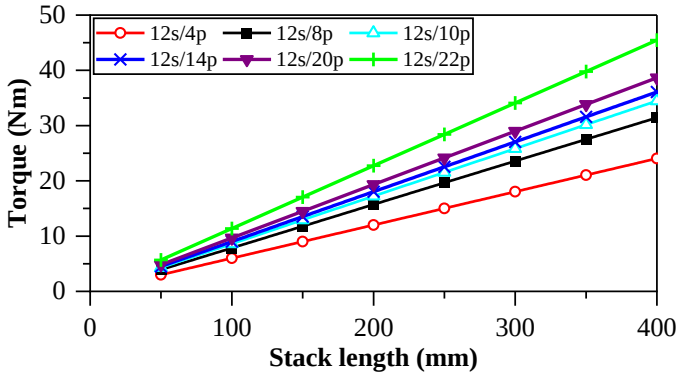

(a) Average torque.

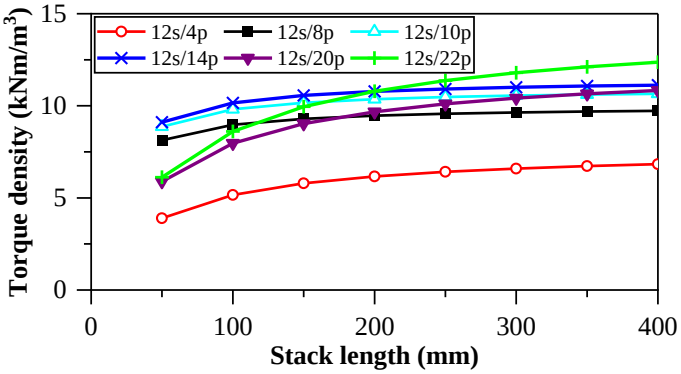

(b) Torque density.

Fig. 2.16. Comparison of average torques and torque densities of optimized SPMSMs with fixed 40 W copper loss and different stack lengths.

2.3.3. Considering iron loss and PM loss

2.3.3.1. Optimization under different speeds

Iron loss varies with machine topologies and operating conditions. In some cases, higher iron loss leads to high temperature rise due to higher frequency, which should be taken into consideration during optimization [HE21]. The iron losses in the optimized SPMSMs under different speeds are compared in Fig. 2.17. The iron loss increases with the rotor pole number and speed. The iron losses of 12s/20p and 12s/22p vernier machines are much larger than other SPMSMs. Hence, in this Section, the iron loss will be considered in the design optimization for a fair comparison, especially for high speed SPMSMs and SPMSMs with large pole numbers.

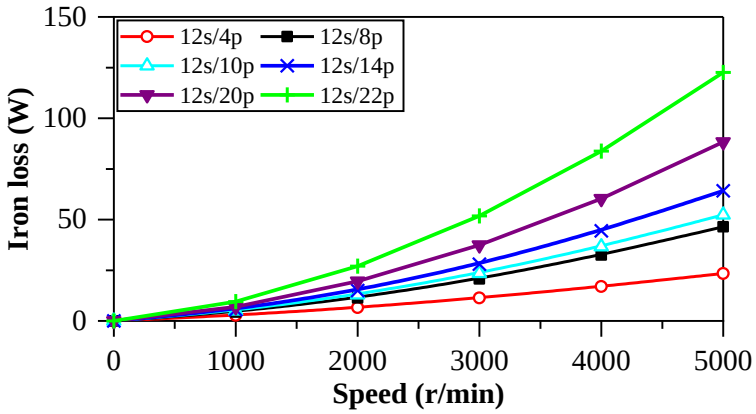

Fig. 2.17. Iron losses of optimized SPMSMs under 40 W copper loss and different speeds.

It is worth mentioning that PM loss is usually negligible at low speeds, while PM segmentation can be used to reduce PM loss. Further, PM loss is relatively small compared with the total copper and iron losses. The PM loss also varies with rotor pole number as shown in Fig. 2.18. The PM loss with higher rotor pole numbers (14-pole, 20-pole, and 22-pole) is much higher than that with lower rotor pole numbers (4-pole, 8-pole, and 10-pole). Therefore, PM loss is neglected during the optimization under low speed conditions but considered under high speed conditions in this chapter.

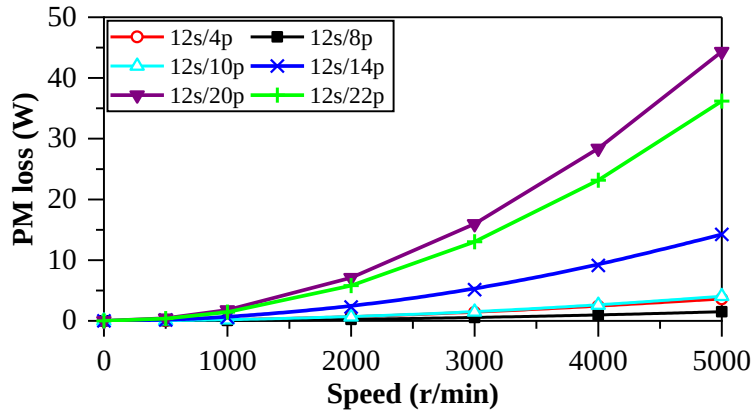

Fig. 2.18. Comparison of PM losses of SPMSMs under fixed 40 W copper loss and different speeds.

Both iron loss and PM loss are calculated by FEA [ANS18].

The iron loss density is computed as [BER88]:

$$P_v = k_h f B_m + k_{ec} f^{1.5} {B_m}^{1.5} + k_{ex} f^2 {B_m}^2 \tag{2.3}$$

The PM loss is computed as:

$$P_{PM} = \iiint_{Vol} \frac{J \cdot J^*}{2\sigma} dVol \tag{2.4}$$

where B_m is the amplitude of the AC flux component, f is the frequency, k_h is the hysteresis core loss coefficient, k_{ec} is the eddy-current core loss coefficient, k_{ex} is the excess core loss coefficient (where the coefficients are 109.91W/m^3, 0.42W/m^3, and 4.94W/m^3, respectively), J is the current density, J^* is the complex conjugate of the current density, and σ is the conductivity. In the optimization, there are four design variables as shown in Fig. 2.3, i.e., the stator inner diameter, the thickness of the stator yoke, the width of the stator tooth, and the stator slot opening width. In addition, the phase current is regarded as a variable. With various phase currents, the electromagnetic torques accounting for the influence of copper and iron losses can be calculated by FEA. Finally, the optimal design with the maximum torque can be selected from the designs with total copper, iron, and PM losses less than or equal to 40 W.

The SPMSMs are optimized for maximum average torque under fixed 40 W total copper, iron, and PM losses accounting for end windings. As the iron loss increases with rotor rotation speed, the SPMSMs are optimized under two different specific speeds to illustrate the influence of iron and PM losses in the design optimization.

During the optimization, the fixed parameters are the same as the optimization in previous sections as shown in Table 2.1. Parametric analysis in FEA is used to calculate the electromagnetic performance of all SPMSMs with the same active lamination stack length and with different stator inner diameter (d_{si}), thickness of stator yoke (h_y), width of stator tooth (w_t), slot opening width (b_{so}), and phase current. According to the calculation, the optimal SPMSMs with maximum torque are selected from those results with 40 W or less copper, PM, and iron losses.

- Low Speed Optimization (400 r/min)

The optimized parameters of the SPMSMs under fixed 40 W total copper and iron losses accounting for end windings at 400 r/min are shown in Table 2.3.

Fig. 2.19 shows the optimization results compared with SPMSMs optimized under 40 W copper loss. As copper loss plays a dominant role in lower speed conditions in Fig. 2.19 (e), the optimized dimensional parameters remain almost unchanged between the optimization considering fixed 40 W copper loss only and considering fixed 40 W total copper and iron loss

together at lower speed conditions (400 r/min), such as split ratio and yoke thickness. The optimized torque and phase current decrease slightly as the total copper loss decreases slightly.

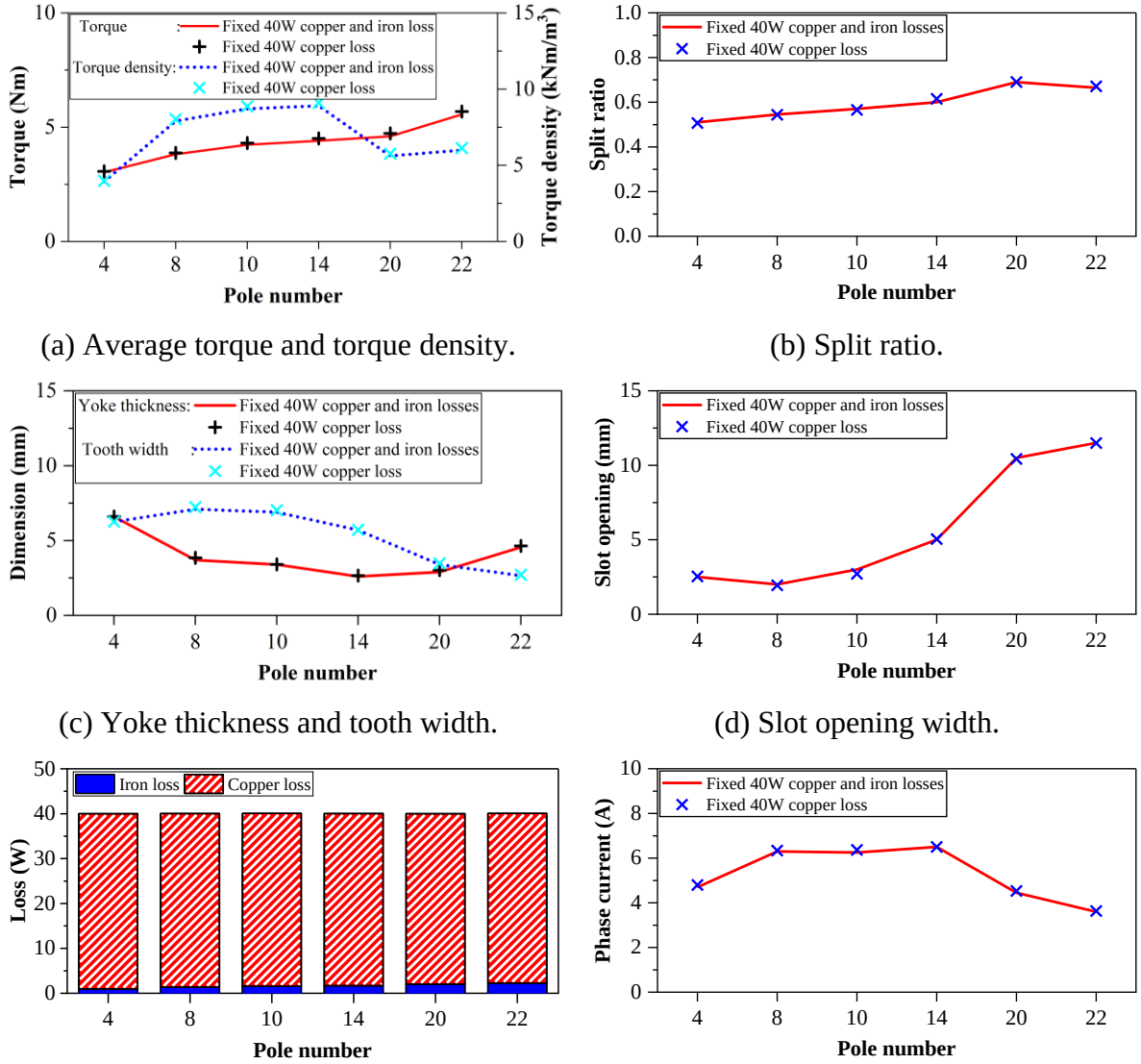

(a) Average torque and torque density.

(b) Split ratio.

(c) Yoke thickness and tooth width.

(d) Slot opening width.

(e) Loss distribution.

(f) Phase current amplitude.

Fig. 2.19. Optimization results of SPMSMs with the same active lamination stack length under fixed 40 W copper and iron losses accounting for end windings.

- High Speed Optimization (2000 r/min)

The optimized parameters of the SPMSMs under fixed 40 W total copper, iron, and PM losses accounting for end windings and 2000 r/min are shown in Table 2.4.

Table 2.3 Results of Global Optimization under Fixed 40 W Total Copper and Iron Losses at 400 r/min

Rotor pole number	4	8	10	14	20	22
Coil pitch	3	1	1	1	3	6
d_{si} (mm)	51	54.5	57.0	60.0	69.0	66.5
h_y (mm)	6.6	3.7	3.4	2.6	2.9	4.5
w_t (mm)	6.2	7.1	6.9	5.7	3.4	2.6
b_{so} (mm)	2.5	2	3	5	10.5	11.5
Torque (Nm)	3.03	3.82	4.23	4.41	4.61	5.56
I_{peak} (A)	4.7	6.3	6.25	6.5	4.45	3.6

Table 2.4 Results of Global Optimization under Fixed 40 W Total Copper, Iron, and PM Losses at 2000 r/min

Rotor pole number	4	8	10	14	20	22
d_{si} (mm)	50.5	54	56.3	59.3	66.3	65.5
h_y (mm)	6.6	3.8	3.4	2.4	2.9	4.3
w_t (mm)	6.2	7.4	6.7	5.7	3	2.3
b_{so} (mm)	2	1.5	3	5	10	11.5
Torque (Nm)	2.67	3.29	3.47	3.32	2.84	2.91
I_{peak} (A)	4.3	5.3	5.2	5	3	1.9

Fig. 2.20 shows the optimization results between 2000 r/min and 400 r/min. When the speed increases, the iron and PM losses increase, and the copper loss is no longer the dominant loss especially when the pole number increases, as shown in Fig. 2.20 (f). Therefore, the phase current, torque, and torque density decrease. Fig. 2.20 (b) shows that the torque reduction ratio between lower speed and higher speed increases with the pole number because PM and iron losses increase with the pole number under the same speed. In general, vernier machines have higher torque output capacity [ZHU18a] [LI18a] [LIU19] [LIU18a] [LIU18b] [LI16]. However, the optimized average torque of 12s/20p and 12s/22p vernier machines under 40 W total copper, iron, and PM losses is lower than that of 12s/10p and 12s/14p SPMSMs due to its higher PM and iron losses. The optimized dimensional parameters considering iron loss during the optimization in higher speed condition (2000 r/min) are almost unchanged compared with those optimized results in lower speed condition (400 r/min), such as split ratio and yoke thickness.

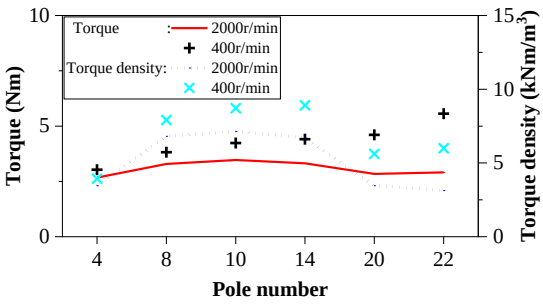

(a) Average torque and torque density.

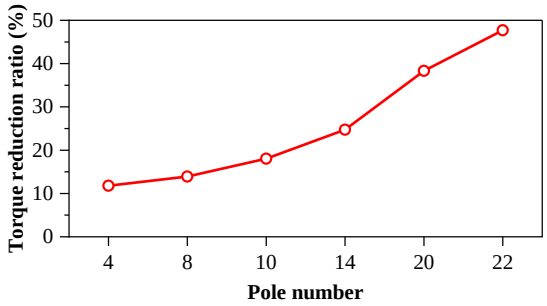

(b) Torque reduction ratio.

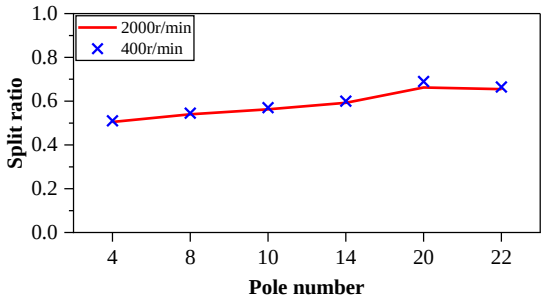

(c) Split ratio.

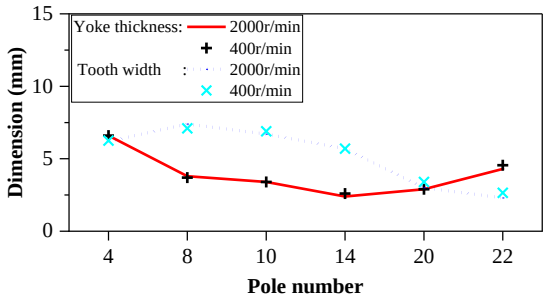

(d) Yoke thickness and tooth width.

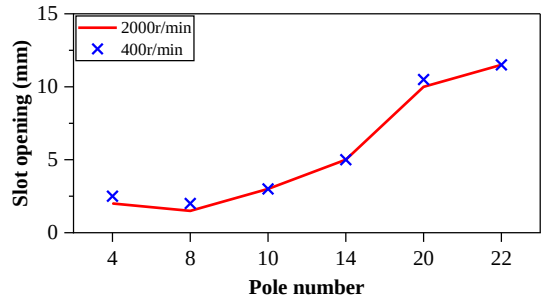

(e) Slot opening width.

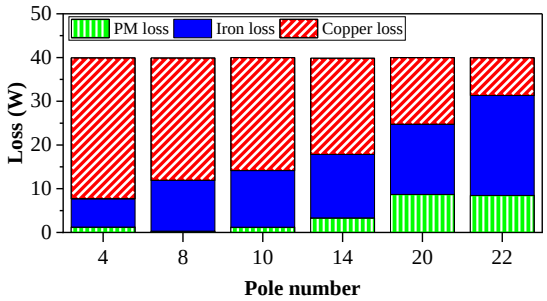

(f) Loss distribution.

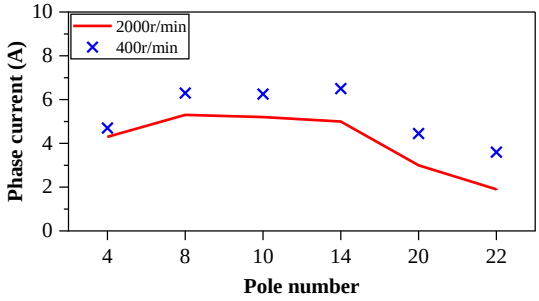

(g) Phase current amplitude.

Fig. 2.20. Comparison of optimization results of SPMSMs with the same active lamination stack length under fixed 40 W total copper, iron, and PM losses accounting for end windings between 2000 r/min and 400 r/min.

2.3.3.2. **Comparison**

- Efficiency

As shown in previous sections, the average torque, copper loss, PM loss, and iron loss vary with the rotor pole number. Therefore, the efficiencies of the optimized machines are compared in this Section.

The efficiency η is calculated by

$$\eta = \frac{P_{out}}{P_{out} + P_{Cu} + P_S + P_R + P_{PM}} \tag{2.5}$$

where P_{out} is the output power, P_{Cu} is the copper loss, P_S is the stator iron loss, P_R is the rotor iron loss, and P_{PM} is the PM loss.

Fig. 2.21 compares the efficiencies of SPMSMs with 40 W copper loss accounting for end windings and iron loss under different speeds. The efficiencies of SPMSMs with larger rotor pole numbers are higher at lower speeds. As the speed increases, the efficiencies of SPMSMs with larger rotor pole numbers become lower than those of SPMSMs with smaller rotor pole numbers because the losses of SPMSMs with larger rotor pole numbers increase faster with the increase of speed, as shown in Fig. 2.22.

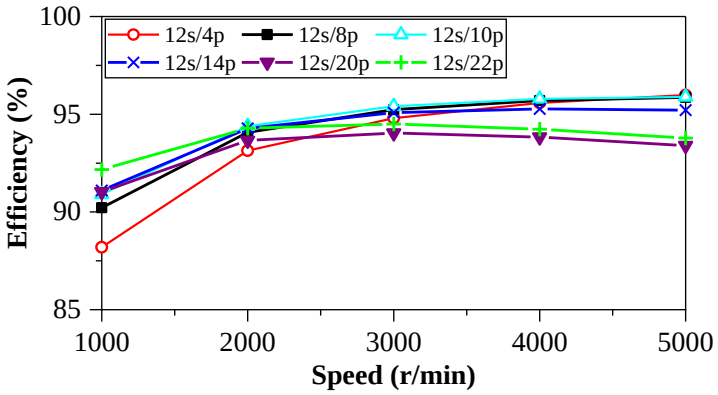

Fig. 2.21. Comparison of efficiencies of SPMSMs under fixed 40 W copper loss accounting for end windings and different speeds.

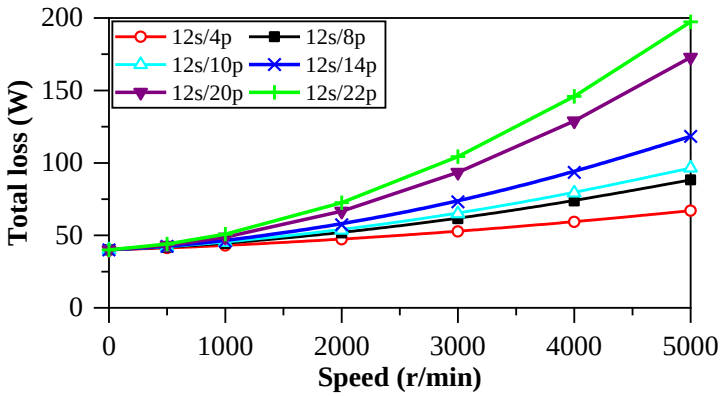

Fig. 2.22. Comparison of total losses of SPMSMs under fixed 40 W copper loss accounting for end windings and different speeds.

As the parameters of the SPMSMs optimized with fixed 40 W total copper and iron losses at lower speed conditions are almost the same as those of under 40 W copper loss, the efficiencies of SPMSMs optimized with fixed 40 W total copper, iron, and PM losses at higher speed conditions are shown in Fig. 2.23. The efficiencies of SPMSMs optimized considering PM and iron losses are slightly improved but decrease for vernier machines (20-pole and 22-pole) because of their low torques.

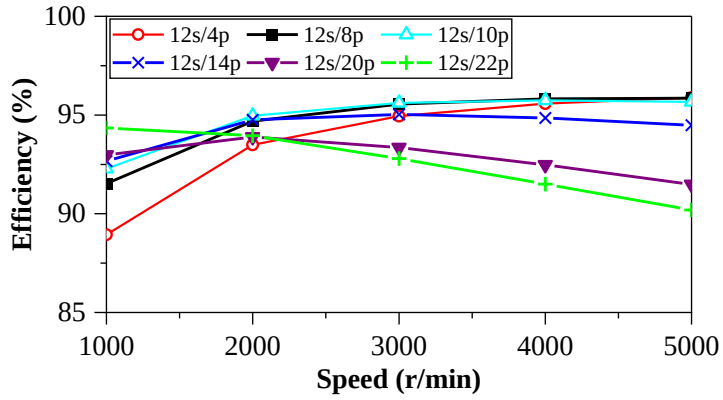

Fig. 2.23. Comparison of efficiencies of SPMSMs under fixed 40 W total copper, iron, and PM losses accounting for end windings and different speeds.

Fig. 2.24 compares the efficiencies of SPMSMs optimized under fixed 40 W total copper, iron, and PM losses and under fixed 40 W copper loss only at 2000 r/min. The efficiencies of SPMSMs optimized considering PM and iron losses are slightly improved compared with those optimized with fixed 40 W copper loss only in general.

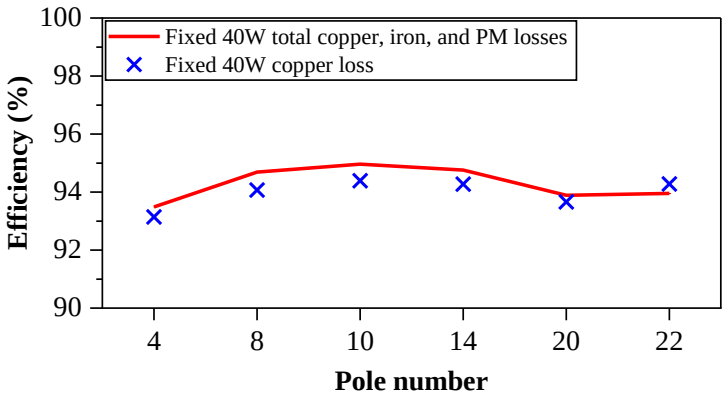

Fig. 2.24. Comparison of efficiencies between SPMSMs optimized under fixed 40 W total copper, iron, and PM losses and fixed 40 W copper loss only accounting for end windings at 2000 r/min.

- Inductance

Winding inductances have significant effects on the electromagnetic performances of SPMSMs. The phase inductance includes synchronous inductance, harmonic leakage inductance, slot leakage inductance, and end-leakage inductance [ZHU94] [REF08]. The differences in end winding length and disposition between FSCW and ISDW lead to different end winding leakage inductances. However, end-leakage inductance cannot be calculated in 2-D FEA, and thus, the simplified calculation method for end winding leakage inductance in [REF08] is used.

$$L_{end-phase} = n_{coils} n_{conds}^2 K_{w1}^2 (2 l_{end,avg})(1.2\mu_0) \tag{2.6}$$

where n_{cond} is the number of conductors per slot, n_{coils} is the number of coils per phase, K_{w1} is the winding factor, and $l_{end,avg}$ is the average end-turn length.

The *d*-axis inductances (L_d) of optimized SPMSMs with fixed 40 W copper loss only and 40 W total copper, iron, and PM losses at 2000 r/min are similar, as shown in Fig. 2.25 (a). The comparison between *d*-axis inductances of SPMSMs optimized with fixed 40 W copper loss neglecting and considering end-leakage inductance is also shown in Fig. 2.25 (b). L_d of ISDW SPMSMs is much higher than those of FSCW SPMSMs. As ISDW SPMSMs have longer end winding and overlapping parts, the end winding leakage inductance cannot be ignored for accurate calculation.

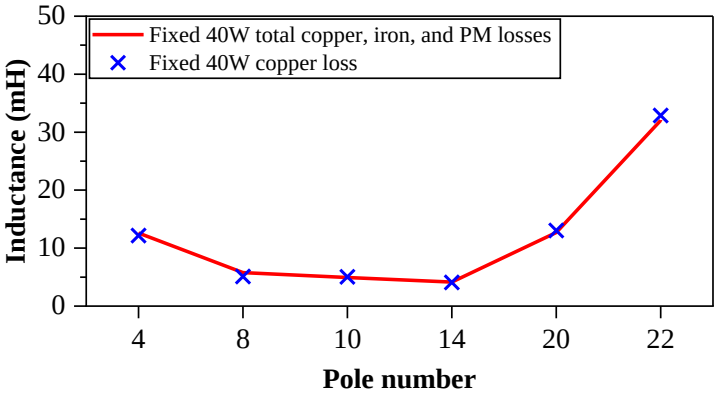

(a) Comparison of *d*-axis inductances of SPMSMs optimized with different scenarios.

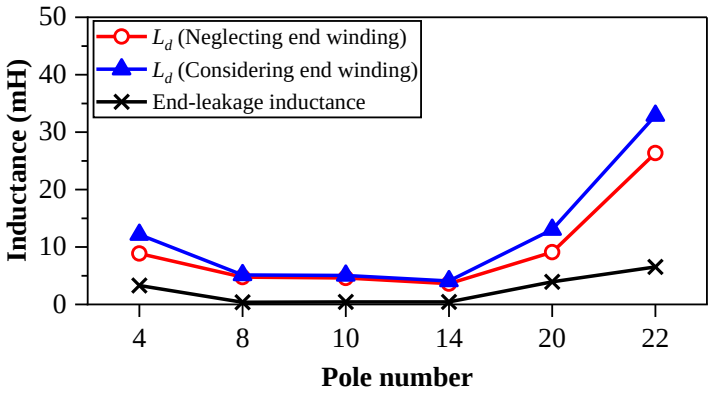

(b) Comparison of *d*-axis inductances and end winding leakage inductance with 40 W fixed copper loss.

Fig. 2.25. Comparison of *d*-axis inductances of SPMSMs with different slot/pole number combinations.

- Power factor

The power factor is calculated by (2.6) when SPMSMs are under I_d=0 control and the winding resistance is ignored [LIU18b] [LI14].

$$cos\,\varphi = \frac{1}{\sqrt{1+\left(\frac{I_q X_q}{E_1}\right)^2}} \tag{2.7}$$

where E_1 is the no-load back EMF, X_q is the *q*-axis inductive reactance, and I_q is the *q*-axis current. In SPMSMs, the *d*-axis and *q*-axis inductances (and reactances) are similar.

As the power factor increases with the decrease of the *q*-axis current, *q*-axis currents of SPMSMs optimized with fixed 40 W total copper, iron, and PM losses at 2000 r/min are adjusted to the same values of currents of SPMSMs optimized with fixed 40 W copper loss only for fair comparison. The power factors neglecting end winding leakage inductance of

SPMSMs optimized with fixed 40 W total copper, iron, and PM losses at higher speed conditions are shown in Fig. 2.26. The power factors between SPMSMs optimized under 40 W copper loss only are almost the same as those of under 40 W total copper, iron, and PM losses at 2000 r/min. The power factor of 12-slot SPMSMs decreases with the rotor pole number, and the power factors of vernier machines are much lower than those of other SPMSMs.

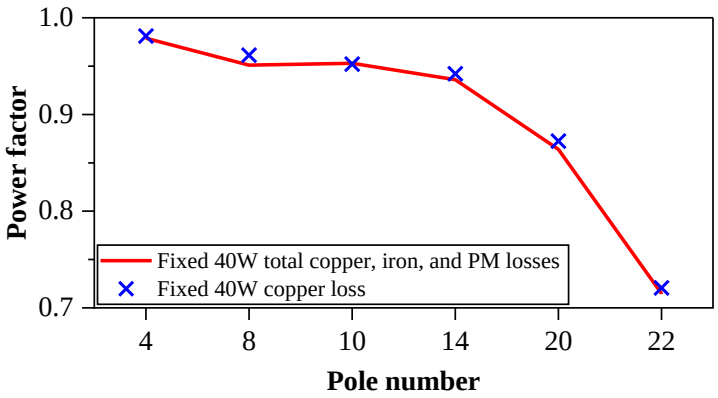

Fig. 2.26. Comparison of power factors between SPMSMs optimized under fixed 40 W copper and iron losses and fixed 40 W copper loss at 2000 r/min.

It can be seen from (2.6) that the *q*-axis inductance has a large impact on the power factor. Fig. 2.27 compares the power factors of SPMSMs optimized with fixed 40 W copper loss considering end winding or not. The end winding leakage inductance will decrease the power factor, especially for 12s/20p and 12s/22p ISDW VPMSMs.

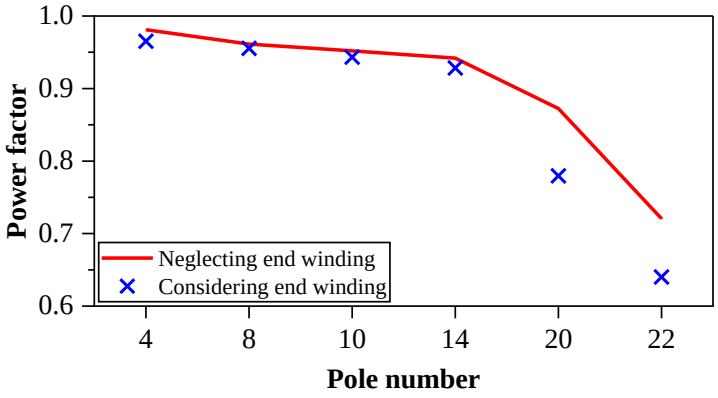

(a) Power factor.

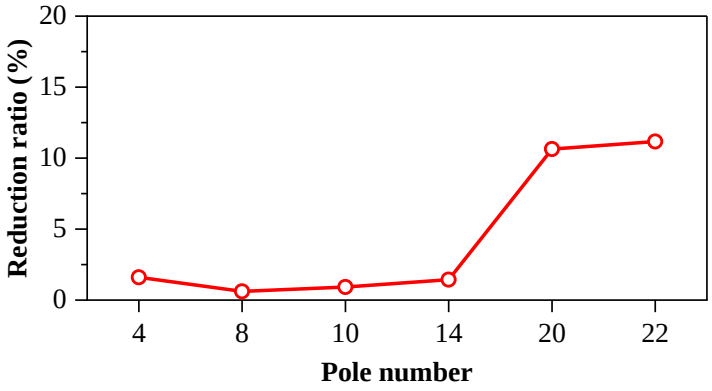

(b) Reduction rate.

Fig. 2.27. Comparison of power factors of SPMSMs optimized with fixed 40 W copper loss considering end winding or not.

2.4. Comparison of North-South Pole and Consequent Pole Rotors

2.4.1. Optimization of consequent pole machines

CP SPMSMs have alternate PM and iron poles on the rotor, which can reduce PM volume and thus improve PM utilization. Furthermore, it is well known that due to the large winding inductance and high armature reaction field, the CP rotor can enhance field modulation and torque production. This section investigates the electromagnetic performances of CP SPMSMs, with reference to the above analyzed conventional NSP SPMSMs.

Likewise, all CP SPMSMs are globally optimized to achieve the maximum average torque production, where the copper loss (including end winding) is fixed to 40 W. The fixed geometric parameters are the same as NSP SPMSMs in section 2.3 while the optimized variables are shown in Fig. 2.28. The pole arc to pole pitch ratio (p_{rPM}) is defined as θ_{pm}/θ_1 in Fig. 2.28. The optimized variables are listed in Table 2.5.

The optimized structures and corresponding magnetic field distributions under on-load conditions with 40 W copper loss are also shown in Fig. 2.29. The optimized yoke thickness of the 12s/14p CP PMSM is the lowest since it has the largest pole number of stator armature field. Moreover, since the pole number of the stator armature field in 12s/22p CP VPMSM is two, its optimized yoke thickness is larger than that of the 12s/20p CP VPMSM, whose pole number of the stator armature field is four.

Table 2.5 Results of Global Optimization of CP SPMSMs under Fixed 40 W Copper Loss Considering End Winding

Parameter	**Value**					
Rotor pole number	4	8	10	14	20	22
Coil pitch	3	1	1	1	3	5
r_{si} (mm)	26.7	28.5	28.9	30.3	34.1	33.9
h_y (mm)	6.8	3.9	3.3	2.7	3.3	5.5
w_t (mm)	6.7	7.3	6.5	5.5	3.9	3.1
b_{so} (mm)	2.2	2.0	3.8	5.5	10.3	11.8
h_{PM} (mm)	5.8	5.2	5.0	4.4	3.8	4.0
p_{rPM}	0.58	0.60	0.61	0.65	0.63	0.63
Average torque (Nm)	2.96	3.89	4.20	4.62	5.26	6.15
Torque density (kNm/m^3)	3.92	8.07	8.64	9.26	6.44	6.68
Phase current (A)	4.51	6.15	6.44	6.53	4.42	3.38

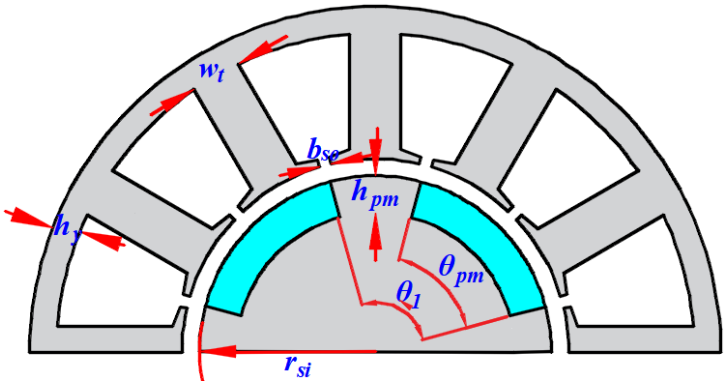

Fig. 2.28. Geometric variables for optimization in CP SPMSMs.

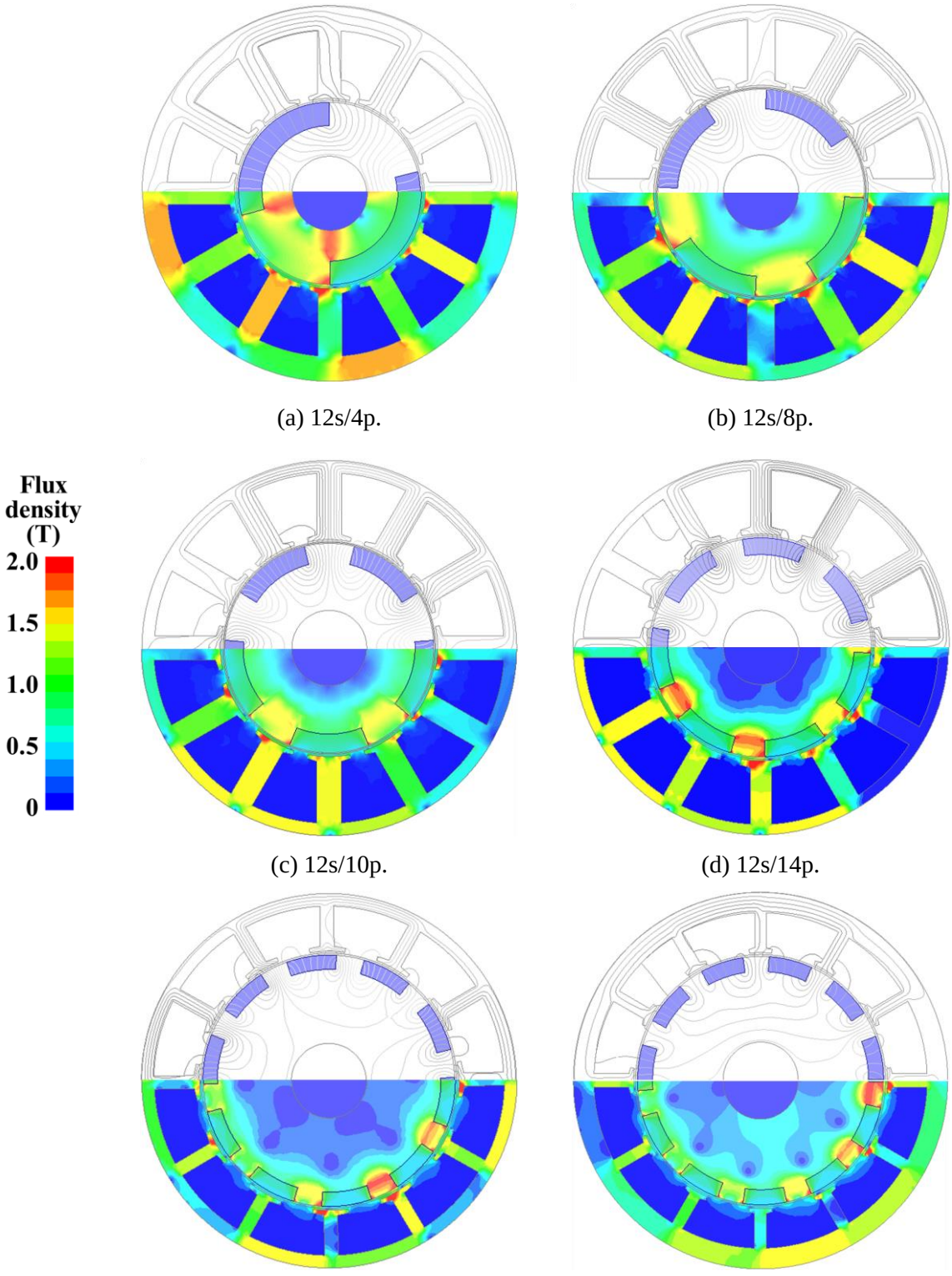

(a) 12s/4p. (b) 12s/8p.

(c) 12s/10p. (d) 12s/14p.

(e) 12s/20p. (f) 12s/22p.

Fig. 2.29. Optimized structures and corresponding magnetic field distributions under on-load conditions with 40 W copper loss.

2.4.2. Comparison of electromagnetic performance

The electromagnetic performances of optimized 12-slot NSP and CP SPMSMs with different slot/pole number combinations are compared in this section, including open-circuit conditions, torque characteristics, efficiency, power factor, overload capability, etc.

2.4.2.1. **Open-circuit**

Open-circuit radial air-gap flux densities and their FFT spectra of optimized 12-slot NSP and CP SPMSMs with different rotor pole numbers are shown in Fig. 2.30. NSP structures have higher fundamental components of open-circuit radial air-gap flux density but CP structures have higher modulated field harmonics, especially for 14-pole, 20-pole, and 22-pole CP SPMSMs, whose modulated field harmonics (5^{th}, 2^{nd}, and 1^{st}, respectively) are higher than their NSP counterparts. In general, fundamental components of open-circuit radial air-gap flux density decrease with the increase of rotor pole number for both NSP and CP VPMSMs.

Open-circuit back EMFs and their FFT spectra of optimized 12-slot NSP and CP SPMSMs with different rotor pole numbers are shown in Fig. 2.31. The NSP SPMSMs with lower rotor pole numbers (4-pole, 8-pole, and 10-pole) have slightly higher fundamental components of back EMFs than their corresponding CP counterparts. However, the CP structure with high rotor pole numbers (14-pole, 20-pole, and 22-pole) has higher fundamental components of back EMFs than the corresponding NSP counterparts due to better field modulation effect as shown in Fig. 2.30 (c).

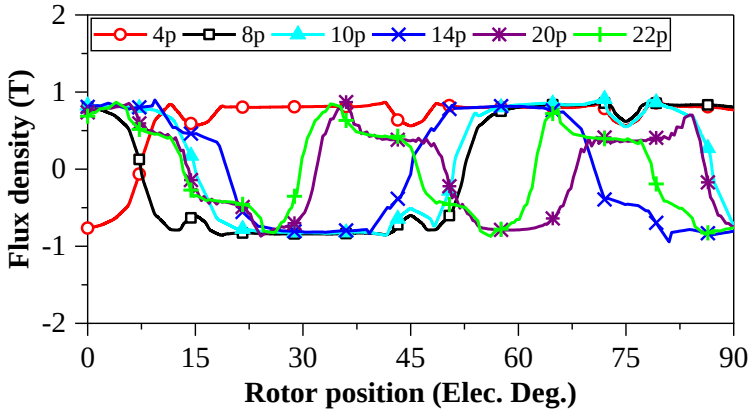

(a) NSP rotors.

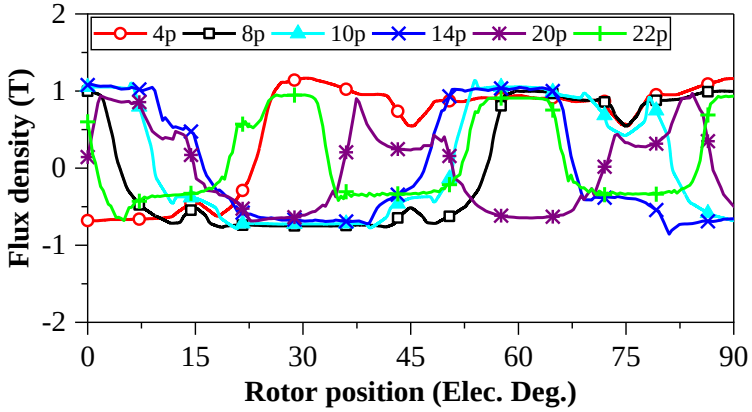

(b) CP rotors.

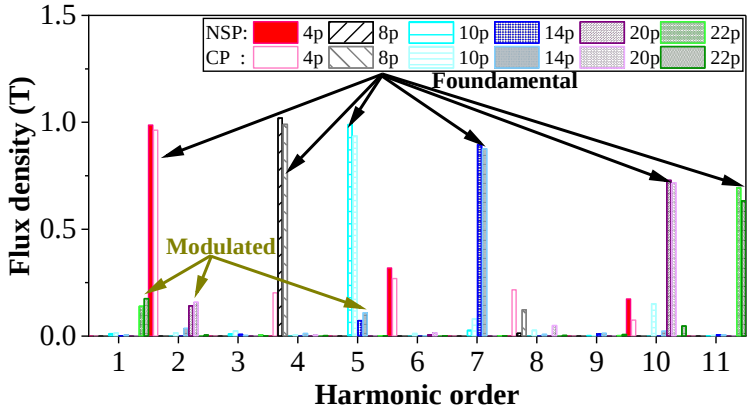

(c) Spectra.

Fig. 2.30. Open-circuit radial air-gap flux densities of 12-slot NSP and CP SPMSMs with different rotor pole numbers.

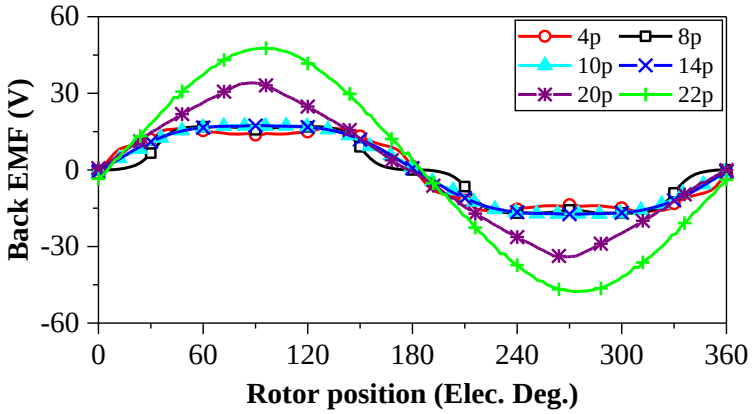

(a) NSP rotors.

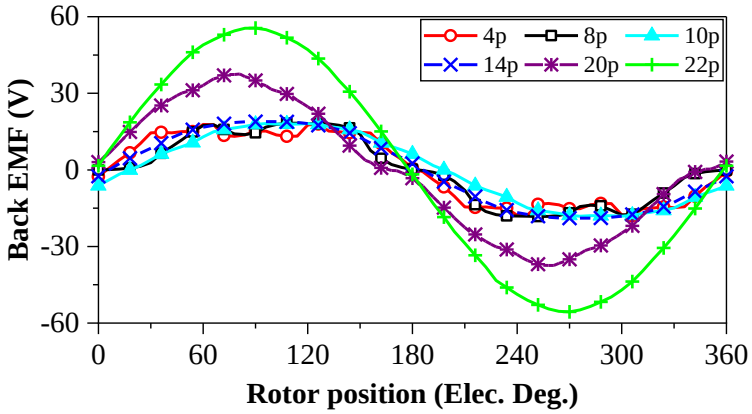

(b) CP rotors.

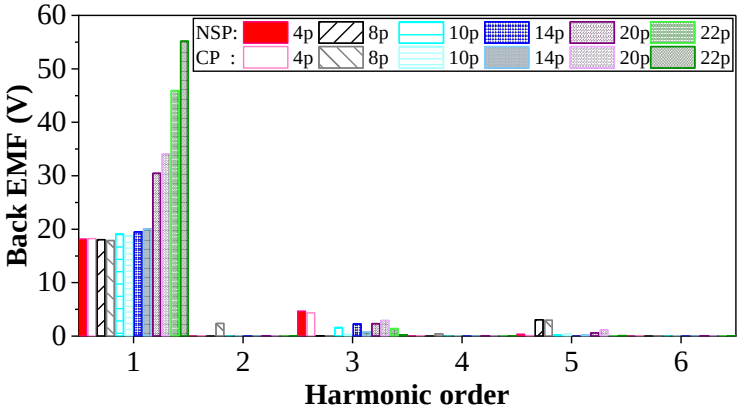

(c) Spectra.

Fig. 2.31. Open-circuit back EMFs of 12-slot NSP and CP SPMSMs with different rotor pole numbers.

2.4.2.2. **Torque characteristics**

Fig. 2.32 shows cogging torques of optimized 12-slot NSP and CP SPMSMs with different rotor pole numbers. The 4-pole and 8-pole NSP and CP SPMSMs have relatively higher cogging torque, as well as the 20-pole NSP VPMSM. Other SPMSMs with higher rotor pole numbers are relatively small.

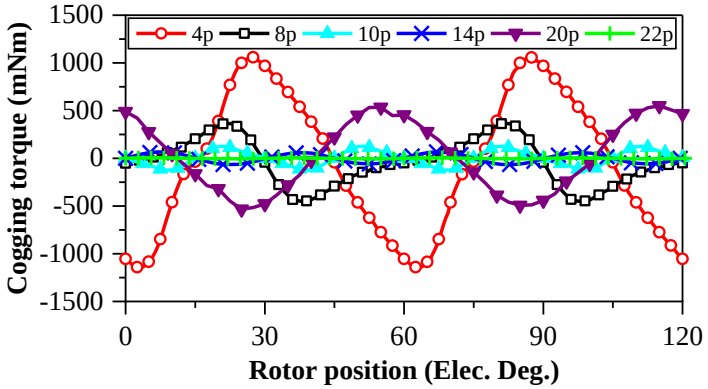

(a) NSP rotors.

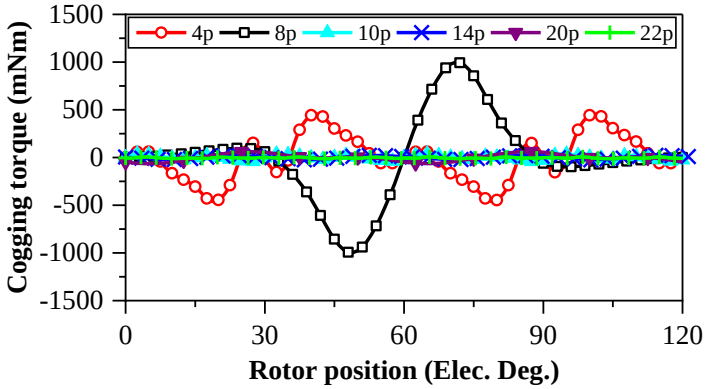

(b) CP rotors.

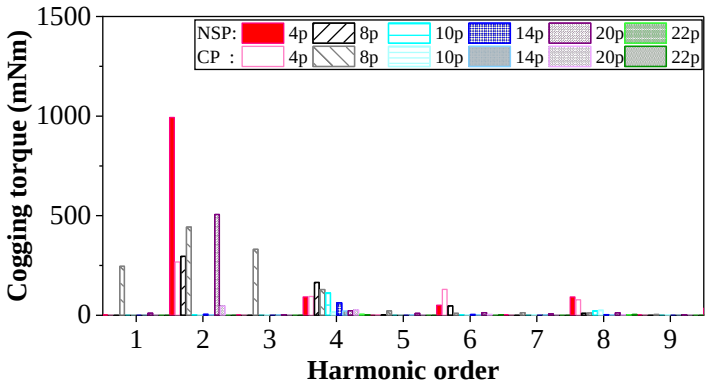

(c) Spectra.

Fig. 2.32. Cogging torques of 12-slot NSP and CP SPMSMs with different rotor pole numbers.

On-load torques under 40 W copper loss of optimized 12-slot NSP and CP SPMSMs with different rotor pole numbers are shown in Fig. 2.33.

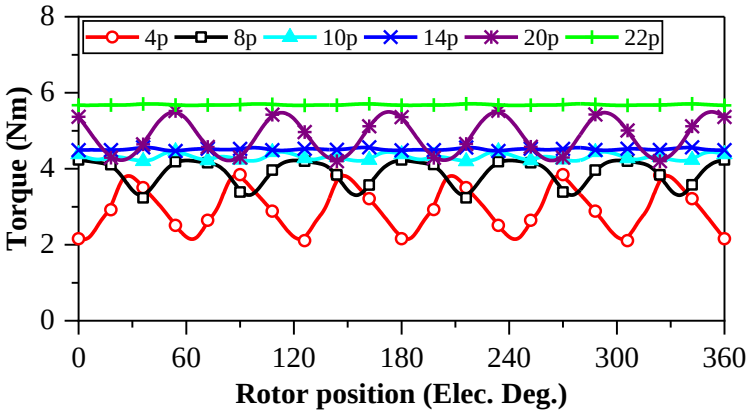

(a) NSP rotors.

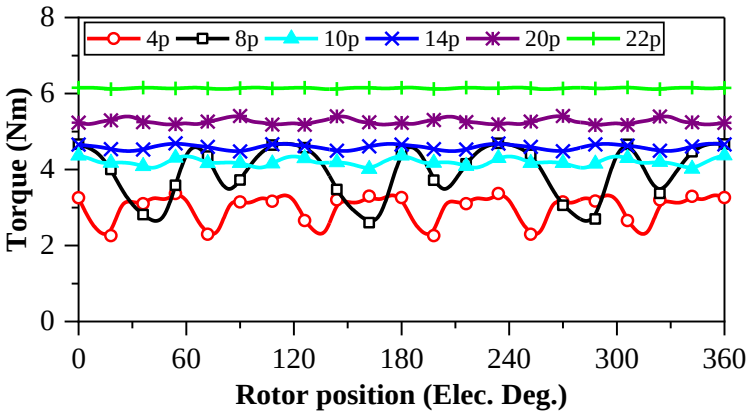

(b) CP rotors.

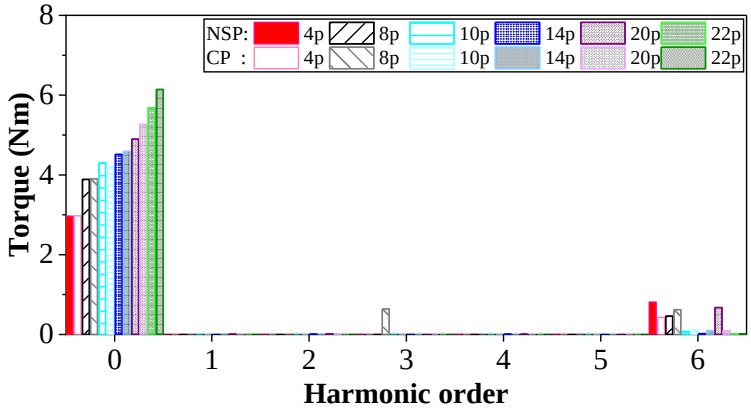

(c) Spectra.

Fig. 2.33. On-load torques under 40 W copper loss of 12-slot NSP and CP SPMSMs with different rotor pole numbers.

According to Fig. 2.33 (c), average torques of optimized 12-slot NSP and CP SPMSMs show almost the same trend as open-circuit back EMFs. The NSP SPMSMs with lower rotor pole numbers (4-pole, 8-pole, and 10-pole) have slightly higher average torques than their corresponding CP counterparts while CP structure with higher rotor pole numbers (14-pole, 20-pole, and 22-pole) has higher average torques than corresponding NSP counterparts due to

better field modulation effect. The torque ripple shows almost the same trend as the cogging torque.

To investigate the effect of field modulation on torque enhancement of 12-slot NSP and CP SPMSMs, the torque separation method [LIU17] is employed. The detailed torque separation method has been illustrated in Section 2.3. Similarly, the torques produced in the CP SPMSMs can also be divided into two parts, i.e., T_U and T_M, which represent the torque components produced by the principle of the conventional electrical machine and the magnetic gearing effect, respectively. Fig. 2.34 compares the torque components produced by the CP SPMSMs against the conventional SPMSMs.

As can be seen, the NSP SPMSMs with 4-pole, 8-pole, and 10-pole could produce slightly larger torques than their CP counterparts since their torques are mainly produced by the principle of the conventional electrical machine, i.e., T_U. Therefore, due to higher amplitudes of the fundamental component of air-gap flux density as shown in Fig. 2.30, i.e., 2^{nd}, 4^{th}, and 5^{th} for 4-pole, 8-pole, and 10-pole, respectively, the NSP SPMSMs have slightly larger average torques.

On the other hand, for 14-pole, 20-pole, and 22-pole CP SPMSMs, the magnetic gearing effect contributes greater percentages of output torque than the respective conventional ones, from 10% to 15% for 14-pole, 59% to 76% for 20-pole, and 82% to 84% for 22-pole CP SPMSMs, respectively.

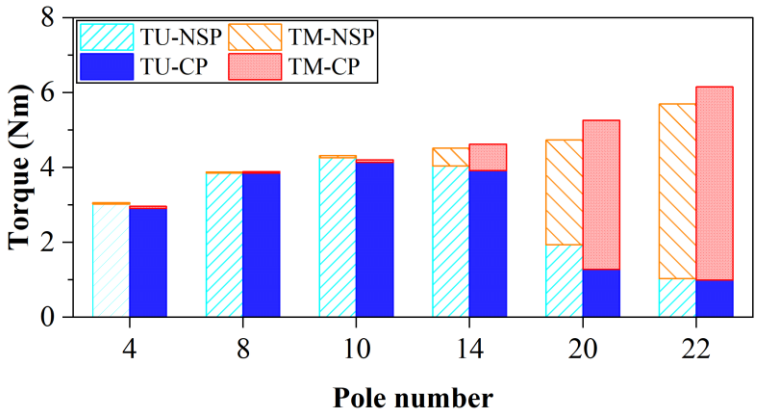

(a) Torque components.

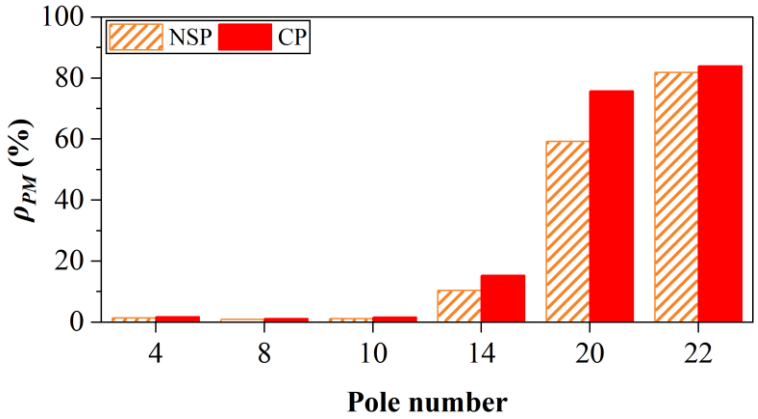

(b) Ratio (ρ_{MG}) of torque produced by magnetic gearing effect.

Fig. 2.34. Comparison of torque components of 12-slot NSP and CP SPMSMs with different rotor pole numbers.

2.4.2.3. **Loss and efficiency**

Fig. 2.35 compares losses and efficiencies of optimized 12-slot NSP and CP SPMSMs with different rotor pole numbers under 40W copper loss and 400 r/min. The iron loss and PM loss increase with the increase of rotor pole numbers. CP rotors with high rotor pole numbers (14-pole, 20-pole, and 22-pole) have higher iron loss. Moreover, CP SPMSMs have lower PM loss than their NSP counterparts. CP SPMSMs with high rotor pole numbers (14-pole, 20-pole, and 22-pole) have higher efficiency at 400 r/min as they have higher average torque output capability.

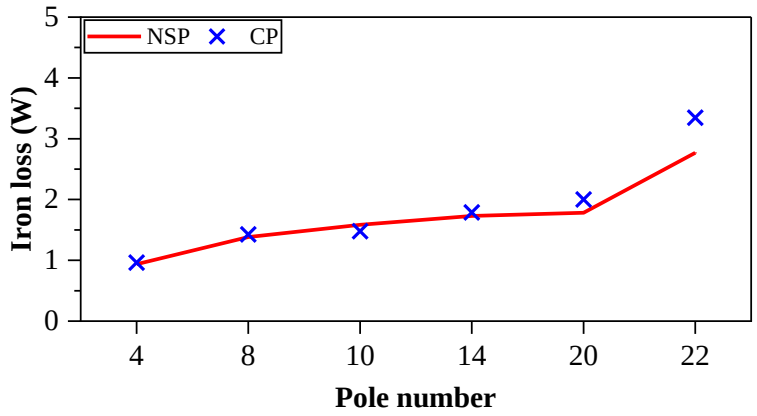

(a) Iron loss.

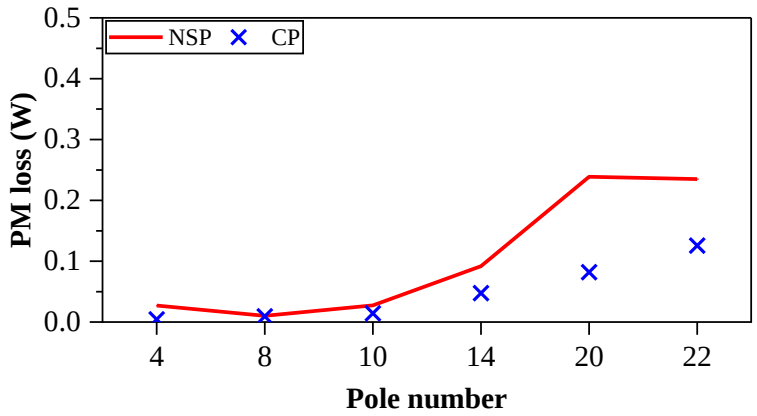

(b) PM loss.

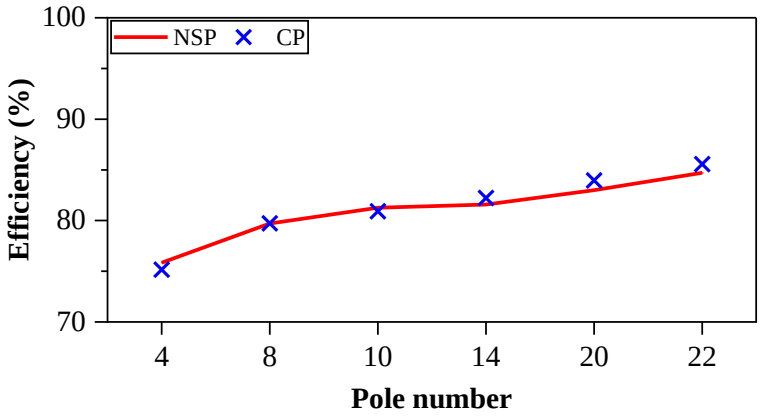

(c) Efficiency.

Fig. 2.35. Comparison of losses and efficiencies of 12-slot NSP and CP SPMSMs with different rotor pole numbers under 40 W copper loss and 400 r/min.

2.4.2.4. **Inductance and power factor**

Fig. 2.36 shows the comparison of *d*-axis inductances and power factors of 12-slot NSP and CP SPMSMs with different rotor pole numbers. The power factors of NSP and CP SPMSMs decrease with the increasing rotor pole number. The CP SPMSMs have higher *d*-axis inductances because of smaller equivalent air-gap lengths, which lead to lower power factors

compared with NSP SPMSMs. It is worth highlighting that the power factors for the 12s/20p and 12s/22p CP VPMSMs are even lower, being 0.67 and 0.54, respectively.

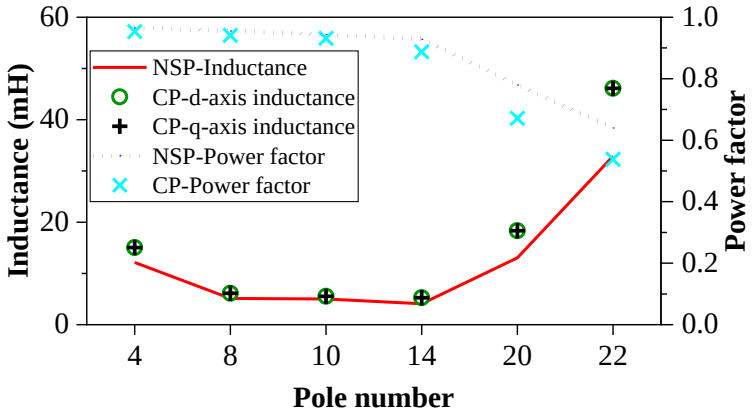

Fig. 2.36. Comparison of *d*-axis inductances and power factors of 12-slot NSP and CP SPMSMs with different rotor pole numbers.

2.4.2.5. **Overload capability**

Fig. 2.37 shows the comparison of overload capabilities of 12-slot NSP and CP SPMSMs with different rotor pole numbers. Even though the CP SPMSMs with higher rotor pole numbers (14-pole, 20-pole, and 22-pole) have higher torque output capability at rated-condition with 40 W copper loss, NSP SPMSMs have better overload capability.

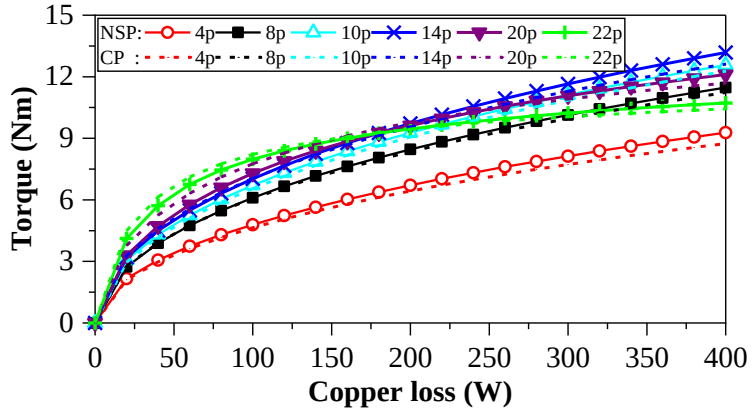

Fig. 2.37. Comparison of overload capability of 12-slot NSP and CP SPMSMs with different rotor pole numbers.

2.5. Experimental Verification

Prototypes are manufactured and tested to verify the analysis and FEA results, including 12s/8p NSP and CP SPMSMs, and 12s/20p NSP and CP VPMSMs as shown in Fig. 2.38. Table 2.6 shows the key parameters of prototypes.

Table 2.6 Key Parameters of Prototypes

	r_{si} (mm)	h_y (mm)	w_t (mm)	b_{so} (mm)	p_{rPM} for CP only
12s/8p	27	4.2	8	2	0.61
12s/20p	32	3.4	4	8	0.64

2.5.1. Open-circuit back EMF

At first, the open-circuit back EMFs of the prototypes are measured at 400 r/min with the test rig shown in Fig. 2.39. Fig. 2.40 and Fig. 2.41 show measured and FEA predicted open-circuit back EMFs at 400 r/min. Even though there are minor distortions between the experiment and FEA simulation caused by the measurement and manufacturing errors, the results match well and verify the FEA analysis.

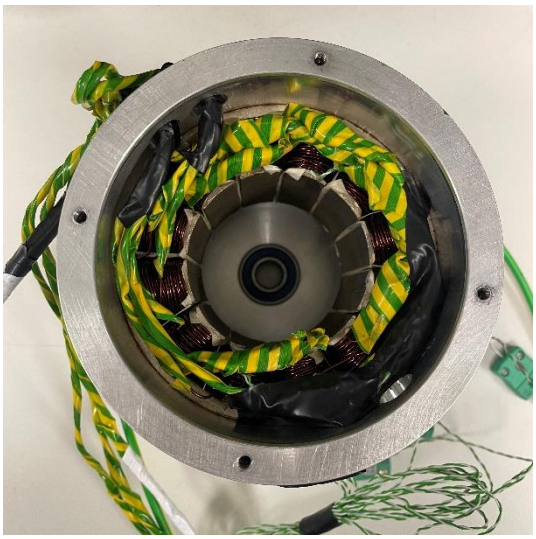

(a) 12s/8p stator.

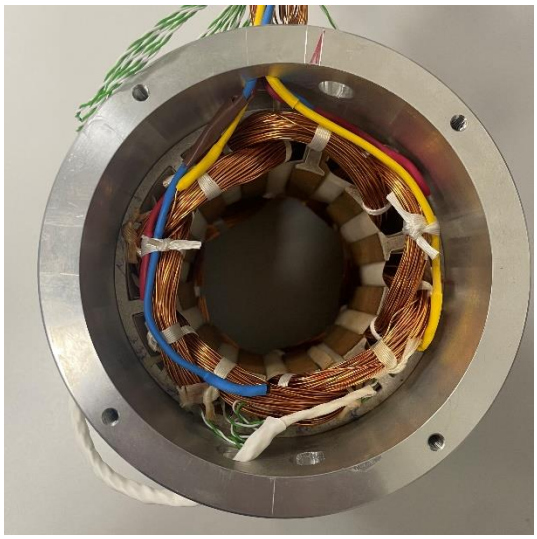

(b) 12s/20p stator.

(c) 12s/8p NSP and CP rotors.

(d) 12s/20p NSP and CP rotors.

Fig. 2.38. Prototypes of 12s/8p NSP and CP SPMSMs, and 12s/20p NSP and CP VPMSMs.

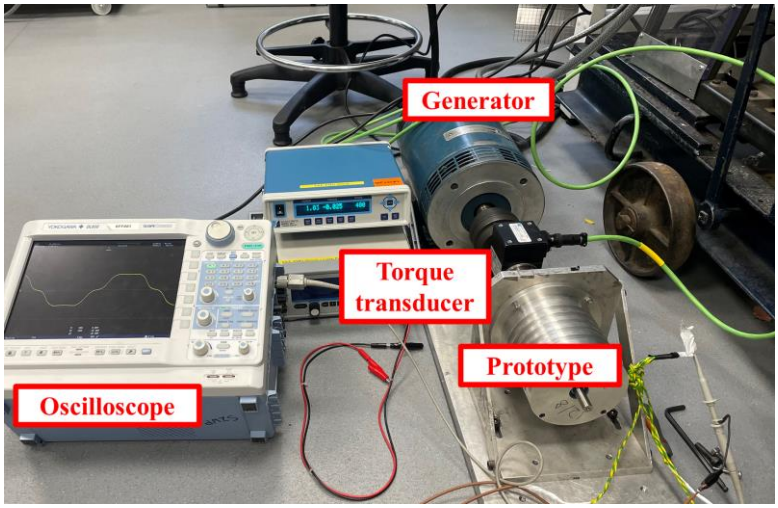

Fig. 2.39. Test rigs for open-circuit back EMF.

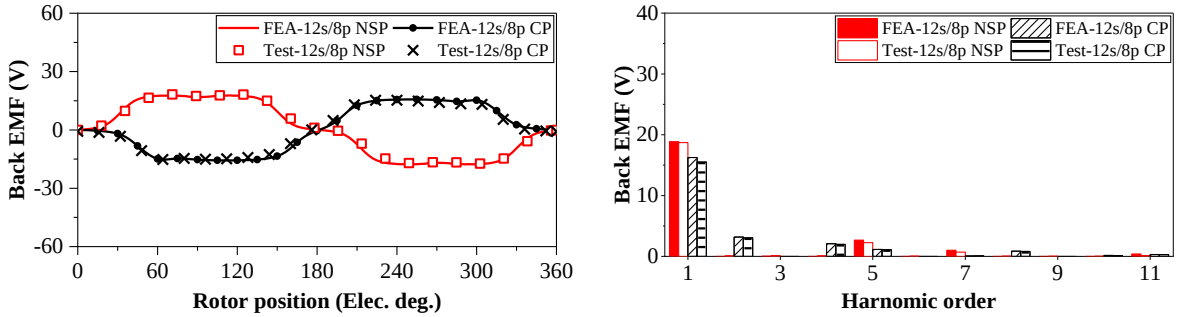

(a) Waveforms. (b) Spectra.

Fig. 2.40. Measured and FEA predicted open-circuit back EMFs of 12s/8p NSP and CP SPMSMs at 400 r/min.

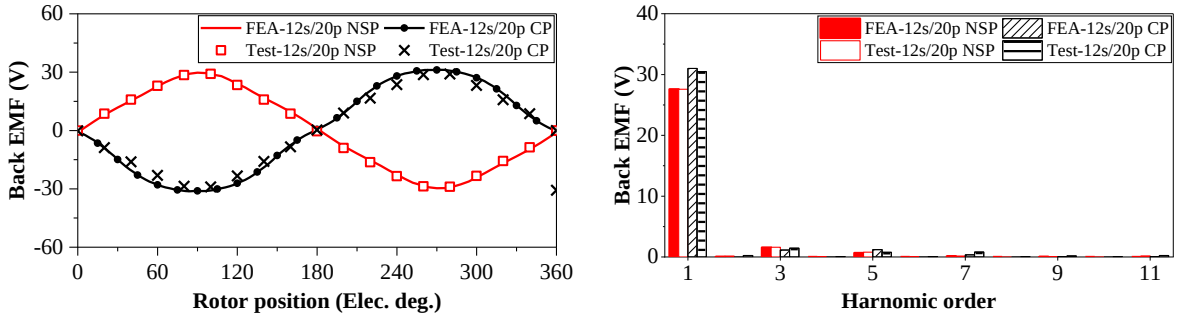

(a) Waveforms. (b) Spectra.

Fig. 2.41. Measured and FEA predicted open-circuit back EMFs of 12s/20p NSP and CP VPMSMs at 400 r/min.

2.5.2. Cogging torque

The cogging torques are measured according to the method proposed in [ZHU09] with the test rig shown in Fig. 2.42. Fig. 2.43 and Fig. 2.44 show measured and FEA predicted cogging torques, which match well and verify the FEA analysis.

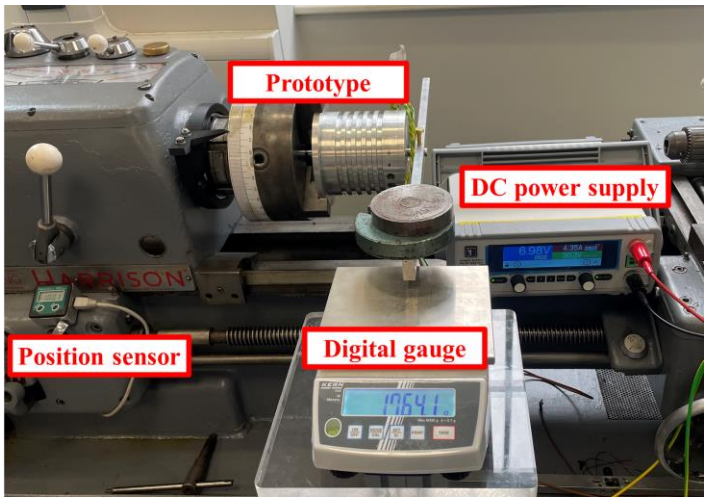

Fig. 2.42. Test rig for cogging torque and static torque.

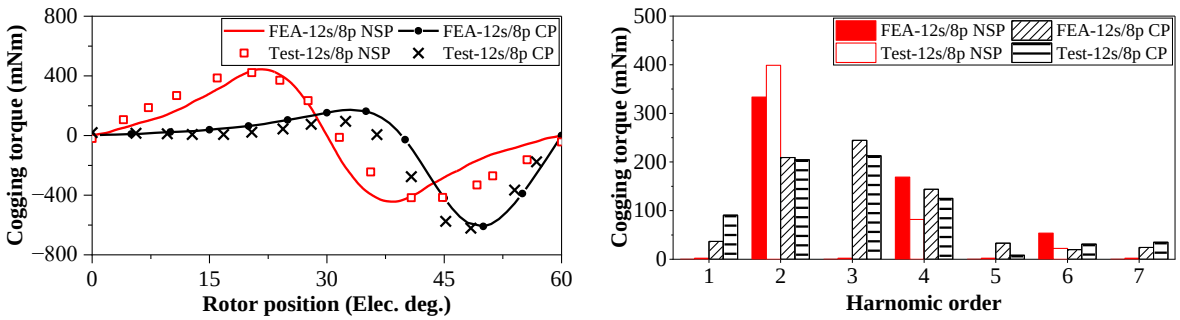

(a) Waveforms. (b) Spectra.

Fig. 2.43. Measured and FEA predicted cogging torques of 12s/8p NSP and CP SPMSMs.

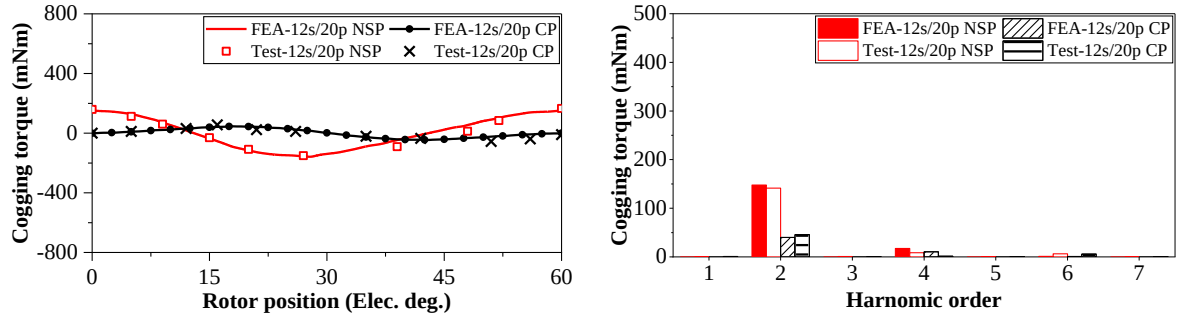

(a) Waveforms. (b) Spectra.

Fig. 2.44. Measured and FEA predicted cogging torques of 12s/20p NSP and CP VPMSMs.

2.5.3. Static torque

The static torque is measured according to the method proposed in [ZHU09]. By injecting current through the DC power supply (I_b=I_c= - 0.5I_a) and rotating the stator while keeping the rotor stationary, the relationship between static torque and rotor position can be measured. The test rig for static torque is shown in Fig. 2.42. The measured and FEA predicted static torques match well as shown in Fig. 2.45 and Fig. 2.46.

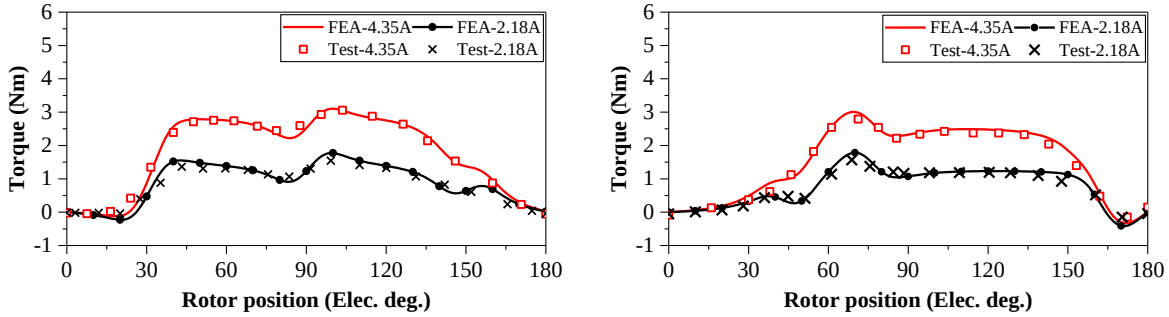

(a) NSP rotors. (b) CP rotors.

Fig. 2.45. Measured and FEA predicted static torques of 12s/8p NSP and CP SPMSMs.

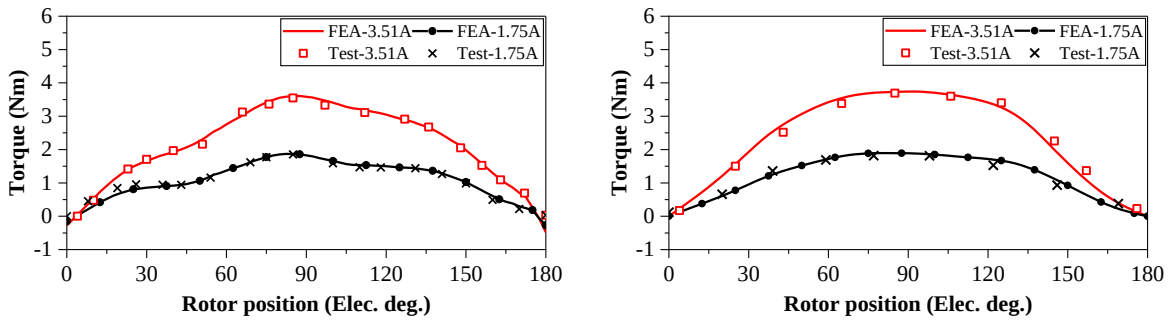

(a) NSP rotors. (b) CP rotors.

Fig. 2.46. Measured and FEA predicted static torques of 12s/20p NSP and CP VPMSMs.

2.5.4. Dynamic torque

Transient torque waveforms and torque–current characteristics can be measured by adopting the dynamic test platform and using the torque transducer and torque reader as shown in Fig. 2.47. The measured and FEA predicted dynamic torques of prototypes with 2 Arms phase current are shown in Fig. 2.48 and Fig. 2.49 while the torque–current characteristics are compared in Fig. 2.50. The measured results agree well with the simulation results.

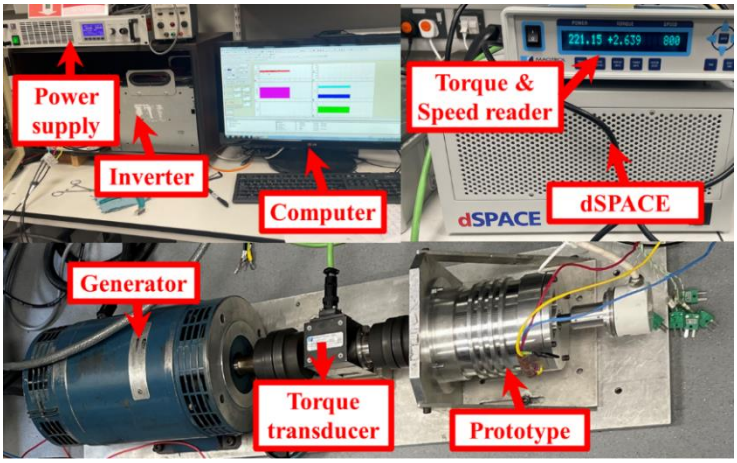

Fig. 2.47. Test rigs for dynamic torque.

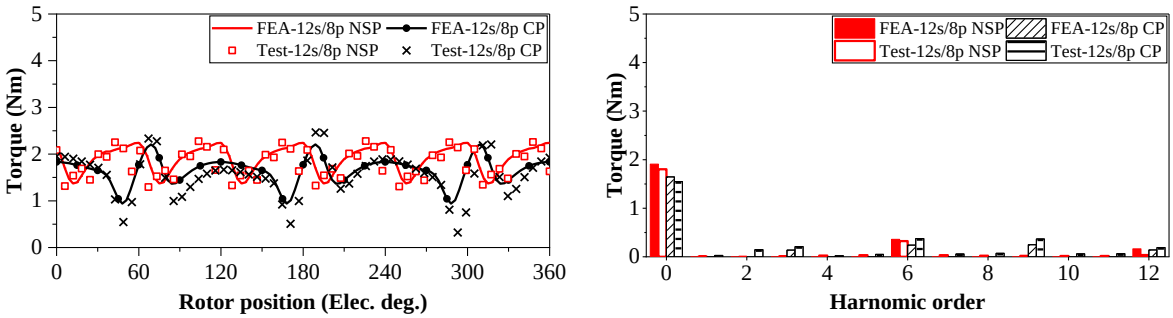

(a) Waveforms. (b) Spectra.

Fig. 2.48. Measured and FEA predicted dynamic torques of 12s/8p NSP and CP SPMSMs.

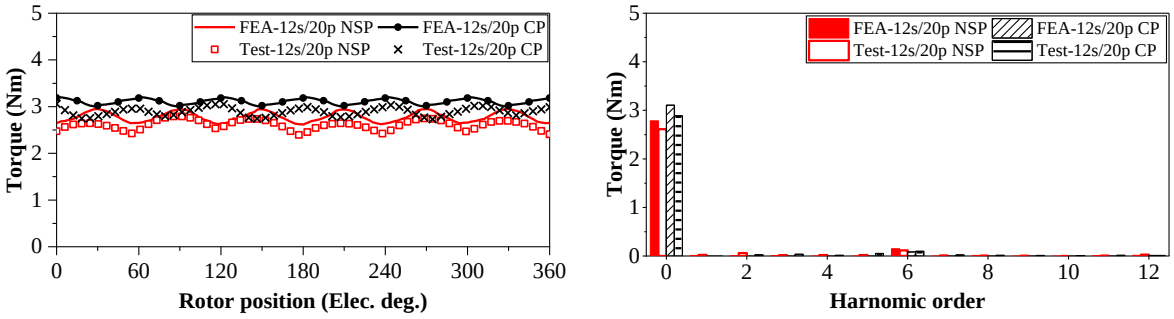

(a) Waveforms. (b) Spectra.

Fig. 2.49. Measured and FEA predicted dynamic torques of 12s/20p NSP and CP VPMSMs.

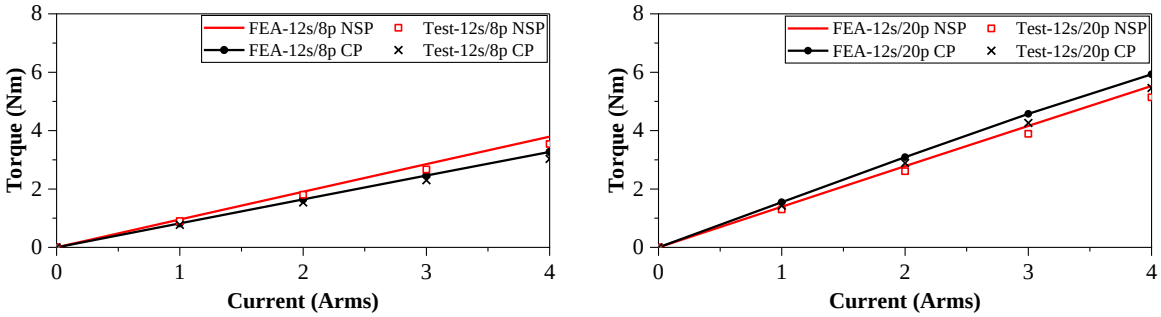

(a) 12s/8p. (b) 12s/20p.

Fig. 2.50. Measured and FEA predicted torque-current characteristics of 12s/8p and 12s/20p NSP and CP SPMSMs.

The measured and FEA predicted efficiencies of prototypes eliminating the mechanical loss under 700 r/min are shown in Table 2.7. The FEA predicted efficiency is calculated by (2.5) while the measured efficiency is calculated (2.8). V_{dc} and I_{dc} are the voltage and current of the inverter. The measured efficiencies are lower than the FEA predicted results because the prototype in FEA is assumed to be driven by a three-phase sinusoidal current without current harmonics. Meanwhile, the inverter loss is not considered in the FEA.

$$\eta = \frac{T\omega}{V_{dc}I_{dc}} \tag{2.8}$$

Table 2.7 Measured and FEA Predicted Efficiencies of Prototypes under 700 r/min

	12s8p NSP	12s8p CP	12s20p NSP	12s20p CP
Torque - FEA (Nm)	2.49	2.15	2.10	2.36
Torque - Test (Nm)	2.28	1.97	1.90	2.14
Efficiency - FEA (%)	89.4	88.1	85.5	86.6
Efficiency - Test (%)	82.2	80.1	78.6	78.4

2.6. Summary

In this chapter, 12-slot SPMSMs with different slot/pole number combinations, winding configurations, and rotor PM topologies are optimized and compared. The effects of end winding, machine optimization scenarios (without/with considering iron loss under different speeds), different lamination stack lengths, and rotor PM topologies (NSP and CP) on the electromagnetic performance of SPMSMs are systematically investigated. The optimal coil pitch and winding factor for each slot/pole number combination have been determined for maximum average torque. The conclusions can be summarized as follows:

1. When the SPMSMs are optimized for maximum average torque under fixed 40 W copper loss neglecting end winding, the optimized average torques almost show the same trend with winding factors.
2. The optimized torque neglecting end winding increases with the rotor pole numbers due to better field modulation effect, especially for vernier machines.
3. The optimized torque considering end winding also increases with the rotor pole numbers but the torque densities of vernier machines are lower than those of FSCW SPMSMs due to the long axial end winding length. However, the vernier machines with long lamination stack lengths can maintain high average torque and torque density simultaneously.
4. End winding will deteriorate the optimized torque, torque density, and power factor, especially of overlapping winding vernier machines.
5. As copper loss plays a dominant role at lower speed conditions, the optimization results considering iron loss at lower speed conditions are almost unchanged. However, the optimized torques reduce obviously while considering iron loss at higher speed, especially for SPMSMs with higher rotor pole numbers. The machines optimized considering iron loss have slightly higher efficiency compared with those optimized neglecting iron loss.
6. CP structure has a better field modulation effect, especially for SPMSMs with high rotor pole numbers (14-pole, 20-pole, and 22-pole), which can also generate higher rated torque compared with NSP counterparts.
7. Higher rotor pole number and CP rotor structure will deteriorate overload capability and power factor even though they have higher rated torque.

CHAPTER 3
ANALYSIS AND REDUCTION OF UNIPOLAR END LEAKAGE FLUX IN CONSEQUENT POLE PM MACHINES

As mentioned in Chapter 2, the CP rotor structure has the advantages of better field modulation effect, high torque output capability, and high PM utilization. However, unbalanced magnetic circuits in the CP structure result in unipolar end leakage flux, which may magnetize the components in the end region and pose threats to system safety [WU16] [GE16] [ZHU17] [WAN19] [LI19d] [LI19e] [QI22a] [QI22b]. By way of example, both the shaft and bearing will be magnetized by unipolar end leakage flux, attracting screws and nuts in the end region. Furthermore, this issue will be more severe for machines with short stack lengths and high saturation levels [WU16] [WAN19].

This chapter investigates the unipolar end leakage flux of CP PMSMs with different slot-pole number combinations and winding configurations. It demonstrates that the unipolar end leakage flux, mainly due to the CP rotor structure, is affected by slot-pole number combinations, while the armature reaction field has a negligible effect on the amplitude of end leakage flux. The unipolar end leakage flux decreases with the increase of rotor pole number for the analyzed FSCW CP PMSMs but increases when the rotor pole number further increases for overlapping winding VMs. Moreover, a simple and effective non-magnetic rotor structure, either a non-magnetic shaft or a non-magnetic shaft together with a non-magnetic ring inside the rotor core (which could be integrated into a single shaft), is proposed for the first time to reduce the unipolar end leakage flux without sacrificing the torque capability. The non-magnetic shaft alone can reduce approximately 90% of end leakage flux, while the non-magnetic ring alone can reduce approximately 40%. Additionally, 95% of end leakage flux can be reduced when combining a non-magnetic ring with a non-magnetic shaft (which could be integrated into a single shaft) compared with the conventional rotor with a magnetic shaft. Considering the manufacturing complexity, a non-magnetic shaft alone is highly recommended. The analyses have been validated by experiments on prototyping consequent pole machines with different slot-pole number combinations, magnetic/non-magnetic shafts, and conventional/composite rotors.

This chapter has been accepted by IEEE Transactions on Industry Applications:

[ZHE24a] Y. Zheng, Z. Q. Zhu, D. Liang, H. Xu, Y. Zhou, H. Liu, and L. Chen, "Analysis and reduction of unipolar end leakage flux in consequent-pole PM machines," *IEEE Trans. Ind. Appl.*, accepted.

3.1. Introduction

Nowadays, PMSMs have been widely employed in many industrial and domestic applications due to high efficiency and torque density [ZHU07] [PEL12]. The CP structure is attractive and has been employed in PMSMs to reduce the PM volume and increase the PM utilization [TOB00] [ZHU18a] [LI18b] [HEN94] [CHU12] [CHU15], especially in VPMSMs.

However, the unbalanced magnetic circuits caused by unbalanced equivalent north and south poles in the CP structure result in unipolar end leakage flux, which has been investigated in various CP PMSMs, including spoke-type CP IPMSMs [GE16], CP partitioned stator flux reversal PMSMs [WU16], CP FSCW PMSMs [WAN19] [LI19d] [LI19e] [QI22a], and CP VPMSMs [CHU11] [XU23]. To mitigate the unipolar end leakage flux in conventional CP PMSMs, several methods have been developed.

The step-staggered rotor structure, where two spoke-type CP rotors with equal stack lengths are step-staggered by one pole pitch, effectively reduces unipolar leakage flux in the end region by approximately 70-80% [GE16]. However, this staggered rotor structure increases the manufacturing complexity of the machine. Novel pole sequences are employed to reduce end leakage in CP FSCW PMSMs, with approximately 65% reduction, including N-Iron-N-Iron-N-S-Iron-S-Iron-S, Iron-S-Iron-S-Iron-Iron-N-Iron-N-Iron, and N-S-N-Iron sequences [WAN19] [LI19d] [LI19e]. However, these new pole sequences may cause large subharmonics in airgap flux density, reduce torque, and increase the PM volume compared with their conventional CP counterparts. In addition, the unipolar end leakage flux in CP VPMSMs has also been investigated. Replacing the magnetic rotor end-cap with non-magnetic material is suggested to reduce the unipolar end leakage flux in external rotor CP VPMSMs [CHU11]. Combining two conventional CP structures with opposite polarities, with half of the circumferential rotor having north-pole PMs and the other part having south-pole PMs, is proposed to reduce unipolar end leakage flux in CP VPMSM by approximately 65% on average [XU23]. However, this structure increases iron loss, cogging torque, and torque ripple compared with its conventional counterpart.

Therefore, considering the manufacturing difficulty, electromagnetic performance, and practicability, the various solutions for reducing unipolar leakage flux in CP PMSMs remain to be further investigated.

The main contributions of this chapter can be summarized as follows:

1. The unipolar end leakage flux in both conventional CP PMSMs and CP VPMSMs is investigated systematically.
2. A simple and effective non-magnetic rotor structure, either a non-magnetic shaft or a non-magnetic shaft together with a non-magnetic ring inside the rotor core (which could be integrated into a single shaft), is proposed for the first time to reduce the unipolar end leakage flux without sacrificing the torque capability.
3. This design offers several advantages: it maintains a simple structure, reduces unipolar end leakage flux, preserves torque capability, and avoids increasing iron loss and torque ripple compared to alternative methods.
4. The non-magnetic shaft alone can reduce approximately 90% of end leakage flux, while the non-magnetic ring alone can reduce approximately 40%. Additionally, 95% of end leakage flux can be reduced when combining a non-magnetic ring with a non-magnetic shaft compared with the conventional rotor with a magnetic shaft. Considering the manufacturing complexity, a non-magnetic shaft alone is highly recommended.

This chapter is organized as follows. Firstly, six optimized 12-slot CP PMSMs are presented, including CP PMSMs (12-slot/4-pole (12s/4p), 12s/8p, 12s/10p, and 12s/14p) and CP VPMSMs (12s/20p and 12s/22p) in section 3.2. Then, the unipolar end leakage flux distributions of the analyzed machines are discussed, where the influence of the armature reaction is also considered in section 3.3. Afterward, the influence of critical design parameters on end leakage and average torque of CP PMSMs, including shaft diameter, PM thickness, PM pole arc, air-gap length, and slot opening, is investigated in section 3.4. Furthermore, the proposed non-magnetic shaft or composite rotor structure is presented, and the end leakage fluxes of 12-slot CP PMSMs with magnetic/non-magnetic shafts and conventional/composite rotors are calculated and compared by 3-D FEA analysis in section 3.5. Moreover, 12s/10p FS CP PMSM and 12s/20p CP VPMSM prototypes with magnetic/non-magnetic shafts and conventional/composite rotors are manufactured to experimentally validate the analyses in section 3.6. Finally, this chapter is concluded in section 3.7.

3.2. Machine Topologies

Fig. 3.1 shows the analyzed 12-slot CP PMSMs with different rotor pole numbers and winding configurations with optimal coil pitches [ZHE22], including the overlapping winding 12s/4p CP PMSM, non-overlapping winding FSCW CP PMSMs (12s/8p, 12s/10p, and 12s/14p), and overlapping winding CP VPMSMs (12s/20p and 12s/22p).

For the CP VMs, the magnetic fields produced by armature reactions and PMs interact with each other through the field modulation effect of stator slots and rotor iron poles to generate steady torque. The stator slot number (N_s), rotor pole pair number (p_r), and pole-pair number of armature winding (p_a) should satisfy:

$$p_a = |N_s - p_r| \tag{3.1}$$

Therefore, for the 12-slot/20-pole and 12-slot/22-pole VMs, the pole pair numbers of the armature winding are 2 and 1, respectively.

The CP rotor structure consists of the salient rotor and north pole PMs only. One pole pair of the CP rotor consists of one piece of PM and one adjacent iron pole. The salient rotor structure helps to enhance the magnetic gearing effect. Therefore, the number of PMs can be reduced to half compared with its conventional NSP counterpart.

For a fair comparison, all CP PMSMs are globally optimized to achieve maximum average torque production, with the copper loss (including end winding) fixed at 40 W for considering the general thermal limit of small-size machines under natural cooling conditions [BIA04] [ZHE22]. As the machines are operated at a relatively low speed (400 r/min), PM and iron losses are neglected during the optimization. The fixed geometric parameters are the stator outer diameter, the stack length, the air-gap length, the shaft diameter, and the PM volume. The design parameters, including the stator inner radius, the stator yoke thickness, the stator tooth width, the stator slot opening width, the coil pitch, and the ratio of pole arc to pole pitch (p_{rPM}), are shown in Fig. 3.2 and will be globally optimized. The pole arc to pole pitch ratio is defined as θ_{pm}/θ_1 in Fig. 3.2. The fixed parameters and the optimized variables are listed in Table 2.1 and Table 2.5, respectively.

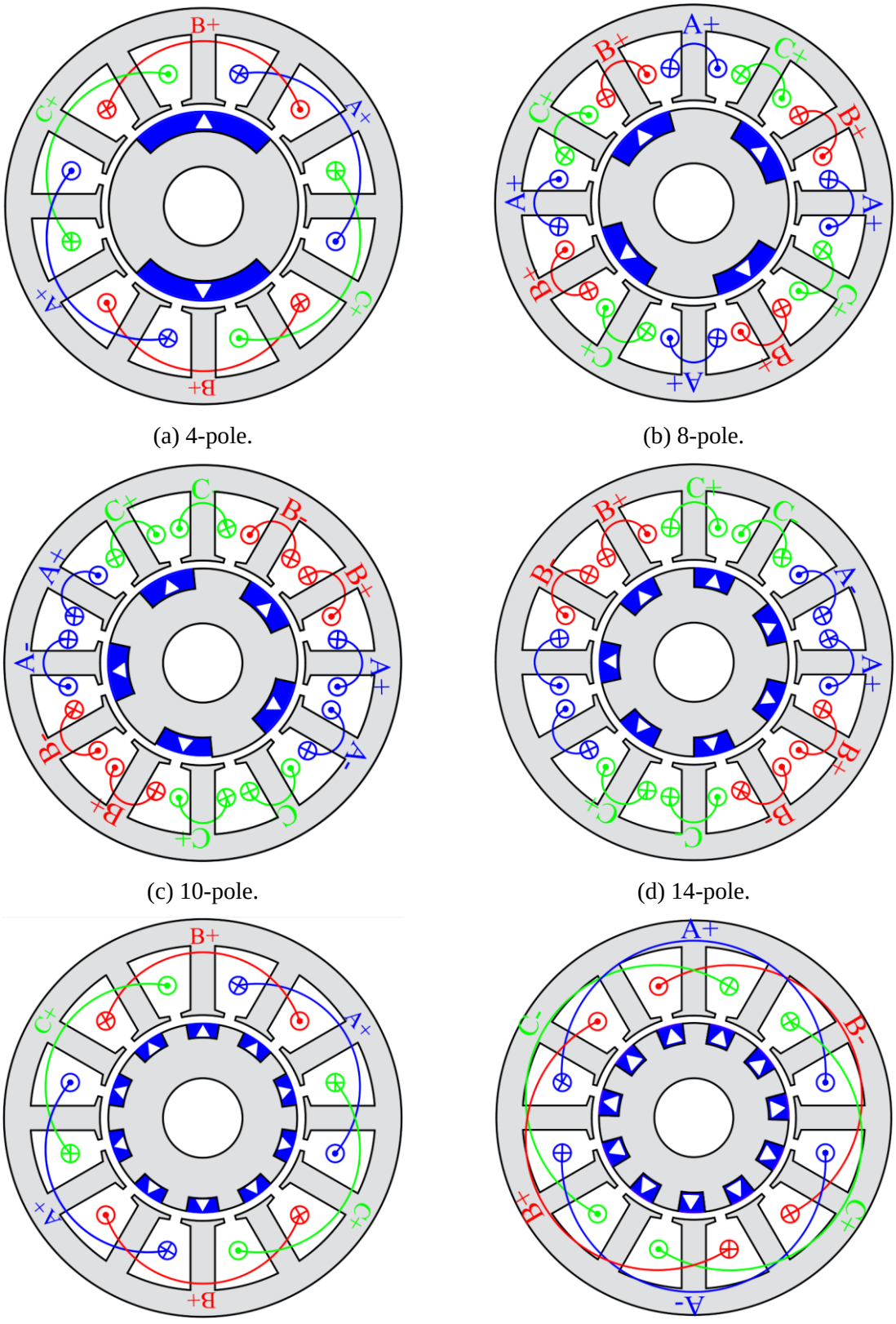

(a) 4-pole. (b) 8-pole.

(c) 10-pole. (d) 14-pole.

(e) 20-pole. (f) 22-pole.

Fig. 3.1. Machine topologies of 12-slot CP PMSMs.

The optimized structures and corresponding magnetic field distributions under the open-circuit and on-load conditions with 40 W copper loss are also shown in Fig. 3.3 and Fig. 2.29. It can

be seen that the on-load magnetic fields are slightly more saturated than those under open-circuit conditions. Meanwhile, the optimized yoke thickness of the 12s/14p CP PMSM is the lowest since it has the largest pole number of stator armature field. Moreover, since the pole number of the stator armature field in 12s/22p CP VPMSM is two, its optimized yoke thickness is larger than that of the 12s/20p CP VPMSM, whose pole number of the stator armature field is four.

The optimized torque varies across different winding configurations and field modulation effects. The overlapping winding 12/4p PMSM exhibits relatively lower torque due to its longer end winding. In contrast, FSCW PMSMs (12s/8p, 12/10p, and 12s/14p) have similar torques and higher than 12s/4p PMSM, benefiting from shorter end windings. VMs (12s/20p and 12s/22p) achieve higher torques despite longer end windings, attributed to the better field modulation effect. However, the torque density of VPMSMs is lower than that of FSCW PMSMs as shown in Table 2.5.

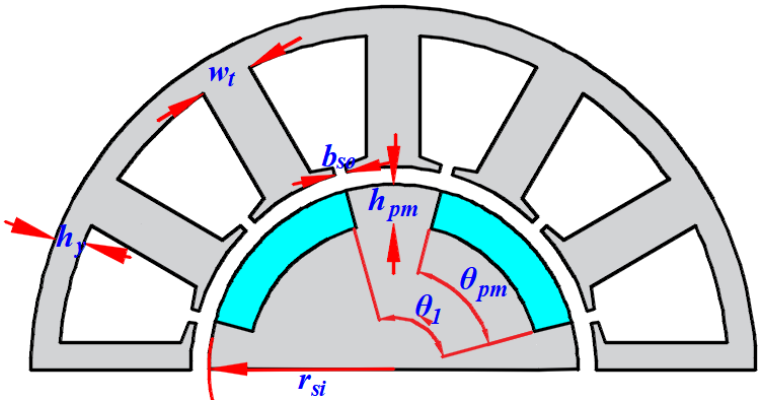

Fig. 3.2. Illustration of design variables for CP PMSMs.

3.3. Unipolar End Leakage Flux Distribution

In this section, the 3-D FEA models are established to analyze the unipolar end leakage flux of the optimized CP PMSMs, where the magnetic shaft SUS430 is employed.

3.3.1. Comparison between north-south pole and consequent pole

At first, end leakage flux distributions between NSP and CP PMSMs are compared. The 12s/14p FSCW PMSM and 12s/22p ISDW VPMSM are taken as examples.

NSP and CP PMSMs are shown in Fig. 2.1 and Fig. 3.1. NSP PMSMs are optimized in section 2.3.2 while CP PMSMs are optimized in section 3.2. End leakage flux distributions of 12-

slot/14-pole and 12-slot/22-pole NSP and CP PMSMs under open-circuit and on-load conditions with 40 W copper loss are shown in Fig. 3.4. For the clear observation of end leakage on the shaft, the stator has been removed from the figures. However, all analyses regarding end leakage are conducted with the stator around the rotor. Compared with CP PMSMs, NSP counterparts have negligible end leakage fluxes on the shaft and without unipolar distribution. Maximum end leakage fluxes under different armature reactions are shown in Fig. 3.5, which also shows the same conclusion.

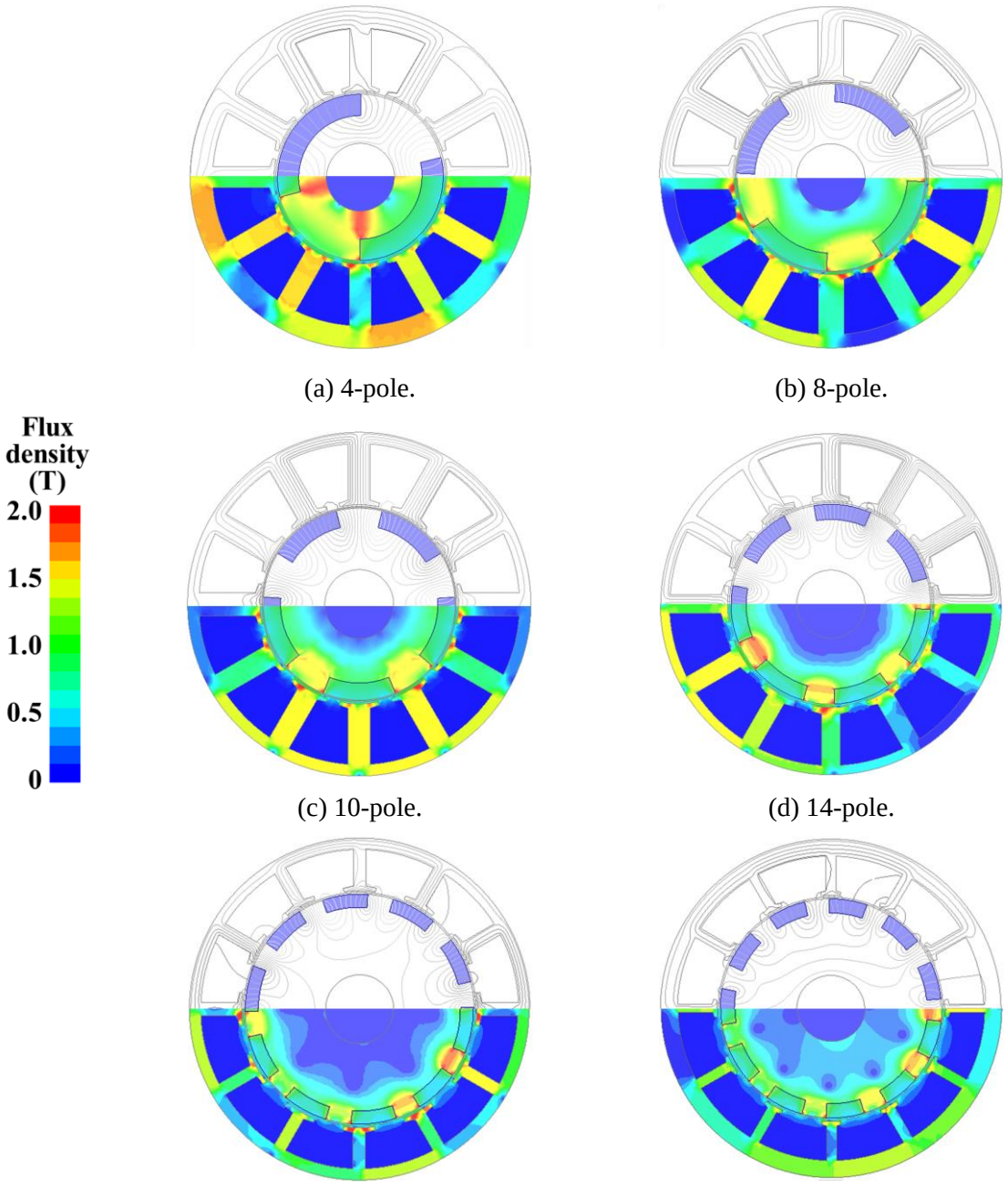

(a) 4-pole. (b) 8-pole.

(c) 10-pole. (d) 14-pole.

(e) 20-pole. (f) 22-pole.

Fig. 3.3. Open-circuit magnetic field distributions of 12-slot CP PMSMs.

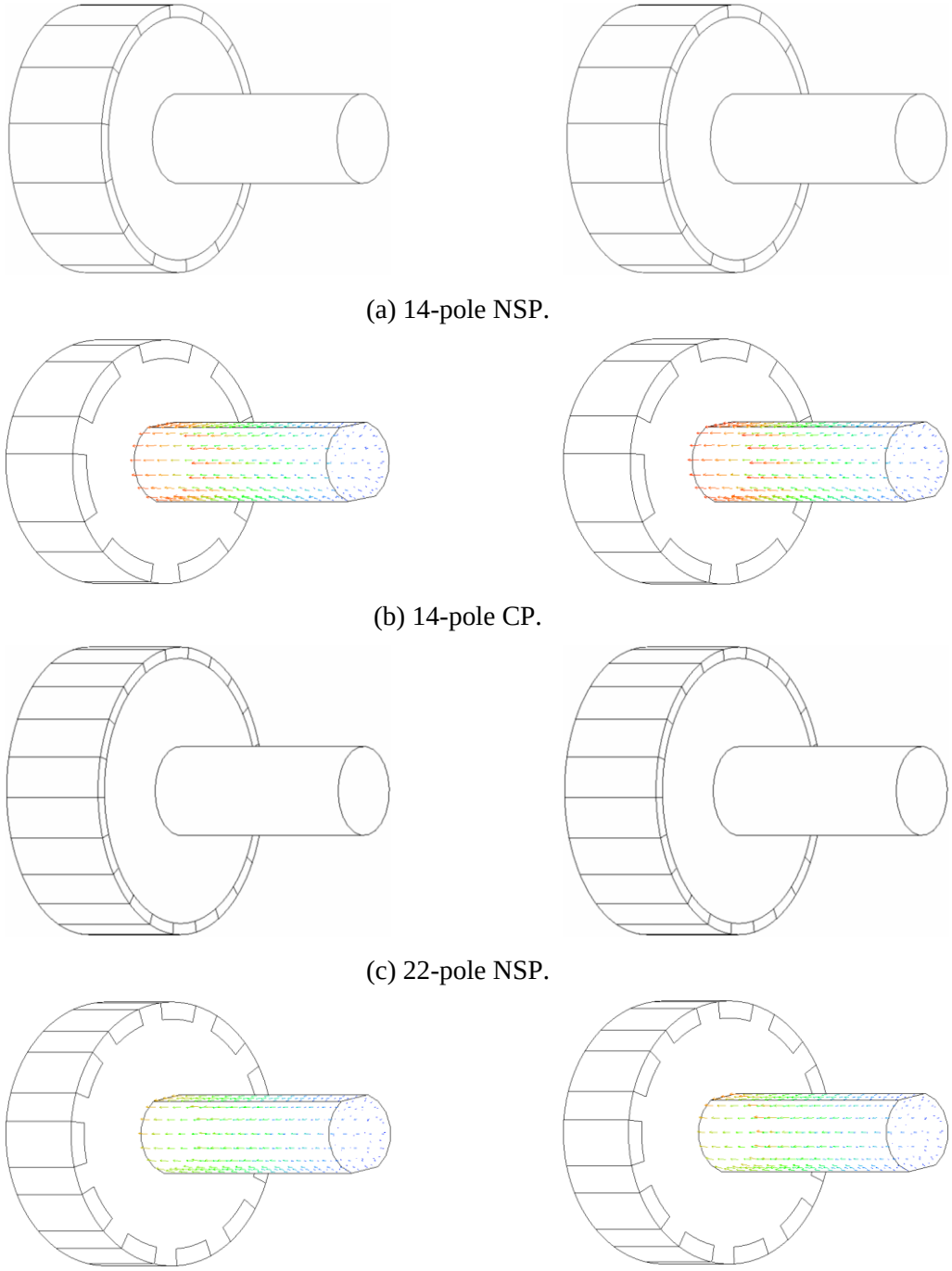

Fig. 3.4. End leakage flux distributions of 12-slot/14-pole and 12-slot/22-pole NSP and CP PMSMs under open-circuit and on-load conditions with 40 W copper loss. Stators have been removed from the figures for clarity.

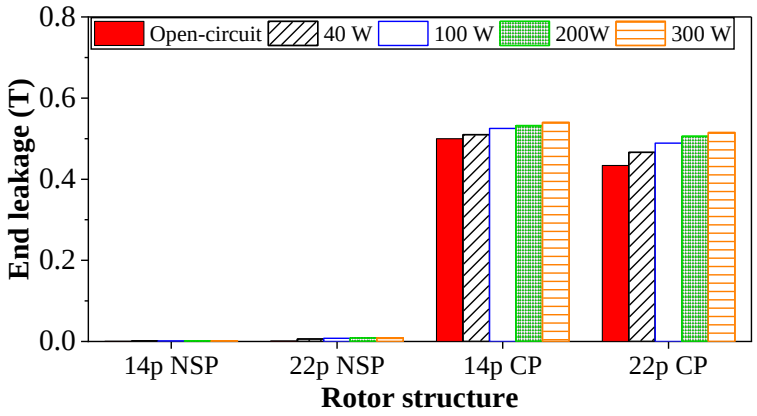

Fig. 3.5. Maximum end leakage fluxes of 12-slot/14-pole and 12-slot/22-pole NSP and CP PMSMs under different armature reactions.

3.3.2. Unipolar end leakage flux in consequent pole machines

Due to the unbalanced magnetic circuit of the CP rotor structure, the end leakage flux in the end region shows unipolar distribution. Fig. 3.6 shows the simplified magnetic circuit of the CP PMSM. The magnetic path with red color is the main flux magnetic field while that with green color is the end leakage flux magnetic field, where F_{PM} and R_{PM} are the magnetomotive force and reluctance of the PM. R_S, R_σ, R_{RT}, and R_{RY} are the equivalent reluctance of stator, airgap, rotor tooth, and rotor yoke, respectively. R_{ER} and R_{SH} are the equivalent reluctance of end region and shaft.

Moreover, Fig. 3.7 shows the distributions of unipolar end leakage flux for all CP PMSMs under open-circuit and on-load (with 40 W copper loss) conditions. As can be seen, the effect of armature reaction magnetic fields is minor, and the distribution of the end leakage flux on the shaft for each CP PMSM always exhibits almost the same unipolar distribution.

Furthermore, with the increasing current density, i.e., the copper loss, the distributions of the end leakage flux on the shaft and their maximum values are compared in Fig. 3.8 and Fig. 3.9, respectively. Fig. 3.10 shows the maximum values of unipolar end leakage fluxes and armature pole-pair numbers of 12-slot CP PMSMs under load condition with 40 W copper loss.

Some phenomena can be observed from Fig. 3.7-Fig. 3.10.

1. Under both open-circuit and on-load conditions, the unipolar end leakage fluxes in all CP PMSMs are significant.

2. The armature reaction field only has a minor effect on the unipolar distribution of end leakage flux, although high armature reaction slightly increases the end leakage fluxes due to the magnetic saturation.
3. From 1) and 2), the unipolar end leakage fluxes are mainly due to the CP rotor structure.
4. The unipolar end leakage flux decreases with the increase of rotor pole number for the analyzed FSCW CP PM machines since the radial leakage flux increases with the rotor pole number, and less leakage flux will travel in the axial direction.
5. When the rotor pole number further increases, the unipolar end leakage flux increases with the increase of the rotor pole number for overlapping winding VMs.

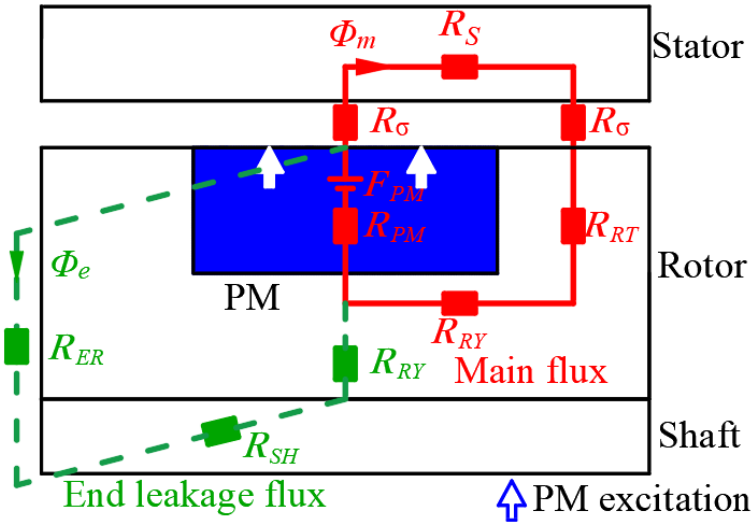

Fig. 3.6. Simplified magnetic circuit of CP PMSM.

Since the optimized torques of PMSMs under 40 W copper loss are different, the maximum unipolar end leakage fluxes under different conditions are compared. The currents of PMSMs are adjusted to ensure each PMSM generates the same average torque for a fair comparison. Table 3.1 lists the currents of PMSMs for different torque output conditions, including currents and torques at 40 W copper loss, currents for generating 2.97 Nm torque, and currents for generating 6.15 Nm torque. The maximum unipolar end leakage flux under open-circuit, rated-load with 40 W copper loss, 2.97 Nm torque output, and 6.15 Nm torque output conditions are compared in Fig. 3.11. The variations between maximum unipolar end leakage flux and rotor pole number under different load conditions show the same trend. Therefore, the unipolar end leakage flux under fixed 40 W copper loss conditions will be selected for analysis and comparison in this thesis.

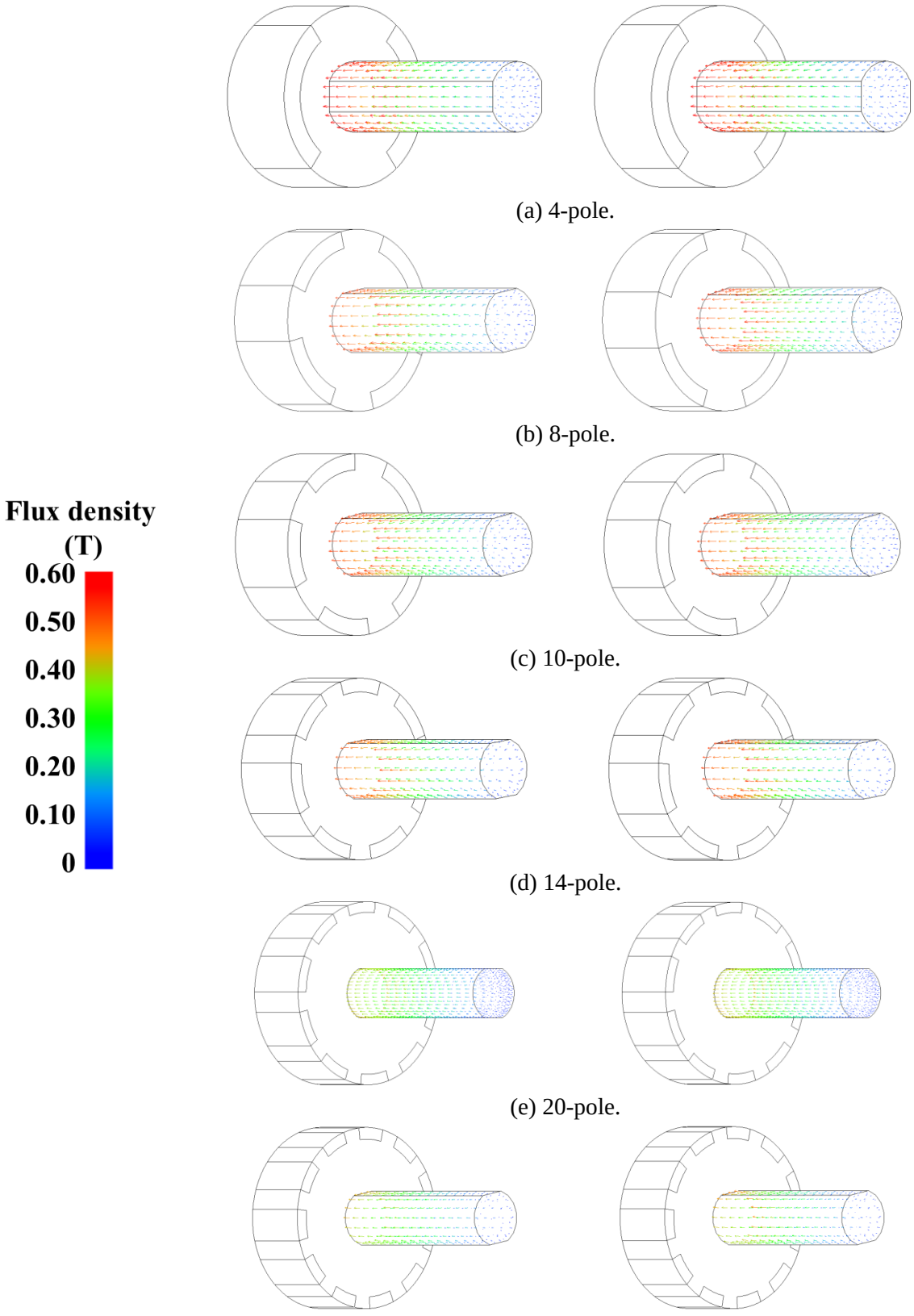

Fig. 3.7. Unipolar end leakage flux distributions of 12-slot CP PMSMs under open-circuit and on-load conditions with 40 W copper loss. Stators have been removed from the figures for clarity.

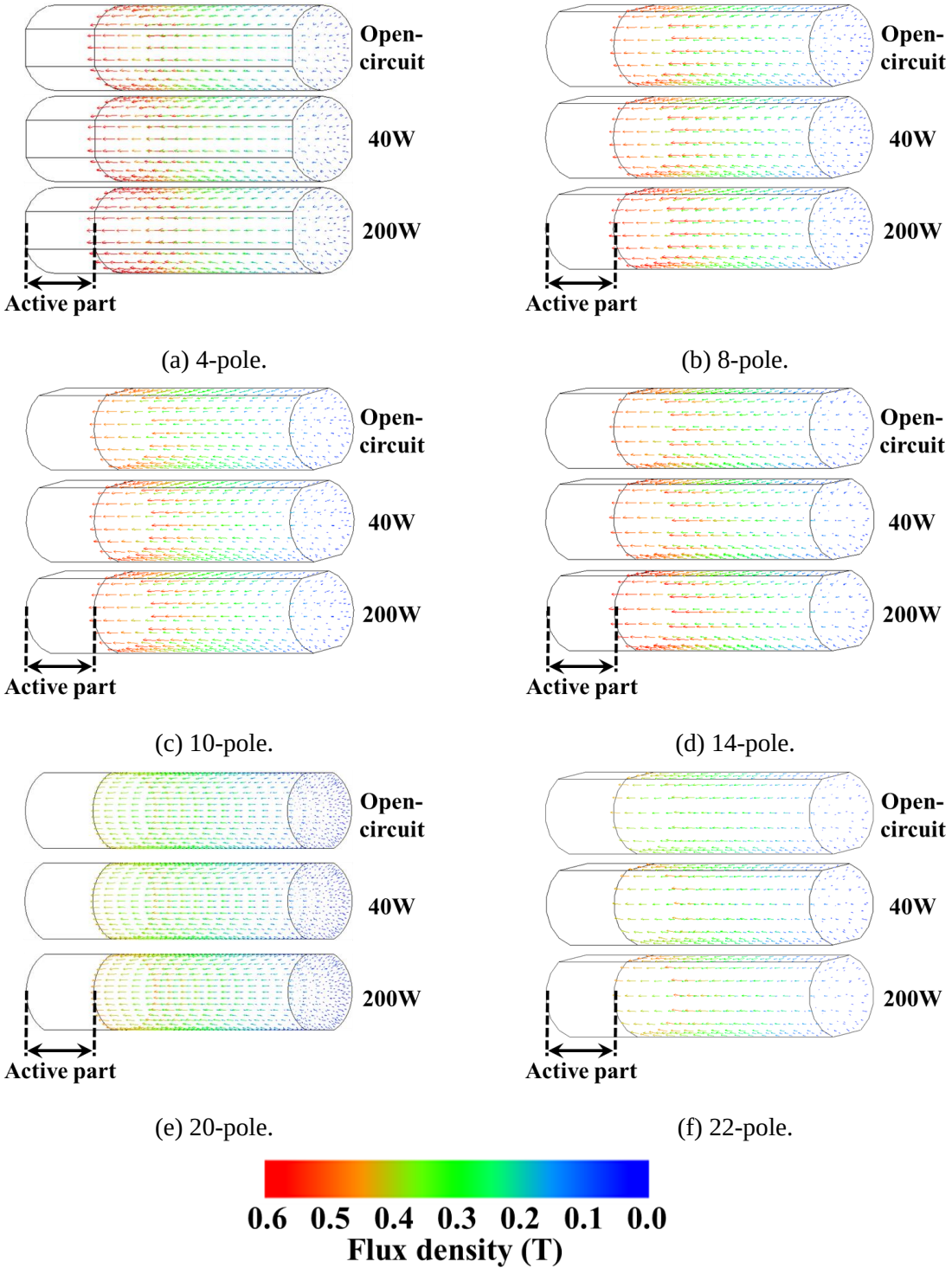

Fig. 3.8. End leakage flux distributions on shafts of 12-slot CP PMSMs under open-circuit and on-load conditions with different armature reactions.

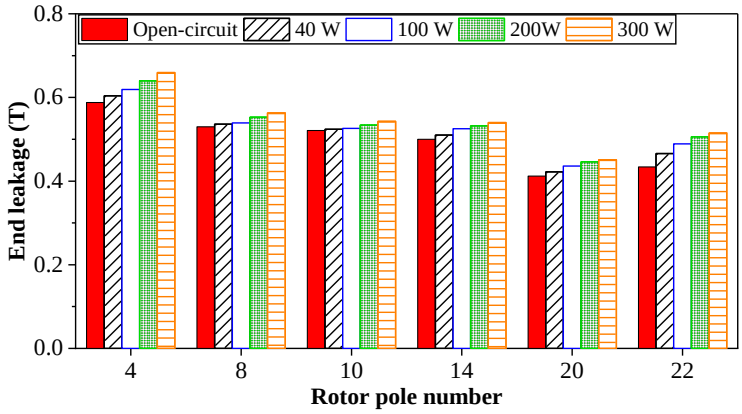

Fig. 3.9. Maximum end leakage flux amplitudes of 12-slot CP PMSMs with different rotor pole numbers and armature reactions on shaft surface about 3 mm away from rotor end.

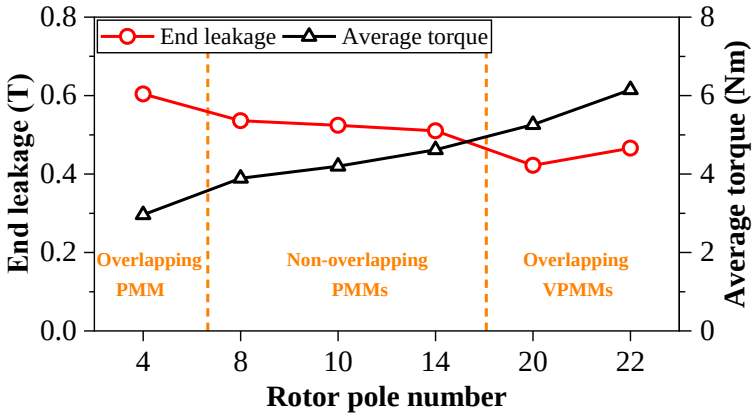

Fig. 3.10. Maximum values of unipolar end leakage fluxes and average torques of 12-slot CP PMSMs under load condition with 40 W copper loss.

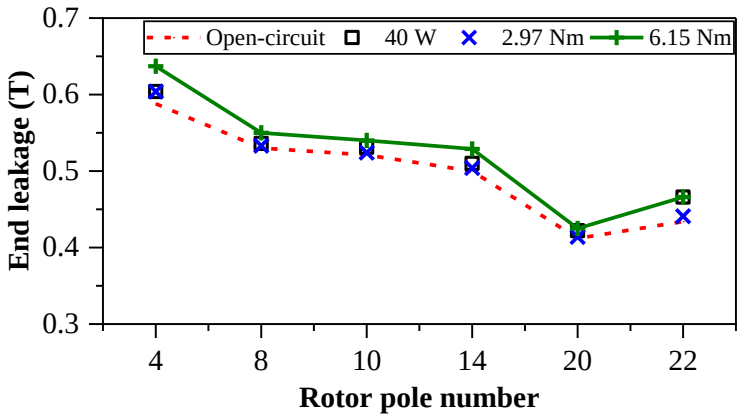

Fig. 3.11. Maximum unipolar end leakage flux under open-circuit, rated-load with 40 W copper loss, 2.97 Nm torque output, and 6.15 Nm torque output conditions.

Table 3.1 Currents of PMSMs for Different Torque Output Conditions

Parameter	**Value**					
Rotor pole number	4	8	10	14	20	22
Torque for 40 W copper loss (Nm)	2.96	3.89	4.20	4.62	5.26	6.15
Current for 40 W copper loss (A)	4.51	6.15	6.44	6.53	4.42	3.38
Current for 2.96 Nm torque (A)	4.51	4.55	4.54	4.18	2.45	1.58
Current for 6.15 Nm torque (A)	9.8	9.75	9.56	8.9	5.25	3.38

3.4. Influence of Critical Design Parameters

In this section, the influence of critical design parameters on end leakage and average torque of CP PMSMs is investigated, including shaft diameter, PM thickness, PM pole arc, air-gap length, and slot opening.

3.4.1. Shaft diameter

The minimum necessary shaft diameter is determined by the torque. Since the optimized torques of CP PMSMs with different slot/pole number combinations vary, the influence of the shaft diameter on average torque and end leakage is investigated. Fig. 3.12 illustrates that shaft diameter has a negligible effect on average torque. However, smaller shaft diameters lead to higher end leakage. The 20 mm diameter shaft is selected for all CP PMSMs to ensure mechanical strength and reduce end leakage.

3.4.2. PM thickness

Fig. 3.13 shows the influence of PM thickness on average torque and end leakage. The torques of conventional CP PMSMs (4-pole to 14-pole) increase with the PM thickness. However, thicker PM does not guarantee higher torque for CP VPMSMs due to higher saturation in vernier machines. Additionally, end leakage increases with PM thickness.

3.4.3. PM pole arc

Fig. 3.14 shows the influence of the PM pole arc on average torque and end leakage. The optimal PM pole arc for each CP PMSM is approximately 0.6. The larger PM pole arc provides more magnetic flux, leading to higher saturation and increased end leakage.

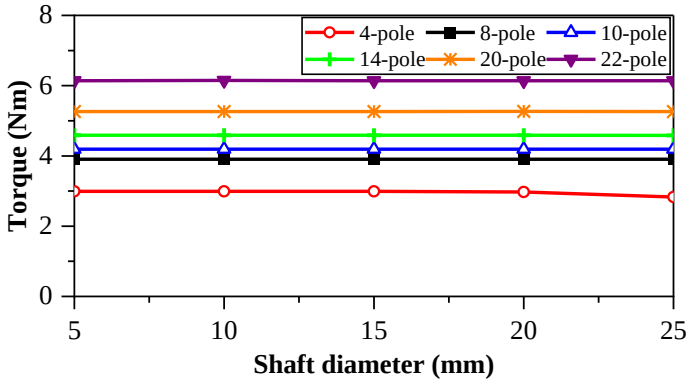

(a) Average torque.

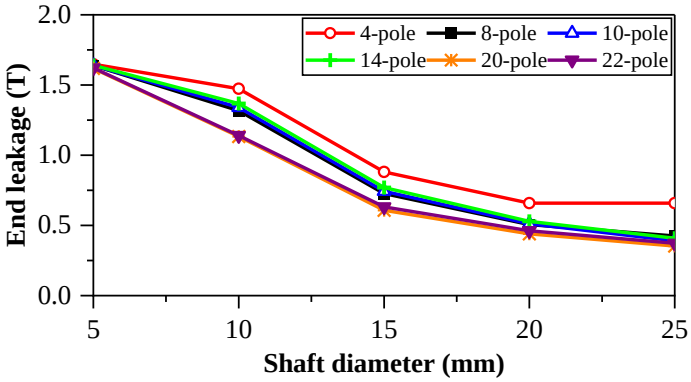

(b) Maximum unipolar end leakage flux.

Fig. 3.12. Influence of shaft diameter on average torque and end leakage.

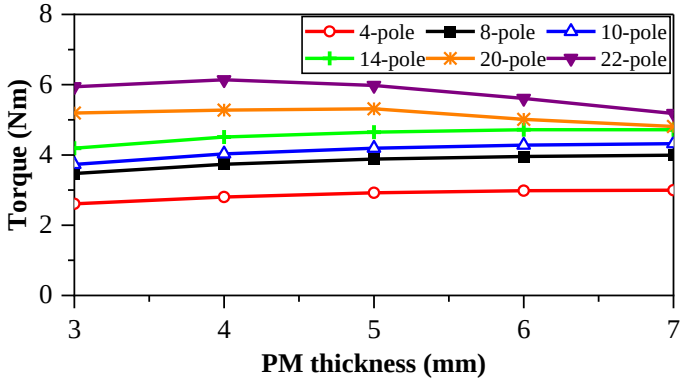

(a) Average torque.

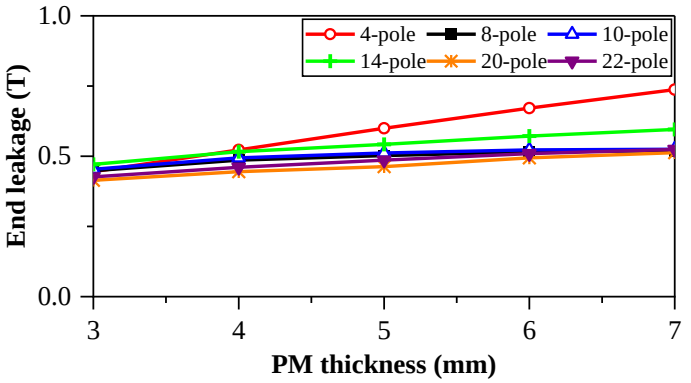

(b) Maximum unipolar end leakage flux.

Fig. 3.13. Influence of PM thickness on average torque and end leakage.

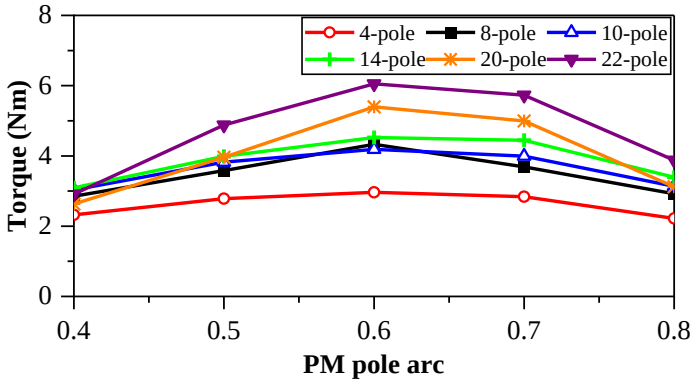

(a) Average torque.

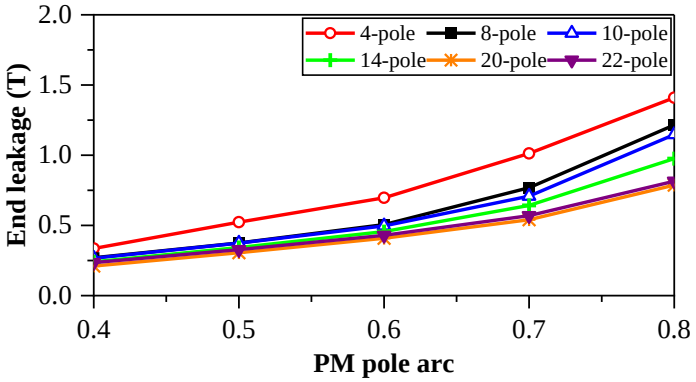

(b) Maximum unipolar end leakage flux.

Fig. 3.14. Influence of PM pole arc on average torque and end leakage.

3.4.4. Air-gap length

Fig. 3.15 shows the influence of the air-gap length on average torque and end leakage. Torque sensitivity to air-gap length is evident, decreasing as the air-gap length increases, whereas end leakage exhibits the opposite trend.

3.4.5. Slot opening

Fig. 3.16 shows the influence of the slot opening on average torque and end leakage. The range of slot openings in Fig. 3.16 varies from closed slots to open slots. Due to variations in stator inner diameter and tooth width among PMSMs with different pole numbers, the ranges of slot openings also differ for each PMSM. The average torques of machines with high rotor pole numbers (14-pole, 20-pole, and 22-pole) are sensitive to slot opening due to the field modulation effect of the stator tooth, whereas the slot opening has a negligible effect on the torques of other machines. End leakage remains almost unchanged with variations in slot opening.

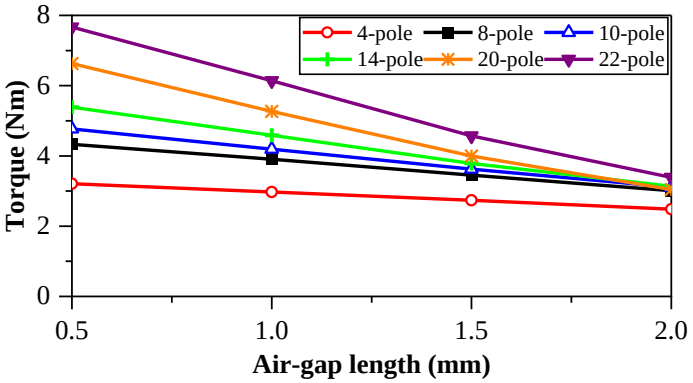

(a) Average torque.

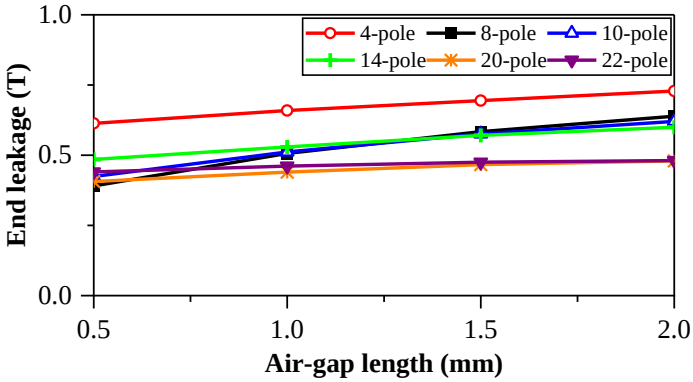

(b) Maximum unipolar end leakage flux.

Fig. 3.15. Influence of air-gap length on average torque and end leakage.

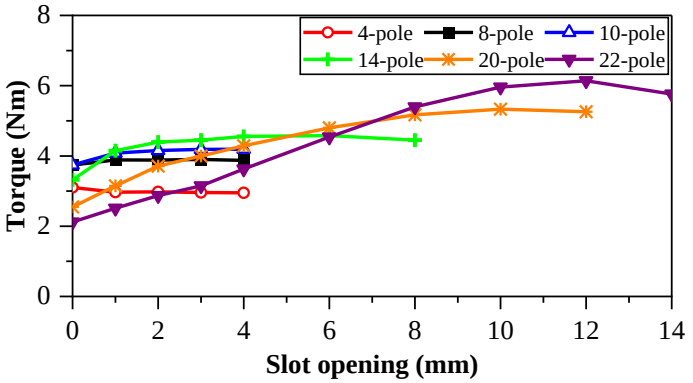

(a) Average torque.

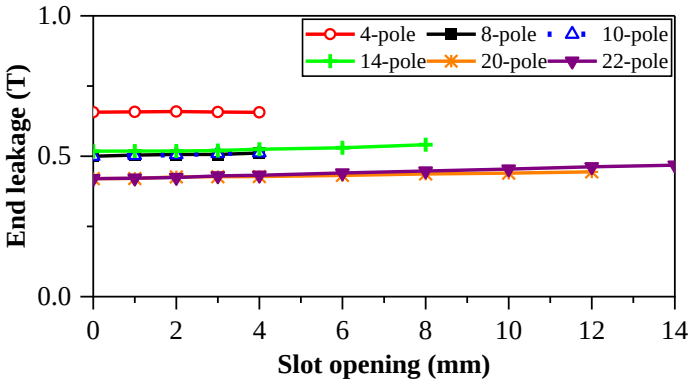

(b) Maximum unipolar end leakage flux.

Fig. 3.16. Influence of slot opening on average torque and end leakage.

In conclusion, the average torque of the analyzed machines shows high sensitivity to PM pole arc, air-gap length, and slot opening, while the end leakage exhibits significant sensitivity to shaft diameter and PM pole arc.

3.5. Proposed Non-magnetic Shaft and Composite Rotor Structures for End Leakage Flux Reduction

For the reliable and safe operation of the CP PMSM system, reducing or eliminating unipolar end leakage flux is essential. According to the magnetic circuit of the CP PMSM shown in Fig. 3.6, the unipolar end leakage flux on the shaft can be reduced by increasing the equivalent reluctance of the rotor yoke and shaft (R_{RY} and R_{SH}) while maintaining the main flux. This section proposes a simple and effective non-magnetic rotor structure, either a non-magnetic shaft or a non-magnetic shaft together with a non-magnetic ring inside the rotor core (which could be integrated into a single shaft).

3.5.1. Non-magnetic shaft

Firstly, the simplest method is using the non-magnetic shaft to reduce the end leakage flux. The SUS303 non-magnetic shaft with a relative permeability of approximately 2 is applied. Fig. 3.17 compares the unipolar end leakage flux distributions of the 12-slot CP PMSMs with magnetic shaft and non-magnetic shaft under on-load condition with 40 W copper loss. It is obvious that the non-magnetic shaft can significantly reduce the unipolar end leakage flux (around 90%) as shown in Fig. 3.18 (a), where the maximum values are reduced from 0.60 T, 0.54 T, 0.52 T, 0.52 T, 0.42 T, and 0.47 T to 0.045 T, 0.038 T, 0.038 T, 0.035 T, 0.037 T, and 0.029 T, respectively. Moreover, Fig. 3.18 (b) compares the average torques between magnetic and non-magnetic shafts under on-load condition with 40 W copper loss. As can be observed, the non-magnetic shaft can effectively reduce the end leakage flux without sacrificing the torque capability.

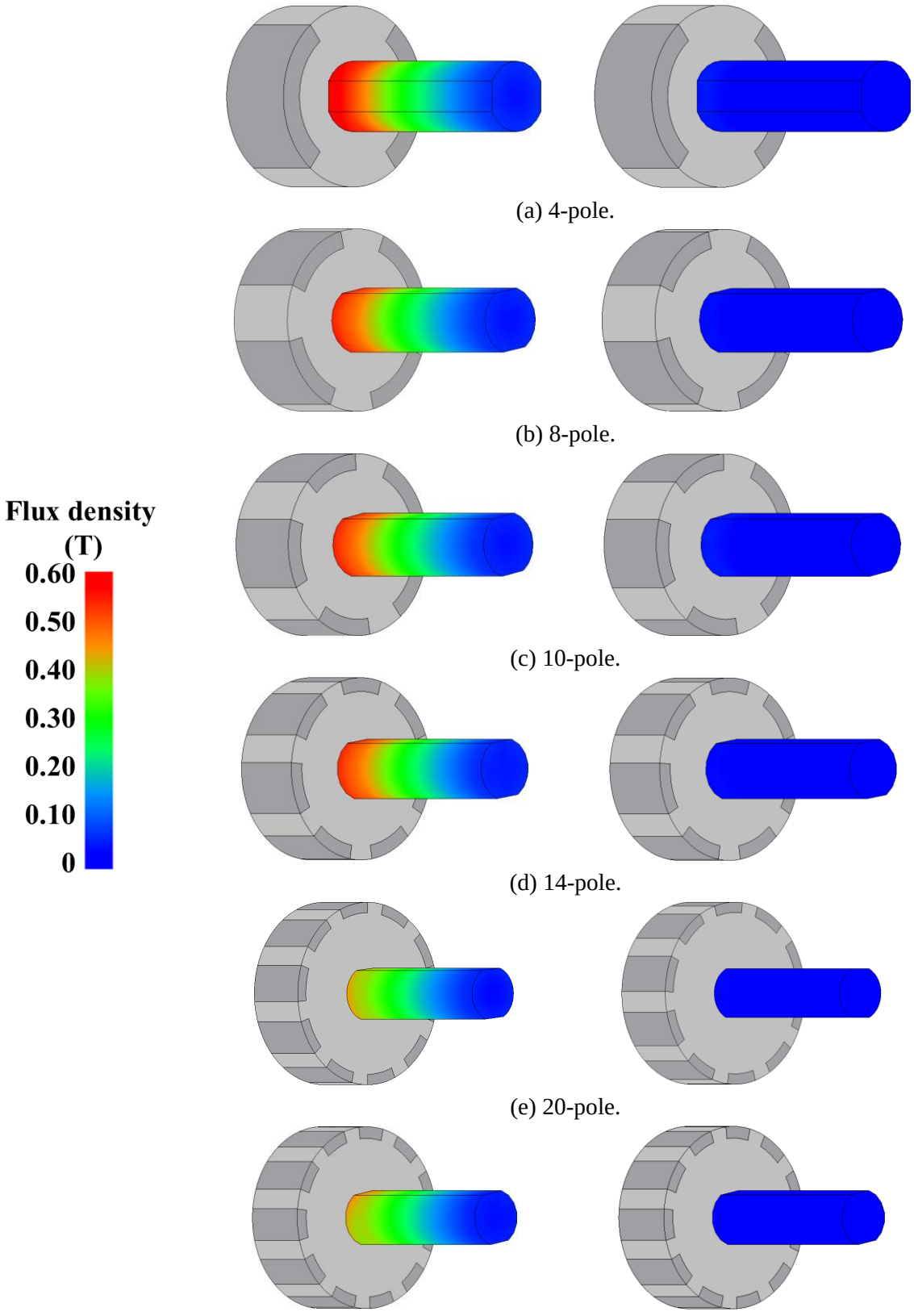

(a) 4-pole.

(b) 8-pole.

(c) 10-pole.

(d) 14-pole.

(e) 20-pole.

(f) 22-pole.

(i) Magnetic shaft. (ii) Non-magnetic shaft.

Fig. 3.17. Unipolar end leakage flux distributions of 12-slot CP PMSMs with magnetic and non-magnetic shafts under on-load conditions with 40 W copper loss. Stators have been removed from the figures for clarity.

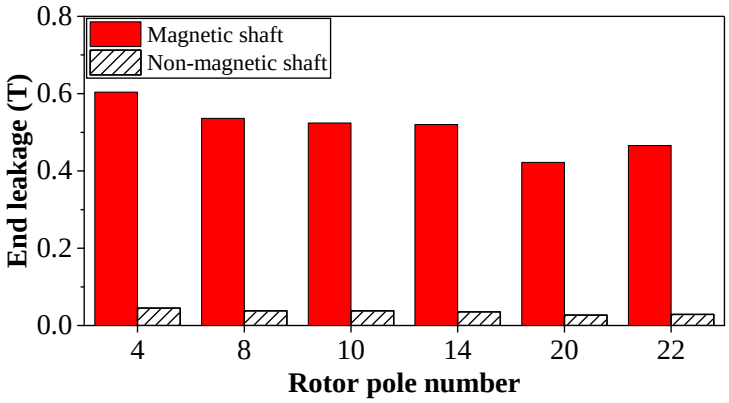

(a) Maximum unipolar end leakage flux.

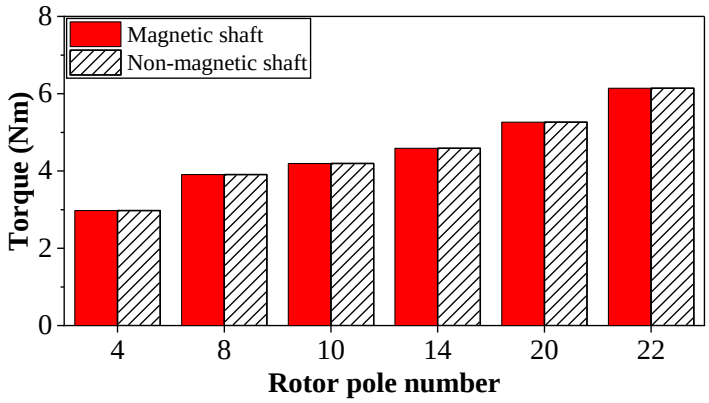

(b) Average torque.

Fig. 3.18. Comparison of maximum unipolar end leakage fluxes and average torques of 12-slot CP PMSMs with magnetic and non-magnetic shafts under on-load condition with 40 W copper loss.

3.5.2. Non-magnetic ring between rotor and shaft

Secondly, instead of using a non-magnetic shaft, a composite rotor structure with a non-magnetic ring between the rotor core and the magnetic shaft as shown in Fig. 3.19 can also be adopted to address the same issue.

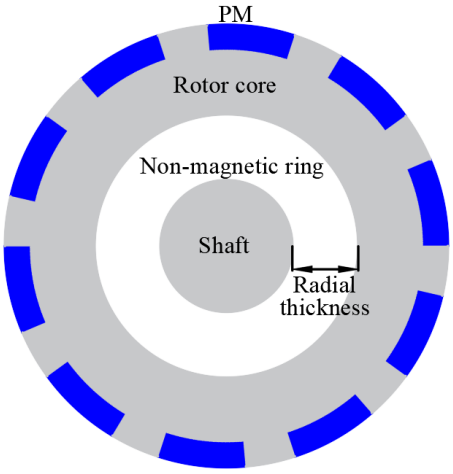

Fig. 3.19. Composite rotor structure with a non-magnetic ring between rotor core and shaft.

Fig. 3.20 shows the unipolar end leakage flux distributions of 12s/20p CP VPMSMs with magnetic shaft and non-magnetic ring with different radial thicknesses under on-load conditions with 40 W copper loss. The composite rotor structure helps to reduce the unipolar end leakage flux effectively. As can be seen from Fig. 3.21 (a), when the radial thickness of the non-magnetic ring increases from 0 mm to 15mm (to ensure the rotor back iron is not saturated and the torque capability is not sacrificed), the end leakage flux decreases continually from 0.42 T (conventional rotor with non-magnetic ring) to 0.28 T, 0.23 T, and 0.20 T, respectively. The composite rotor structure helps to reduce around 34-51% of end leakage while maintaining the same torque capability as the original case as shown in Fig. 3.21 (b).

Fig. 3.22 compares the average torques of 12-slot CP PMSMs with non-magnetic rings with different radial thicknesses under on-load conditions with 40 W copper loss. The proper radial thickness of a non-magnetic ring should be selected to avoid the saturation of the rotor back iron and maintain the torque output capability.

The selected radial thicknesses of the non-magnetic ring are 3 mm for 4-pole CP PMSM and 8 mm for the other CP PMSMs to ensure the rotor back iron is not saturated, and the torque capability is not sacrificed. Fig. 3.23 shows the unipolar end leakage flux distributions of the 12-slot CP PMSMs with magnetic shaft and composite rotor under on-load condition with 40 W copper loss. The composite rotor structure helps to reduce by approximately 40% unipolar end leakage for CP PMSMs compared with its conventional rotor counterpart in Fig. 3.17 (i), except for the 4-pole PMSM which has a thin non-magnetic ring (about 20% reduction). Fig. 3.24 shows that the maximum end leakage fluxes are reduced from 0.60 T, 0.54 T, 0.52 T, 0.52 T, 0.42 T, and 0.47 T to 0.514 T, 0.324 T, 0.32 T, 0.3118 T, 0.25 T, and 0.257 T, respectively. However, it is worth mentioning that its effectiveness is inferior to that of the non-magnetic shaft.

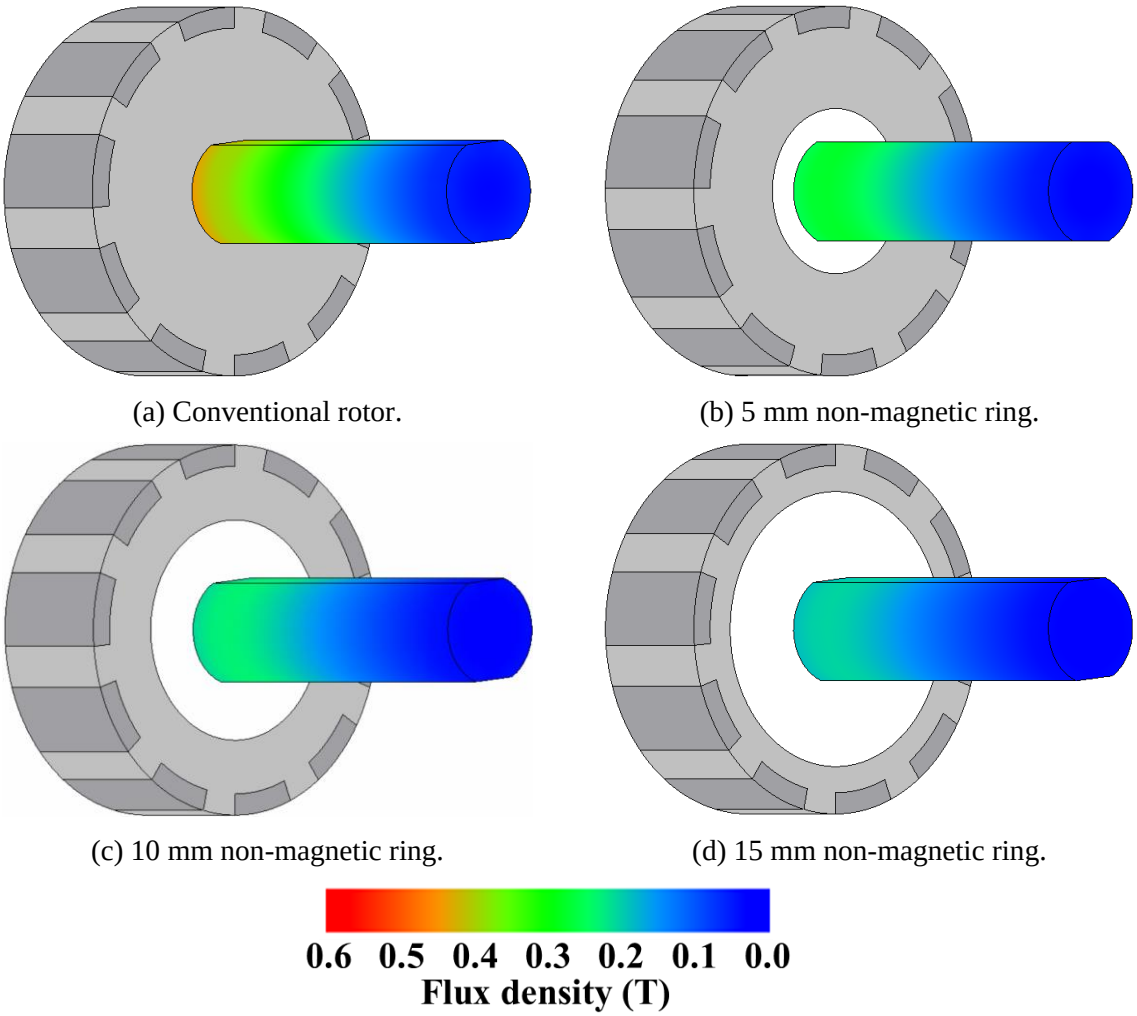

(a) Conventional rotor.

(b) 5 mm non-magnetic ring.

(c) 10 mm non-magnetic ring.

(d) 15 mm non-magnetic ring.

Fig. 3.20. Unipolar end leakage flux distributions of 12s/20p CP VPMSMs with magnetic shaft and non-magnetic ring with different radial thicknesses under on-load conditions with 40 W copper loss. Stators have been removed from the figures for clarity.

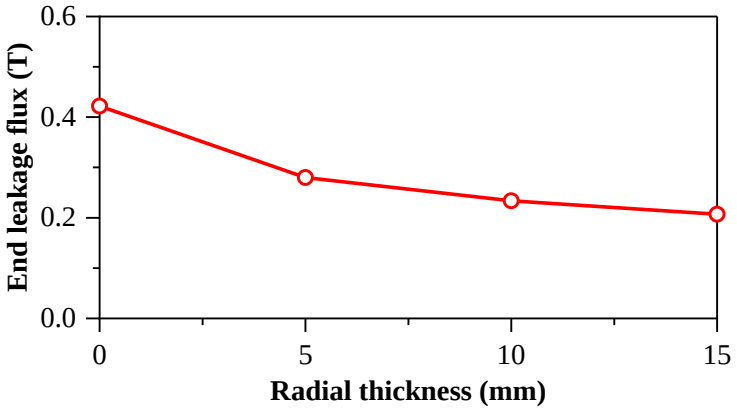

(a) Maximum end leakage flux.

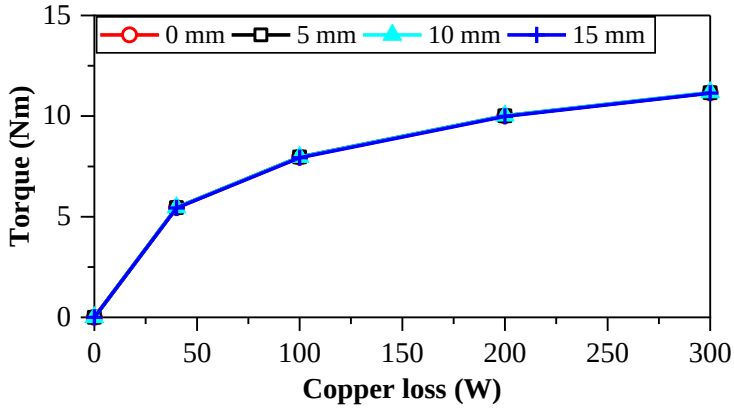

(b) Overload capability.

Fig. 3.21. Comparison of maximum end leakage flux of 12s/20p CP VPMSMs under on-load conditions with 40 W copper loss with magnetic shaft and non-magnetic ring with different radial thicknesses and corresponding overload capability.

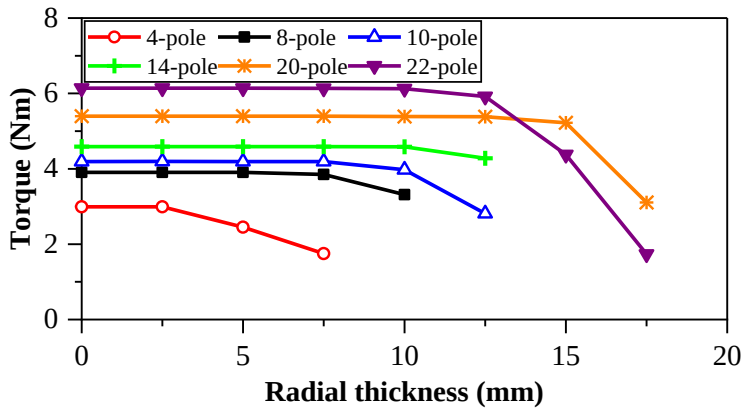

Fig. 3.22. Average torques of 12-slot CP PMSMs with non-magnetic rings of different radial thicknesses under on-load conditions with 40 W copper loss.

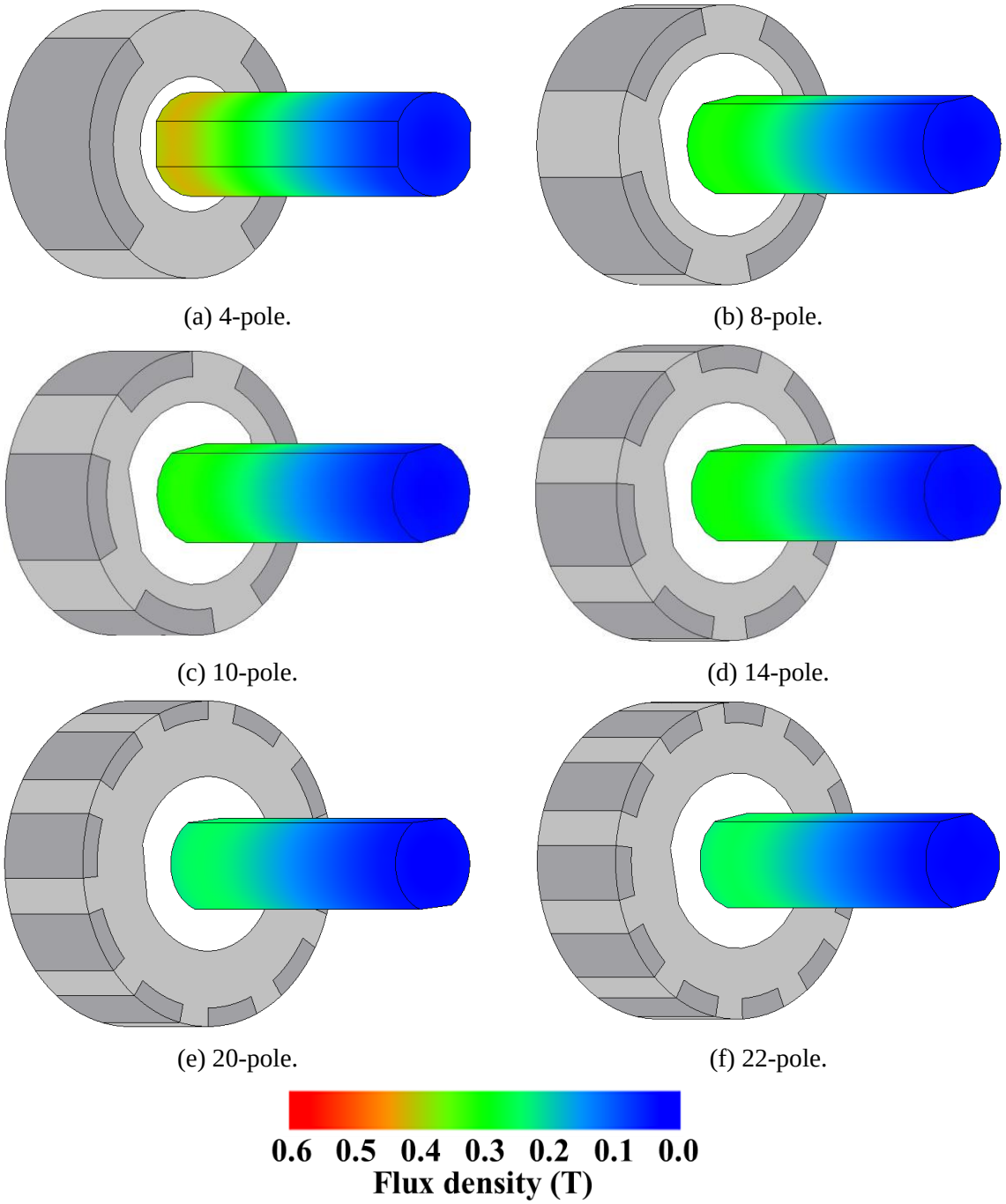

Fig. 3.23. Unipolar end leakage flux distributions of 12-slot CP PMSMs with composite rotors and magnetic shafts under on-load condition with 40 W copper loss. Stators have been removed from the figures for clarity.

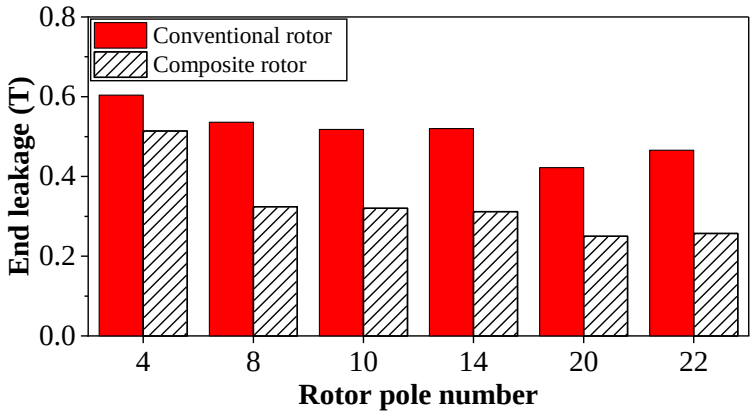

Fig. 3.24. Comparison of maximum unipolar end leakage fluxes of 12-slot CP PMSMs with conventional/composite rotors and magnetic shaft under on-load condition with 40 W copper loss.

3.5.3. Combination of non-magnetic ring and shaft

Thirdly, when both the non-magnetic shaft and the non-magnetic ring are combined as a composite rotor, it can be expected that the unipolar end leakage flux will be further reduced. Fig. 3.25 shows the unipolar end leakage flux distributions of the 12-slot CP PMSMs with composite rotor and non-magnetic shaft under on-load condition with 40 W copper loss. Approximately 95% of unipolar end leakage flux can be reduced for all CP PMSMs with their conventional rotor and magnetic shaft counterparts in Fig. 3.17 (i). Fig. 3.26 shows the maximum end leakage fluxes of CP PMSMs with different rotor structures (conventional/composite rotor and magnetic/non-magnetic shaft). Obviously, compared with the former two structures in sections 3.5.2 and 3.5.3, the proposed composite rotor and non-magnetic shaft structure can achieve the best reduction performance. The maximum end leakage fluxes under on-load condition with 40 W copper loss for all CP PMSMs are 0.042 T, 0.030 T, 0.030 T, 0.028 T, 0.021 T, and 0.023 T, respectively.

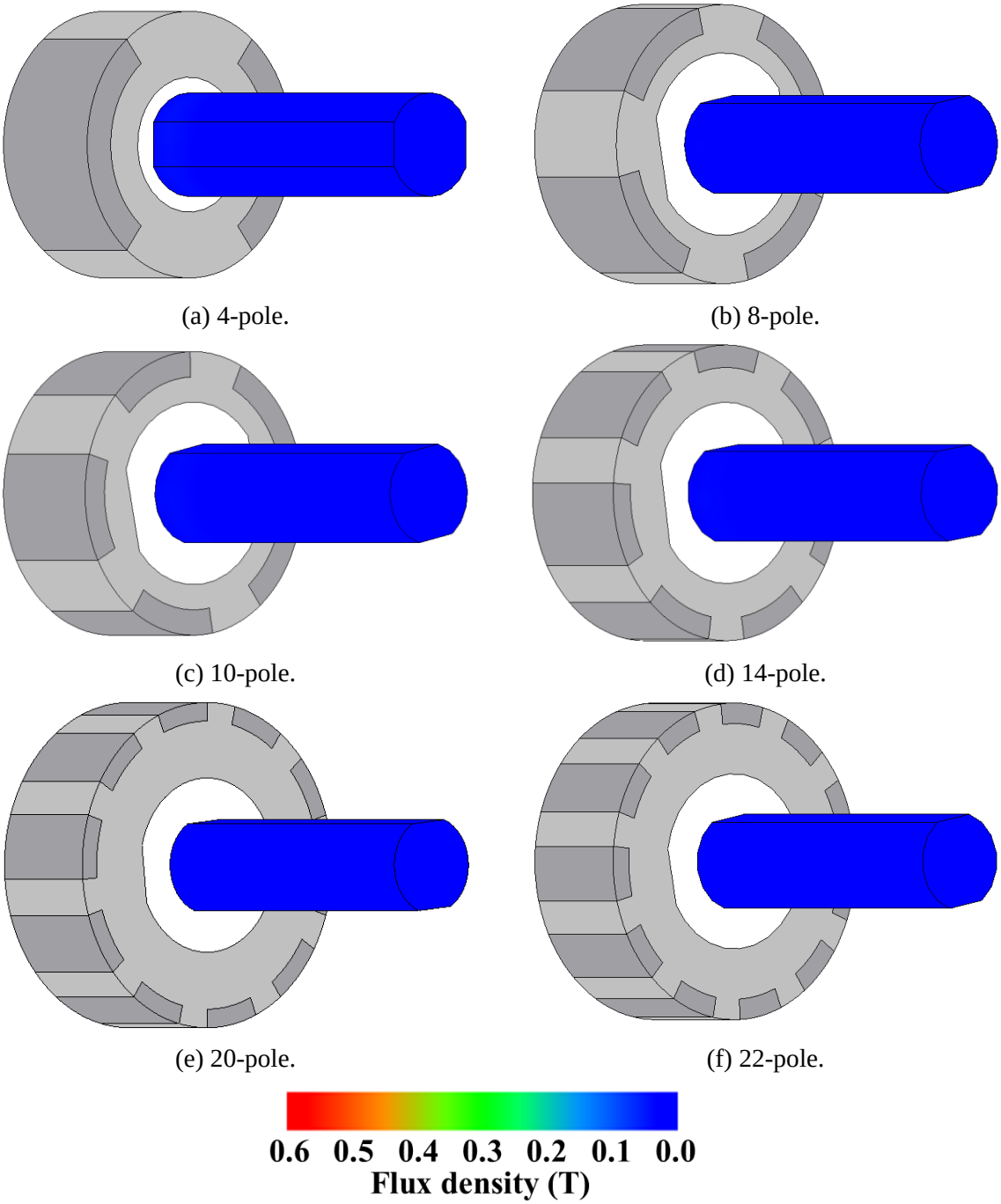

Fig. 3.25. Unipolar end leakage flux distributions of 12-slot CP PMSMs with composite rotor and non-magnetic shaft under on-load condition with 40 W copper loss. Stators have been removed from the figures for clarity.

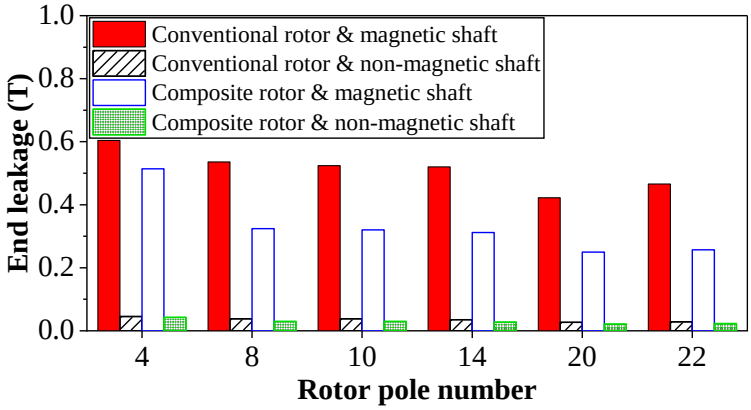

(a) Maximum end leakage flux.

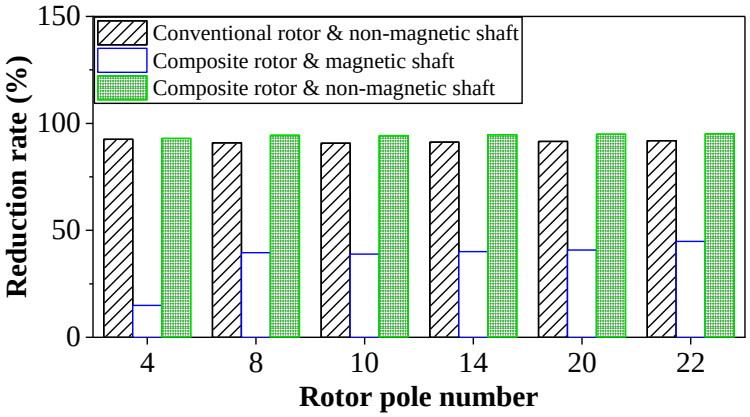

(b) End leakage flux reduction rate.

Fig. 3.26. Comparison of maximum end leakage flux and reduction rates (compared to the conventional rotor with magnetic shaft) of 12-slot CP PMSMs with conventional/composite rotors and magnetic/non-magnetic shafts.

3.5.4. Non-magnetic ring with shafts of different materials

Fig. 3.27 shows the effect of non-magnetic rings on shafts made from different materials for a 12-slot/20-pole CP PMSM. Applying non-magnetic rings reduces end leakage by approximately 40-50%.

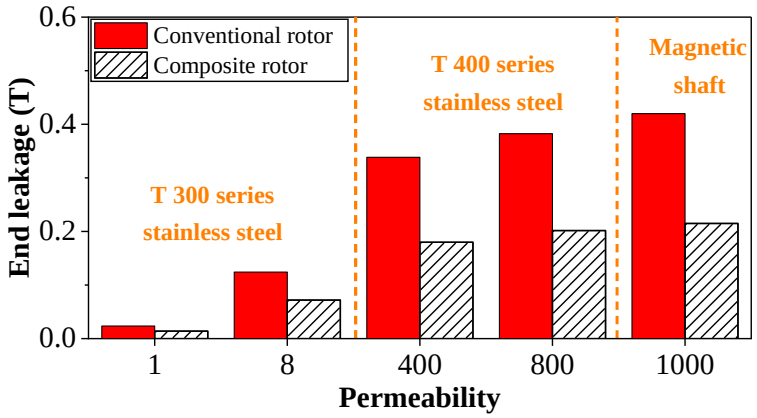

Fig. 3.27. Effect of non-magnetic rings on shafts made from different materials for 12-slot/20-pole CP PMSM.

In conclusion, the non-magnetic shaft can significantly reduce the unipolar end leakage flux for CP PMSMs (by around 90% reduction compared with the magnetic shaft). Moreover, the application of a composite rotor with a non-magnetic ring between the rotor core and shaft can further reduce approximately 40% of end leakage flux. Approximately 95% of unipolar end leakage flux can be eliminated when combining the non-magnetic ring and non-magnetic shaft, which could be integrated into a single shaft. Considering the manufacturing complexity, a non-magnetic shaft alone is highly recommended.

3.6. Experimental Verification

The 12-slot/10-pole and 12-slot/20-pole CP PMSMs with magnetic shaft (magnetic stainless steel SUS430), non-magnetic shaft (non-magnetic stainless steel SUS304), conventional rotor, and composite rotor are manufactured and tested to verify the effectiveness of the proposed composite rotor structure for reducing unipolar end leakage flux.

Fig. 3.28 shows the stators, the conventional rotor with a magnetic shaft (left), and the composite rotor with a non-magnetic shaft (right) of the prototypes. In the composite rotor, the rotor lamination, non-magnetic ring, and shaft are nested together and aligned concentrically, as shown in Fig. 3.28 (c). Table 2.6 shows the key parameters of the prototypes.

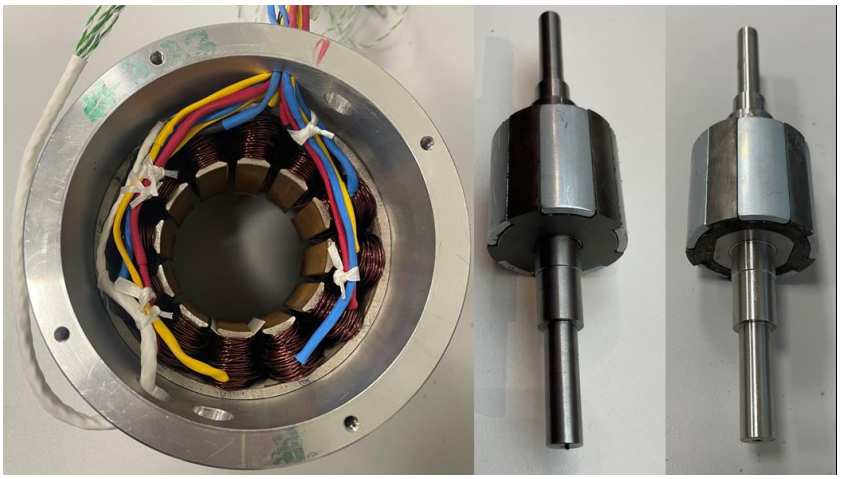

(a) 12s/10p stator, conventional rotor with magnetic shaft (left), and composite rotor with non-magnetic shaft (right).

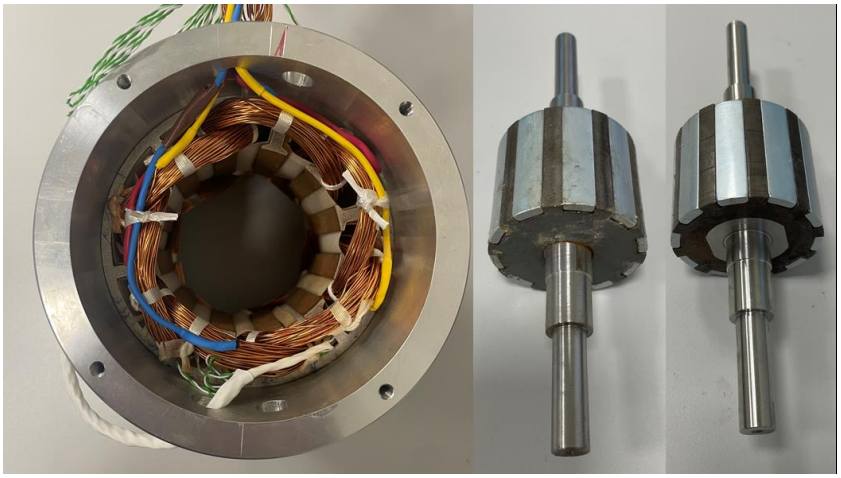

(b) 12s/20p stator, conventional rotor with magnetic shaft (left), and composite rotor with non-magnetic shaft (right).

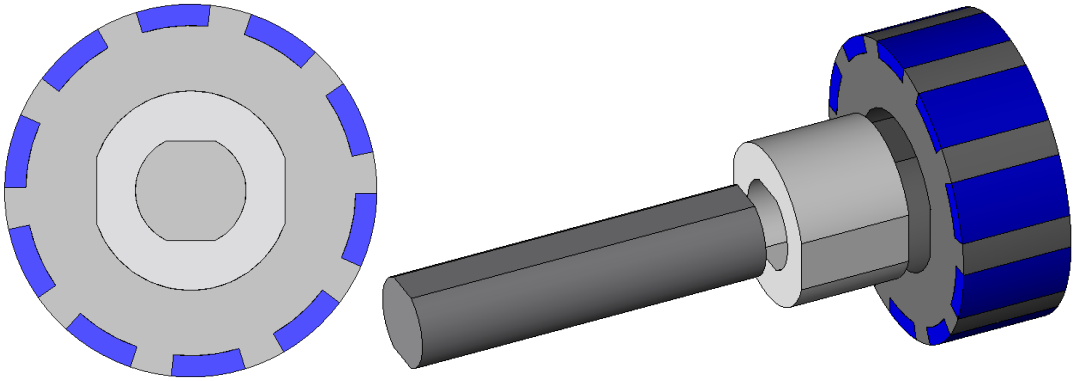

(c) Illustration of manufacturing process of composite rotor.

Fig. 3.28. Prototypes of 12s/10p and 12s/20p CP PMSMs.

3.6.1. Electromagnetic test

The test rigs for back EMF, cogging torque, and static torque are shown in Fig. 3.29.

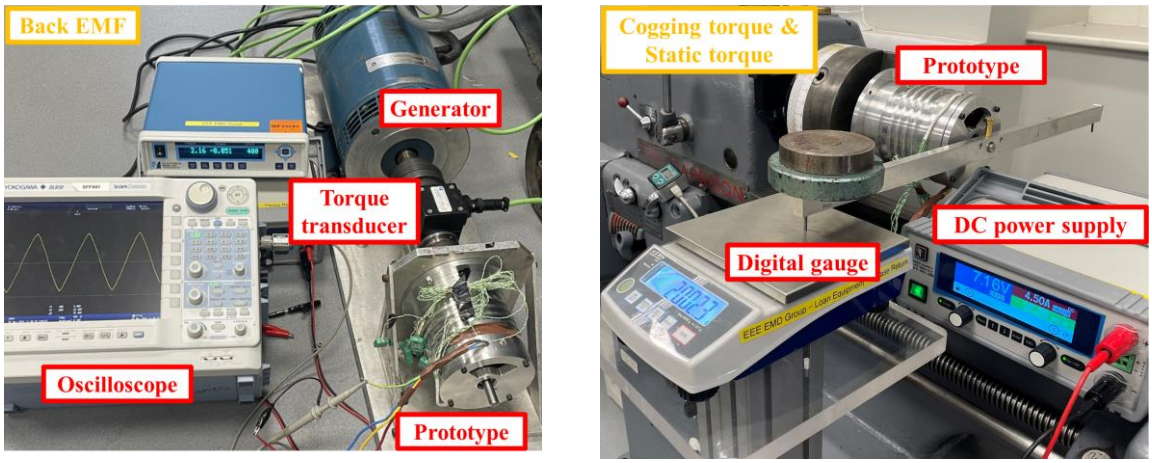

(a) Back EMF. (b) Cogging torque and static torque.

Fig. 3.29. Test rigs for back EMF, cogging torque, and static torque.

Fig. 3.30 shows the measured and FEA predicted open circuit back EMFs at 400 r/min. Fig. 3.31 shows the measured and FEA predicted cogging torques [ZHU09]. The results show good agreement between the measured and FEA predicted results. The composite rotor with non-magnetic shaft structure has almost the same open circuit electromagnetic performance compared with the conventional rotor with magnetic shaft from the measured and FEA predicted results.

The static torque is measured by injecting current through the DC power supply (I_b=I_c= - 0.5I_a) and rotating the stator while keeping the rotor stationary, then the relationship between static torque and rotor position can be measured. The measured and FEA predicted static torques match well as shown in Fig. 3.32. The static torque of the conventional rotor with magnetic shaft is almost the same as that of the composite rotor with magnetic shaft, which means that the proposed composite rotor structure can maintain torque output capability.

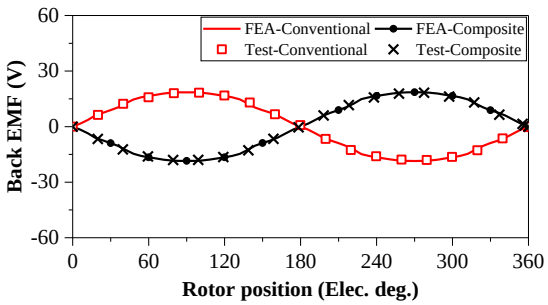

(a) 12s/10p waveforms.

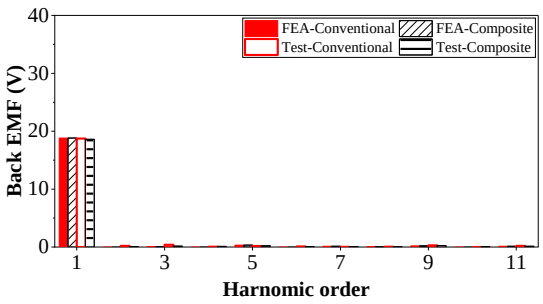

(b) 12s/10p spectra.

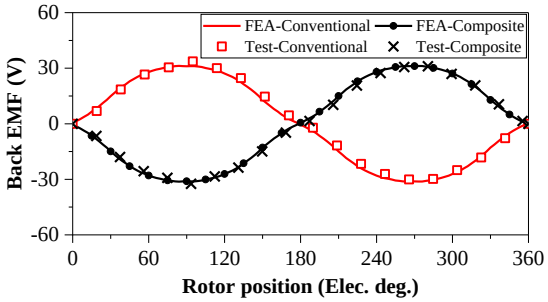

(c) 12s/20p waveforms.

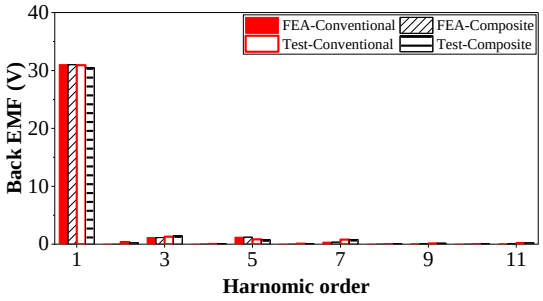

(d) 12s/20p spectra.

Fig. 3.30. Measured and FEA predicted open circuit back EMFs at 400 r/min.

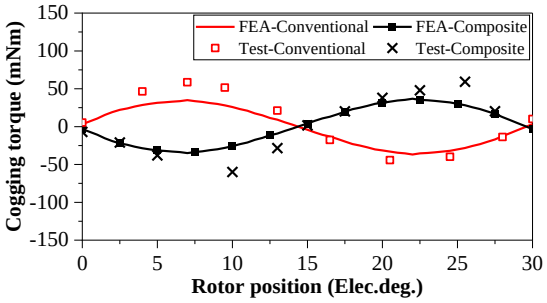

(a) 12s/10p waveforms.

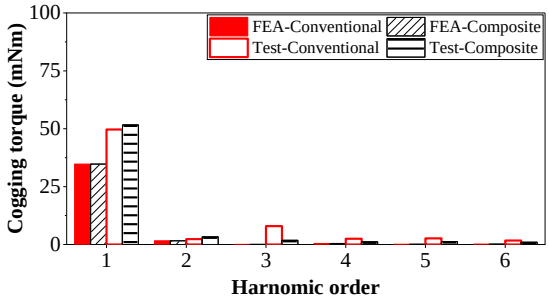

(b) 12s/10p spectra.

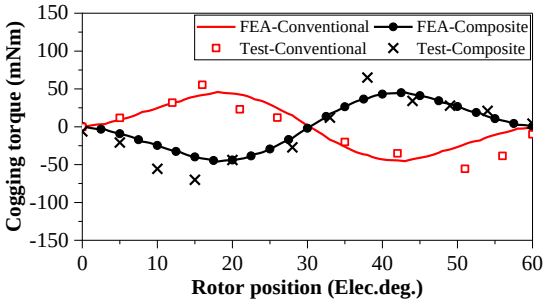

(c) 12s/20p waveforms.

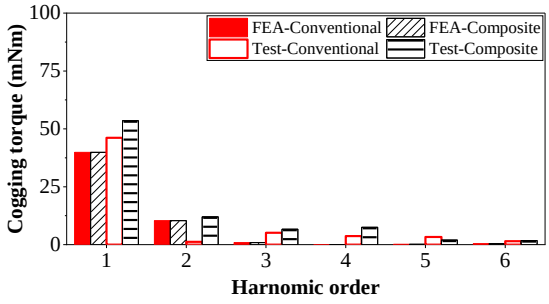

(d) 12s/20p spectra.

Fig. 3.31. Measured and FEA predicted cogging torque.

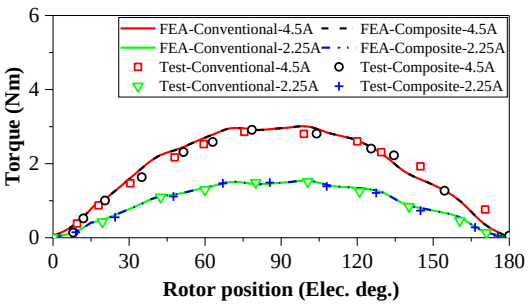

(a) 12s/10p.

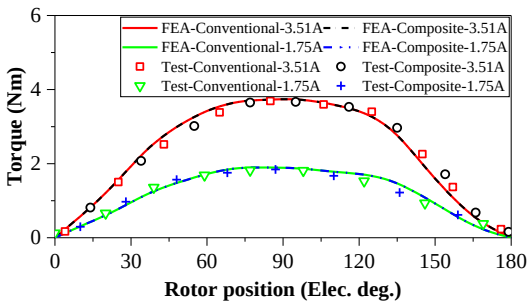

(b) 12s/20p.

Fig. 3.32. Measured and FEA predicted static torque.

Transient torque waveforms and torque–current characteristics can be measured by adopting the dynamic test platform and using the torque transducer and torque reader as shown Fig. 2.47. The measured and FEA predicted dynamic torques of prototypes with 2 Arms phase current are shown in Fig. 3.34 while the torque–current characteristics are compared in Fig. 3.34. The measured results agree well with the simulation results.

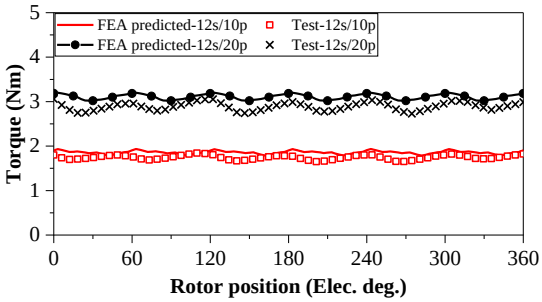

(a) Waveforms.

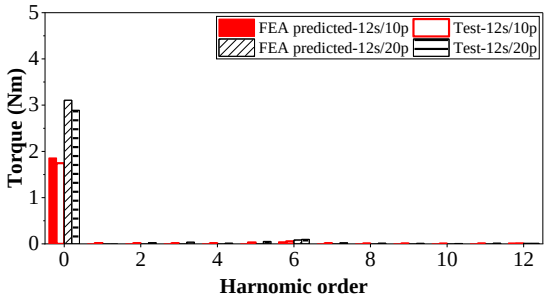

(b) Spectra.

Fig. 3.33. Measured and FEA predicted dynamic torques.

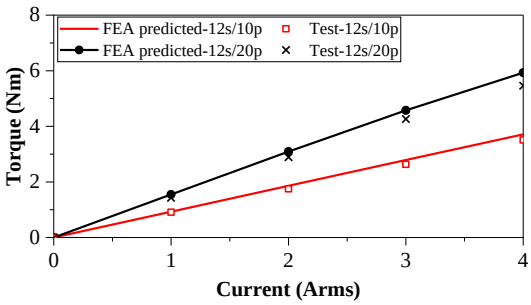

Fig. 3.34. Measured and FEA predicted torque-current characteristics.

3.6.2. Test for end leakage

Fig. 3.35 shows the 12s/10p PMSM with conventional rotor and magnetic shaft after assembling. The shaft will attract crews and nuts in the end region which might threaten the safety operation of the machine system.

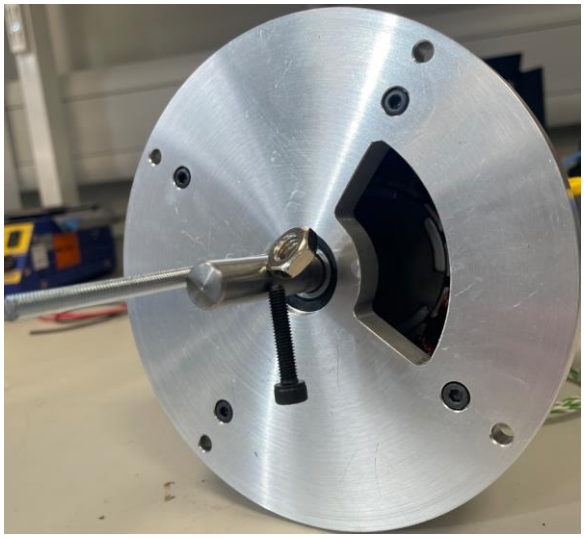

Fig. 3.35. Crews and nuts attracted in the end region of the 12s/10p machine with conventional rotor and magnetic shaft after assembling due to the unipolar end leakage.

3.6.2.1. Bare rotors before assembling

The unipolar end flux leakage of the whole shaft region can be measured with the bare rotor before assembling as shown in Fig. 3.36. For the FEA predicted results, the unipolar end flux leakage curve is obtained by calculating the flux density along a line in the air region close to the shaft (approximately 0.1 mm away from the shaft) as illustrated in Fig. 3.37.

The comparisons of the unipolar end leakage fluxes of two machines before assembling with conventional rotor and magnetic shaft as well as with composite rotor and non-magnetic shaft obtained by FEA and measurements are shown in Fig. 3.38. It can be seen that the end leakage flux is unipolar, and the FEA predicted results match well with the measurements. In addition, employing the non-magnetic ring and non-magnetic shaft effectively reduces the unipolar end leakage flux for both prototypes.

(a) 12s/10p with conventional rotor and magnetic shaft.

(b) 12s/10p with composite rotor and non-magnetic shaft.

(c) 12s/20p with conventional rotor and magnetic shaft.

(d) 12s/20p with composite rotor and non-magnetic shaft.

Fig. 3.36. Illustration of measuring unipolar end leakage flux of bare rotors before assembling.

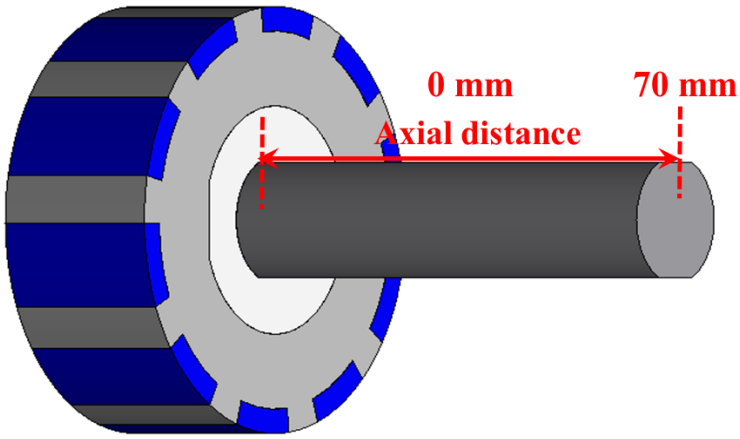

Fig. 3.37. Illustration of measuring line in FEA.

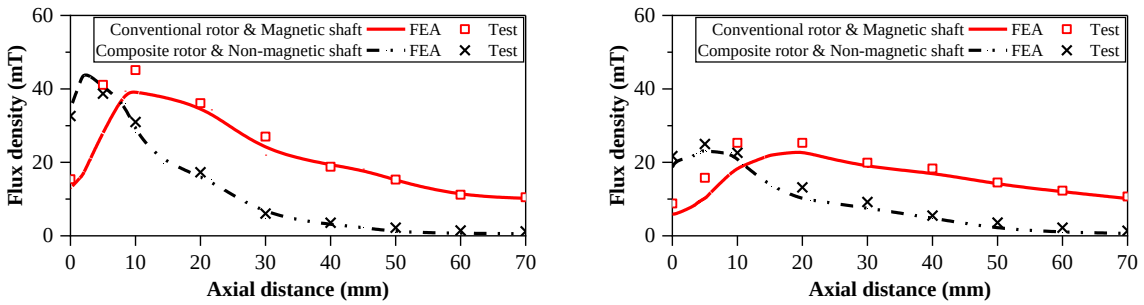

(a) 12s/10p. (b) 12s/20p.

Fig. 3.38. Comparison of FEA predicted and measured unipolar end leakage fluxes on the whole shaft region with bare rotor before assembling.

3.6.2.2. **Prototypes after assembling**

The unipolar end flux leakage of the shaft region outside the end cap after assembling can be measured as shown in Fig. 3.39.

The comparisons of the unipolar end leakage fluxes of two machines after assembling, one with the conventional rotor and magnetic shaft and the other with the composite rotor and non-magnetic shaft, obtained by FEA and measurements are shown in Fig. 3.40. It can be seen that the end leakage flux is unipolar, and the FEA predicted results match well with the measurements.

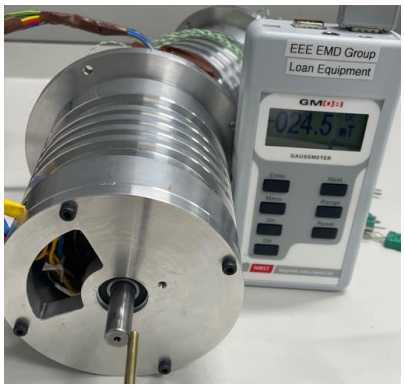

(a) 12s/10p with conventional rotor and magnetic shaft.

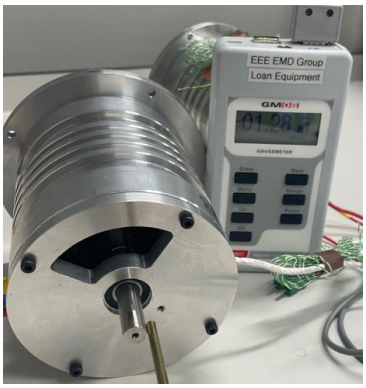

(b) 12s/10p with composite rotor and non-magnetic shaft.

(c) 12s/20p with conventional rotor and magnetic shaft.

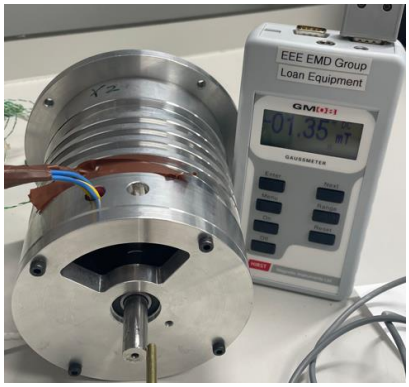

(d) 12s/20p with composite rotor and non-magnetic shaft.

Fig. 3.39. Illustration of measuring unipolar end leakage flux of prototypes after assembling.

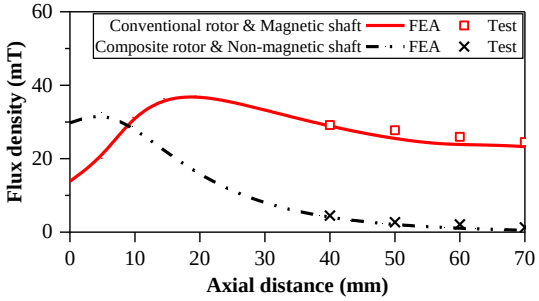

(a) 12s/10p.

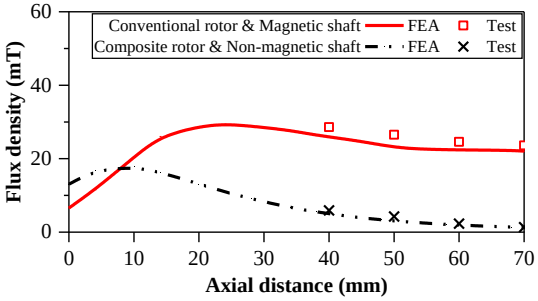

(b) 12s/20p.

Fig. 3.40. Comparison of FEA predicted and measured unipolar end leakage fluxes on the shaft region outside the end cap after assembling.

3.7. Summary

In this chapter, unipolar end leakage fluxes of CP PMSMs with different slot/pole number combinations and winding configurations have been investigated. The conclusions can be summarized as follows:

1. The unipolar end leakage flux is mainly generated by the CP rotor structure and is affected by the slot/pole number combination, while the armature reaction has a negligible effect.
2. The unipolar end leakage flux decreases with the increase of rotor pole number for the analyzed FSCW CP PMSMs but increases when the rotor pole number further increases for overlapping winding VMs.
3. The end leakage exhibits significant sensitivity to shaft diameter and PM pole arc.
4. To reduce unipolar end leakage, a simple and effective non-magnetic rotor structure, either a non-magnetic shaft or a non-magnetic shaft together with a non-magnetic ring inside the rotor core (which could be integrated into a single shaft), has been proposed and can effectively reduce unipolar end leakage flux without sacrificing torque capability.
5. Applying the non-magnetic shaft alone reduces approximately 90 % of end leakage flux compared with the magnetic shaft. Additionally, the non-magnetic ring alone can reduce approximately 40% of end leakage flux. Furthermore, 95% of unipolar end leakage flux can be eliminated when combining the non-magnetic ring and non-magnetic shaft, which could be integrated into a single shaft, compared with the conventional rotor with a magnetic shaft for all the analyzed CP PM machines. Considering the manufacturing complexity, a non-magnetic shaft alone is highly recommended.

CHAPTER 4
OPTIMAL MULTI-TOOTH NUMBERS FOR VERNIER PM SYNCHRONOUS MACHINES

PMSMs with different winding configurations (overlapping winding and FSCW) and rotor topologies (NSP and CP) are investigated in Chapters 2 and 3. The results show that FSCW improves the torque density while the CP rotor structure enhances torque output capability and PM utilization, especially for VMs. This chapter focuses on the effect of stator structures on VMs, specifically the impact of multi-tooth numbers on the electromagnetic performance of NSP and CP VPMSMs. The optimal multi-tooth numbers for average torque, overload torque capability, PM utilization, loss, efficiency, power factor, and unipolar end leakage flux are systematically investigated. It confirms that CP rotor and multi-tooth stator structures exhibit better field modulation effects compared with conventional NSP and non-multi-tooth stator structures. It reveals that there exists an optimal multi-tooth number for torque output capability and PM utilization, as well as unipolar end leakage flux. In particular, it shows that the multi-tooth stator structure significantly saves PM volume for CP VPMSMs and suppresses unipolar end leakage flux. The PM utilization rate of CP VPMSM with 5 multi-teeth is more than 50% higher than that with the single-tooth structure, while the unipolar end leakage flux is reduced by around 60%. However, the overload capability and power factor will be sacrificed. Finally, prototypes with 2 and 3 multi-teeth numbers are manufactured and tested to verify the FEA analyses.

This chapter has been accepted by IEEE ACCESS:

[ZHE24b] Y. Zheng, Z. Q. Zhu, H. Xu, J. Yan, and D. Liang, “Optimal multi-tooth numbers for vernier PM synchronous machines,” *IEEE Access*, vol. 12, pp. 89599-89612, 2024.

4.1. Introduction

VPMSMs become more popular in low-speed and high-torque applications due to their high torque density, high PM utilization, and relatively simple structure [ISH95] [TOB00] [CHU12] [CHU15]. The overlapping winding open-slot stator and non-overlapping CW multi-tooth stator are two common structures for VMs in terms of stator and armature winding configurations [TOB99]. According to rotor topologies, there are NSP and CP rotor structures [TOB99]. The multi-tooth stator and non-overlapping FSCW VMs have the advantages of short axial end winding, high torque/power density, high efficiency, and enhanced flux weakening capability compared with their single-tooth and overlapping winding counterparts [REF10] [LI10] [HO11] [XU15] [XU22]. Furthermore, PM utilization and torque output capability can be further enhanced when combined with the CP rotor structure [CHU15] [ZHA19].

The torque characteristics of NSP VMs with different stator slots and multi-tooth numbers are investigated and the optimal multi-tooth number is determined [OKA13] [ZOU17a] [LI19c] [XIE19] [YU19]. The field modulation effect of different stator slot structures on NSP and/or CP PM machines is investigated, and the results show that slot openings have a significant influence on the field modulation effect [ZHU18a] [LI18b] [LI23a]. Innovative designs such as the coding shaped tooth [FAN22], uniformly distributed split-teeth [DU22], and unequal element coil and stator teeth unit [FAN23] are proposed in NSP VMs to improve machine performance, leading to increased average torque, reduced torque ripple, improved power factor, and better fault-tolerant performance compared with regular multi-tooth VMs.

The field modulation effects between NSP and CP structures are compared, showing that the CP structure can generate higher modulated torque [GAO16] [LI21]. Field modulation effects and torque components of CP VMs with 2 multi-teeth are investigated in [XU17] [JAN19] [ZHO19a] [ZHA20] [LI22], which demonstrate that the torque output capacity can be enhanced compared with conventional NSP and single-tooth stator VMs.

Although the CP structure has the advantages of high PM utilization and improved average torque, the unbalanced equivalent north and south poles in the CP structure lead to unipolar end leakage flux, which threatens the safety of the machine system. The unipolar end leakage flux in CP PMSMs [GE16] [ZHU17] [WAN19] [LI19d] [QI22a] and CP VMs [CHU11] [XU23] [ZHE23] is investigated. The stator with 4-multi-teeth is proposed to suppress the magnetic unbalance caused by the CP structure and using non-magnetic material for the rotor end-cap is

suggested [CHU11]. Two conventional CP structures with opposite polarities are combined to reduce the unipolar end leakage in CP VMs [XU23]. A simple composite rotor structure is proposed in [ZHE23] to eliminate the unipolar end leakage in CP VMs. However, the effect of different multi-tooth numbers on the electromagnetic performance, as well as unipolar end leakage flux, of CP VPMSMs has not been systematically investigated so far and will be the subject of this chapter.

The main contributions of this chapter can be summarized as follows:

1. The optimal multi-tooth number, in terms of torque characteristics, PM utilization, efficiency, etc., is determined. It reveals that the CP rotor combined with the multi-tooth stator structure has a better field modulation effect and helps increase torque output capability and improve PM utilization. However, the efficiency at higher speeds, power factor, and overload capability are sacrificed while using the CP rotor and multi-tooth stator.
2. The electromagnetic performances of NSP and CP VPMSMs with different multi-tooth numbers are compared. The CP rotor has better average torque output capability and PM utilization, but higher cogging torque, poorer overload capability, and lower power factor compared with the NSP rotor.
3. The influence of critical design parameters of multi-tooth CP VPMSMs is investigated. It is found that the field modulation effect and torque output capability are very sensitive to the dimensions of multi-tooth and PMs.
4. The effect of different multi-tooth numbers on the unipolar end leakage flux is investigated for the first time, which reveals that the multi-tooth structure helps suppress the unipolar end leakage flux, with approximately 60% reduction for the CP VPMSM with 5 multi-teeth compared with that with single-tooth.

This chapter is organized as follows. Firstly, machine topologies of 6-slot VPMSMs with different multi-tooth numbers and rotor topologies (CP and NSP) are presented in section 4.2. Then, all machines are optimized for maximum average torque with the same active lamination stack length and fixed copper loss considering end-winding in section 4.3. Afterward, the effect of multi-tooth numbers on the electromagnetic performance of NSP and CP VPMSMs, including torque characteristics, PM utilization, loss, efficiency, and power factor, is investigated in section 4.4. Moreover, section 4.5 analyzes the influence of critical design parameters on field modulation effect and torque output capability while the unipolar end leakage flux of VPMSMs with different multi-tooth numbers is investigated in section 4.6.

Prototypes with different stator structures (2 and 3 multi-teeth numbers) and rotor topologies (NSP and CP) are manufactured and tested to verify the FEA analysis in section 4.7, and this chapter is concluded in section 4.8.

4.2. Machine Topologies

VMs with multi-tooth stators and FSCWs have short end windings, enabling compact structure and higher torque density. The cross-sections of 6-slot FSCW VPMSMs with different multi-tooth numbers and rotor topologies (NSP and CP), namely 6-slot/1-tooth/8-pole (6s/1t/8p), 6-slot/2 multi-teeth/20-pole (6s/2mt/20p), 6-slot/3 multi-teeth/32-pole (6s/3mt/32p), 6-slot/4 multi-teeth/44-pole (6s/4mt/44p), and 6-slot/5 multi-teeth/56-pole (6s/5mt/56p) FSCW VPMSMs, are illustrated in Fig. 4.1. It should be noted that the conventional stator without multi-tooth structure, as shown in Fig. 4.1 (a), is named 1-tooth (1t) in this chapter for convenience.

For VMs, the relationship between stator slot number (N_s), armature winding pole pair number (P_a), and rotor pole pair number (P_r) should satisfy

$$N_s = P_r \pm P_a \tag{4.1}$$

For VMs with n_{st}-multi-teeth in stator big tooth (N_s), the relationship should be

$$n_{st}N_s = P_r \pm P_a \tag{4.2}$$

The analytical method is used to reveal field modulation and magnetic gearing effects. Magnetic saturation, magnetic leakage, end-effect, and fringing effect are neglected to simplify the analysis.

The MMF of rotating PMs can be expressed as

$$F_{PM}(\theta, t) = \sum_{i=1}^{\infty} A_{PMi} \cos(ip_r(\theta - \omega t)) \tag{4.3}$$

where p_r is the pole-pair number of rotor PMs, ω is the electrical velocity, θ is the mechanical angle, and A_{PMi} is the magnitude of i^{th} order harmonic.

For the NSP rotor,

$$A_{PMi} = \frac{4B_r h_{PM}}{i\mu_0\mu_r\pi}\sin\left(\frac{i\pi}{2}\right)\sin\left(\frac{ip_r\theta_{PM}}{2}\right) \tag{4.4}$$

For the CP rotor,

$$A_{PMi} = \frac{4B_r h_{PM}}{i\mu_0\mu_r\pi}\sin\left(\frac{ip_r\theta_{PM}}{2}\right) \tag{4.5}$$

where B_r, h_{PM}, μ_r, and θ_{PM} are the remanence, the thickness, the relative permeability, and the pole arc of rotor PMs, respectively.

The air-gap permeance accounting for the stator slots can be expressed as

$$\Lambda_s(\theta) = \Lambda_{s0} + \sum_{j=1}^{\infty}\Lambda_{sj}\cos(jN_s\theta + \pi) \tag{4.6}$$

When slot pitches of multi-tooth are equal, N_s is replaced by $n_{st}N_s$, which is the total stator multi-tooth numbers, i.e., 12 and 18 in Fig. 4.1 (b) and Fig. 4.1 (c). n_{st} is the multi-tooth number per stator-tooth.

The open-circuit air-gap flux density is

$$B_m(\theta,t) = F_{PM}(\theta,t)\Lambda_s(\theta) =$$
$$\Lambda_{s0} * \sum_{i=1}^{\infty} A_{PMi}\cos[ip_r(\theta-\omega t)] + \frac{1}{2}\sum_{i=1}^{\infty}\sum_{j=1}^{\infty}\Lambda_{sj}\mathrm{A}_{PMi}\cos\left[(ip_r \pm jp_s)\theta - ip_r\omega t\right] \tag{4.7}$$

The pole-pair number of armature winding should satisfy $p_a=n_{st}N_s-p_r$ for achieving high torque [ZHO19a]. The back-EMF induced by the rotor PM magnetic field is

$$e_A(t) = -\frac{d}{dt}\lambda_{PM}(t) = -\frac{d}{dt}\left[r_\delta l_{ef} n_c \int_0^{\frac{2\pi}{N_s}} B_m(\theta,t)d\theta\right] = \omega r_\delta l_{ef} n_c$$
$$\{\Lambda_{s0}\sum_{i=1}^{\infty} A_{PMi}\left[\cos(ip_r\frac{2\pi}{N_s} - ip_r\omega t) - \cos(ip_r\omega t)\right] + \frac{1}{2}\sum_{i=1}^{\infty}\sum_{j=1}^{\infty}\frac{ip_r}{ip_r \pm jN_s}\Lambda_{sj}\mathrm{A}_{PMi} \tag{4.8}$$
$$\left[\cos((ip_r \pm jN_s)\theta - ip_r\omega t) - \cos\left(ip_r\omega t\right)\right]\}$$

where r_δ is the air-gap radius, l_{ef} is the axial length of stator lamination, and n_c is the number of turns per coil.

To simplify the analysis, higher order harmonics are neglected due to their low amplitudes. Only considering i=1, j=1 or n_{st}, and $ip_r \pm jN_s$ in $ip_r \pm jN_s$, the back-EMF can be rewritten as

$$e_A(t) = \omega r_\delta l_{ef} n_c [\cos(p_a \frac{2\pi}{N_s} + p_r \omega t) - \cos(p_r \omega t)] \\ (\Lambda_{s0} A_{PM1} + \frac{1}{2}\frac{p_r}{p_r - N_s}\Lambda_{s1} \mathrm{A}_{PM1} - \frac{1}{2}\frac{p_r}{p_a}\Lambda_{sn_{st}} \mathrm{A}_{PM1}) \tag{4.9}$$

The back-EMF contains EMFs generated by unmodulated and modulated field components. The first term is generated by the unmodulated field. The second term is generated by the field modulation effect of stator big tooth (N_s) while the third term is generated by the field modulation effect of multi-tooth ($n_{st}N_s$).

When three-phase sinusoidal current and i_d=0 control are applied, the average electromagnetic torque is expressed as:

$$T_{av} = \frac{3E_A I_A}{2\omega} = \frac{3}{2} I_A r_\delta l_{ef} n_c (\Lambda_{s0} A_{PM1} + \frac{1}{2}\sum_{j=1}^{\infty} \frac{p_r}{p_r \pm jN_s} \Lambda_{sj} \mathrm{A}_{PM1}) \tag{4.10}$$

The average electromagnetic torque can be simplified as:

$$T_{av} = \frac{3}{2} I_A r_\delta l_{ef} n_c (\Lambda_{s0} A_{PM1} + \frac{1}{2}\frac{p_r}{p_r - N_s}\Lambda_{s1} \mathrm{A}_{PM1} - \frac{1}{2}\frac{p_r}{p_a}\Lambda_{sn_{st}} \mathrm{A}_{PM1}) \tag{4.11}$$

4.3. Machine Optimization

The 6-slot VPMSMs with different multi-tooth numbers (one to five) and rotor topologies (NSP and CP) are globally optimized for maximum average torque under fixed 40 W copper loss considering end winding. During the optimization, fixed parameters are listed in Table 4.1, including stator outer diameter (100 mm), active stack length (50 mm), air-gap length (1 mm), shaft diameter (20 mm), and copper loss considering end winding (40 W). Stator inner radius (r_{si}), yoke thickness (h_y), tooth width (w_t), slot opening height (h_{s0}), stator slot opening width (b_{s0}), width of multi-tooth and depth of dummy slot (w_{mt} and h_{mt} (w_{mt1}=w_{mt2})), and pole arc to pole pitch ratio of rotor PM (p_{rPM}) will be globally optimized as shown in Fig. 4.2. The p_{rPM} is defined as θ_{pm}/θ_1.

(a) 6s/1t/8p.

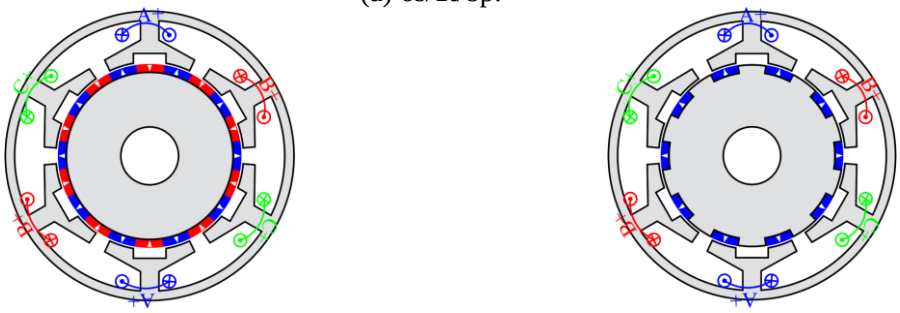

(b) 6s/2mt/20p.

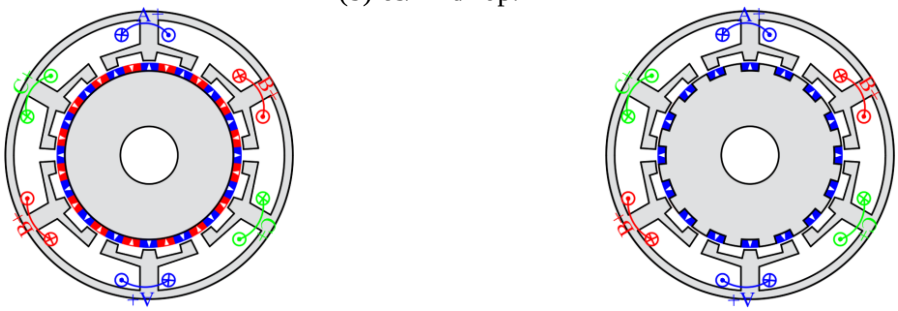

(c) 6s/3mt/32p.

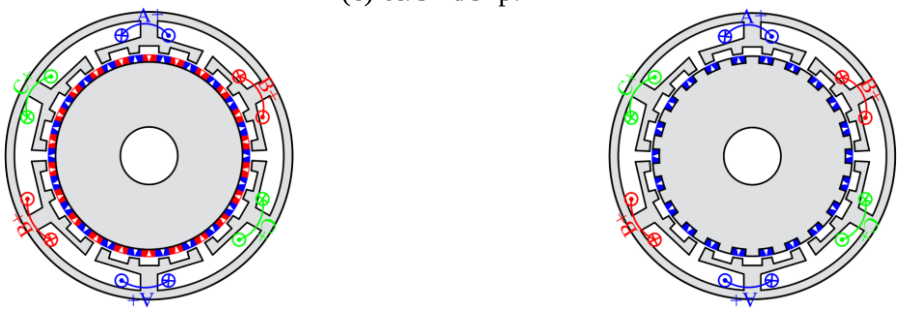

(d) 6s/4mt/44p.

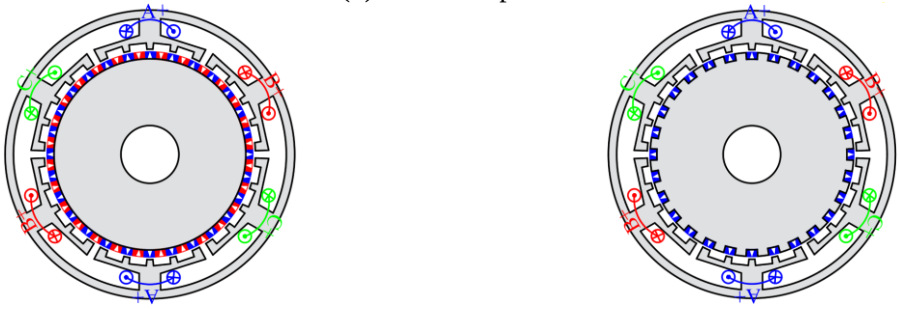

(e) 6s/5mt/56p.

(i) NSP. (ii) CP.

Fig. 4.1. Machine topologies of 6-slot FSCW VPMSMs with different multi-tooth numbers and rotor topologies.

For NSP VPMSMs, the PM volume is fixed at 24.5 cm^3 while two scenarios are considered for CP VPMSMs, i.e., fixed 24.5 cm^3 PM volume and unfixed PM volume. Fig. 4.3 compares the optimized torques of NSP and CP VPMSMs, where the optimized torque increases first and then decreases with the increase of multi-tooth number. When the PM volume for CP VPMSMs is fixed the same as that of NSP VPMSMs, the average torques of CP with 1-3 multi-tooth numbers are higher while the torques of CP with 4 and 5 multi-tooth numbers are lower than that of NSP counterparts. However, when the PM volume is not fixed during optimization, the optimized torques of CP VPMSMs with different multi-tooth numbers will increase and always be higher than those of the corresponding NSP counterparts with any multi-tooth number. Moreover, the optimal PM volumes of CP VPMSMs with different multi-tooth numbers are less than 24.5 cm^3. The optimized CP VPMSMs with less than 24.5 cm^3 PM volume are chosen to be analyzed in this chapter. Optimal parameters are listed in Table 4.2 (NSP) and Table 4.3 (CP). Meanwhile, optimal machine structures and on-load magnetic field distributions under 40 W copper loss are shown in Fig. 4.4.

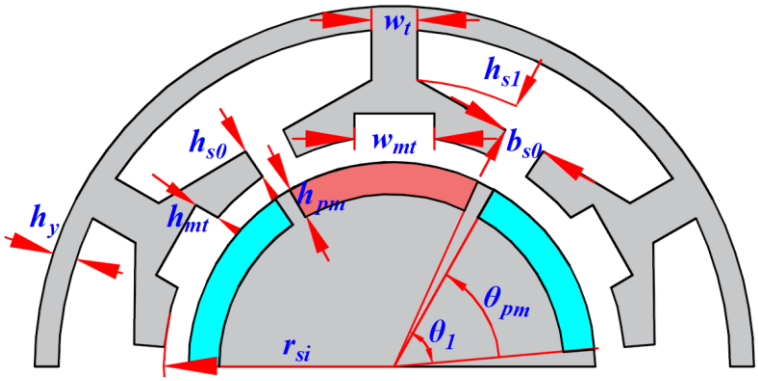

(a) NSP with 2mt.

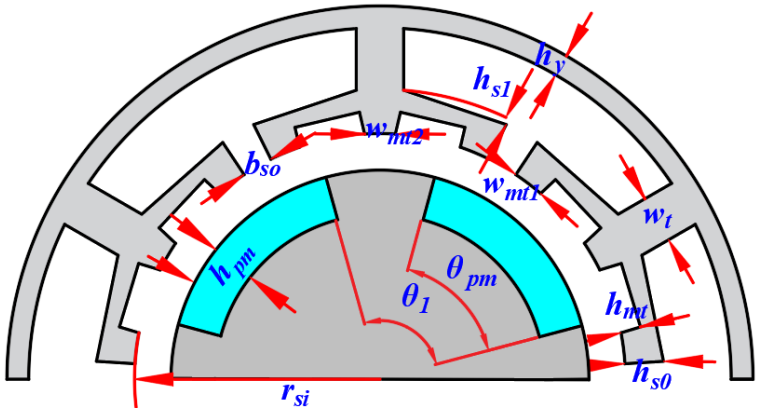

(b) CP with 3mt.

Fig. 4.2. Illustration of variables of 6-slot VPMSMs during the optimization.

Table 4.1 Fixed Parameters of NSP and CP VPMSMs

Parameters	Unit	Value
Number of stator slot (Z_s)	-	6
Number of rotor pole ($2p$)	-	8/20/32/44/56
Stator outer diameter (d_{so})	mm	100
Active stack length (l_{fe})	mm	50
Number of turns per phase (N_{ph})	-	184
Slot filling factor (s_f)	-	0.28
Air-gap length (δ)	mm	1
Shaft diameter (d_{sh})	mm	20
PM remanence (B_r)	T	1.20
PM relative permeability (μ_r)	-	1.05

Table 4.2 Optimized Variables of NSP VPMSMs

Parameters	Unit	Value				
Multi-tooth	-	1	2	3	4	5
r_{si}	mm	29.4	32.1	32.5	35.9	36.4
h_y	mm	4.6	3.3	3.1	3.0	2.9
w_t	mm	8.9	6.4	6.0	6.0	7.4
b_{s0}	mm	11.7	10.4	10.5	10.3	11.8
h_{s0}	mm	2.0	4.2	5.2	5.0	4.6
w_{mt1}	mm	-	8.6	4.1	3.4	2.4
h_{mt}	mm	-	3.4	2.5	2.3	2.2
h_{PM}	mm	3.1	2.7	2.6	2.4	2.3
V_{PM}	cm^3	24.5	24.5	24.5	24.5	24.5
p_{rPM}	-	0.93	0.99	0.98	0.98	0.98
T_{av}	Nm	3.94	4.68	4.78	4.68	4.28
T_{ripple}	%	14.91	7.23	6.97	3.70	2.86
I_{peak}	A	5.60	5.14	5.19	4.31	4.24

Table 4.3 Optimized Variables of CP VPMSMs

Parameters	Unit	Value				
Multi-tooth	-	1	2	3	4	5
r_{si}	mm	28.9	31.3	33.4	34.9	35.2
h_y	mm	5.4	3.8	3.5	3.5	3.4
w_t	mm	10.0	7.3	7.1	7.2	9.2
b_{s0}	mm	1.6	4.8	5.5	4.8	4.6
h_{s0}	mm	12.8	6.1	4.9	4.1	2.7
w_{mt1}	mm	-	7.8	4.0	2.8	2.5
h_{mt}	mm	-	3.4	2.8	2.7	1.7
h_{PM}	mm	5.0	4.3	3.4	2.8	2.2
V_{PM}	cm^3	24.5	23.7	20.0	17.5	13.8
p_{rPM}	-	0.61	0.63	0.61	0.61	0.62
T_{av}	Nm	4.15	4.90	4.97	4.82	4.36
T_{ripple}	%	50.16	40.18	19.11	18.77	18.39
I_{peak}	A	5.54	5.14	4.61	4.29	4.13

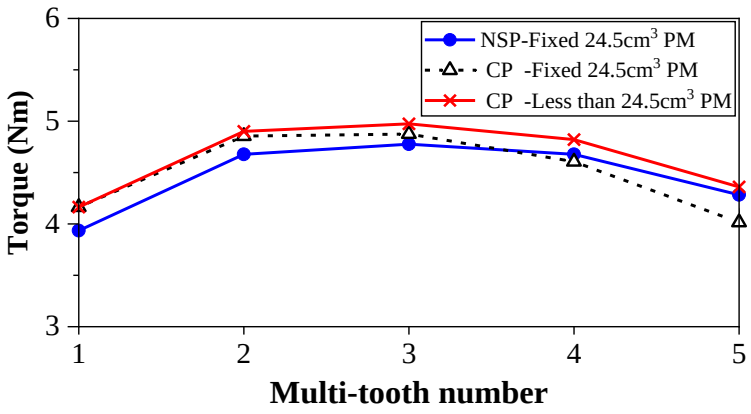

Fig. 4.3. Optimized torques of 6-slot VPMSMs with different multi-tooth numbers and rotor topologies.

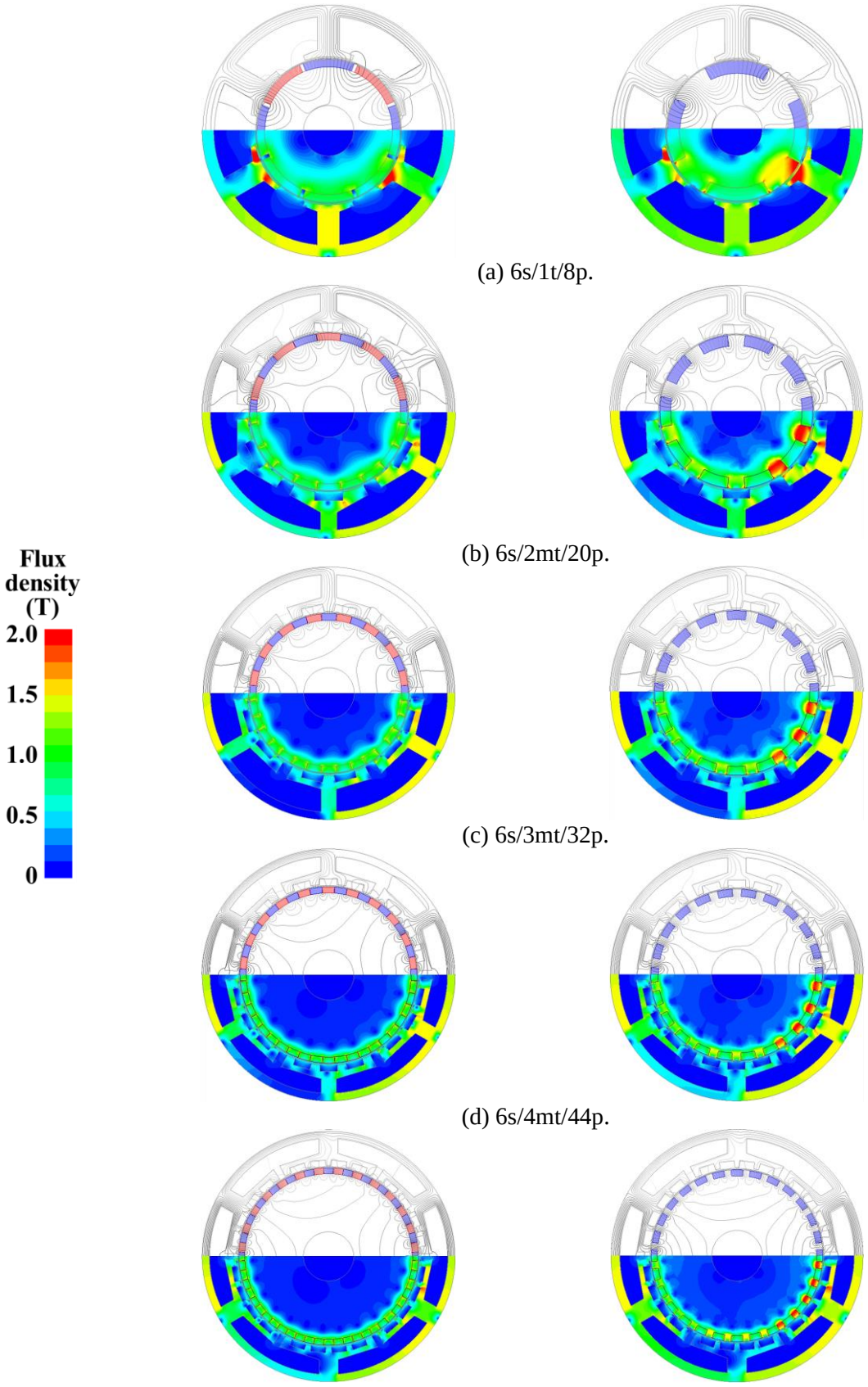

(a) 6s/1t/8p.

(b) 6s/2mt/20p.

(c) 6s/3mt/32p.

(d) 6s/4mt/44p.

(e) 6s/5mt/56p.

(i) NSP. (ii) CP.

Fig. 4.4. On-load magnetic field distributions of 6-slot VPMSMs with different multi-tooth numbers and rotor topologies.

4.4. Comparison of Electromagnetic Performances

4.4.1. Open-circuit

The electromagnetic performances of optimized NSP and CP VPMSMs are compared in this section, including torque characteristics, PM utilization, efficiency, power factor, overload capability, etc.

Open-circuit radial air-gap flux densities, back-EMFs, and their FFT spectra of optimized 6-slot NSP and CP VPMSMs with different multi-tooth numbers are shown in Fig. 4.5. NSP structures have higher fundamental components of open-circuit radial air-gap flux density, whereas CP structures exhibit higher modulated field harmonics, as shown in Fig. 4.5 (c). This implies that CP structures have superior field modulation effects and the potential to generate higher back-EMFs. Fundamental components of open-circuit radial air-gap flux density decrease with the increase of multi-tooth number for both NSP and CP VPMSMs. However, due to the field modulation effect, fundamental components of open-circuit back-EMFs show different trends, increasing first and then decreasing. For both NSP and CP VPMSMs, the fundamental components of back EMF reach their maximum when the multi-tooth number is four.

4.4.2. Torque characteristics

Fig. 4.6 and Fig. 4.7 show the torque characteristics of optimized 6-slot NSP and CP VPMSMs with different multi-tooth numbers. Average torques of CP VPMSMs with different multi-tooth numbers show the same trend as that of NSP VPMSMs, increasing first and then decreasing with the increase of multi-tooth numbers. The optimal multi-tooth numbers for maximum average torque under 40 W copper loss and 50 mm lamination stack length are three for both NSP and CP structures. The cogging torque and torque ripple decrease with the increase of multi-tooth number. The average torque of the CP structure is higher than that of the NSP counterpart, but the torque ripple and cogging torque are also higher. The multi-tooth structure helps reduce cogging torque and torque ripple. However, the multi-tooth stator and CP rotor structures exhibit poor overload capabilities, as shown in Fig. 4.7.

Fig. 4.8 shows the comparison of average torque, torque ripple, and PM utilization between optimized 6-slot NSP and CP VPMSMs with different multi-tooth numbers. It indicates that the CP rotor combined with the multi-tooth stator structure can help reduce the PM volume and

increase PM utilization. For the CP structure, the optimal PM volume decreases with the increase of multi-tooth number. Thus, CP VPMSMs with higher multi-tooth numbers exhibit higher PM utilization. Specifically, for the CP VPMSM with 5 multi-teeth, the PM volume is reduced by about 50% compared with the corresponding NSP counterpart. Table 4.4 provides detailed data on average torque, PM usage, and PM utilization of CP VPMSMs with different multi-tooth numbers.

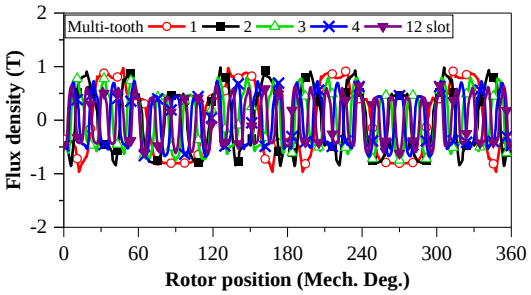

(a) Air-gap flux densities of NSP.

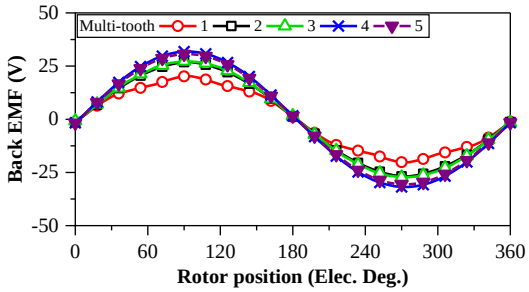

(b) Back-EMFs of NSP.

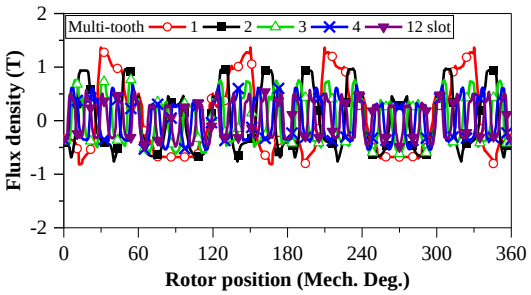

(c) Air-gap flux densities of CP.

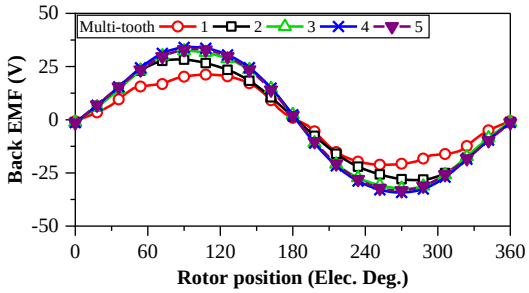

(d) Back-EMFs of CP.

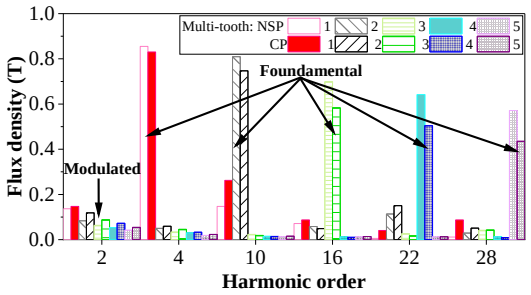

(e) FFT spectra of air-gap flux density.

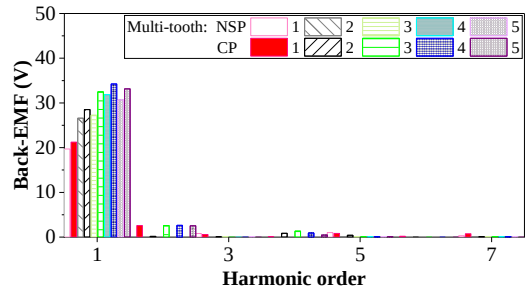

(f) FFT spectra of back-EMF.

Fig. 4.5. Open-circuit radial air-gap flux densities and back-EMFs of 6-slot NSP and CP VPMSMs with different multi-tooth numbers.

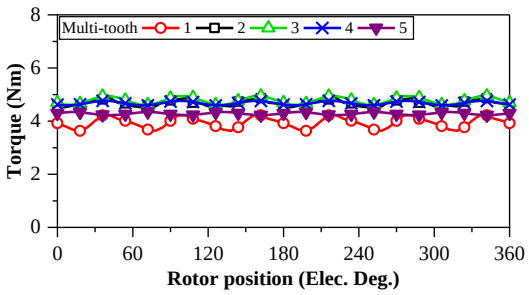

(a) On-load torques of NSP.

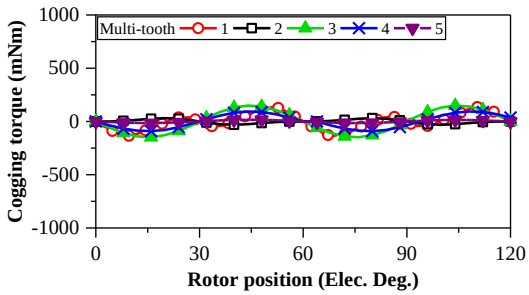

(b) Cogging torques of NSP.

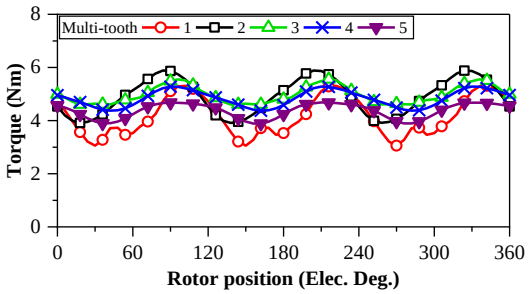

(c) On-load torques of CP.

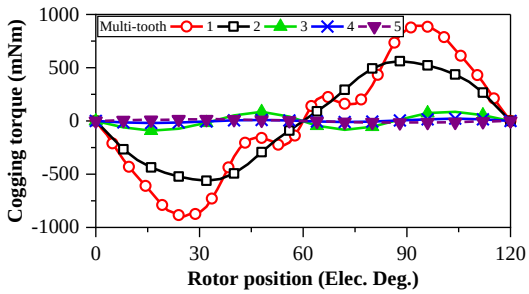

(d) Cogging torques of CP.

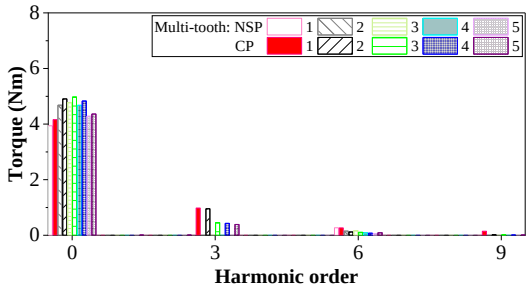

(e) FFT spectra of on-load torque.

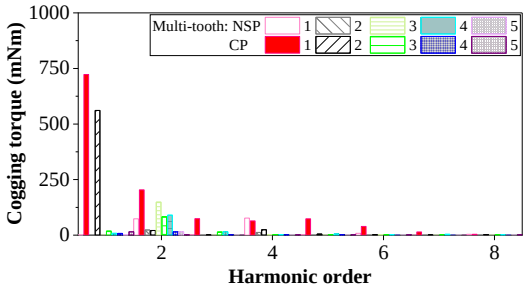

(f) FFT spectra of cogging torque.

Fig. 4.6. On-load torques and cogging torques of 6-slot NSP and CP VPMSMs with different multi-tooth numbers.

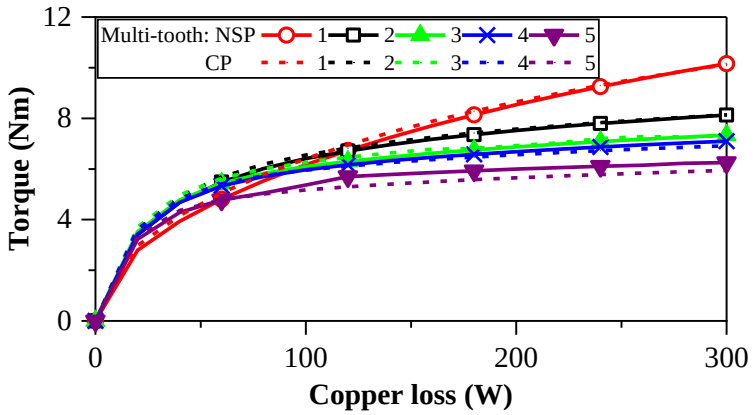

Fig. 4.7. Overload capabilities of 6-slot NSP and CP VPMSMs with different multi-tooth numbers.

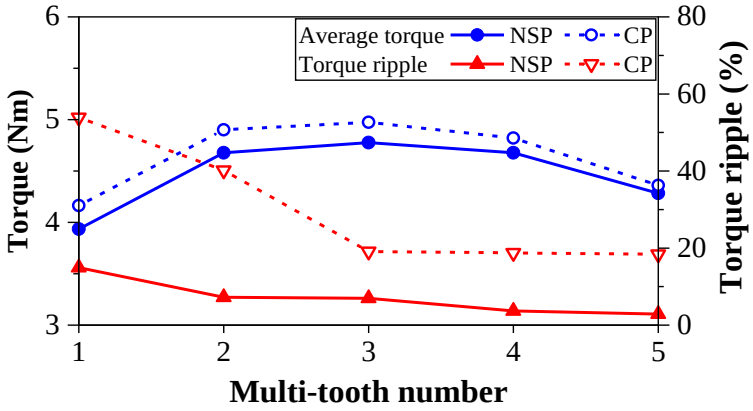

(a) Average torque and torque ripple.

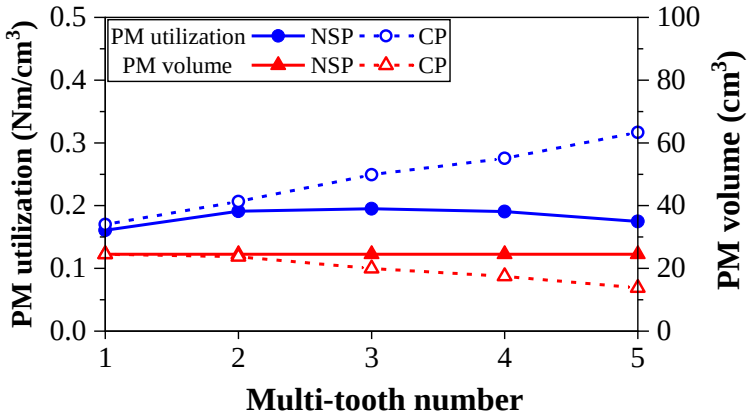

(b) PM volume and PM utilization.

Fig. 4.8. Average torques, torque ripples, and PM utilization comparison between optimized 6-slot NSP and CP VPMSMs with different multi-tooth numbers.

Table 4.4 Comparison of PM Volume, Average Torque, and PM Utilization among CP VPMSMs with Different Multi-tooth Numbers

Multi-tooth number	V_{PM} (cm^3)	T_{av} (Nm)	PM utilization (Nm/cm^3)
1	24.50	4.16	0.17
2	23.72	4.90	0.21
3	19.96	4.98	0.25
4	15.73	4.84	0.28
5	12.31	4.34	0.32

4.4.3. Loss, efficiency, and power factor

Fig. 4.9 shows losses, efficiencies, power factors, and *d*-axis inductances of optimized 6-slot NSP and CP VPMSMs under 40W copper loss and different speeds (400 and 1500 r/min). The iron loss increases with the number of multi-teeth, while the PM loss shows the opposite trend

because the PM volume per piece decreases as the multi-tooth number increases, leading to lower PM loss. The lower total PM volume of the CP structure also results in lower total PM loss. As the VPMSM with 3 multi-teeth has the highest average torque, it achieves higher efficiency at lower speeds. When the speed increases, the iron loss increases with the number of multi-teeth, leading to decreased efficiency at high speed conditions. The power factor decreases with the increase of multi-tooth number and the CP structure further decreases the power factor because the multi-tooth stator and CP rotor structures increase the *d*-axis inductance.

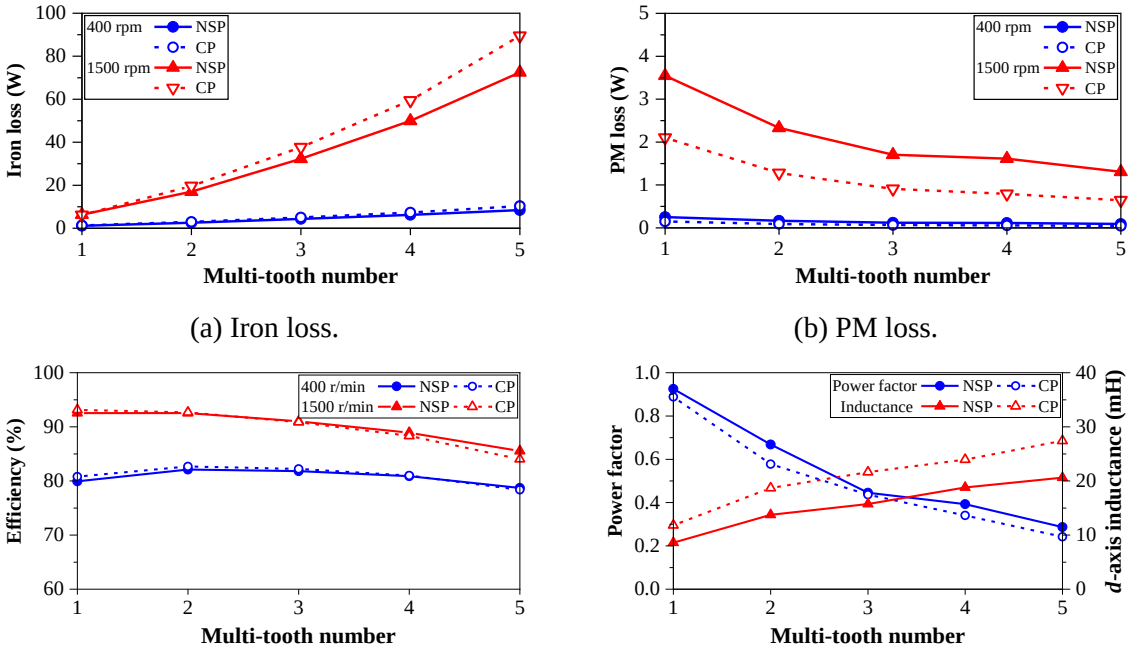

(a) Iron loss. (b) PM loss.

(c) Efficiency. (d) Power factor and d-axis inductance.

Fig. 4.9. Losses, efficiencies, and power factors of optimized 6-slot CP and NSP VPMSMs with different multi-tooth numbers.

In conclusion, CP VPMSMs have higher torque output capability and higher efficiency at lower speed conditions (400 r/min) compared with their NSP counterparts. Moreover, PM utilization is significantly improved when combining the CP rotor and stator with higher numbers of multi-teeth. Approximately 50% of PM volume can be saved for the CP VPMSM with 5 multi-teeth compared with the corresponding NSP counterpart. However, CP VPMSMs have lower power factor, much higher torque ripple and cogging torque, and poorer overload capability compared with their NSP counterparts.

4.5. Influence of Critical Design Parameters

In this section, the influence of critical design parameters on the field modulation effect and average torque of CP VPMSMs is investigated, including the width of multi-tooth (w_{mt}) and the depth of dummy slot (h_{mt}) on the stator side, as well as the pole arc to pole pitch ratio and the thickness of rotor PM (p_{rPM} and h_{PM}) on the rotor side, as shown in Fig. 4.10.

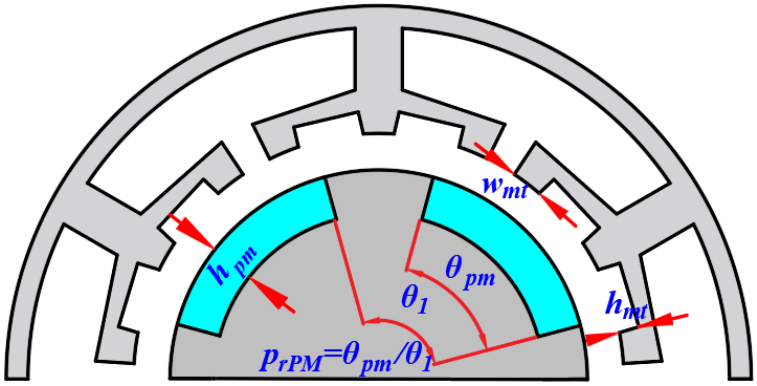

Fig. 4.10. Illustration of critical parameters of CP VPMSMs.

4.5.1. Width of multi-tooth

The width of multi-tooth directly affects the equivalent air-gap permeance, and thus, affects the field modulation effect and average torque output capability of CP VPMSMs. Fig. 4.11 shows the influence of the width of multi-tooth on open-circuit air-gap flux density and average torque. The larger the multi-tooth width, the higher the equivalent air-gap permeance, and thus, the higher the fundamental component of open-circuit air-gap flux density. However, the modulated component of open-circuit air-gap flux density increases and then decreases with the increase of multi-tooth width. Consequently, the torque of CP VPMSMs is very sensitive to the width of multi-tooth. The multi-tooth width should be carefully selected to maintain fundamental air-gap flux density while achieving relatively higher modulated air-gap flux density to maximize torque output capability. There is an optimal width for each CP VPMSM with different multi-tooth numbers.

4.5.2. Depth of dummy slot

The influence of the depth of dummy slot on open-circuit air-gap flux density and average torque of CP VPMSMs is shown in Fig. 4.12. Increasing the multi-tooth height will reduce the fundamental component of air-gap flux density while increasing the modulated component, indicating that the height is also critical to the torque output capability. There exist optimal

heights of multi-tooth numbers for different multi-tooth numbers, which decrease as multi-tooth numbers increase.

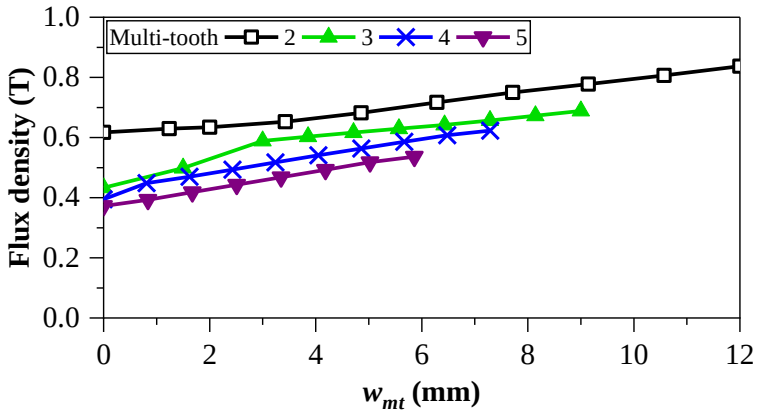

(a) Fundamental component of air-gap flux density.

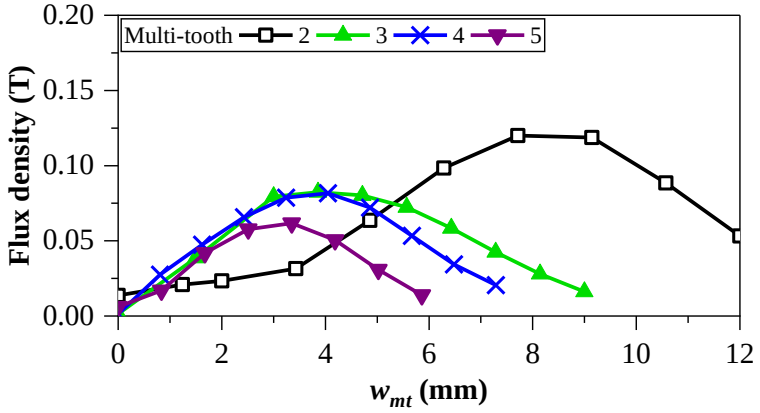

(b) Modulated component of air-gap flux density.

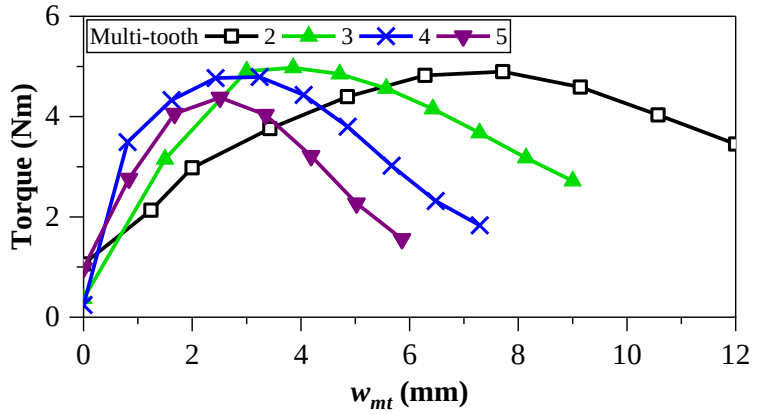

(c) Torque.

Fig. 4.11. Influence of width of multi-tooth on air-gap flux density and average torque of CP VPMSMs.

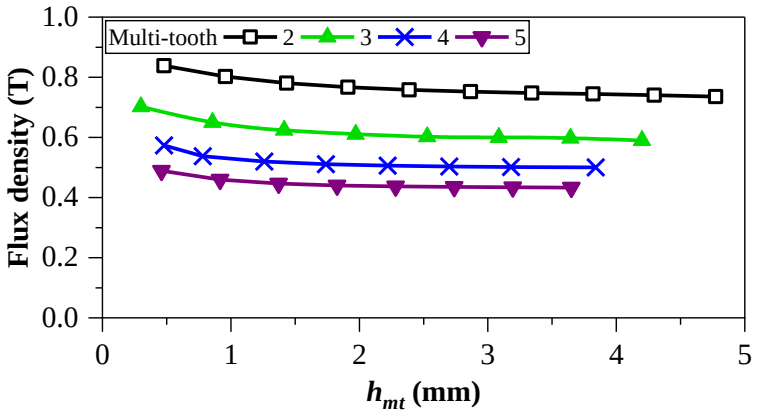

(a) Fundamental component of air-gap flux density.

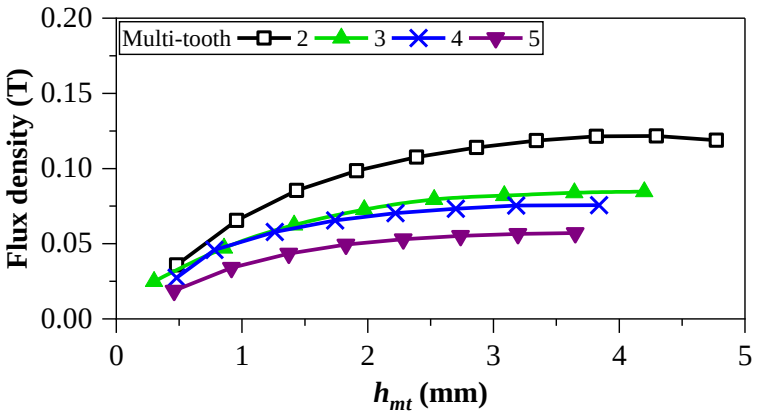

(b) Modulated component of air-gap flux density.

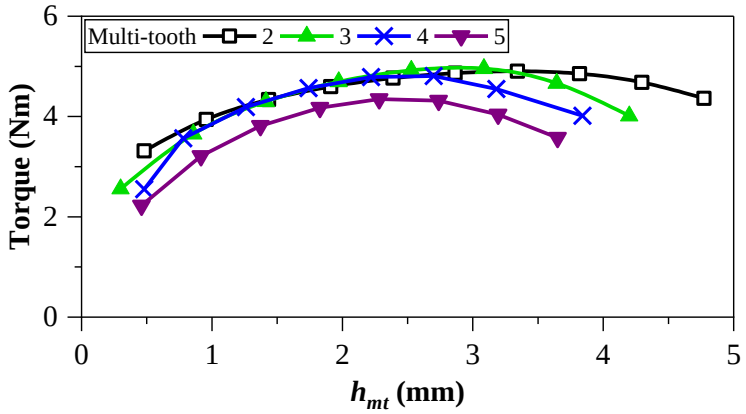

(c) Torque.

Fig. 4.12. Influence of depth of dummy slot on air-gap flux density and average torque of CP VPMSMs.

4.5.3. Pole arc to pole pitch ratio

The dimensions of PMs affect the MMF of rotor PMs and the equivalent air-gap permeance of CP VPMSMs. Unlike the pole arc to pole pitch ratio in NSP VPMSMs, which is usually 0.5, the pole arc to pole pitch ratio can exceed 0.5 for better field modulation effect and torque output capability in CP VPMSMs. Fig. 4.13 shows the influence of pole arc to pole pitch ratio of rotor PMs on open-circuit air-gap flux density and average torque. Both the fundamental and modulated components of air-gap flux density increase and then decrease with the increase of pole arc to pole pitch ratio. For all CP VPMSMs, the maximum fundamental components are achieved at a pole arc to pole pitch ratio of 0.7, while the maximum modulated components are achieved at a pole arc to pole pitch ratio of 0.6. There is a trade-off between fundamental and modulated components of air-gap flux density for achieving maximum torque output, therefore, the optimal pole arc to pole pitch ratio of each CP VPMSM with different multi-tooth numbers is almost the same, ranging between 0.60 and 0.63.

4.5.4. PM thickness

The influence of rotor PM thickness on open-circuit air-gap flux density and average torque of CP VPMSMs is shown in Fig. 4.14. The fundamental component of air-gap flux density increases first and then remains almost unchanged with the increase of PM thickness, while the modulated component increases first and then decreases. As the PM thickness affects the MMF of rotor PMs (4.5), flux leakage, and rotor core saturation, thicker PMs do not guarantee higher average torque. The optimal PM thickness decreases significantly with the increase of multi-tooth number.

Overall, the field modulation effect and torque output capability are very sensitive to the dimensions of multi-tooth and PMs. The optimal width of multi-tooth and depth of dummy slot vary with the multi-tooth number. With the increase of multi-tooth number, the optimal PM thickness decreases significantly, while the optimal pole arc to pole pitch ratios are similar. Hence, the PM volume decreases with the increase of multi-tooth number.

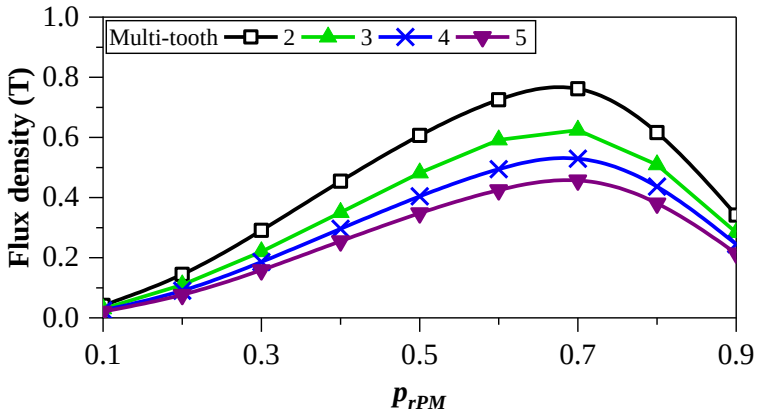

(a) Fundamental component of air-gap flux density.

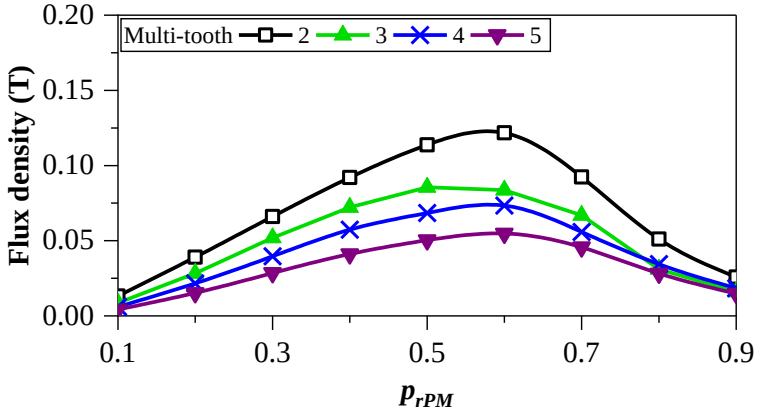

(b) Modulated component of air-gap flux density.

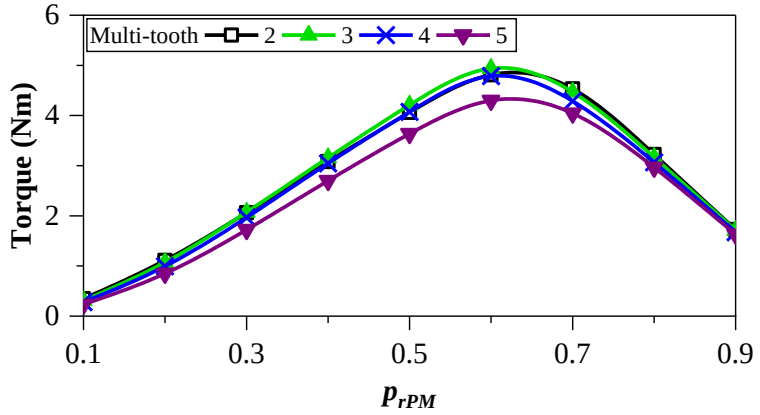

(c) Torque.

Fig. 4.13. Influence of pole arc to pole pitch ratio of rotor PMs on air-gap flux density and average torque of CP VPMSMs.

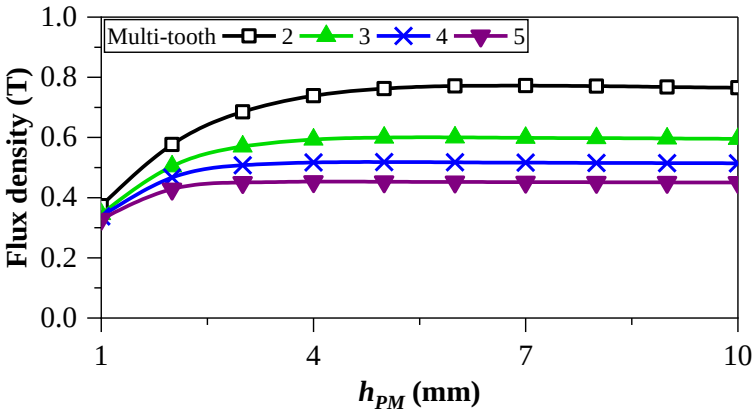

(a) Fundamental component of air-gap flux density.

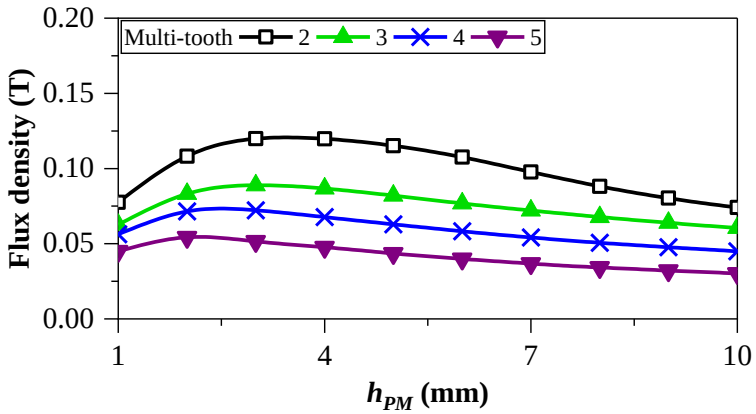

(b) Modulated component of air-gap flux density.

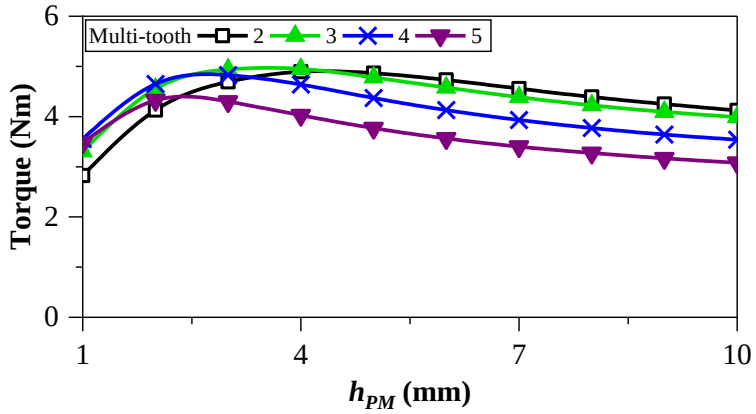

(c) Torque.

Fig. 4.14. Influence of PM thickness on air-gap flux density and average torque of CP VPMSMs.

4.6. Unipolar End Leakage Flux of CP VPMSMs

Unbalanced magnetic circuits in the CP rotor structure lead to unipolar end leakage flux and magnetization on the shaft, which may threaten the safe operation of the machine system. The end leakage flux of CP VPMSMs with different multi-tooth numbers and rotor structures (conventional/composite rotor with magnetic/non-magnetic shaft) is investigated in this section.

4.6.1. Unipolar end leakage flux distribution

3-D FEA models are built to analyze end leakage flux distributions of CP VPMSMs with different multi-tooth numbers. Magnetic paths of end leakage flux for CP VPMSM with 3 multi-teeth are shown in Fig. 4.15. The path with orange color represents the end leakage caused by the PM magnetic field, while that with green color represents the armature reaction magnetic field. The unipolar end leakage flux is mainly caused by the PM magnetic field, while the armature reaction only has a minor effect on end leakage flux because it enhances the magnetic saturation [ZHE23].

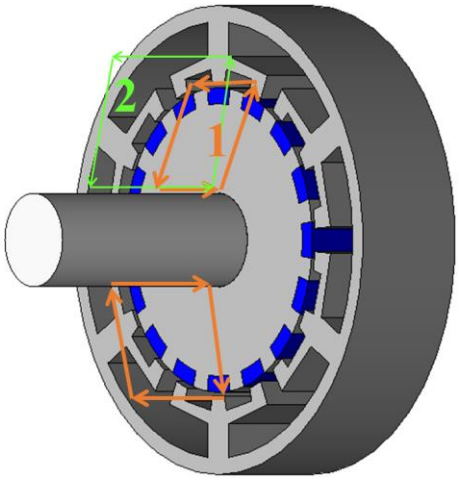

Fig. 4.15. Magnetic paths of end leakage flux for CP VPMSM with 3 multi-teeth.

End leakage flux distributions of CP VPMSMs with magnetic shaft (SUS430 magnetic stainless steel) and different multi-tooth numbers under on-load condition with 40 W copper loss are shown in Fig. 4.16.

End leakage fluxes of all CP VPMSMs show significant unipolar distributions. Fig. 4.17 shows the maximum end leakage fluxes of VPMSMs on the shaft surface about 3 mm away from the rotor end. It demonstrates that the multi-tooth stator structure helps reduce the end leakage flux and the higher the multi-tooth number, the lower the unipolar end leakage flux. As the rotor

pole number increases with the multi-tooth number, the radial leakage flux becomes higher. Consequently, the axial end leakage flux (indicated by the magnetic path in Fig. 3.6) decreases. Additionally, the increasing rotor pole number also results in a reduction in the total flux per pole, further lowering the axial end leakage flux. The maximum end leakage flux of CP VPMSMs with 5 multi-teeth (6s/5mt/56p) is 0.20 T, more than 60% lower compared with VPMSMs without multi-tooth stator structure (6s/1t/8p), which is 0.54 T.

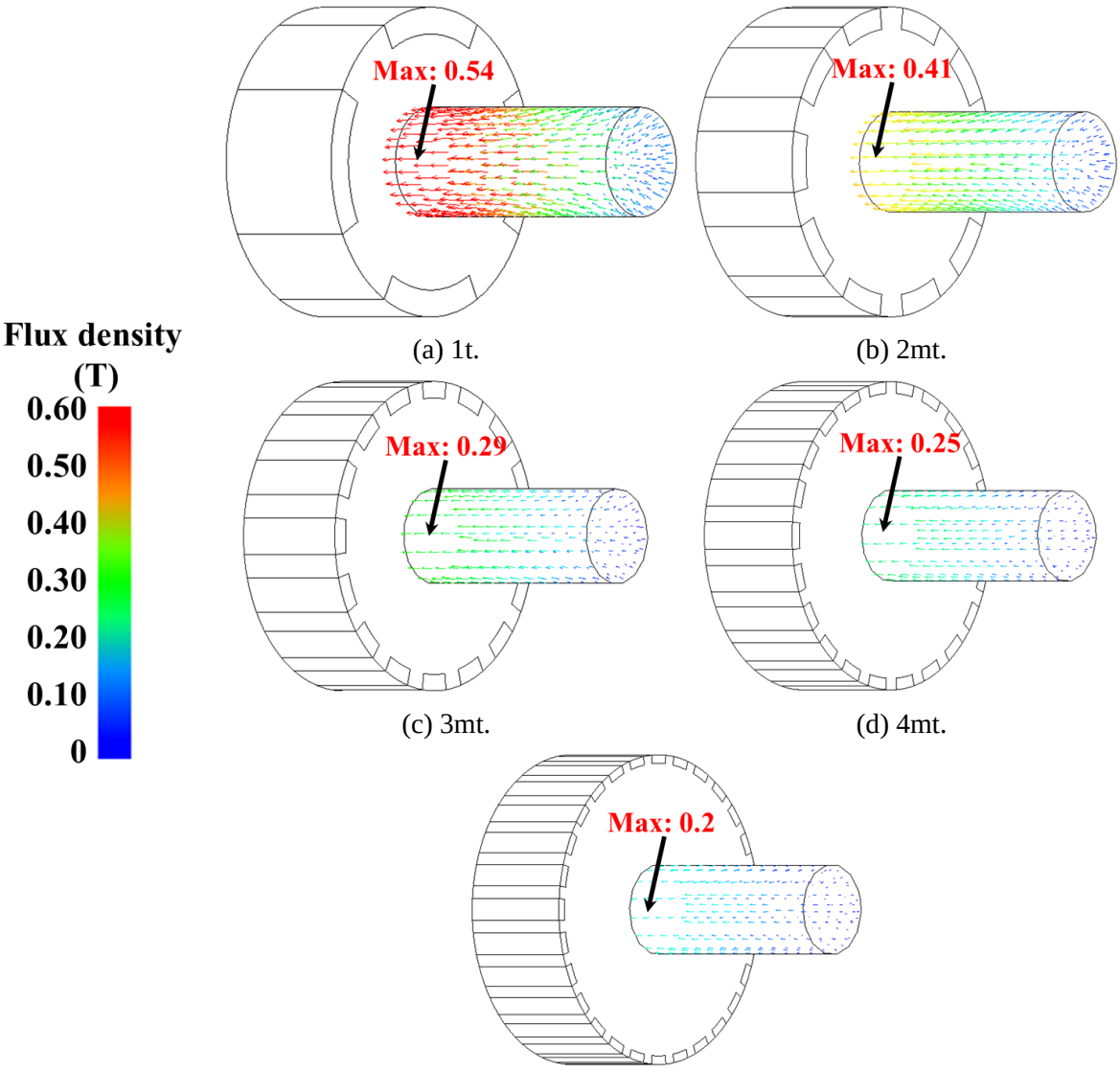

(a) 1t. (b) 2mt. (c) 3mt. (d) 4mt. (e) 5mt.

Fig. 4.16. End leakage flux distributions of CP VPMSMs with magnetic shaft and different multi-tooth numbers under on-load condition with 40 W copper loss. Stators have been removed from the figures for clarity.

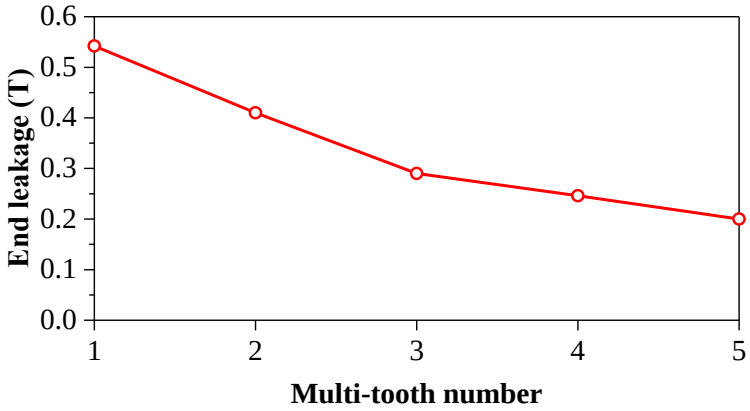

Fig. 4.17. Maximum end leakage fluxes of VPMSMs on shaft surface.

4.6.2. Non-magnetic shaft

The non-magnetic shaft can be used to reduce the unipolar end leakage flux. Fig. 4.18 compares the end leakage flux distributions between CP VPMSMs with different multi-tooth numbers using magnetic and non-magnetic shafts under 40 W copper loss. Additionally, Fig. 4.19 shows the comparison of maximum end leakage fluxes. The non-magnetic shaft can significantly reduce the unipolar end leakage flux, with more than a 90% reduction of the maximum end leakage flux on the shaft.

4.6.3. Composite rotor

Inserting a non-magnetic ring between the rotor and shaft, forming a composite rotor structure, increases the magnetic reluctance of the end leakage flux path. It helps reduce the unipolar end leakage flux while maintaining the average torque output capability, especially when the non-magnetic shaft is used [ZHE23]. Fig. 4.20 shows end leakage flux distributions of CP VPMSMs with different rotor structures under 40 W copper loss. Fig. 4.21 shows the maximum unipolar end leakage flux and reduction rate of CP VPMSMs with different rotor structures. Compared with the conventional rotor structure, the composite rotor structure can reduce approximately 40% of the maximum end leakage flux on the shaft. Furthermore, compared with the conventional rotor and magnetic shaft structure, the composite rotor with a non-magnetic shaft can reduce approximately 95% of the maximum end leakage flux on the shaft. Table 4.5 provides the maximum end leakage on the shaft of CP VPMSMs with different rotor structures. It shows that the end leakage flux of the shaft can be reduced significantly by applying the composite rotor and non-magnetic shaft structure.

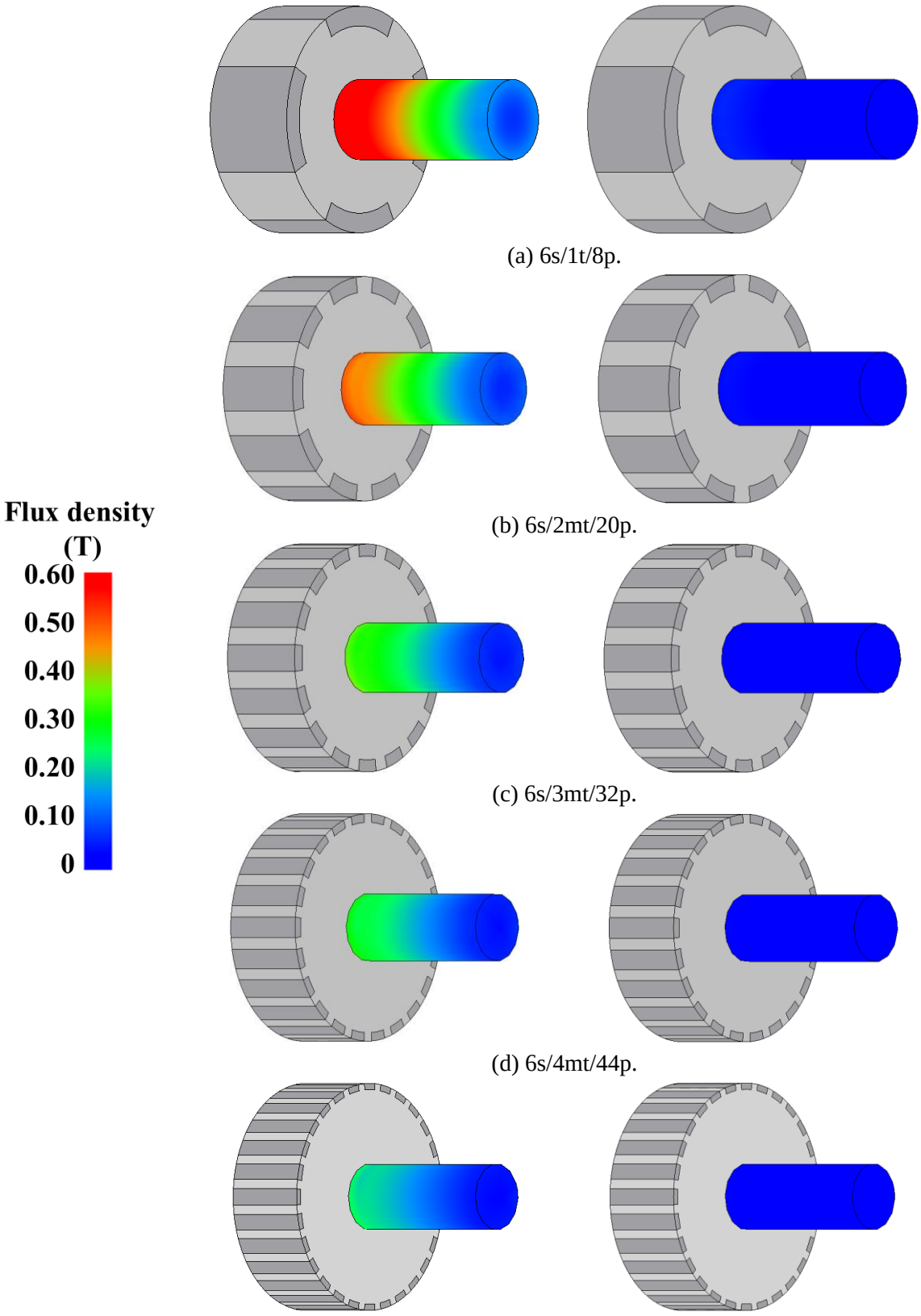

(a) 6s/1t/8p.

(b) 6s/2mt/20p.

(c) 6s/3mt/32p.

(d) 6s/4mt/44p.

(e) 6s/5mt/56p.

(i) Magnetic shaft. (ii) Non-magnetic shaft.

Fig. 4.18. End leakage flux distributions of CP VPMSMs with magnetic and non-magnetic shafts under on-load condition with 40 W copper loss. Stators have been removed from the figures for clarity.

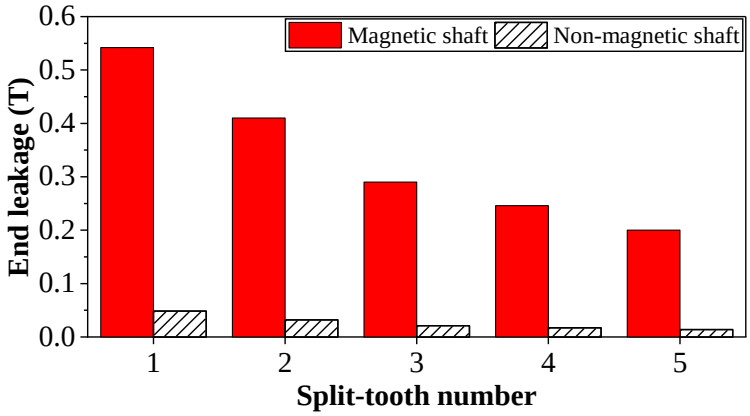

Fig. 4.19. Maximum end leakage fluxes of VPMSMs on shaft surface about 3 mm away from rotor end.

Table 4.5 Maximum End Leakage on Shaft of CP VPMSMs with Different Rotor Structures

FMP	1	2	3	4	5
Conventional rotor & magnetic shaft	0.54	0.41	0.29	0.25	0.20
Composite rotor & magnetic shaft	0.34	0.23	0.16	0.14	0.11
Conventional rotor & non-magnetic shaft	0.048	0.032	0.021	0.017	0.014
Composite rotor & non-magnetic shaft	0.036	0.023	0.016	0.013	0.010

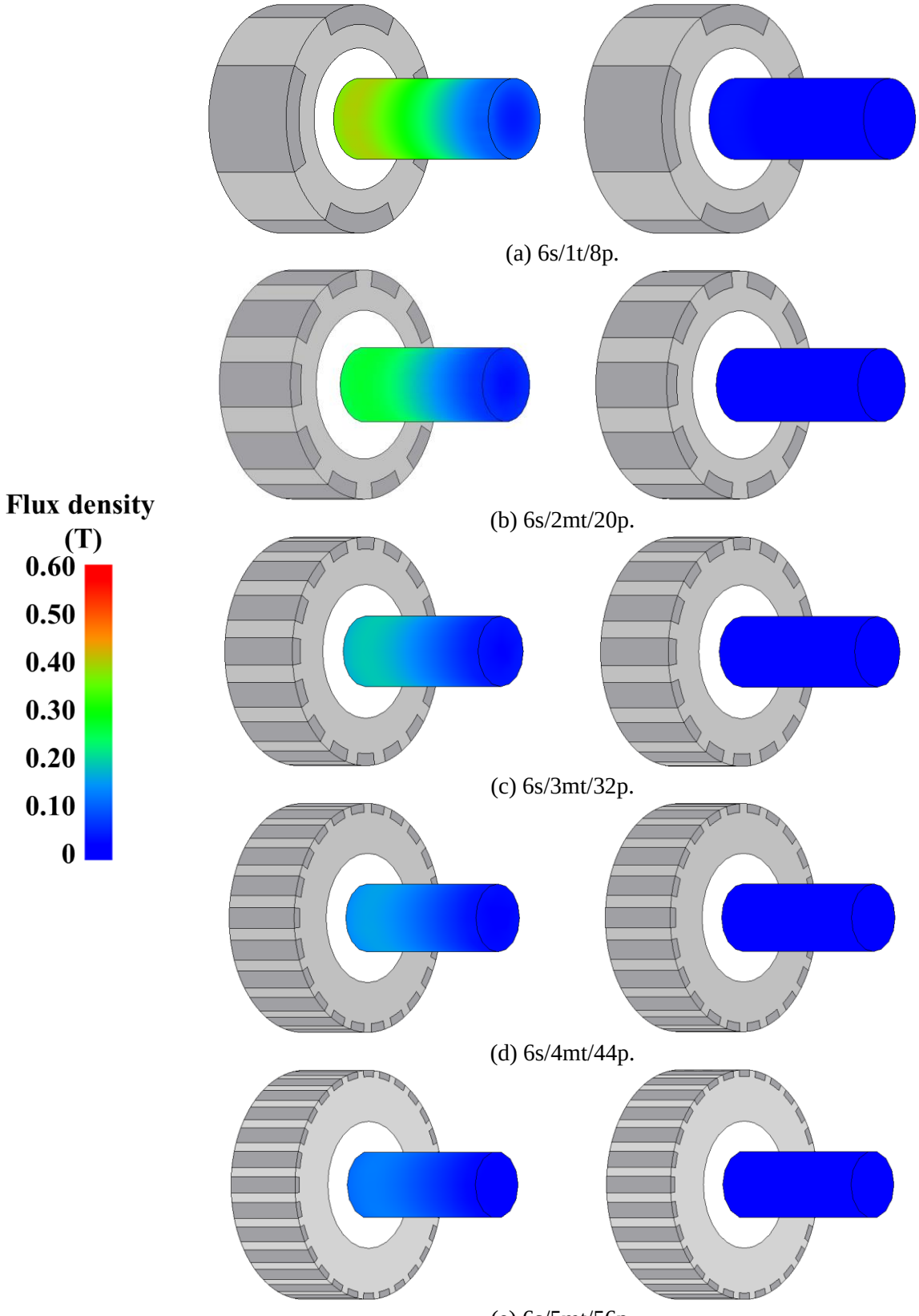

(a) 6s/1t/8p.

(b) 6s/2mt/20p.

(c) 6s/3mt/32p.

(d) 6s/4mt/44p.

(e) 6s/5mt/56p.

(i) Magnetic shaft. (ii) Non-magnetic shaft.

Fig. 4.20. End leakage flux distributions of composite rotor CP VPMSMs with magnetic and non-magnetic shafts under on-load condition with 40 W copper loss. Stators have been removed from the figures for clarity.

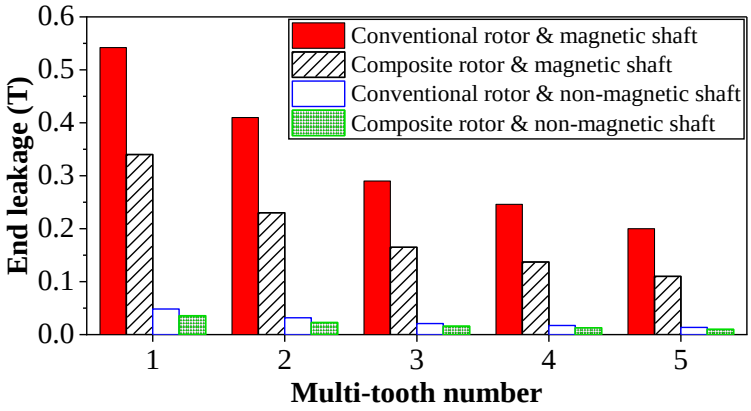

(a) Maximum unipolar end leakage flux.

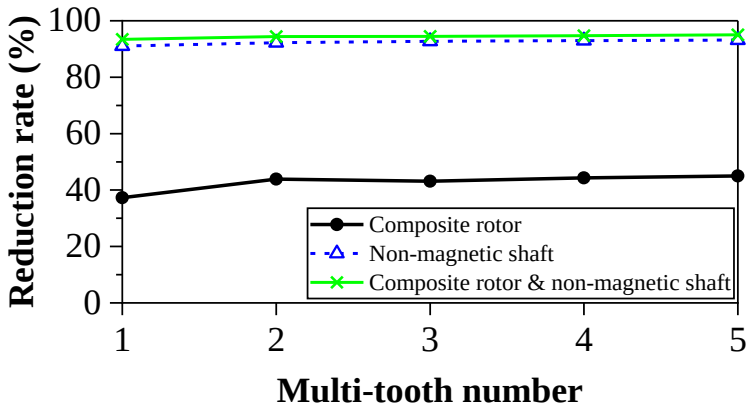

(b) Reduction rate.

Fig. 4.21. Comparison of maximum unipolar end leakage flux and reduction rate of CP VPMSMs with different rotor structures.

4.7. Experimental Validation

4.7.1. Electromagnetic test

Two VPMSMs (6s/2mt/20p and 6s/3mt/32p) with NSP and CP rotors have been prototyped. For the CP rotor, both the conventional rotor with a magnetic shaft (stainless steel SUS430) and the composite rotor with a non-magnetic shaft (stainless steel SUS304) are manufactured. Prototypes are tested to verify the effectiveness of FEA analysis.

Fig. 4.22 shows stators, NSP rotors, CP conventional rotors, and CP composite rotors of prototypes. Table 4.6 lists the key parameters of prototypes. The test rigs for back EMF, cogging torque and static torque [ZHU09], and dynamic torque are shown in Fig. 2.39 and Fig. 2.42.

Table 4.6 Key Parameters of Prototypes

Parameters	Unit	Value	
Multi-tooth number	-	2	3
Stator inner radius (r_{si})	mm	32.0	33.5
Yoke thickness (h_y)	mm	3.4	3.5
Stator tooth width (w_t)	mm	6.6	7.0
Stator tooth tip height (h_{s0})	mm	4.4	5.64
Slot opening width (b_{s0})	mm	6.10	5.1
Multi-tooth width (w_{mt1})	mm	7.45	4.15
Multi-tooth height (h_{mt})	mm	3.64	3.0
PM height (h_{PM})	mm	4.0	4.0
Pole arc to pole pitch ratio (p_{rPM})	-	0.64	0.60
PM remanence (B_r)	T	1.20	
PM relative permeability (μ_r)	-	1.05	

Fig. 4.23 shows the measured and FEA predicted open-circuit back EMFs at 400 r/min, showing good agreement. VPMSMs with 3 multi-teeth exhibit higher fundamental components of back EMF compared with 2 multi-teeth ones. Additionally, the CP rotor structure can generate a higher fundamental component of back EMF compared with its NSP counterpart.

Fig. 4.24 shows the measured and FEA predicted cogging torques. VPMSMs with 3 multi-teeth have lower cogging torque compared with those with 2 multi-teeth, while the CP rotor structure has higher cogging torque compared with its NSP counterpart.

The static torque is measured by injecting current through the DC power supply (I_b=I_c= - 0.5I_a) and rotating the stator while keeping the rotor stationary. Subsequently, the relationship between static torque and rotor position can be measured. Measured and FEA predicted static torques match well as shown in Fig. 4.25. The static torque of CP VPMSM is slightly higher than that of the NSP counterpart.

Measured and FEA predicted dynamic torques match well as shown in Fig. 4.26. Additionally, Fig. 4.27 shows measured and FEA predicted torque-current characteristics, which also show good agreement.

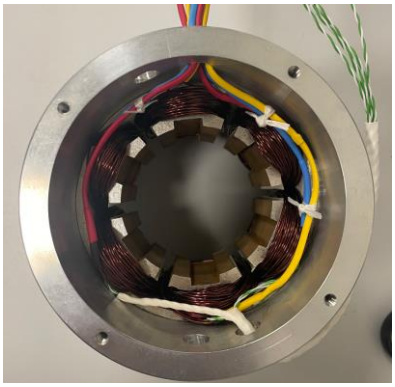

(a) 6s/2mt/20p stator.

(b) 20p NSP rotor.

(c) 20p CP conventional rotor with magnetic shaft.

(d) 20p CP composite rotor with non-magnetic shaft.

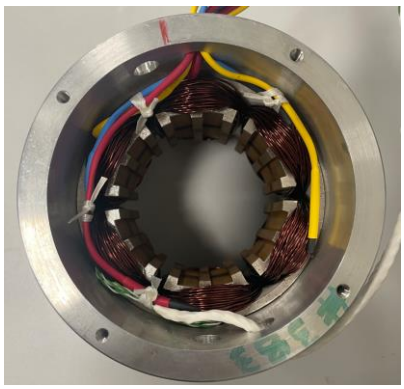

(e) 6s/3mt/32p stator.

(f) 32p NSP rotor.

(g) 32p CP conventional rotor with magnetic shaft.

(h) 32p CP composite rotor with non-magnetic shaft.

Fig. 4.22. Prototype 6s/2mt/20p and 6s/3mt/32p VPMSMs.

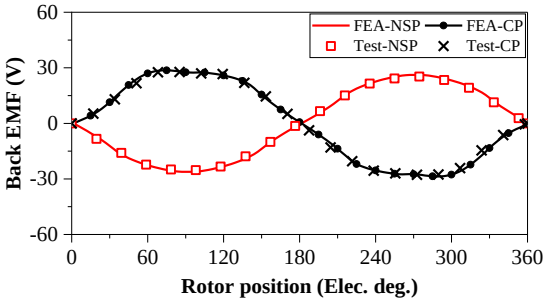

(a) Waveforms of 6s/2mt/20p.

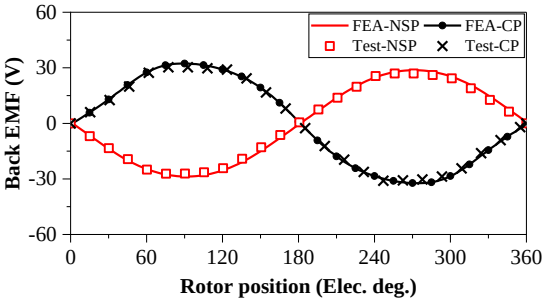

(b) Waveforms of 6s/3mt/32p.

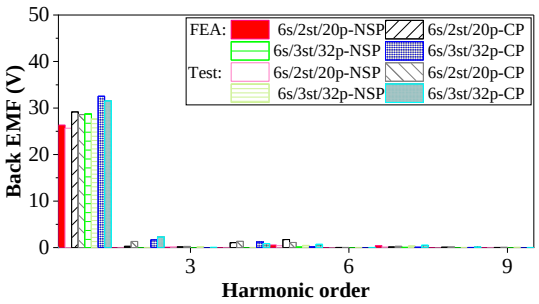

(c) FFT spectra.

Fig. 4.23. Measured and FEA predicted open-circuit back EMFs at 400 r/min.

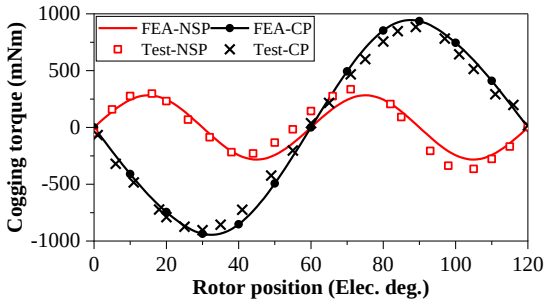

(a) Waveforms of 6s/2mt/20p.

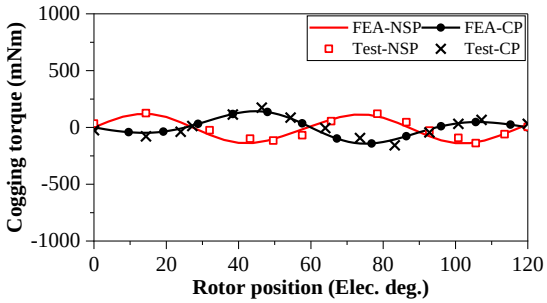

(b) Waveforms of 6s/3mt/32p.

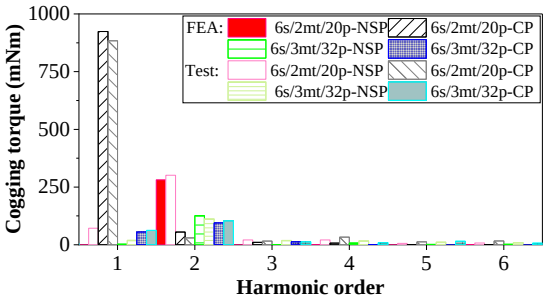

(c) FFT spectra.

Fig. 4.24. Measured and FEA predicted cogging torques.

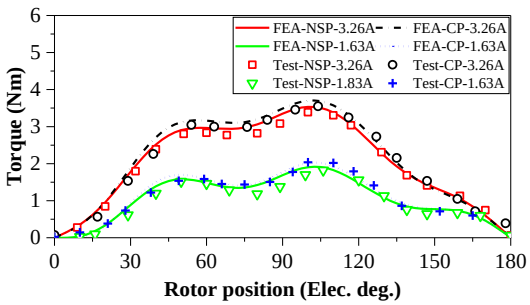

(a) 6s/2mt/20p.

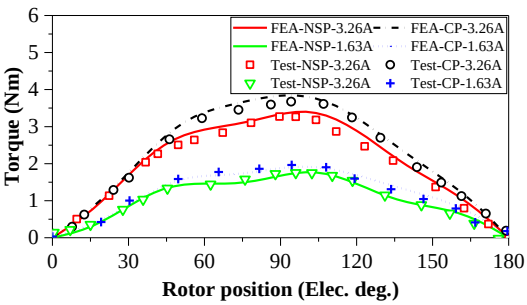

(b) 6s/3mt/32p.

Fig. 4.25. Measured and FEA predicted static torques.

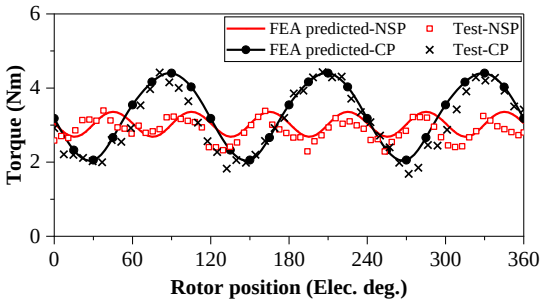

(a) Waveforms of 6s/2mt/20p.

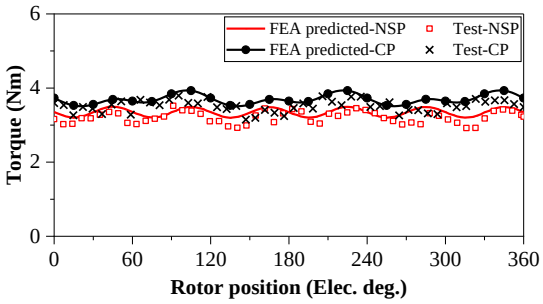

(b) Waveforms of 6s/3mt/32p.

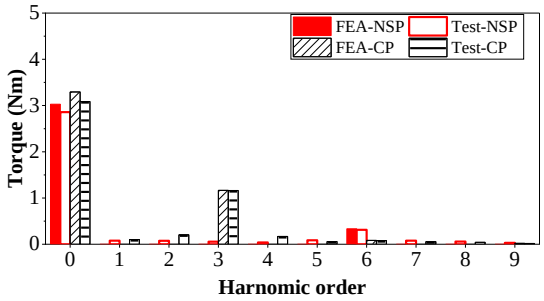

(c) FFT spectra of 6s/2mt/20p.

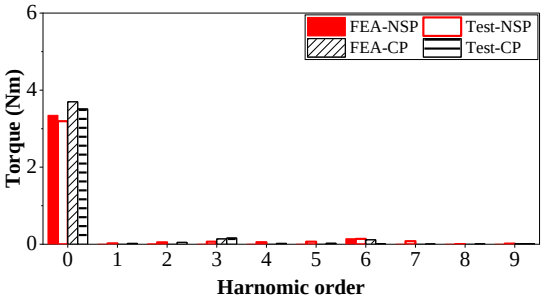

(d) FFT spectra of 6s/3mt/32p.

Fig. 4.26. Measured and FEA predicted dynamic torques and FFT spectra.

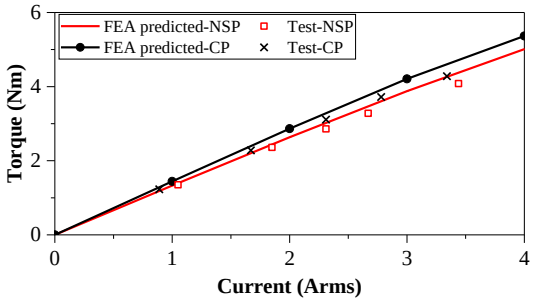

(a) 6s/2mt/20p.

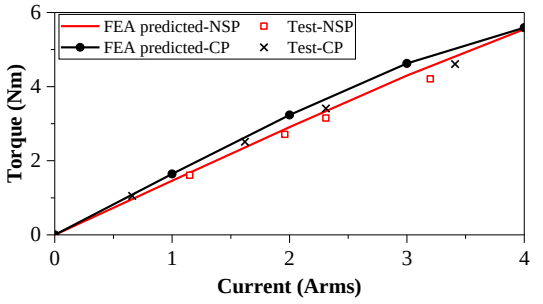

(b) 6s/3mt/32p.

Fig. 4.27. Measured and FEA predicted torque-current characteristics.

4.7.2. Test for end leakage

The unipolar end leakage flux of the entire shaft region can be measured with the bare rotor before assembling as shown in Fig. 4.28. Meanwhile, the end leakage flux can be measured in the shaft region outside the end cap after assembling.

(a) 6s/2mt/20p conventional rotor and magnetic shaft.

(b) 6s/2mt/20p composite rotor and non-magnetic shaft.

(c) 6s/3mt/32p conventional rotor and magnetic shaft.

(d) 6s/3mt/32p composite rotor and non-magnetic shaft.

Fig. 4.28. Illustration of measuring unipolar end leakage flux.

The unipolar end leakage fluxes of two machines obtained by FEA and measurements are compared in Fig. 4.29, including prototypes both before and after assembling with conventional rotor and magnetic shaft, as well as with composite rotor and non-magnetic shaft. The FEA predicted results match well with the measurements. The 6s/3mt/32p VPMSM has lower end leakage flux than the 6s/2mt/20p VPMSM. In addition, employing the non-magnetic ring and non-magnetic shaft effectively reduces the unipolar end leakage flux for both prototypes.

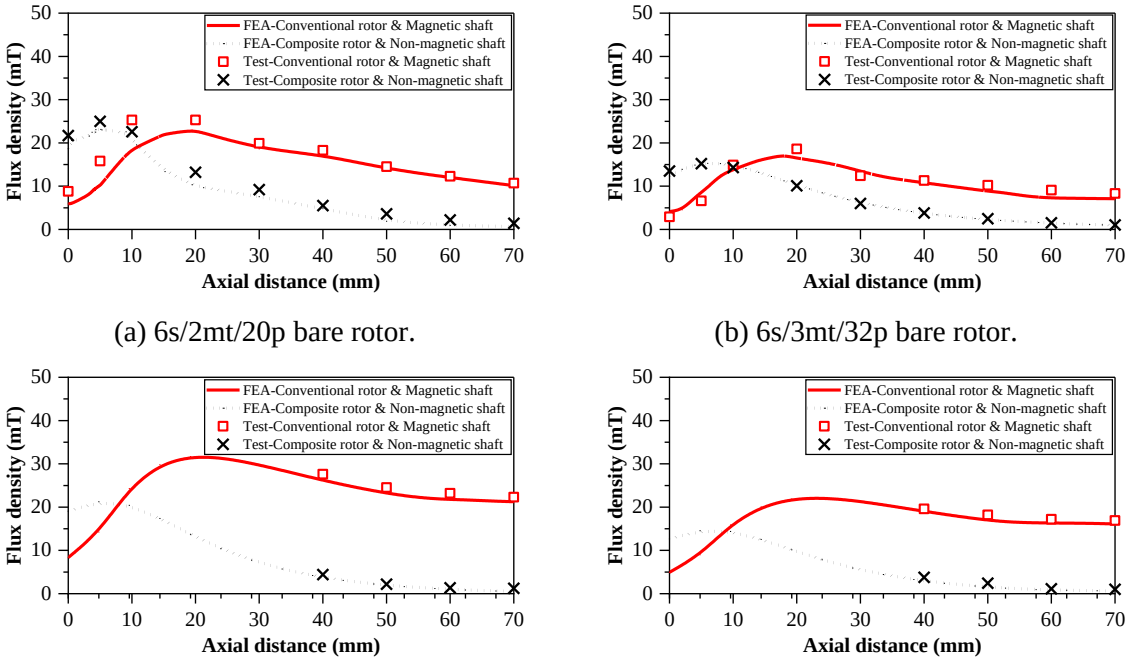

(a) 6s/2mt/20p bare rotor.

(b) 6s/3mt/32p bare rotor.

(c) 6s/2mt/20p assembled.

(d) 6s/3mt/32p assembled.

Fig. 4.29. Measured and FEA predicted end leakage fluxes.

4.8. Summary

In this chapter, the effect of multi-tooth numbers on electromagnetic performances of CP VPMSMs is investigated. Two prototypes are manufactured and tested to verify the FEA analysis. The conclusions can be summarized as follows:

1. The CP rotor combined with the multi-tooth stator structure enhances the field modulation effect and helps increase torque output capability and PM utilization.
2. There is an optimal multi-tooth number (3 for the analyzed machines) for maximizing average torque. With the increase of multi-tooth number, the PM utilization will be improved significantly (saved about 50% for 5 multi-teeth), but the efficiency at higher speeds, power factor, and overload capability will be sacrificed.

3. It has been found, for the first time, that the multi-tooth stator structure helps reduce more than 60% of the maximum unipolar end leakage flux of CP VPMSMs compared with CP VPMSMs with single-tooth stator structure.
4. The influence of critical design parameters of CP VPMSMs, which should be carefully selected to achieve better field modulation effect and maximum torque output capability, is investigated, including the width of multi-tooth, the depth of dummy slot, the pole arc to pole pitch ratio, and the PM thickness.

CHAPTER 5
ASYMMETRIC PM EDDY CURRENT LOSS AND TEMPERATURE DISTRIBUTIONS IN SURFACE-MOUNTED PM SYNCHRONOUS MACHINES

This chapter investigates the mechanism of asymmetric PM eddy current loss and temperature distributions of SPMSMs with different slot/pole number combinations. An FEA based harmonic restoration method is utilized to evaluate and quantify contributions of individual armature reaction spatial harmonics to PM eddy current loss and temperature distributions for 12-slot SPMSMs with different pole numbers. It shows that there is one dominant armature reaction spatial harmonic contributing to the majority of PM loss for each SPMSM with different slot/pole number combinations. The average PM loss distribution is symmetrical to the center line in the circumferential direction with only the armature reaction or PM magnetic field. However, the interaction between the armature reaction and PM fields causes the asymmetric PM loss distribution. Additionally, the maximum loss density in one PM pole tends to move from the circumferential center to the edge when the rotor pole number increases. Consequently, the resultant PM local hotspot temperature has been calculated through the 3-D thermal finite element method, which shows the same trend as the loss density distribution. Finally, two prototypes are manufactured, and the corresponding electromagnetic and thermal tests are carried out to verify the validity of the FEA simulation.

This chapter has been submitted to IEEE Transactions on Industry Applications and is currently under review:

[ZHE24c] Y. Zheng, D. Liang, Z. Q. Zhu, J. Yan, Y. Zhou, H. Liu, and H. Xu, "Asymmetric PM Eddy Current Loss and Temperature Distributions of SPMSMs," *IEEE Trans. Ind. Appl.*, Under review.

5.1. Introduction

Due to high efficiency and high torque density, PMSMs have been widely employed in domestic appliances, servo drives, electric vehicles, wind power generation, etc. [ZHU07]. SPMSM is one of the most preferred choices due to its simple structure, where PMs are mounted on the surface of the rotor and adjacent to the air-gap.

However, the PM eddy current loss in SPMSMs may be significant since PMs are directly exposed to the armature reaction field, particularly in high-speed and high pole-pair SPMSMs [CHE17] [MA19]. Furthermore, the rotor in SPMSMs usually has limited heat dissipation capability, thus making the induced PM loss more likely to cause the risk of over-temperature. Besides, the widely employed NdFeB PM has a high electrical conductivity and a negative temperature coefficient of the coercive field strength, which further aggravates the thermal effect and demagnetization risk [ZHA18].

Therefore, accurate information of PM temperature distribution and PM local hotspots is always important to prevent unexpected demagnetization and improve machine reliability. To date, this issue has been widely investigated from the perspective of thermal analysis [KRA14] [GRO15] [LIA22a] [LIA22b] [LIA22c]. An early study usually assumes that PM temperature is evenly distributed [KRA14]. However, the subsequent research highlights that the SPM has a highly non-uniform PM temperature distribution in the radial direction due to the skin effect, while still assuming the temperature is identical in the circumferential direction [GRO15]. More recently, it has been demonstrated that the 12-slot/10-pole PMSM has asymmetric PM temperature distributions in both radial and circumferential directions, with the local PM hotspot temperature concentrated on one side of the PM outer edge [LIA22a] [LIA22b] [LIA22c]. Moreover, it has also been reported that this asymmetric distribution is affected by the current advancing angle [ZHE22]. However, the mechanism for the asymmetric PM temperature distributions and locations of PM hotspots have not been fully revealed so far.

To elucidate the underlying reason for this phenomenon, the investigation should focus on the PM eddy current loss, which is the primary cause of PM temperature rises. There are two mainstream methods to calculate the PM eddy current loss: the FEA method and the analytical method. As is well known, the FEA method is a common tool and exhibits high accuracy [CHE17] [ZHA18], although it cannot reveal the physical mechanism of asymmetric PM loss. On the other hand, the analytical method is an alternative approach [ATA00] [ZHU04]

[MAR08] [ARU13] [DUB14] [LIU16] [OU19] [TON22], which can separate contributions of different spatial field harmonics and/or temporal current harmonics. Generally, the PM eddy current loss can be calculated analytically based on the Poynting theorem [ZHU04] or the Maxwell theorem [ATA00] [MAR08] [ARU13] [DUB14] [LIU16] [OU19] [TON22].

Firstly, the power dissipated due to the PM loss can be simply calculated by the real part of the Poynting vector [ZHU04], which is defined as the cross-product of electric and magnetic field vectors. However, the Poynting theorem is based on average power flow and, therefore, cannot predict the distribution of eddy currents within PMs. In comparison, based on the Maxwell theorem, spatial eddy current distributions can be calculated by temporal derivations of the magnetic potential vector, which is solved by the Laplace equation [ATA00] [DUB14] [LIU16] [OU19]. Moreover, when the diffusion effect is considered, the Laplace equation needs to be replaced by Helmholtz's equation [MAR08] [ARU13] [TON22]. However, it is worth noting that analytical methods usually focus on the PM loss caused by the armature reaction field, while the PM remanence is usually neglected [ATA00] [MAR08] [ARU13] [DUB14] [LIU16] [OU19] [TON22]. Consequently, the interaction between the armature reaction and PM fields, as well as the resultant asymmetric PM eddy current loss distribution, still cannot be obtained by analytical methods.

Therefore, the FEA based HRM, originally developed to separate torque components of SPMSMs due to the field modulation effect [ZHU18a], is adopted to analyze the effect of armature reaction field and PM field on asymmetric PM eddy current loss and temperature distributions for 12-slot SPMSMs with different rotor pole numbers, including non-overlapping FS SPMSMs and overlapping winding VPMSMs. Furthermore, 12-slot/8-pole and 12-slot/20-pole PMSMs are prototyped and tested to verify FEA simulations in terms of electromagnetic and thermal performance.

The main contributions of this chapter can be summarized as follows:

1. The mechanisms of asymmetric PM eddy current loss and resultant temperature distributions of SPMSMs have been revealed for the first time.
2. The harmonic restoration method is utilized to evaluate and quantify the contributions of individual ARMF harmonics with and without PM field to the asymmetric PM eddy current loss distributions.
3. It is revealed that the hotspot locations of PMs vary with slot/pole number combinations and show consistent trends with PM loss density distributions.

This chapter is organized as follows. Firstly, machine topologies of analyzed 12-slot SPMSMs with different rotor pole numbers are presented in section 5.2. Then, the phenomenon of asymmetric PM eddy current loss distributions is illustrated based on a non-overlapping winding FS 12-slot/8-pole SPMSM and an overlapping winding 12-slot/20-pole VPMVM in section 5.3. Afterward, the developed HRM used for quantifying contributions of individual armature reaction field harmonic and PM field in the PM loss is described in section 5.4, as well as its detailed steps based on 12s/8p and 12s/20p SPMSMs. Furthermore, the HRM is applied to the 12-slot SPMSMs with different rotor pole numbers, i.e., 8-pole, 10-pole, 14-pole, 20-pole, and 22-pole, and the respective dominant armature reaction field harmonics for PM eddy current loss are determined in section 5.5. Consequently, the resultant asymmetric PM temperature distributions are presented in section 5.6 based on 3-D thermal FEA, which is validated experimentally based on 12-slot/8-pole and 12-slot/20-pole prototypes in section 5.7. Finally, this chapter is concluded in section 5.8.

5.2. Machine Topologies

Fig. 2.1 shows the 12-slot SPMSMs with optimal coil pitches, including non-overlapping FSCW SPMSMs (8-pole, 10-pole, and 14-pole), and overlapping winding VPMSMs (20-pole and 22-pole). The design parameters, geometric constraints, and optimized variables are shown in Table 2.1 and Table 2.2.

The open-circuit magnetic flux lines and flux densities are shown in Fig. 5.1 while those under rated-load are shown in Fig. 2.11.

5.3. Asymmetric PM Eddy Current Loss Distribution

As is well known, the PM eddy current is induced by asynchronous air-gap magnetic fields due to non-sinusoidal stator winding magnetomotive force (MMF) distribution, slotting effect, local magnetic saturation, etc. Under open-circuit and rated load (P_{cu}=40 W) conditions, air-gap flux densities, as well as average PM eddy current loss distributions over one mechanical period of non-overlapping winding FS 12s/8p SPMSM and overlapping winding 12s/20p VPMSM are shown in Fig. 5.2 and Fig. 5.3, respectively, where the currents are sinusoidal with 0° advancing current angle.

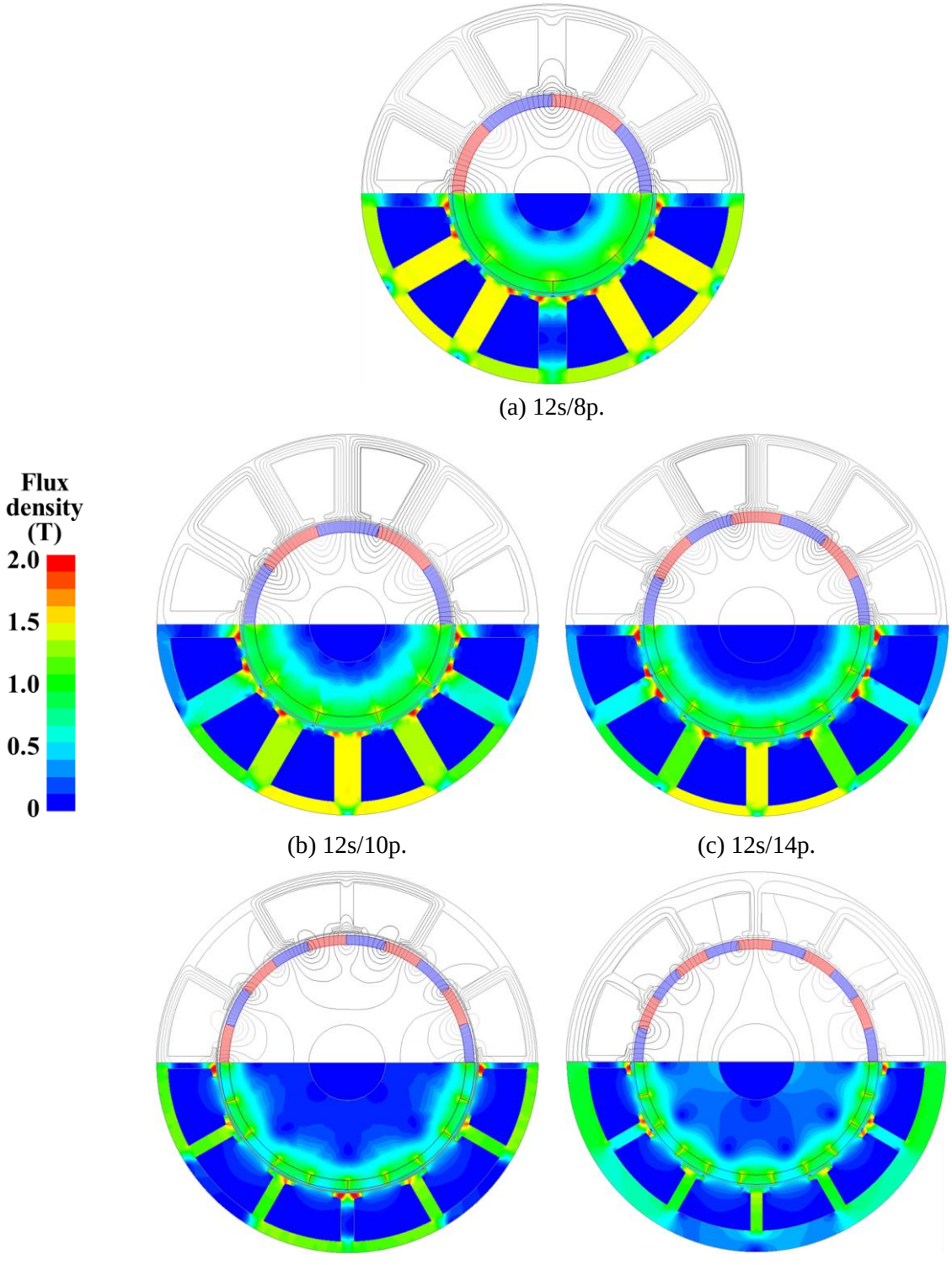

(a) 12s/8p.

(b) 12s/10p.

(c) 12s/14p.

(d) 12s/20p.

(e) 12s/22p.

Fig. 5.1. Open-circuit magnetic field distributions of 12-slot SPMSMs.

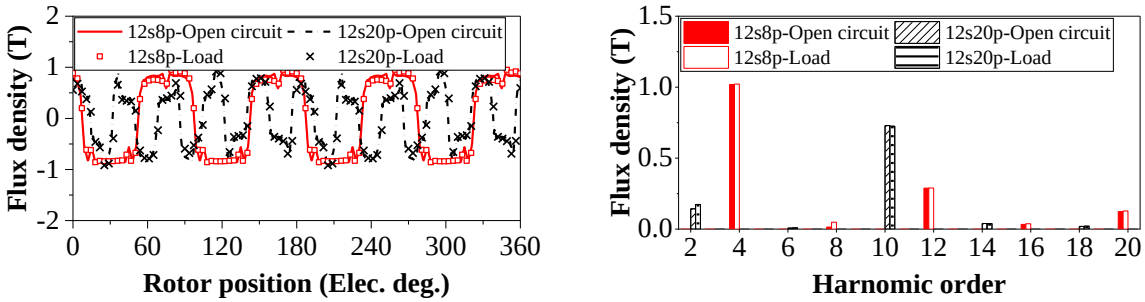

(a) Waveforms. (b) Spectra.

Fig. 5.2. Air-gap flux densities of 12s/8p and 12s/20p SPMSMs under open-circuit condition and rated-load condition with 40 W copper loss.

It can be easily found from Fig. 5.2 that the armature MMF enriches amplitudes of harmonic components of the air-gap flux density, especially the 8th order harmonic for 12s/8p and the 2nd order harmonic for 12s/20p. In Fig. 5.3, the average PM losses in one PM pole under open-circuit and rated-load conditions at 5000 r/min are 0.10 W and 0.48 W for 12s/8p, and 3.0 W and 4.4 W for 12s/20p, respectively. The corresponding maximum local PM loss densities are 1.2×10^5 W/m^3 and 9.5×10^5 W/m^3 for 12s/8p, 6.2×10^6 W/m^3 and 9.9×10^6 W/m^3 for 12s/20p, respectively, based on the average PM loss distribution over one mechanical period. It is obvious that the armature reaction increases the average PM loss density as well as the maximum local loss density.

Moreover, when only the armature reaction field is considered, i.e., the PM remanence is set to zero, the average PM eddy current loss distributions over one mechanical period and the corresponding flux line and density distributions are shown in Fig. 5.4, where the current is set to the rated value for 40 W copper loss.

As can be observed from Fig. 5.3, the open-circuit PM eddy current loss is caused by the distorted air-gap flux density due to the slotting effect and PM field harmonics. Thus, due to periodic symmetry, the average PM loss distribution is symmetrical along the center line in the circumferential direction. When only the armature reaction field is considered, the induced loss density is also almost symmetrical, as shown in Fig. 5.4.

However, when both the PM field and armature reaction field exist, as shown in Fig. 5.3, it is obvious that the interaction of the PM field and armature reaction field not only increases the PM loss density but also causes the asymmetric loss distribution, with the maximum loss density tending to concentrate on one side of the PM edge, especially for the 12s/20p VPMSM. Moreover, the PM loss density distributions vary with different slot/pole number combinations.

For the 12s/8p non-overlapping winding FS SPMSM, PM loss at load conditions tends to accumulate in the center region of PMs, while for the overlapping winding 12s/20p VPMSM, PM loss at load conditions accumulates in the edge region of PMs. Detailed analysis of asymmetric PM loss distributions for SPMSMs accounting for different slot/pole number combinations will be elucidated in the following section using HRM.

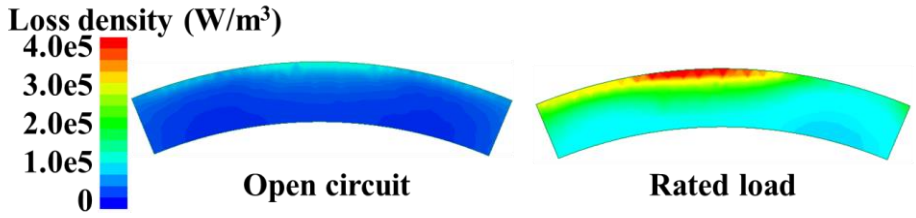

(a) 12s/8p.

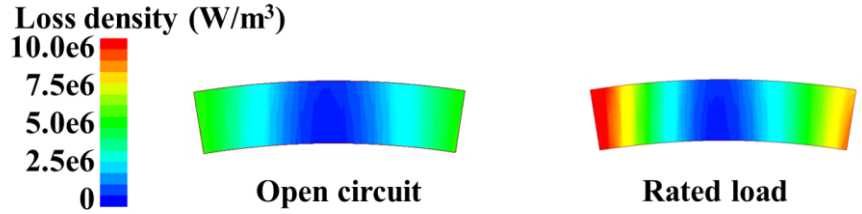

(b) 12s/20p.

Fig. 5.3. Average PM loss density distributions of 12s/8p and 12s/20p SPMSMs over one mechanical period.

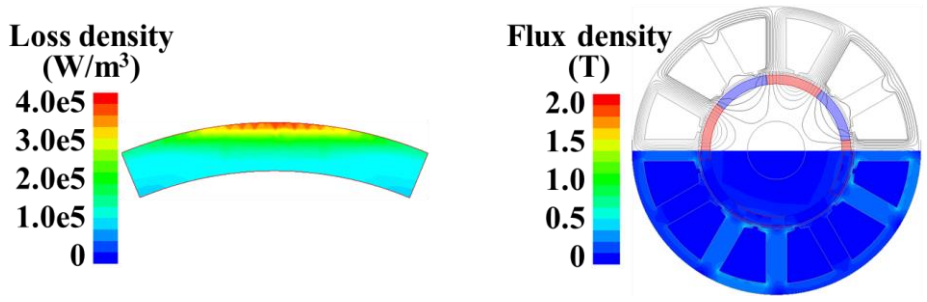

(a) 12s/8p.

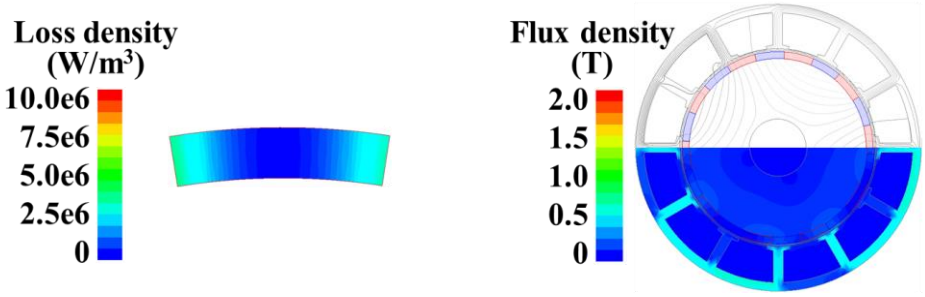

(b) 12s/20p.

Fig. 5.4. Average PM loss density distributions over one mechanical period of 12s/8p and 12s/20p SPMSMs caused by armature reaction only and corresponding magnetic field distributions.

5.4. Quantification of Effect of Armature Reaction Filed Harmonics to Asymmetric PM Loss Distributions Based on Harmonic Restoration Method

As aforementioned, the PM eddy current is induced by asynchronous field harmonics. In general, the relative speed ω_Δ between the *n-th* order asynchronous spatial harmonic caused by the armature reaction field and the synchronous electrical speed ω_r (the *m-th* order synchronous harmonic) can be calculated by:

$$\omega_\Delta = (1 \pm m/n)\omega_r \tag{5.1}$$

where "+" and "–" represent the same or the opposite rotating direction, respectively. By way of example, for the 12s/20p VPMSM, the asynchronous armature reaction field harmonics and corresponding rotating speeds include the 2nd ($-5\omega_r$) and the 14th ($-5\omega_r/7$), etc. Their relative speeds compared to the PM field speed (ω_r) are $6\omega_r$ and $12\omega_r/7$, respectively, which can be calculated by (5.1).

To quantify the contributions of individual armature reaction field harmonic in the PM loss distribution and illustrate the interaction effect between the armature reaction field and the PM field, the HRM is adopted, originally used to separate the torque components produced by the principle of magnetic gearing effect [ZHU18a]. In this study, the developed HRM is described below, consisting of five steps, where the 2nd order harmonic in 12s/20p VPMSM is taken as an example.

(1) The open-circuit PM loss is calculated, where the armature winding is removed, as shown in Fig. 5.5 (a).
(2) To obtain the individual armature reaction field harmonics before being modulated by stator slots, the three-phase windings are replaced by the corresponding thin ECSs on the surface of the stator slot opening. Meanwhile, the stator is replaced by a slotless magnetic steel cylinder, and PM excitation is removed, as shown in Fig. 5.5 (b).
(3) To quantify the contributions of individual armature reaction field harmonics on PM loss, e.g., the 2nd harmonic, the corresponding equivalent FEA model is built in Fig. 5.5 (c), where an equivalent thin PM layer is added at the inner stator radius as an outer rotor with corresponding speed. The PM layer is magnetized sinusoidally with the same

magnetization effect in both amplitude and phase as the corresponding armature reaction field harmonic in Step 2. Meanwhile, the rotor PMs are unmagnetized.

(4) Finally, to evaluate the interaction effect between the PM and the 2nd armature reaction field harmonic, the PMs are magnetized as shown in Fig. 5.5 (d).

(5) For other armature reaction field harmonics, the same procedure of (3) and (4) is performed.

For the PM loss caused by armature reaction, it is found that the 8th order armature reaction field harmonic contributes to the majority of the PM loss for 12s/8p SPMSM while that of 12s/20p VPMSM is the 2nd order armature reaction field harmonic as shown in Fig. 5.6. However, the influences of other armature reaction field harmonics, e.g., 16th and 20th for 12s/8p and 14th and 18th for 12s/20p, on the PM loss can be neglected (smaller than 5% in total). When only armature reaction field harmonics are considered, the resultant loss is distributed symmetrically to the circumferential center. However, when the interaction of the armature reaction field harmonics and PM field is considered, it will result in asymmetric distributions in the circumferential.

Meanwhile, considering the influence of the PM field, the average PM eddy current loss $\bar{P}_{i-\mathrm{pm}}$ caused by the individual armature reaction field harmonic (i^{th}) can also be calculated by (5.2) and (5.3).

$$\bar{P}_{i-\mathrm{pm}} = \iiint_V \bar{\rho}_{i-\mathrm{pm}}(r,\theta)dV \tag{5.2}$$

where $\bar{\rho}_{i-\mathrm{pm}}$ is the average PM loss density over one mechanical period considering the interaction of the i^{th} order armature reaction field harmonic and the PM field (see Fig. 5.6).

By subtracting to average open-circuit PM loss $\bar{P}_{\mathrm{oc-pm}}$ from $\bar{P}_{i-\mathrm{pm}}$ in (5.3), the contribution of i^{th} armature reaction field harmonic $\bar{P}_i$ to the total PM loss can be calculated while assuming the PM working point is unchanged when the armature field is applied.

$$\bar{P}_i = \bar{P}_{i-\mathrm{pm}} - \bar{P}_{\mathrm{oc-pm}} \tag{5.3}$$

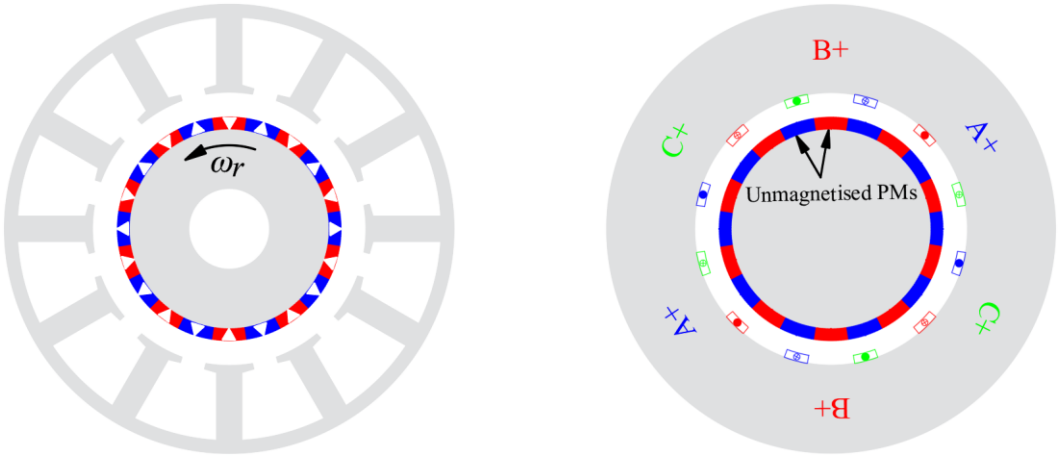

(a) Open-circuit. (b) ECS model.

(c) 2nd armature reaction field only. (d) PM and 2nd armature reaction field.

Fig. 5.5. PM loss separation with armature reaction field harmonic quantification based on HRM.

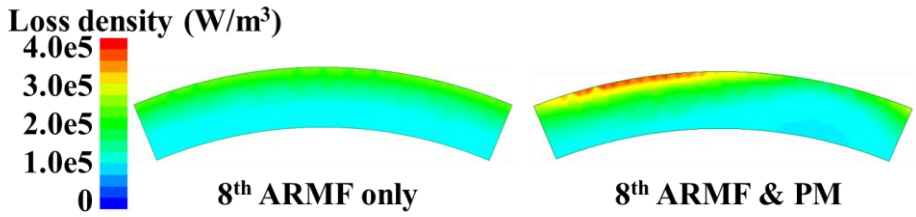

(a) 12s/8p.

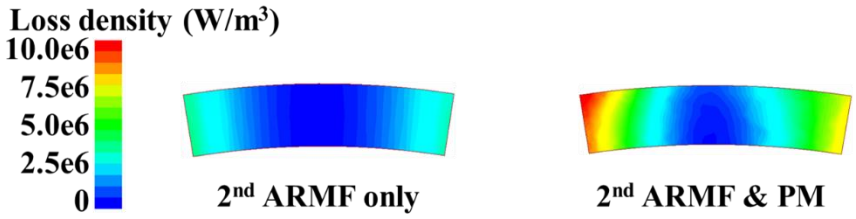

(b) 12s/20p.

Fig. 5.6. PM loss density distributions of 12s/8p and 12s/20p SPMSMs calculated by HRM (40 W copper loss and 5000 r/min).

5.5. Asymmetric PM Loss Distributions of SPMSMs Accounting for Different Slot/Pole Number Combinations

As analyzed earlier, the interaction of individual armature reaction field harmonic and the PM field contributes to the majority of the asymmetric PM loss for 12s/8p and 12s/20p SPMSMs. It can be inferred that different slot/pole number combinations also have a significant impact on PM loss distributions and resultant PM temperature distributions since their dominant asynchronous armature reaction field harmonics vary. Therefore, the HRM described in Section 5.4 is applied to 12-slot SPMSMs with different rotor pole numbers, i.e., 8-pole, 10-pole, 14-pole, 20-pole, and 22-pole.

According to (5.1), the main spatial harmonics of 12-slot SPMSMs are summarised in Table 5.1. By applying the HRM, the main spatial armature reaction field harmonics of all 12-slot SPMSMs can be determined. Under different amplitudes of currents and rotor speeds, contributions of the main armature reaction field harmonics and the PM field only (open-circuit) to on-load PM eddy current losses are compared with the total PM loss calculated by the FEA, as shown in Fig. 5.7.

As observed, although there are abundant field harmonics in the air-gap flux field, especially for 12-slot/20-pole and 12-slot/22-pole vernier SPMSMs [WU17], all 12-slot SPMSMs have their respective dominant armature reaction field harmonic, which contributes to the majority of PM eddy current loss. Specifically, it is the 8^{th} order for 8-pole, 7^{th} order for 10-pole, 5^{th} order for 14-pole, 2^{nd} order for 20-pole, and 1^{st} order for 22-pole.

However, other higher order harmonics have lower relative speed in (5.1), and thus, their influences on PM loss are minor. Meanwhile, with the increasing pole numbers, the proportion of open-circuit PM loss, i.e., caused by the PM field only accounting for the slotting effect, becomes more significant. Additionally, considering the interaction of the dominant armature reaction field harmonic and PM field for 12-slot SPMSMs, resultant asymmetric PM loss distributions are compared with the overall PM loss calculated by FEA in Fig. 5.8.

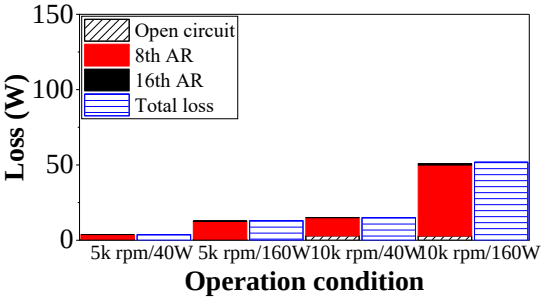

(a) 12s/8p.

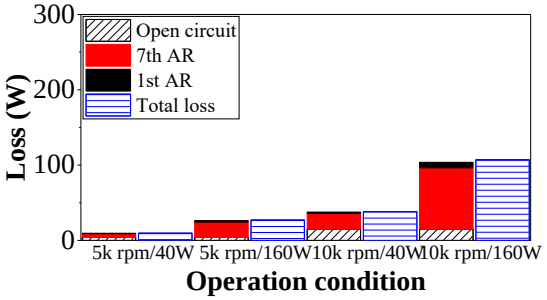

(b) 12s/10p.

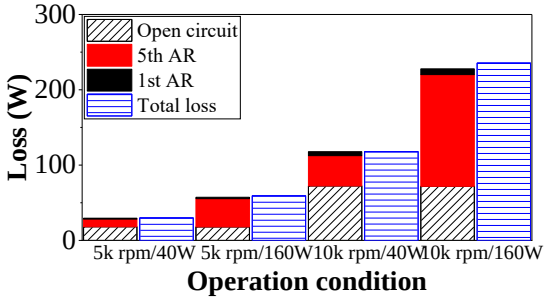

(c) 12s/14p.

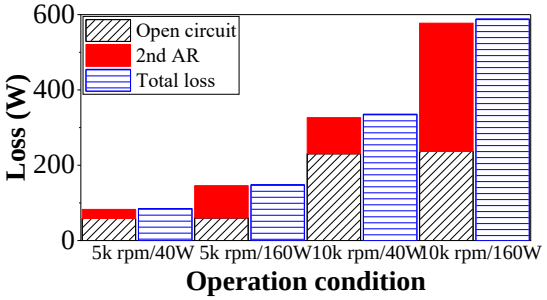

(d) 12s/20p.

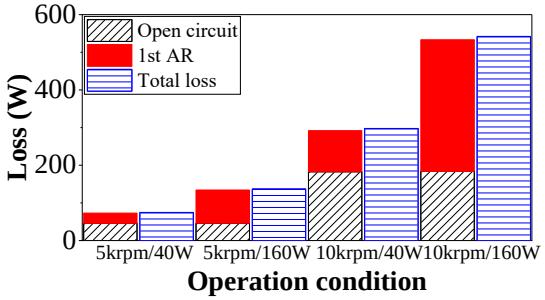

(e) 12s/22p.

Fig. 5.7. Average PM losses caused by main armature reaction field harmonic and PM field only (open-circuit) of 12-slot SPMSMs under different speeds and load conditions based on HRM.

Some important phenomena can be observed:

1. The interaction between the armature reaction and PM magnetic fields results in the asymmetric PM loss distribution.
2. Each SPMSM with different slot/pole number combinations exhibits one dominant armature reaction spatial harmonic contributing to the majority of PM loss.
3. The location of the maximum PM loss density in each PM pole shifts from the circumferential center towards the edge with increasing rotor pole numbers.
4. For the 12-slot/8-pole SPMSM, the 8th armature reaction field harmonic is dominant, which is larger than the fundamental component. Therefore, the PM loss density is more uniform in the circumferential direction, and the maximum loss density approximately occurs in the center.

5. For 14-/20-/22-pole SPMSMs, the PM eddy current loss is mainly caused by the lower-order armature reaction field harmonics. The maximum PM loss density tends to concentrate on the edge, especially for 20-pole and 22-pole VPMSMs, which are mainly caused by the 2nd and 1st armature reaction field harmonics.

Table 5.1 Summary of Main Spatial Harmonics of 12-slot 8-/10-/14-/20-/22-pole SPMSMs

Harmonic order	8-pole	10-pole	14-pole	20-pole	22-pole
1	-	$-5\omega_r$	$7\omega_r$	-	$-11\omega_r$
2	-	-	-	$-5\omega_r$	-
4	ω_r	-	-	-	-
5	-	ω_r	$-7\omega_r/5$	-	-
7	-	$-5\omega_r/7$	ω_r	-	-
8	$-\omega_r/2$	-	-	-	-
10	-	-	-	ω_r	-
11	-	$5\omega_r/11$	$-7\omega_r/11$	-	ω_r
13	-	$-5\omega_r/13$	$7\omega_r/13$	-	$-11\omega_r/13$
14	-	-	-	$-5\omega_r/7$	-
16	$\omega_r/4$	-	-	-	-
17	-	$5\omega_r/17$	$-7\omega_r/17$	-	-
19	-	$-5\omega_r/19$	$7\omega_r/19$	-	-

: Working harmonics. : Dominant armature reaction field harmonic.

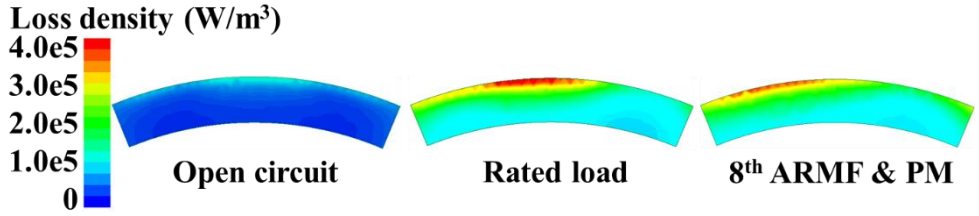

(a) 12s/8p.

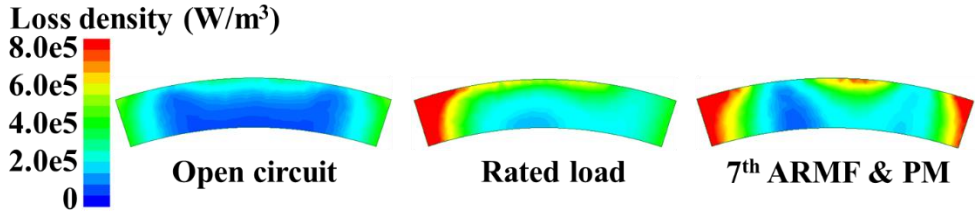

(b) 12s/10p.

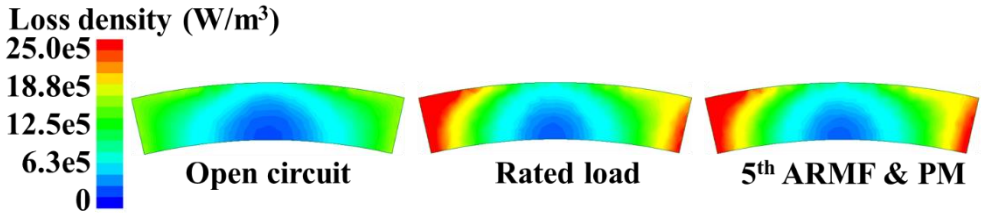

(c) 12s/14p.

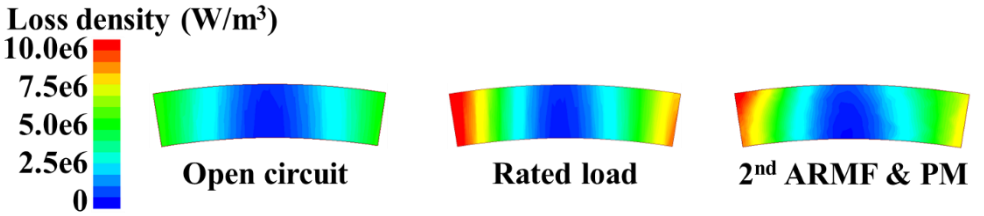

(d) 12s/20p.

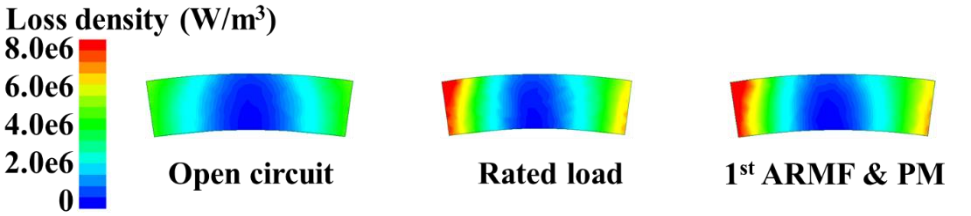

(e) 12s/22p.

Fig. 5.8. Asymmetric PM loss distribution under open-circuit condition, rated-load condition, and interaction of main armature reaction field harmonic with PM field accounting for slot/pole number combinations.

5.6. Analysis of Asymmetric PM Temperature Distributions

To investigate the PM temperature rise caused by asymmetric PM loss for all 12-slot SPMSMs, the corresponding 3-D FEA thermal models are built, where all machines are totally enclosed and equipped with the forced-air cooling system on the outer surface of the frame. To satisfy the critical thermal limits of the F-class winding insulation [ANS16] and N35SH PMs [EMAonline], of which maximum allowable temperatures are set at 155℃ and 150℃, respectively. The convection HTCs for the outer surface of the frames are set as 100 W/(m^{2}K) for all SPMSMs, which are selected in the range of typical forced air cooling conditions, as detailed in [ZHE22].

Under the copper loss of 40 W at 5000 r/min, the main machine losses are shown in Fig. 5.9, where the iron loss is calculated by the three-term model [BER88] via FEA.

$$P_{\text{iron}} = k_h f B_m + k_{ec} f^{1.5} B_m^{1.5} + k_{ex} f^2 B_m^2 \tag{5.4}$$

where k_h, k_{ec}, and k_{ex} are the iron loss coefficients for hysteresis loss, eddy current loss, and excess loss, respectively. f and B_m are the fundamental electrical frequency and the maximum flux density, respectively.

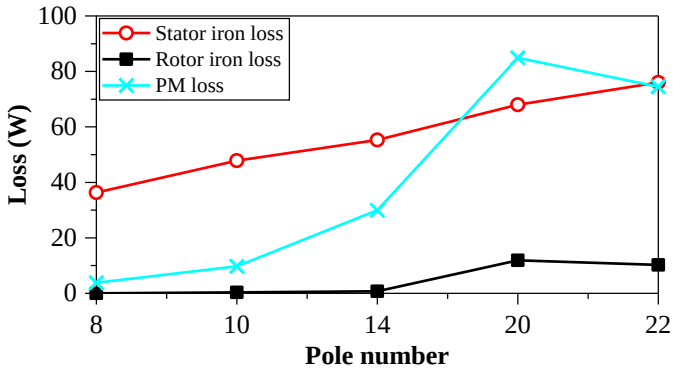

Fig. 5.9. Average iron loss and PM loss of SPMSMs under 40 W copper loss at 5000 r/min.

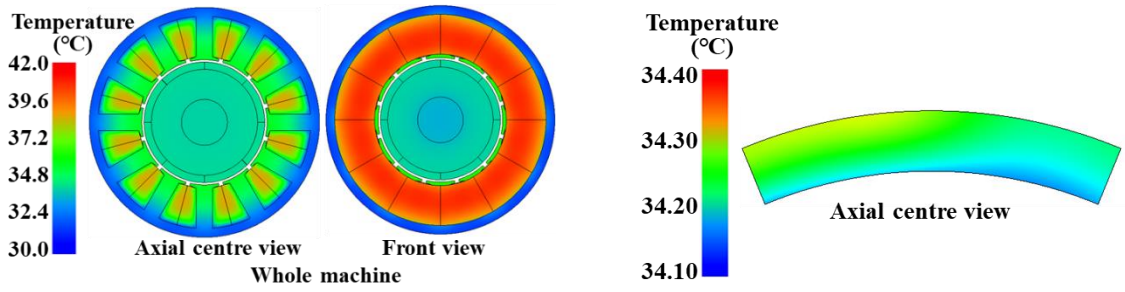

(a) 12s/8p.

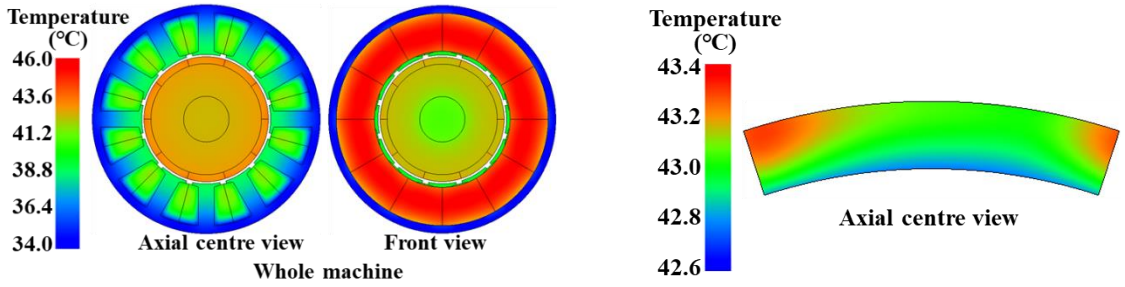

(b) 12s/10p.

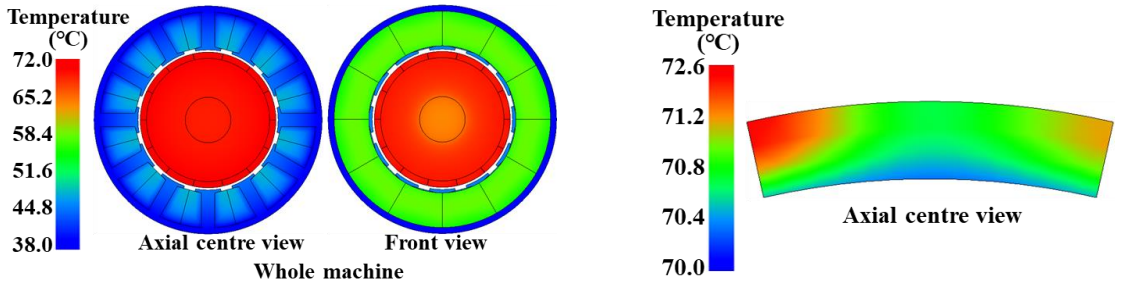

(c) 12s/14p.

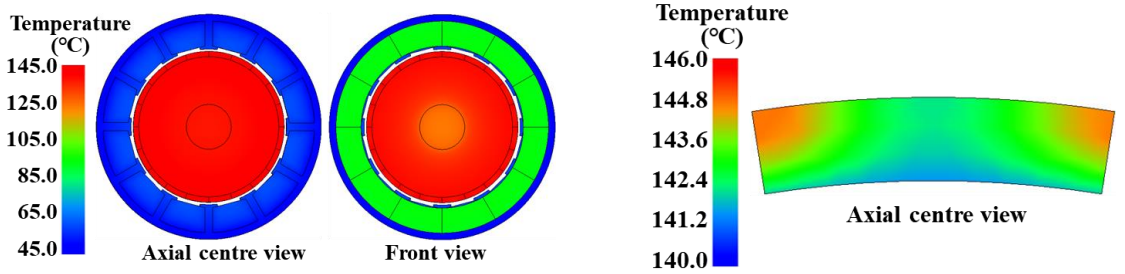

(d) 12s/20p.

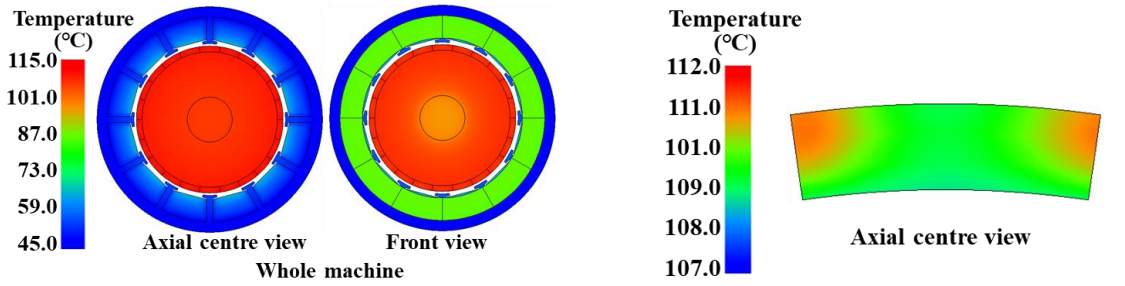

(e) 12s/22p.

(i) Entire machine. (ii) PM only.

Fig. 5.10. Steady-state temperature distributions of entire 12-slot SPMSMs and PMs.

For all five 12-slot SPMSMs, their steady-state temperature distributions of the entire machines and PMs are shown in Fig. 5.10. Several phenomena can be observed:

1. The PM hotspots for SPMSMs always occur at the outer surface due to convection heat transfer when PMs are not retained by a rotor sleeve.
2. Hotspot locations of SPMSMs vary with pole numbers and show consistent trends with PM loss density distributions, which are strongly affected by the interaction of the respective dominant armature reaction field harmonic and the PM field.
3. More specifically, for the 8-pole SPMSM, the hotspot is located near the circumferential center of the PM, while for 10-pole and 14-pole SPMSMs, hotspots tend to move to the edge of the PM. For 20-pole and 22-pole vernier machines, hotspots are concentrated at the edge of PMs.
4. Due to higher PM losses in 20-pole and 22-pole vernier machines, the PM temperature differences between outer surface and inner surface within one PM pole are more significant, the temperature difference is 4~7℃ under 40 W copper loss and 5000 r/min.

5.7. Experimental Verification

The 12s/8p and 12s/20p SPMSMs are manufactured and tested to verify the analysis and FEA results. Fig. 2.38 shows the stators and rotors (NSP) of the prototypes. Table 2.6 shows the key parameters of prototypes.

The results of electromagnetic tests are shown in Section 2.5, where the measured and FEA predicted results match well and verify the FEA analyses.

The static DC test as shown in Fig. 5.11 is carried out, where the PMSMs are cooled naturally with an ambient temperature of 20℃. The three-phase windings are connected in parallel and excited by a DC power supply with 30 W copper loss in the steady-state DC test and the positions of thermal couples are shown in Fig. 5.11 (b). By minimizing the errors between the measured and FEA predicted results, the uncertain thermal parameters can be determined, as listed in Table 5.2, including HTC of the frame to ambient, the thickness of the gap between the frame and stator core, and the thickness of the gap between stator lamination and windings, which will be applied to the 3-D FEA thermal models.

Besides, the 3-D FEA thermal model is validated by another dynamic thermal test. The test platform is shown in Fig. 5.12. The temperatures of the frame, the stator tooth, the stator yoke,

the active winding, and the end winding are measured by inserted thermal couples and recorded by a data logger as shown in Fig. 5.11. The temperatures of PM and end winding surface can be measured through a thermal imager through the measurement window in the end cap of the prototype as shown in Fig. 5.12.

Table 5.2 Uncertain Thermal Parameters after Calibration

	8-pole	**20-pole**
HTC (frame - ambient)	16	16
Gap (frame -stator core)	0.18 mm	0.1 mm
Gap (stator - winding)	0.3 mm	1 mm

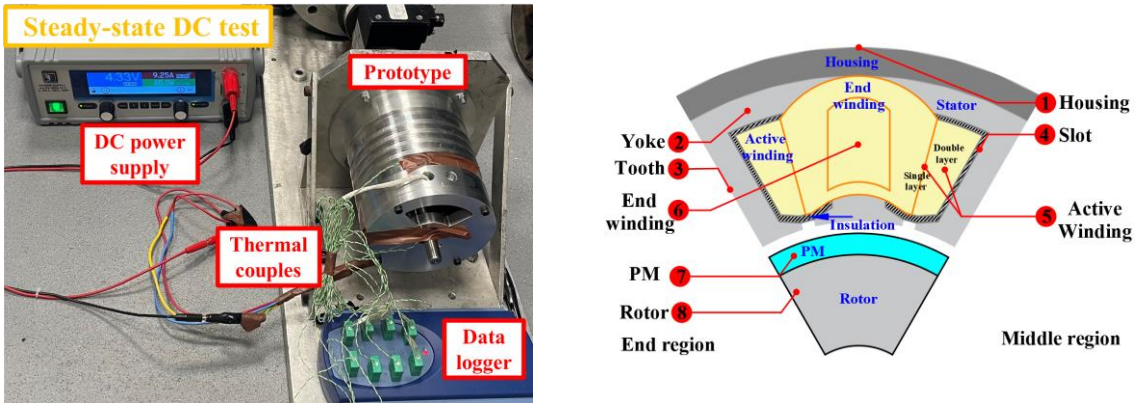

(a) Test rig for steady-state DC test. (b) Positions of thermal couples.

Fig. 5.11. Test rig for steady-state DC test and positions of thermal couples.

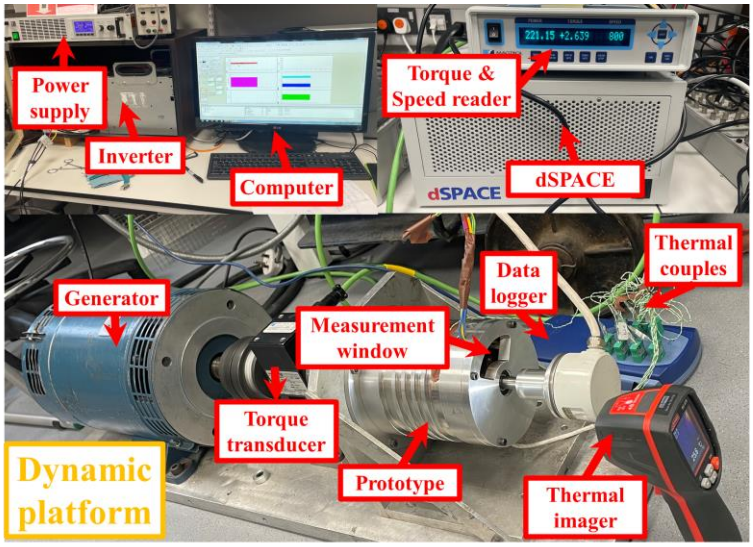

Fig. 5.12. Dynamic test platform for temperature distribution.

Operating conditions and corresponding loss distributions of two prototypes are shown in Table 5.3 with 20℃ initial room temperature. Fig. 5.13 shows the FEA predicted and measured temperatures of two prototypes. The asymmetric PM temperature distribution is more significant in the axial center of the machine, which is difficult to measure directly due to the rotating rotor and small air-gap. Therefore, the measured results are used to validate the employed FEA model, which shows a good agreement. At steady state, measured end-winding (EW) and PM temperatures through a thermal imager are 54.4℃ and 39.1℃ for 12s/8p and 98.9℃ and 61.4℃ for 12s/20p, which are close to FEA predicted temperatures on the axial end-surface. Measured and FEA predicted temperature comparison is shown in Table 5.3 and Fig. 5.13 (f). The errors are kept within 4℃.

Table 5.3 Operating Condition, Loss, and Temperature Distribution

	8-pole		**20-pole**	
Torque and speed	3.02 Nm / 800 r/min		2.64 Nm / 800 r/min	
Copper loss	26 W		46 W	
Stator / Rotor iron loss	3.72 W / 0.01 W		3.90 W / 0.16 W	
PM loss	0.07 W		1.31 W	
Mechanical loss [XUE17]	1.25 W		1.25 W	
Temperature (℃)	FEA	Test	FEA	Test
Frame	36	36	47	48
Yoke	44	45	54	55
Tooth	48	49	65	66
Coil (thermal couple)	53	54	111	107
EW (thermal couple)	54	55	115	112
EW (thermal imager)	53	54	97	99
PM (thermal imager)	41	39	59	61

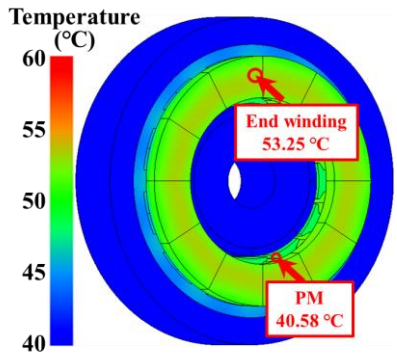

(a) FEA predicted (12s/8p).

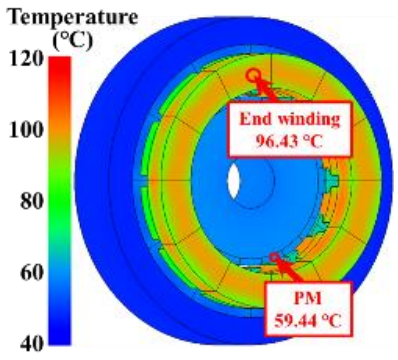

(b) FEA predicted (12s/20p).

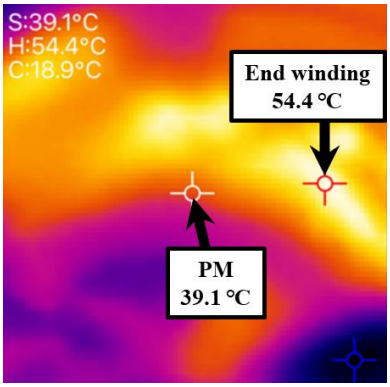

(c) Measured by thermal imager (12s/8p).

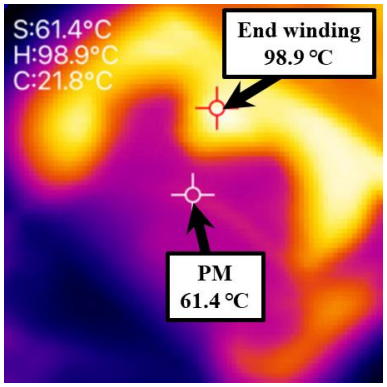

(d) Measured by thermal imager (12s/20p).

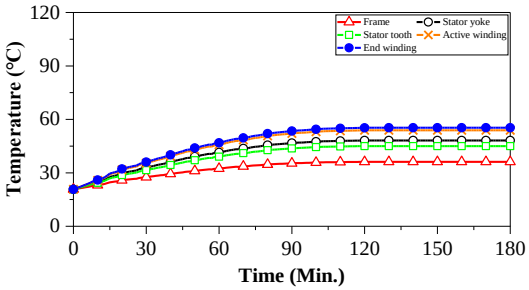

(e) Measured by thermal couples (12s/8p).

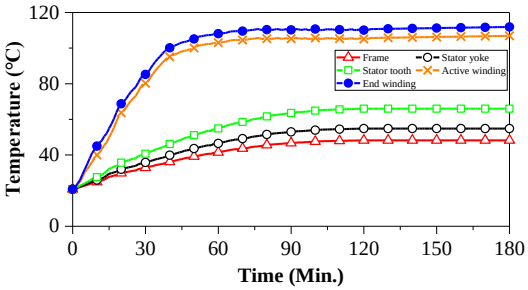

(f) Measured by thermal couples (12s/20p).

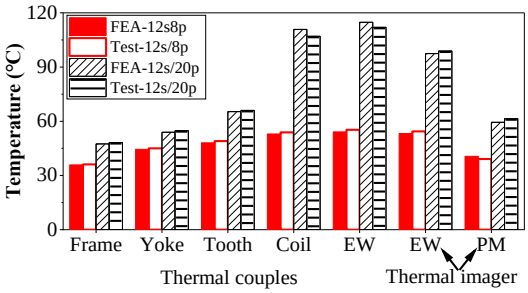

(g) FEA predicted and measured comparison.

Fig. 5.13. 3-D thermal FEA predicted and measured temperature distributions of prototypes.

5.8. Summary

This chapter has revealed the mechanisms of asymmetric PM eddy current loss and resultant temperature distributions for the first time. By utilizing the harmonic restoration method, the contributions of individual armature reaction field harmonics, with and without PM fields, to the on-load PM eddy current loss can be evaluated and quantified individually and/or collectively, where 12-slot SPMSMs with different slot/pole number combinations are used for illustration.

It has been demonstrated that:

1. Each 12-slot SPMSM with different pole numbers exhibits a respective dominant armature reaction field harmonic contributing to the majority of PM loss.
2. The open-circuit PM loss is symmetrically distributed along the circumferential direction. However, the on-load PM loss exhibits asymmetric distribution, primarily due to the interaction between the dominant armature reaction field harmonic and the PM field.
3. The PM losses induced by lower order armature reaction field harmonics tend to concentrate on the edge of the PMs.
4. With the increasing pole numbers, the maximum PM loss densities for 12-slot SPMSMs shift from circumferential centers toward PM edges.
5. Hotspot locations of PMs vary with slot/pole number combinations and show consistent trends with PM loss density distributions.

Two prototypes, i.e., the 12-slot/10-pole PMSM and 12-slot/20-pole VPMSM, are manufactured and tested to validate the analysis based on electromagnetic and thermal tests.

CHAPTER 6
ASYMMETRIC PM LOSS AND TEMPERATURE DISTRIBUTIONS IN V-SHAPE INTERIOR PM SYNCHRONOUS MACHINES

As investigated in the previous chapter, PM loss and temperature distributions in SPMSMs exhibit asymmetric distributions due to the interaction between the armature reaction and PM fields. This chapter investigates the effect of armature reaction on asymmetric PM loss and temperature distributions in a double-layer V-shape IPMSM for EVs. The LPTM and analytical methods are established to predict the average temperature distribution and identify the hotspot in the winding. The 2-D FEA is used to calculate PM eddy current loss distributions, and the results reveal that the phase currents with different current advancing angles produce different armature reaction effects, leading to asymmetric PM eddy current loss distribution. Afterward, the PM and iron loss densities are coupled into the 3-D thermal FEA model to investigate the temperature distributions, especially the asymmetric PM temperature distribution. The asymmetric PM temperature distributions show consistent trends with the asymmetric PM loss distributions.

This chapter has been presented at the 2022 Second International Conference on Sustainable Mobility Applications, Renewables and Technology (SMART 2022):

[ZHE22] Y. Zheng, D. Liang, Z. Q. Zhu, H. Liu, and Y. Zhou, "Effect of armature reaction on asymmetric PM loss and temperature distributions in V-shape interior permanent magnet synchronous machines," in *2nd Int. Conf. Sustain. Mobility Appl., Renew. Tech.* (SMART), 2022, pp. 1-10.

6.1. Introduction

IPMSMs are widely employed in electric vehicles, aerospace, domestic appliances, wind power generators, etc. [ZHU07] [PEL12] [ZHU18b]. Although PM eddy current loss accounts for a negligible proportion in IPMSMs and can usually be neglected in terms of efficiency, it should be considered when the machine operates at high speed, under high electric loading, or with PWM supply [ZHU04] [ISH05] [CHE17] [TON22] [HON19] [TON21]. Due to the poor heat dissipation condition of rotor PMs, higher PM loss may lead to higher temperature rise and even irreversible demagnetization. Therefore, it is important to analyze the PM eddy current loss and its effect on thermal conditions.

The PM eddy current loss and temperature distributions of IPMSMs have been investigated in several studies [KAW00] [KAM07] [NAI16] [ZHU18b] [TON18] [TON21]. The 3-D eddy current loss in IPMSM considering PWM carrier harmonics is investigated in [KAW00]. The results show that the transient PM eddy current loss density distributions vary significantly with rotor rotation position and armature MMF. It reveals that the PM loss density and temperature near the air-gap are higher, especially at the edge of the PM ahead of the rotating direction [KAM07]. A computationally efficient method based on imaging techniques has been proposed to accurately predict the 3-D PM eddy current loss in IPMSMs, and the PM losses generated by different armature current harmonics are separated by using the frozen permeability technique [NAI16]. The PM loss distributions of multi-layer IPMSMs with different PM configurations are compared in [ZHU18b], and the results show that the PM loss tends to accumulate at the edge of the PMs. The PM loss and temperature distributions of IPMSMs with different slot-pole number combinations under sinusoidal or converter supply at various speeds and with different converter parameters are analyzed in [TON18] [TON21]. The PM loss and temperature under the PWM converter supply are much higher than those under the sinusoidal current supply. However, the reasons for PM loss and temperature distributions are not investigated and analyzed in depth, especially the effect of armature reaction with different current advancing angles on asymmetric distributions of PM eddy current loss and temperature in IPMSMs. In this chapter, the influences of armature reaction on asymmetric PM eddy current loss distributions and the corresponding effect on PM temperature distributions in a double-layer V-shape ISDW IPMSM for electric vehicles are studied.

The main contributions of this chapter can be summarized as follows:

1. The effect of armature reaction on the asymmetric distributions of PM eddy current loss and temperature in a double-layer V-shape IPMSM is investigated.
2. The maximum temperature difference between the left- and right-side PMs on one pole is about 9℃ at 15000 r/min with sinusoidal current supply and around 30° current advancing angle.

This chapter is organized as follows. Firstly, the machine topology and electromagnetic performance of a double-layer V-shape ISDW IPMSM for electric vehicles are presented in section 6.2. Then, the influence of armature reactions on asymmetric PM eddy current loss distributions is investigated in section 6.3. Afterward, the calculation of HTCs and establishment of thermal models including LPTM, analytical method, and 3-D FEA thermal model, are presented in section 6.4. Furthermore, temperatures calculated by different thermal models are compared, and the influence of asymmetric PM loss distributions caused by armature reactions on asymmetric PM temperature distributions is investigated by using the 3-D FEA model in section 6.5. The PM loss and temperature distributions in small-size SPMSMs and IPMSMs are compared in section 6.6. Finally, this chapter is concluded in section 6.7.

6.2. Machine Topologies

The machine topology of the 48-slot/8-pole double-layer V-shape ISDW IPMSM is shown in Fig. 6.1. The main geometric parameters are listed in Table 6.1. The open-circuit flux lines, magnetic flux density, and PM eddy current loss distributions under 5000 r/min are shown in Fig. 6.2.

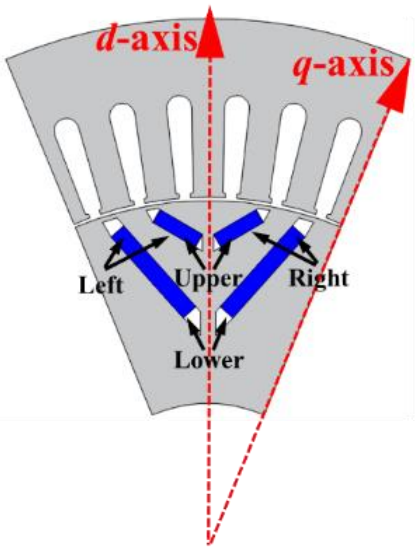

Fig. 6.1. 48-slot/8-pole double-layer V-shape ISDW IPMSM.

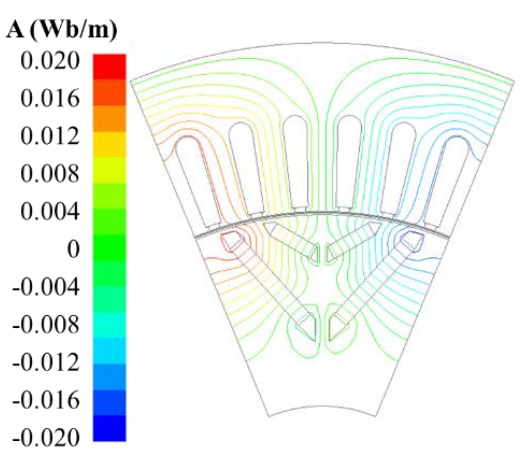

(a) Flux lines.

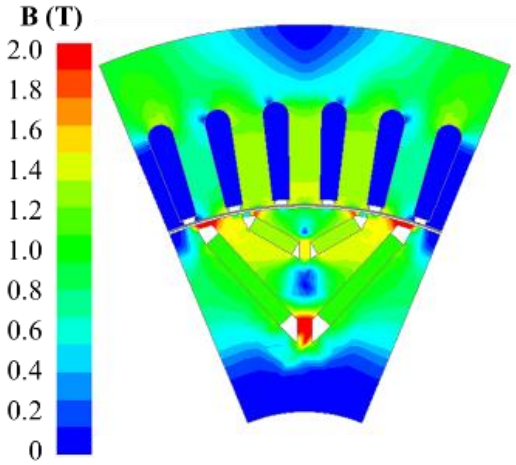

(b) Magnetic flux density.

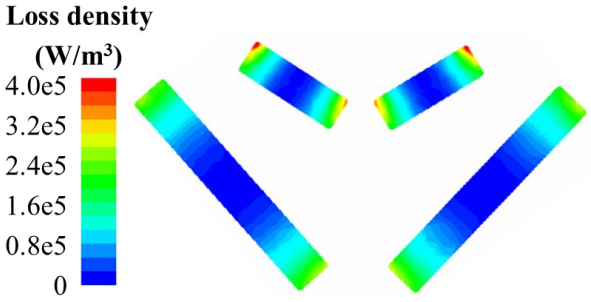

(c) PM eddy current loss distribution.

Fig. 6.2. Open-circuit flux lines, magnetic flux density, and PM eddy current loss distributions.

Table 6.1 Main Geometric Parameters

Symbol	Parameters	Unit	Value
N_s	Number of stator slots	-	48
$2p$	Number of poles	-	8
d_{so}	Stator outer diameter	mm	216
l_{fe}	Lamination stack length	mm	116
N_{ph}	Coils per slot	-	8
δ	Air-gap length	mm	0.7
B_r	PM remanence	T	1.2
μ_r	PM relative permeability	-	1.05

6.3. Asymmetric PM Eddy Current Loss Distribution

To analyze the effect of armature reaction on PM eddy current loss, the phasor diagram of the EV machine is shown in Fig. 6.3, where i_s, i_d, i_q, and Ψ_{PM} are the stator armature current, the *d*-axis current, the *q*-axis current, and the PM flux linkage, respectively. The *d*-axis is located along the central axis of each pole, while the *q*-axis is 90 electrical degrees ahead of the *d*-axis. The current advancing angle (β) is the angle between i_s and i_q.

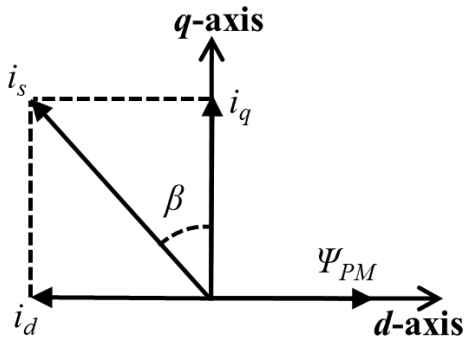

Fig. 6.3. Phasor diagrams of the EV machine.

The average PM eddy current losses under different current advancing angles and speeds are shown in Fig. 6.4. The relationship between PM eddy current loss and current advancing angle exhibits the same trend under different speeds, increasing first and then decreasing with the increase of current advancing angle.

The average PM eddy current loss density distributions under one electrical cycle with different current advancing angles and speeds are shown in Fig. 6.5. The PM loss density of the left-side PMs is higher than that of the right-side PMs, except for the 90° current advancing angle, especially when the current advancing angle is about 30°.

According to Fig. 6.6, the armature reaction field travels through the *q*-axis with minimum magnetic reluctance when the current advancing angle equals 0°, primarily through the iron and having a negligible effect on PM loss and asymmetric PM loss density distribution. When the current advancing angle increases, the magnetic reluctance for the armature reaction field slightly increases as shown in Fig. 6.6 (b). However, more armature reaction fields will travel through the PMs, resulting in higher PM eddy current loss, especially in the left-side PMs. While further increasing the current advancing angle, the magnetic reluctance for the armature reaction field increases significantly as shown in Fig. 6.6 (c), resulting in a decrease in PM loss.

When the current advancing angle equals 90°, the armature magnetic field travels through the *d*-axis with maximum magnetic reluctance, leading to a reduction in PM loss.

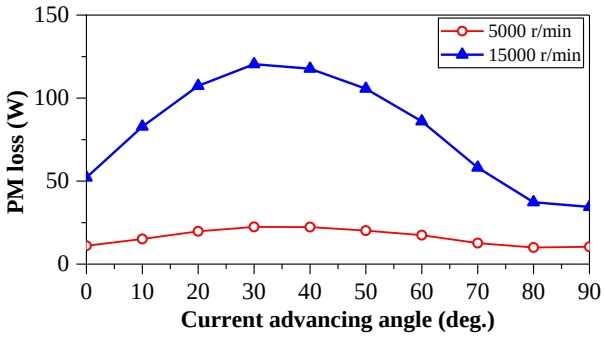

Fig. 6.4. Average PM eddy current loss under different current advancing angles and speeds.

6.4. Thermal Modelling

6.4.1. Heat transfer coefficients

Convection HTCs of different interface regions in an electrical machine are crucial and need to be determined for thermal analysis. Empirical rules are often used to calculate the HTCs [MEL91] [KYL95] [BOG08] [LIA19]. The convection and conduction heat transfers within electrical machines are illustrated in Fig. 6.7. The oil flows of the entire cooling structure are illustrated in Fig. 6.8.

Convection HTCs are calculated by the following equations, where *Nu*, *Re*, *Pr*, *Gr*, and λ are the Nusselt number, the Reynolds number, the Prandtl number, the Grashof number, and the thermal conductivity, respectively.

$$Nu = f(Re, Pr, Gr, \dots) = hL/\lambda \tag{6.1}$$

$$h_{Convection} = Nu\ \lambda/L \tag{6.2}$$

The convection thermal resistance is calculated by:

$$R = \frac{1}{hS} \tag{6.3}$$

where *S* is the area of the convection surface.

The HTC between the frame/end-cup and inner air is:

$$h = k_1 + k_2 \times v^{k_3} \tag{6.4}$$

where v is the rotor peripheral velocity (m/s), k_1=15, k_2= $6.75^{0.65}$, and k_3= 0.65.

The HTC between the rotor/end winding and inner air is:

$$h = 15.51 + 4.495v \tag{6.5}$$

The modified Taylor number Ta_m [BEC62] is used to calculate the air-gap HTC.

$$Ta_m = \frac{\omega^2 r_g \delta^3}{\mu_A^2} \tag{6.6}$$

where δ is the airgap length, r_g is the average airgap radius, and μ_A is the air kinematic viscosity.

Then, the Nusselt number (Nu) can be determined.

$$\begin{array}{ll} Nu = 2 & Ta_m < 1700 \\ Nu = 0.128 Ta_m^{0.367} & 1700 < Ta_m < 10^4 \\ Nu = 0.409 Ta_m^{0.241} & 10^4 < Ta_m < 10^7 \end{array} \tag{6.7}$$

Thus, the stator and rotor film coefficient $h_{s,r}$ can be computed by

$$h_{s,r} = \frac{Nu \lambda_{air}}{2\delta} \tag{6.8}$$

The stator is cooled by a water jacket. The HTC for oil flowing through the channels can be calculated [NAT13]. The Nusselt number for laminar flow in a rectangular channel can be computed by

$$Nu = 7.49 - 17.02(\frac{H}{W}) + 22.43(\frac{H}{W})^2 - 9.44(\frac{H}{W})^3 + (\frac{0.065 RePrD_H/L_{Ch}}{1 + 0.04(RePrD_H/L_{Ch})^{2/3}}) \tag{6.9}$$

where H/W is the ratio of channel height to width, D_H is the hydraulic diameter of the channel, and L_{Ch} is the length of each cooling channel. The property of ATF oil is listed in Table 6.2.

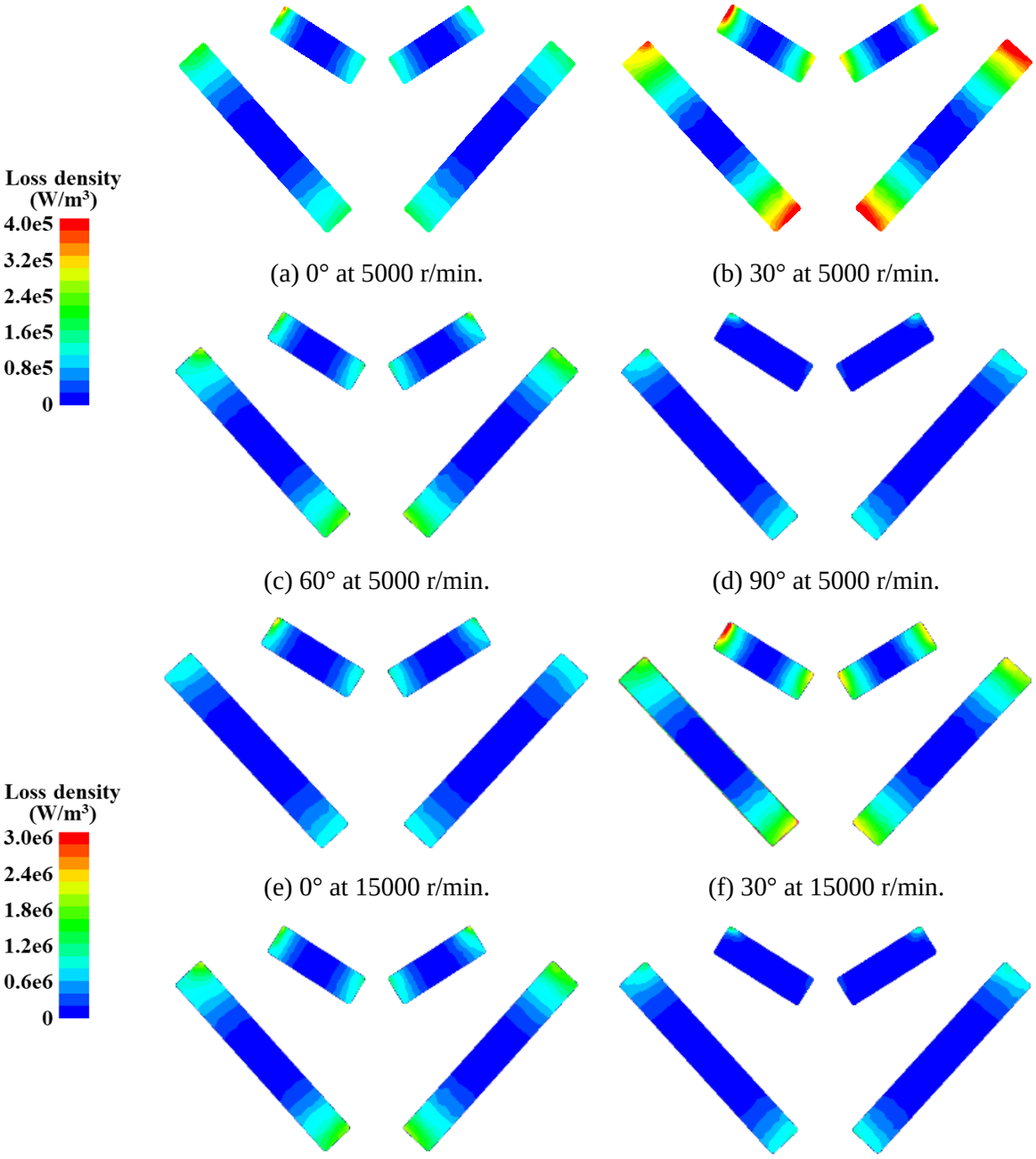

Fig. 6.5. PM eddy current loss density distributions with different current advancing angles and speeds.

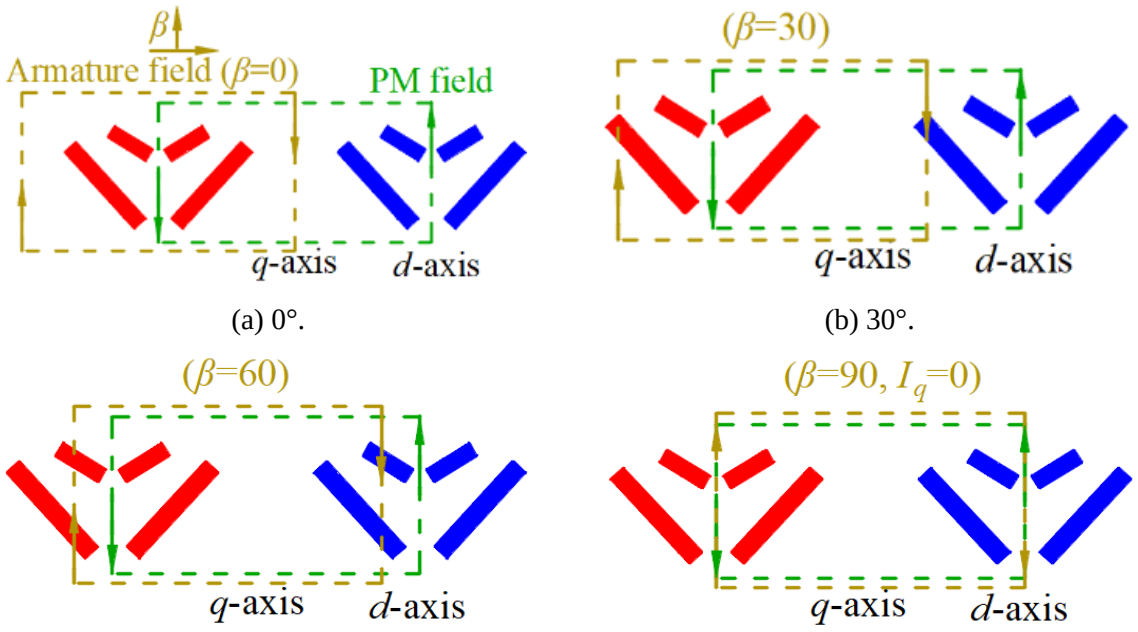

(a) 0°. (b) 30°.

(c) 60°. (d) 90°.

Fig. 6.6. Interaction between PM magnetic field and armature reaction field under different current advancing angles.

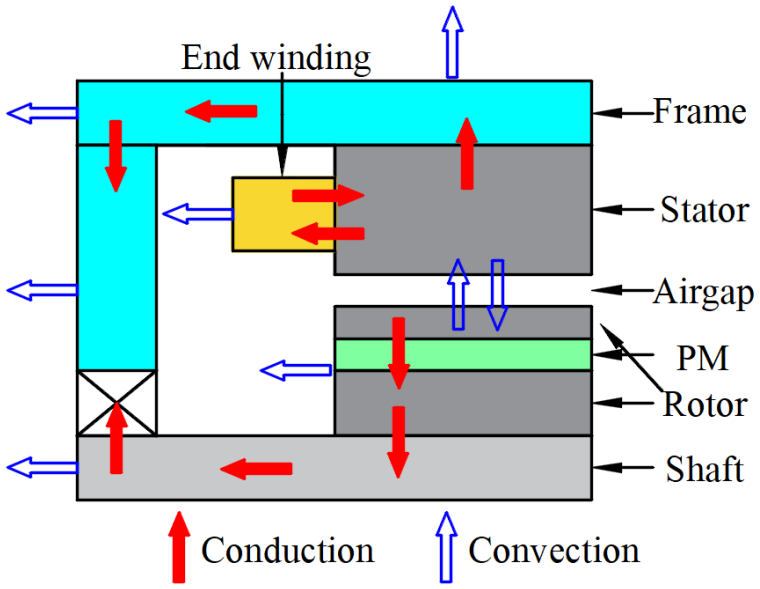

Fig. 6.7. Heat transfer within the IPMSM under natural cooling.

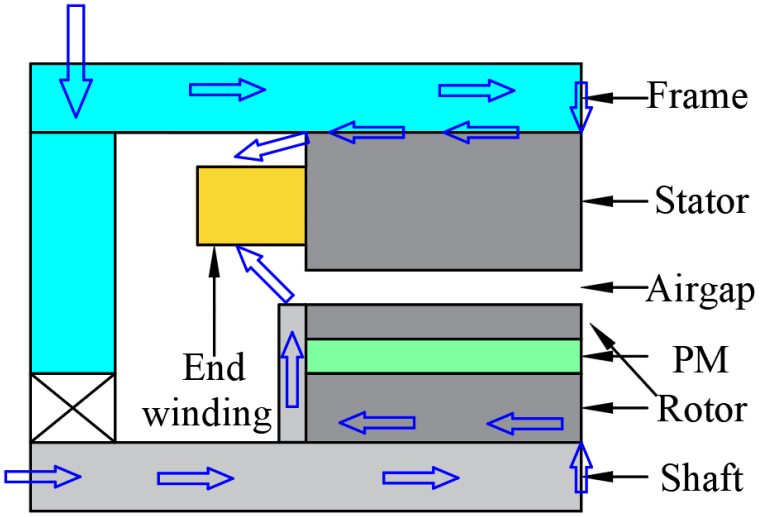

Fig. 6.8. Oil channels of cooling structure.

Table 6.2 Property of ATF Oil

Physical properties	Value
Density, ρ	792 kg/m^3
Specific heat, C_p	2237 J/kg•K
Thermal conductivity, λ	0.135 W/m•K
Dynamic viscosity, μ	0.00392 Pa•s

The oil flowing through the stator will then reach the upper surface of the end winding. The HTC of the upper surface of the end winding can be calculated based on the Reynolds number and the Prandtl number of the liquid [NAT13].

$$Nu = 0.664 Re^{1/2} Pr^{1/3} \tag{6.10}$$

The lower surface of the end winding is cooled by a jet impingement system. The ATF oil is injected into the shaft and then sprayed onto the end winding from four nozzles located on both sides of the shaft. The HTC of the lower surface of the end winding can be calculated based on [GAI18].

$$Nu = 0.745 Re^{1/2} Pr^{1/3} \tag{6.11}$$

The Prandtl number of the ATF is calculated as:

$$Pr = \frac{C_p \mu}{\lambda} \tag{6.12}$$

The Reynolds number is calculated as:

$$Re = \frac{\rho v d}{\mu} \tag{6.13}$$

where d is the diameter of the nozzle and v is the axial velocity at the jet nozzle.

The HTC for shaft can be calculated according to [LU20]:

$$Nu = \frac{f}{8} \frac{(Re_a - 1000)Pr}{1 + 1.27\left(\frac{f}{8}\right)^{0.5}(Pr^{\frac{2}{3}} - 1)} \tag{6.14}$$

where

$$f = (0.79\ln(Re_a) - 1.64)^{-2} \tag{6.15}$$

6.4.2. Lumped parameter thermal model

According to the previous analysis, the average PM loss and loss density distribution vary with the current advancing angle. The effect of asymmetric PM loss distribution on temperature distributions will be investigated.

At first, the T-type LPTM is established to analyze the thermal condition of the IPMSM [WRO10] [SIM14]. Different parts of the machine can be simplified into arc-segment elements (stator yoke, slot, rotor, and shaft) or cuboidal elements (stator teeth and PMs). The LPTMs for the arc-segment element and cuboidal element are shown in Fig. 6.9.

T_r, T_a, T_c, T_x, T_y, and T_z are the average temperatures of corresponding nodes in different directions, i.e., radial, axial, circumferential, x-axial, y-axial, and z-axial directions, respectively. R_r, R_a, R_c, R_x, R_y, and R_z are the corresponding thermal resistances.

As the winding region consists of conductor, insulation, and impregnation, the H+S approximation is used to model the winding with anisotropic thermal conductivities for simplicity [HAS62] [SIM13]. The thermal conductivities of axial (λ_a) and circumferential (λ_c) directions are calculated by (6.16) and (6.18).

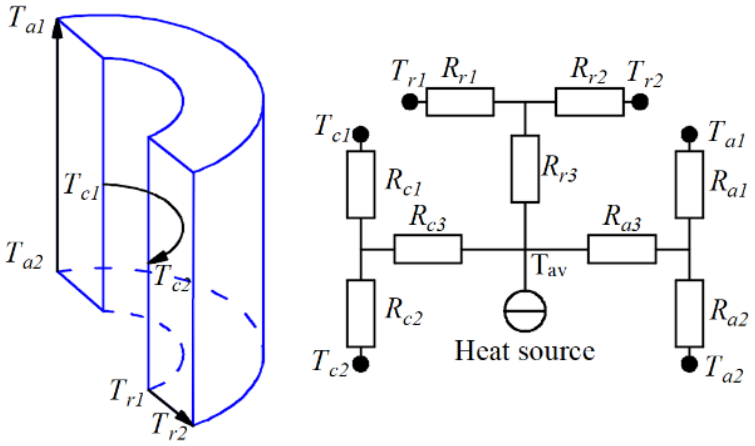

(a) LPTM for arc-segment element.

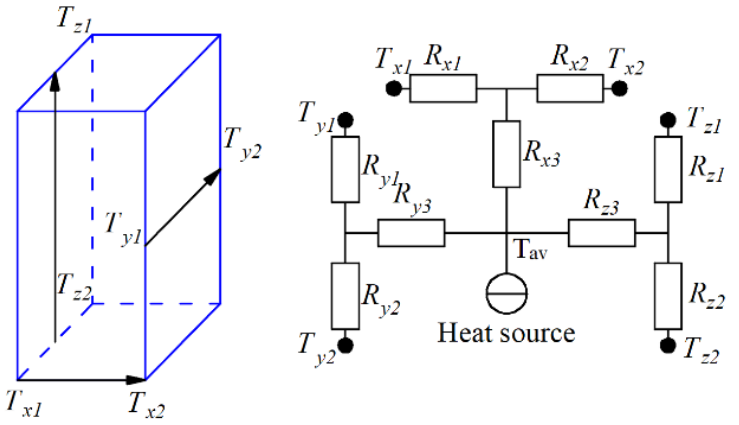

(b) LPTM for cuboidal element.

Fig. 6.9. LPTM models for arc-segment element and cuboidal element.

$$\lambda_a = v_{co}\lambda_{co} \tag{6.16}$$

$$\lambda_{coci} = \lambda_{ii}\frac{v_{ii}}{v_{ii}+v_{ci}} + \lambda_{ci}\frac{v_{ci}}{v_{ii}+v_{ci}} \tag{6.17}$$

$$\lambda_c = \lambda_{coci}\frac{(1+v_{co})\lambda_{co} + (1-v_{co})\lambda_{coci}}{(1-v_{co})\lambda_{co} + (1+v_{co})\lambda_{coci}} \tag{6.18}$$

where v_{co}, v_{ci}, and v_{ii} are the slot filling factor of the conductor, conductor insulation, and impregnation insulation, respectively. λ_{co}, λ_{ci}, λ_{ii}, and λ_{coci} are the thermal conductivity of the conductor, conductor insulation, impregnation insulation, and conductor with insulation, respectively.

The simplified geometry can be used to calculate the thermal network of the multi-layer IPM rotor [REF04]. The simplified rotor geometry is shown in Fig. 6.10 (a), and the corresponding LPTM is shown in Fig. 6.10 (b), where the rotor is simplified into multi-layer cylinders while the PMs are still rectangles.

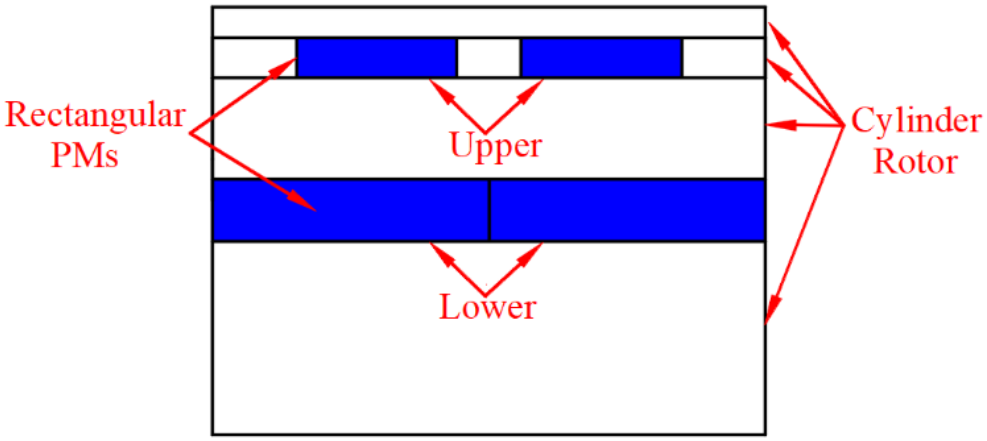

(a) Simplified rotor.

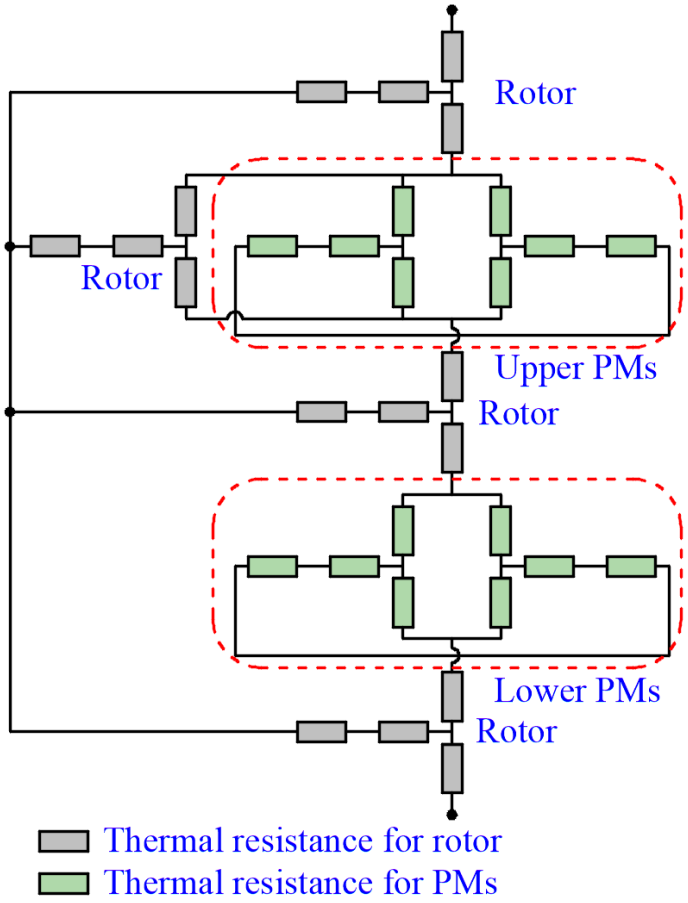

(b) LPTM of simplified rotor.

Fig. 6.10. Simplified rotor and its corresponding LPTM.

The LPTM of the entire machine under natural cooling is shown in Fig. 6.11.

The heat sources in IPMSM are winding copper loss, iron loss, PM loss, etc.

The winding copper loss P_{cu} is calculated by:

$$P_{cu} = 3I^2R_0(1 + (T_1 - T_0)) \tag{6.19}$$

where I is the RMS phase current, R_0 is the phase resistance at the reference temperature T_0, and T_1 is the actual temperature.

The iron loss density P_v is calculated by [BER88]:

$$P_v = k_h f B_m + k_{ec} f^{1.5} {B_m}^{1.5} + k_{ex} f^2 {B_m}^2 \tag{6.20}$$

where B_m is the amplitude of the AC flux component, f is the frequency, k_h is the hysteresis core loss coefficient, k_{ec} is the eddy-current core loss coefficient, and k_{ex} is the excess core loss coefficient.

The PM loss P_{PM} is calculated by [YAM09]:

$$P_{PM} = \sum_n \left\{ \int_{magnet} \frac{|J_n|^2}{2\sigma} dv \right\} \tag{6.21}$$

where J_n is the amplitude of the n-th order time-harmonic eddy currents and σ is the conductivity of the PMs.

6.4.3. Analytical method

The LPTM is based on 1-D heat transfer equations with uniform and independent heat flows. Additionally, only average temperatures can be calculated by LPTM [LIA21]. The 2-D analytical model [LIA21] is used to calculate the temperature distributions of the active-winding and end-winding. The models are shown in Fig. 6.12. The top and bottom boundaries of the stator slot are simplified into arcs to simplify the calculation.

Poisson's equation in the polar coordinate system is used to calculate the temperature distribution of active winding.

$$\frac{1}{r}\frac{\partial}{\partial r}\left(\lambda_r r \frac{\partial T}{\partial r}\right) + \frac{1}{r^2}\frac{\partial}{\partial \theta}\left(\lambda_\theta \frac{\partial T}{\partial \theta}\right) + \dot{q_w} = 0 \tag{6.22}$$

where $\dot{q_w}$ is the internal heat source density.

The end winding is modeled as a hollow cylinder, and the heat dissipation area is regarded as a rectangular region. Poisson's equation of the cartesian coordinate system is used to calculate the temperature distribution of the end winding.

$$\frac{1}{x}\frac{\partial}{\partial x}\left(\lambda_x \frac{\partial T}{\partial x}\right) + \frac{\partial}{\partial y}\left(\lambda_y \frac{\partial T}{\partial z}\right) + \dot{q_w} = 0 \tag{6.23}$$

The temperatures calculated by the LPTM are used as the boundary conditions in the analytical method.

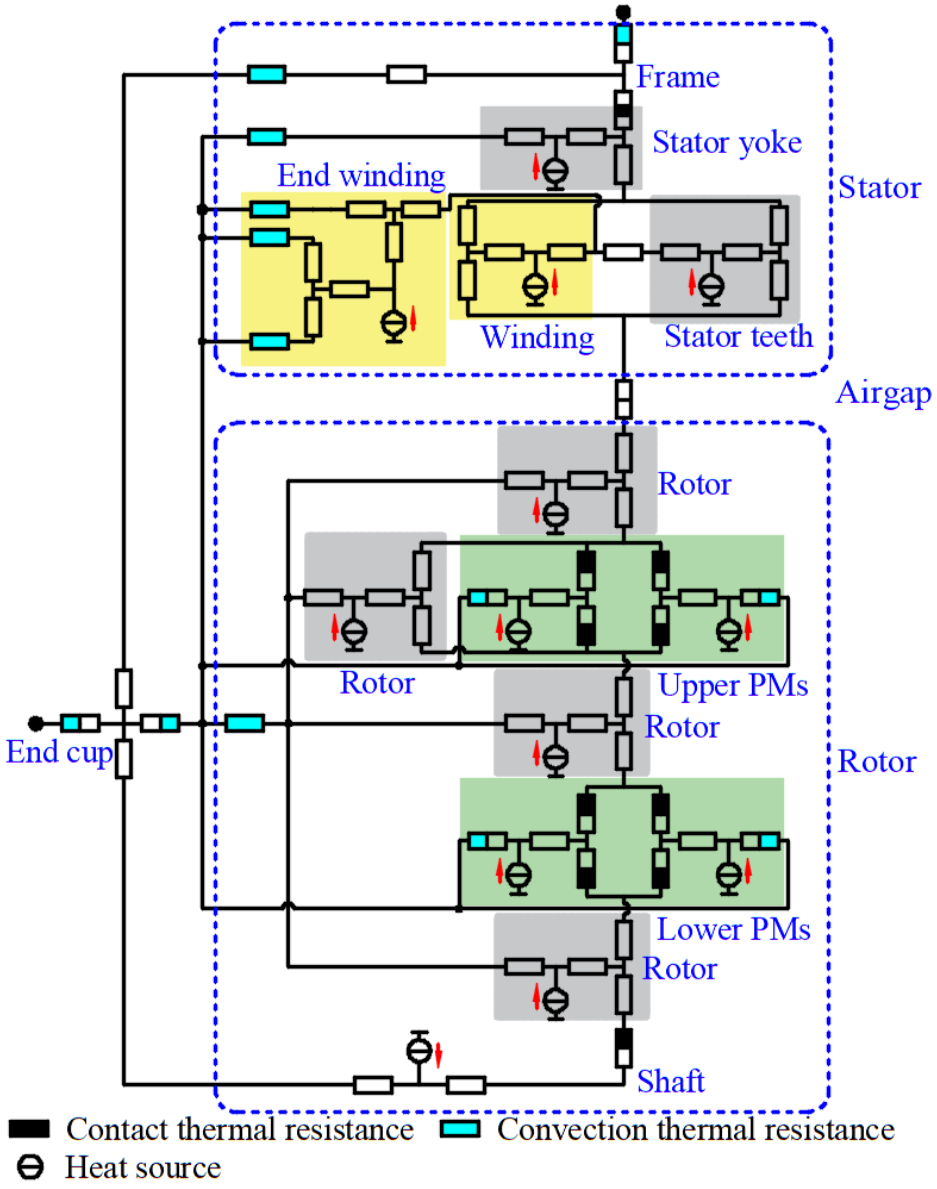

Fig. 6.11. LPTM model for the whole machine with natural cooling.

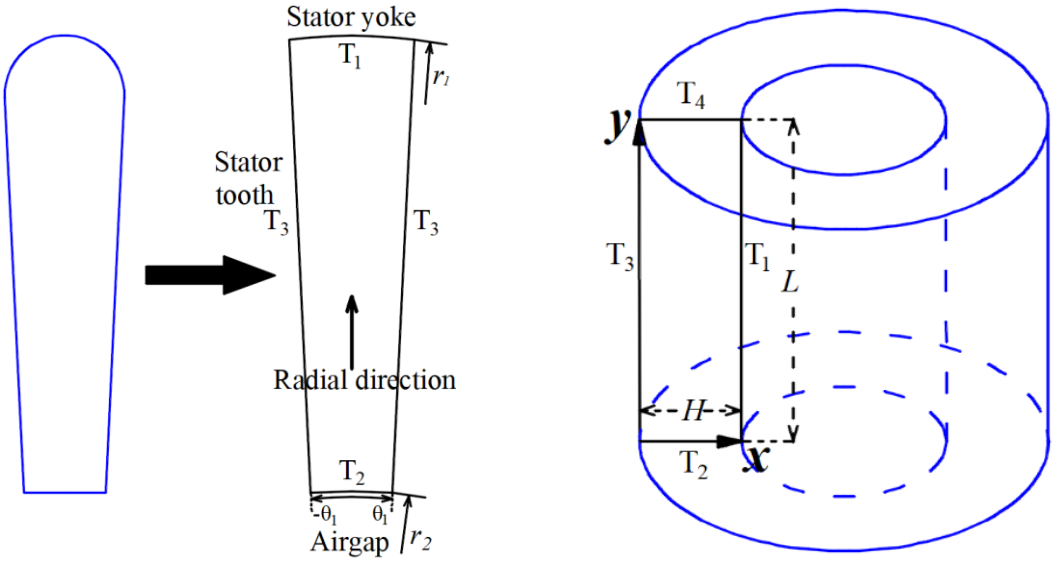

(a) Active winding. (b) End winding.

Fig. 6.12. 2-D analytical models for active winding and end winding.

6.4.4. 3-D FEA thermal model

The 3-D FEA thermal model is built to verify the results of the LPTM as shown in Fig. 6.13. To analyze the steady-state temperature distributions of the IPMSM, the loss distributions calculated by 2-D FEA are imported into the 3-D thermal model. The convection HTCs calculated in section 6.4.1 are assigned to corresponding interfaces in the 3-D thermal model. The flowchart of the thermal analysis procedure is shown in Fig. 6.14.

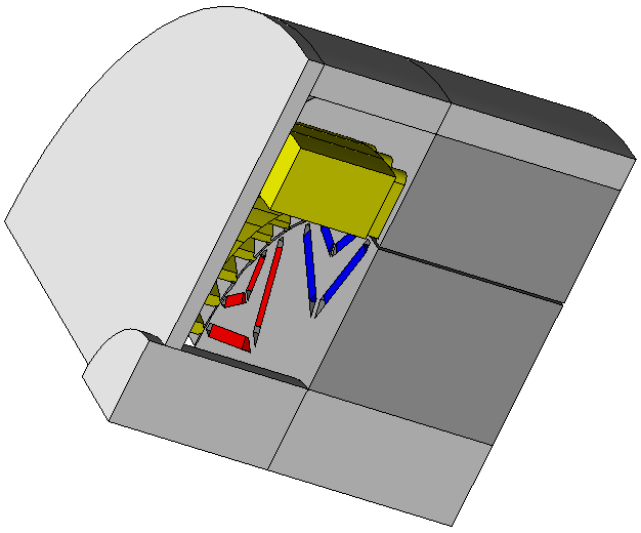

Fig. 6.13. 3-D FEA thermal model.

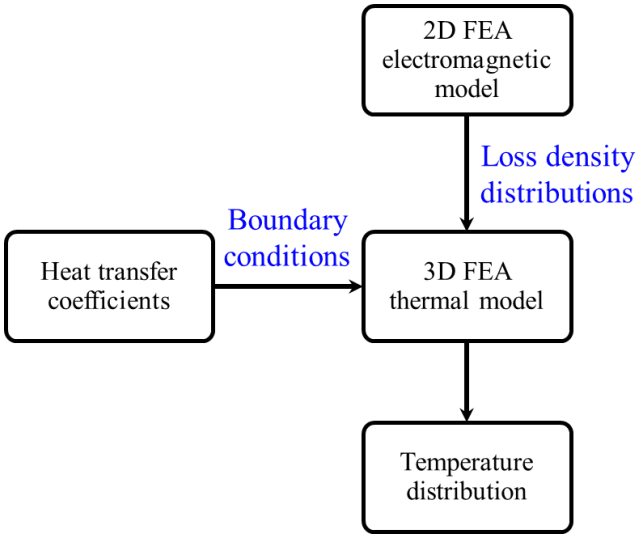

Fig. 6.14. Flowchart of the thermal analysis procedure.

6.5. Thermal Analysis

6.5.1. Comparison between LPTM and FEA

Fig. 6.15 compares the average temperatures of different components of the IPMSM calculated by T-type LPTM and FEA under various load conditions. The LPTM model is based on the 1-D heat transfer equation with uniform and independent heat flows. Only average temperatures can be calculated in T-type LPTM [LIA21]. In most cases, the maximum temperature is the most important. To calculate the maximum temperature of winding, I-type LTPN can be used and the results are shown in Fig. 6.16.

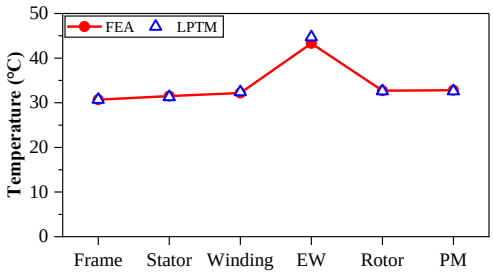

(a) I_{rms}=50A and 1500 r/min.

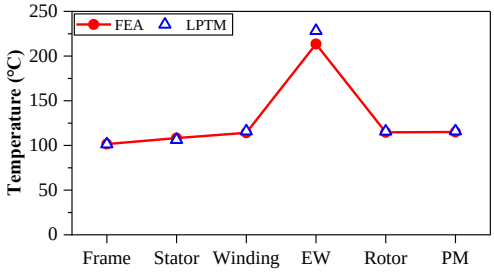

(b) I_{rms}=150A and 1500 r/min.

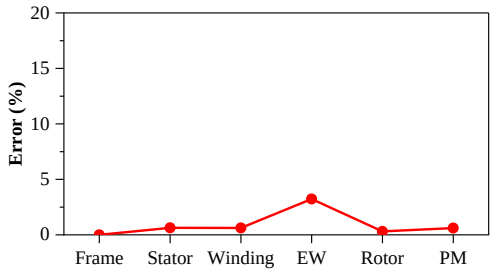

(c) Error (I_{rms}=50A).

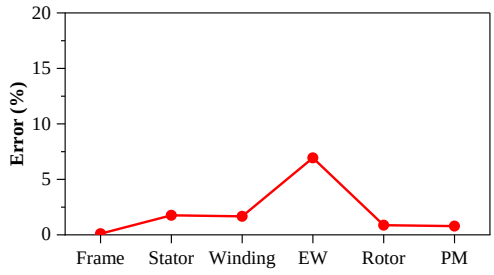

(d) Error (I_{rms}=150A).

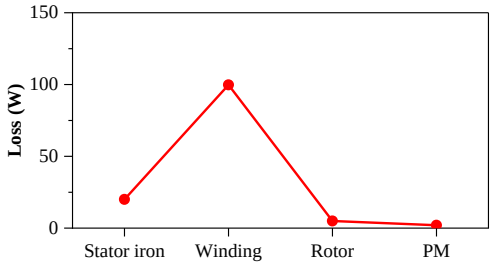

(e) Loss (I_{rms}=50A).

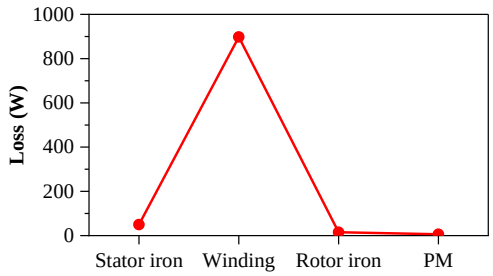

(f) Loss (I_{rms}=150A).

Fig. 6.15. Comparison of average temperatures of different components of the machine calculated by T-type LPTM and FEA.

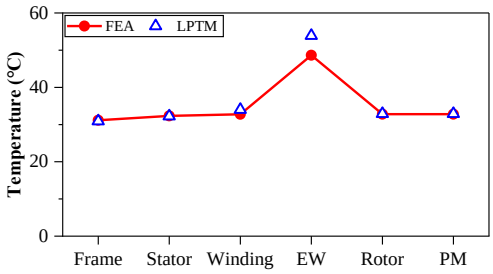

(a) I_{rms}=50A and 1500 r/min.

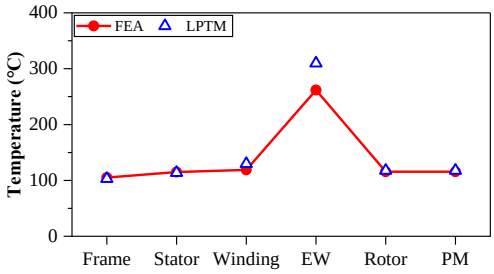

(b) I_{rms}=150A and 1500 r/min.

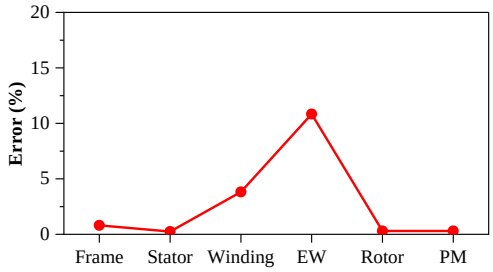

(c) Error (I_{rms}=50A).

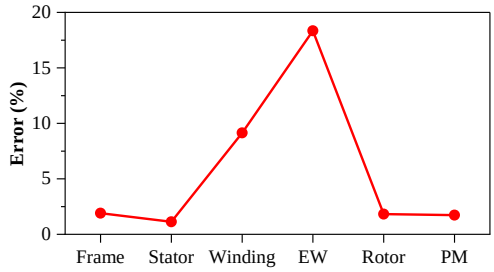

(d) Error (I_{rms}=150A).

Fig. 6.16. Comparison of maximum temperatures of different components of the machine calculated by I-type LPTM and FEA.

6.5.2. Comparison between analytical method and FEA

The I-type LPTM may overestimate the maximum temperature of the active winding and end-winding, especially when the winding loss is high. Therefore, the 2-D analytical model [LIA21] is used to calculate the temperature distributions of the active-winding and end-winding. Fig. 6.17 and Fig. 6.18 show the temperature distribution of the active-winding and end-winding calculated by the analytical method and FEA. Table 6.3 presents the comparison of active winding and end winding temperatures between the analytical method and FEA. The error between the analytical method and FEA significantly decreases compared with the error between LPTM and FEA.

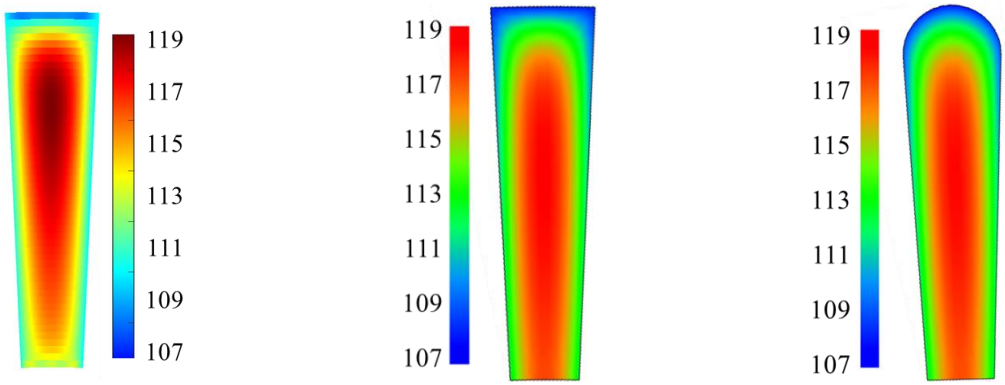

(a) Analytical. (b) FEA (Simplified). (c) FEA (Original).

Fig. 6.17. Winding temperature distributions calculated by analytical method and FEA.

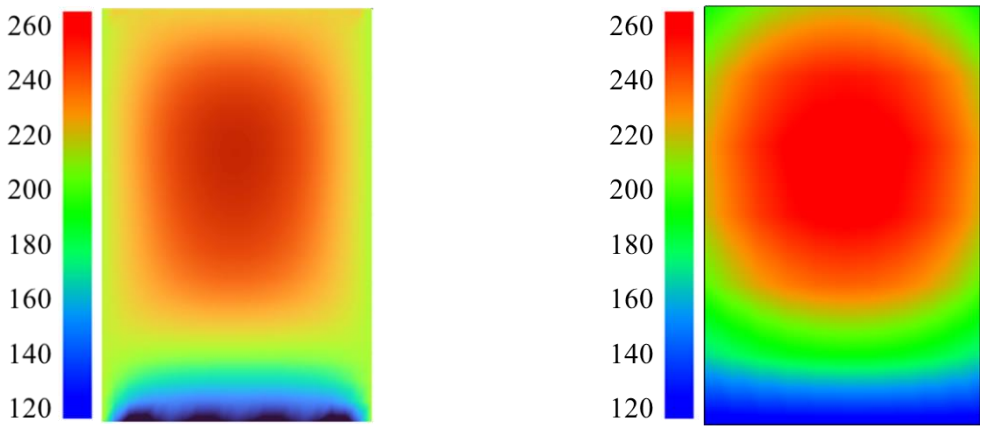

(a) Analytical. (b) FEA.

Fig. 6.18. End winding temperature distribution calculated by analytical method and FEA.

Table 6.3 Comparison of Average and Maximum Active Winding and End Winding Temperatures between Analytical Method and FEA

	Winding		End winding	
	Maximum	Average	Maximum	Average
Analytical (℃)	119	114	263	219
FEA (℃)	118	115	262	213
Error (%)	0.48	0.18	0.65	2.70

6.5.3. Thermal analysis with cooling conditions

The HTCs of different cooling methods are calculated in Section 6.4.1 and assigned to the corresponding surface of the 3-D thermal model as shown in Fig. 6.19. The comparisons of temperatures calculated by LPTM and FEA are shown in Fig. 6.20. Due to the complex structure in the active winding and end winding, consisting of conductor, insulation, and impregnation, the error in winding temperature is slightly higher.

As the uneven PM loss distribution cannot be considered in LPTM, the temperature differences between different PMs in one pole cannot be calculated through the LPTM. The 3-D FEA thermal model will be used to calculate the PM temperature distribution in the next section.

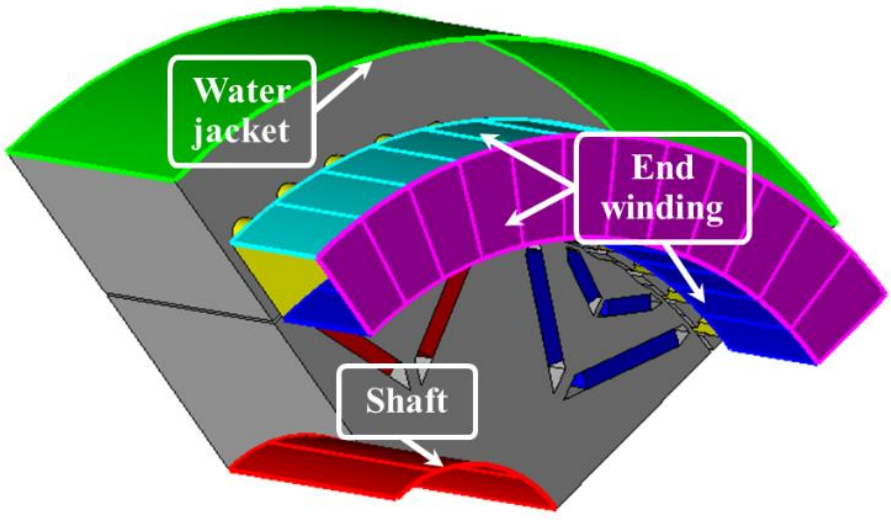

Fig. 6.19. Assignment of HTCs of different cooling methods.

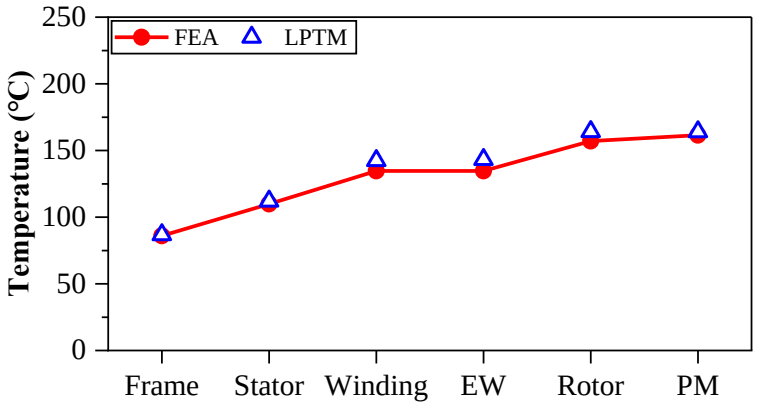

(a) Temperature.

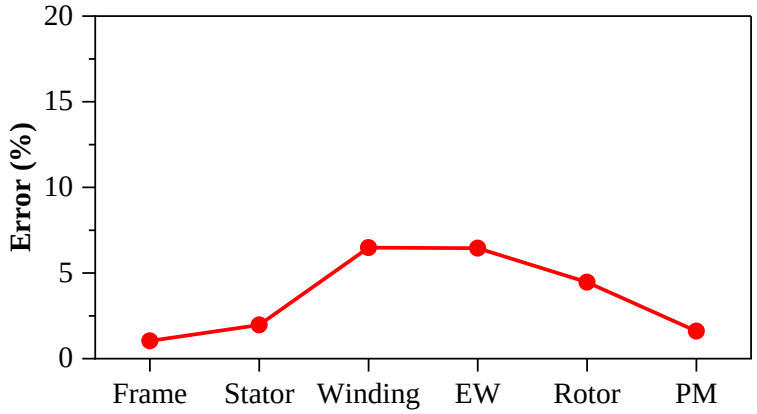

(b) Error.

Fig. 6.20. Temperatures and errors of different parts of the machine calculated by LPTM and FEA.

6.5.4. PM temperature distribution analysis

The PM temperature distribution calculated by 3-D FEA at 0° current advancing angle and 15000 r/min is shown in Fig. 6.21. The highest PM temperature is located in the machine center and decreases towards the ends. It is obvious that the overall temperature of the left side PM is higher than that of the right side PM.

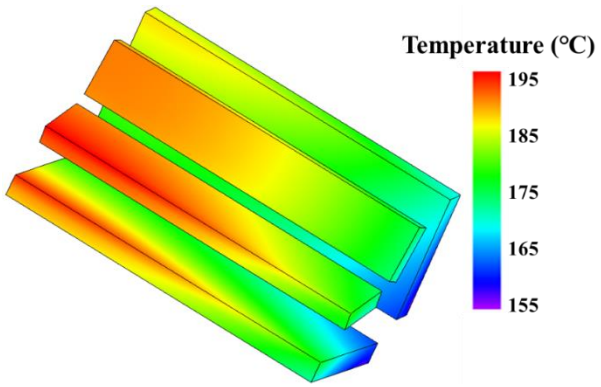

Fig. 6.21. PM temperature distribution at 0° current advancing angle.

Fig. 6.22 shows the temperature distributions of the PMs at the axial center under different current advancing angles and 15000 r/min. The temperature of the left-side PM is slightly higher than that of the right-side PM except at 90° current advancing angle, with the maximum temperature difference being about 6℃ for upper layer PMs and 9℃ for lower layer PMs at around 30° current advancing angle as shown in Fig. 6.23. When the phase current advancing angle reaches 90°, the armature reaction is pure *d*-axis current with a demagnetizing effect, which will not cause asymmetric loss and temperature distributions between left- and right-side PMs.

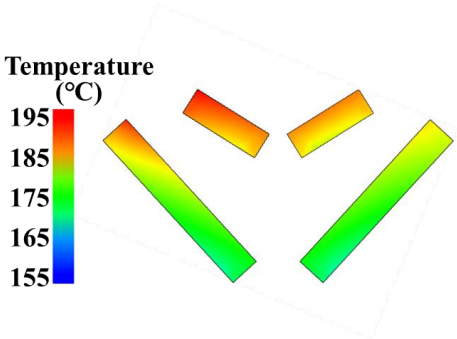

(a) 0°.

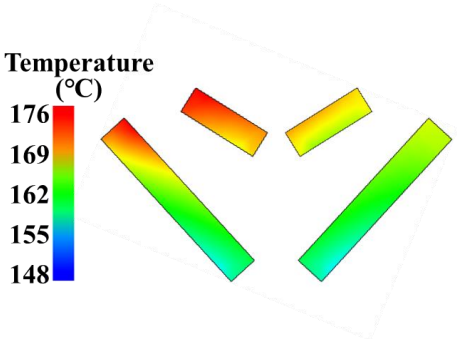

(b) 30°.

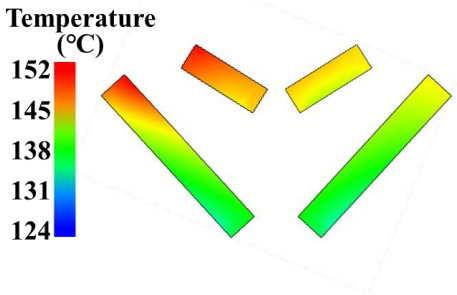

(c) 60°.

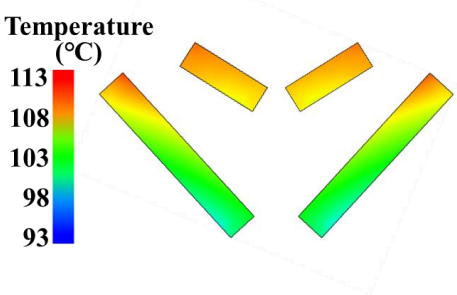

(d) 90°.

Fig. 6.22. PM temperature distributions at the axial center under different current advancing angles at 15000 r/min.

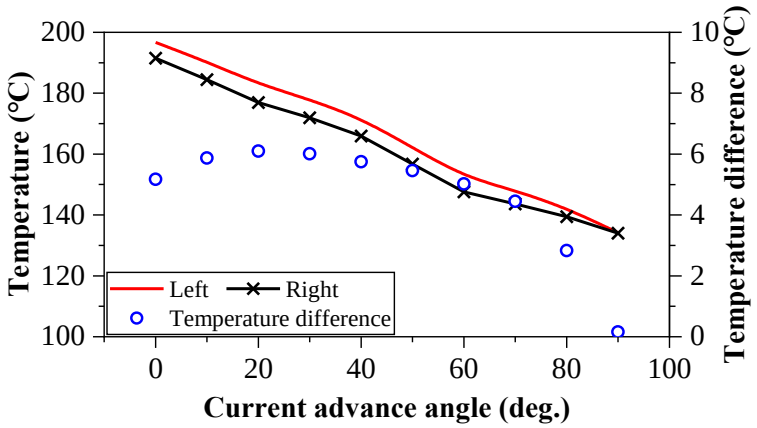

(a) Upper PMs.

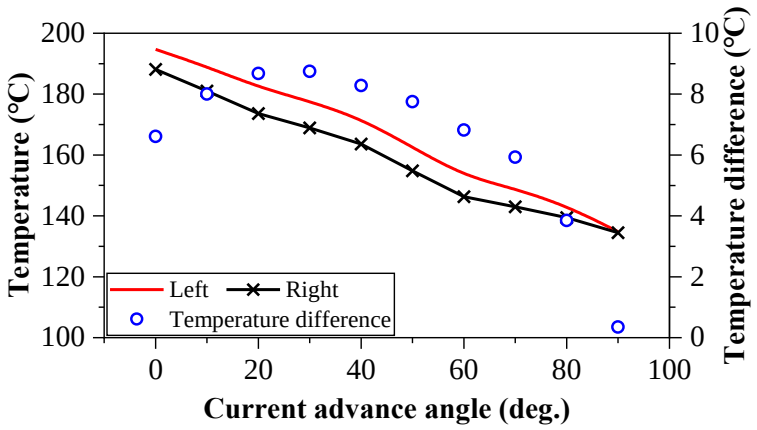

(b) Lower PMs.

Fig. 6.23. Maximum temperature and temperature differences between left- and right-side PMs at 15000 r/min.

6.6. Comparison of PM Losses and Temperature Distributions between SPMSM and IPMSM

6.6.1. Machine optimization

To fairly compare PM loss and temperature distributions between small-size SPMSMs and IPMSMs, the 12s/8p FSCW and 12s/22p ISDW IPMSMs are optimized for maximum torque. Additionally, the optimized stators of SPMSMs are kept the same and used in IPM to generate the same armature reaction. The air-gap length for IPMSMs is set to 0.5 mm since there is no need to add a sleeve to retain the PMs (1 mm for SPMSMs). The IPM rotor is globally optimized for maximum average torque. Fig. 6.24 shows the machine topologies, while Fig. 6.25 shows the optimization variables for the IPM rotor. Table 6.4 presents the optimized parameters and results.

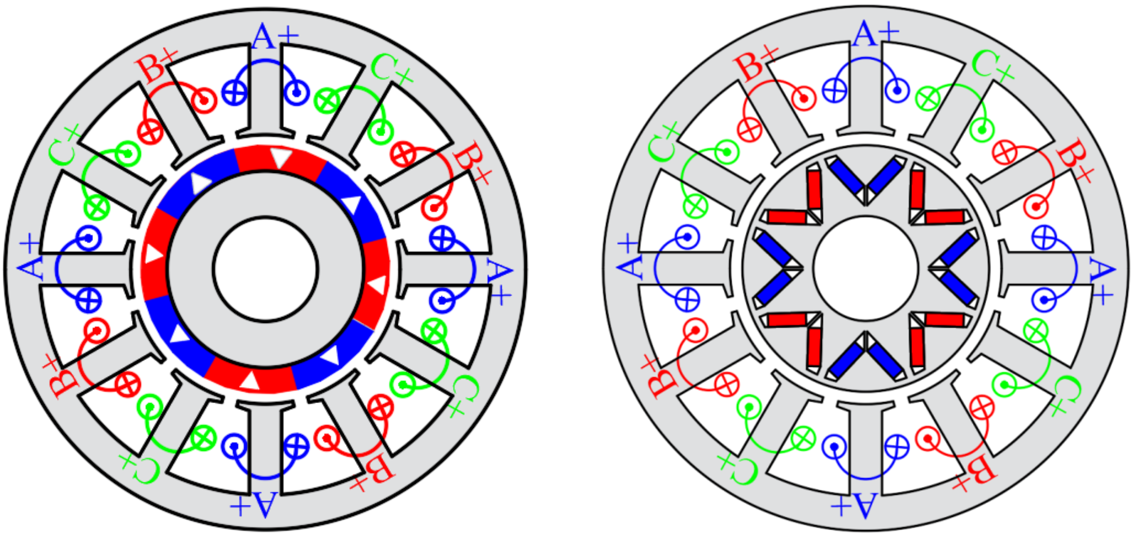

(a) 12s/8p SPM.

(b) 12s/8p IPM.

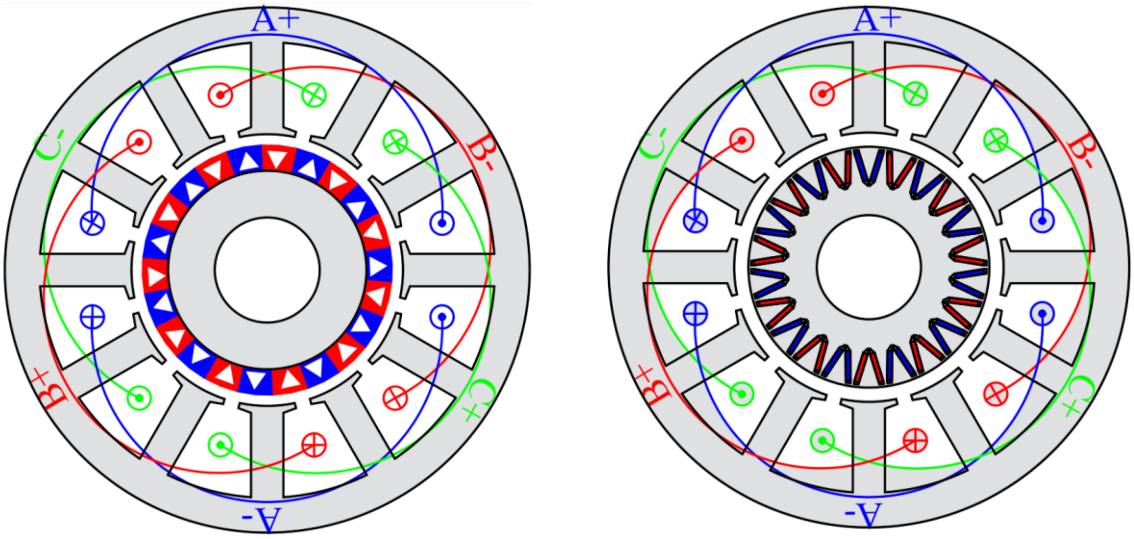

(e) 12s/22p SPM.

(d) 12s/22p IPM.

Fig. 6.24. Machine topologies of SPMSMs and IPMSMs.

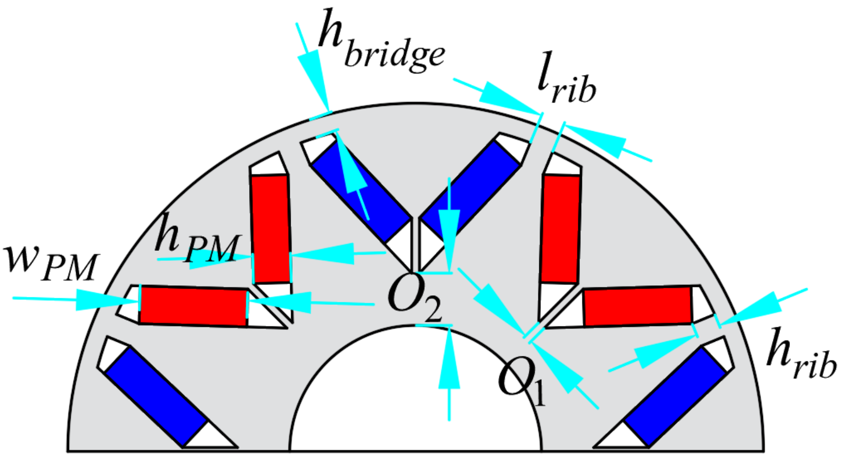

Fig. 6.25. Optimization variables for IPM rotor.

Table 6.4 Optimized Parameters and Results

Rotor pole number	8-pole		22-pole	
PM topology	SPM	IPM	SPM	IPM
IPM uses same optimized stator as SPM for same armature reaction				
d_{si} (mm)	54.4		67.1	
h_y (mm)	3.8		4.6	
w_t (mm)	7.2		2.7	
b_{so} (mm)	1.9		11.5	
I_{peak} (A)	6.34		3.63	
Air-gap (mm)	1	0.5	1	0.5
h_{pm} (mm)	3.2	3.0	2.5	1.3
V_{pm} (cm^3)	24.5	20.56	24.5	24
Torque (Nm)	3.88	3.96	5.69	6.03
Torque ripple (%)	25.75	8.33	0.80	2.57
Optimized IPM rotor variables				
Rotor pole number		8-pole		22-pole
Current advancing angle (Deg.)	0	16	0	28
w_{pm} (mm)		8.6		8.2
h_{pm} (mm)		3.0		1.3
h_{bridge} (mm)		0.57		0.75
O_1 (mm)		0.62		0.58
O_2 (mm)		4		12
h_{rib} (mm)		2		0.7
l_{rib} (mm)		2		1.0

Fig. 6.26 compares magnetic field distributions under open-circuit and rated-load (40 W copper loss) conditions between SPMSMs and IPMSMs.

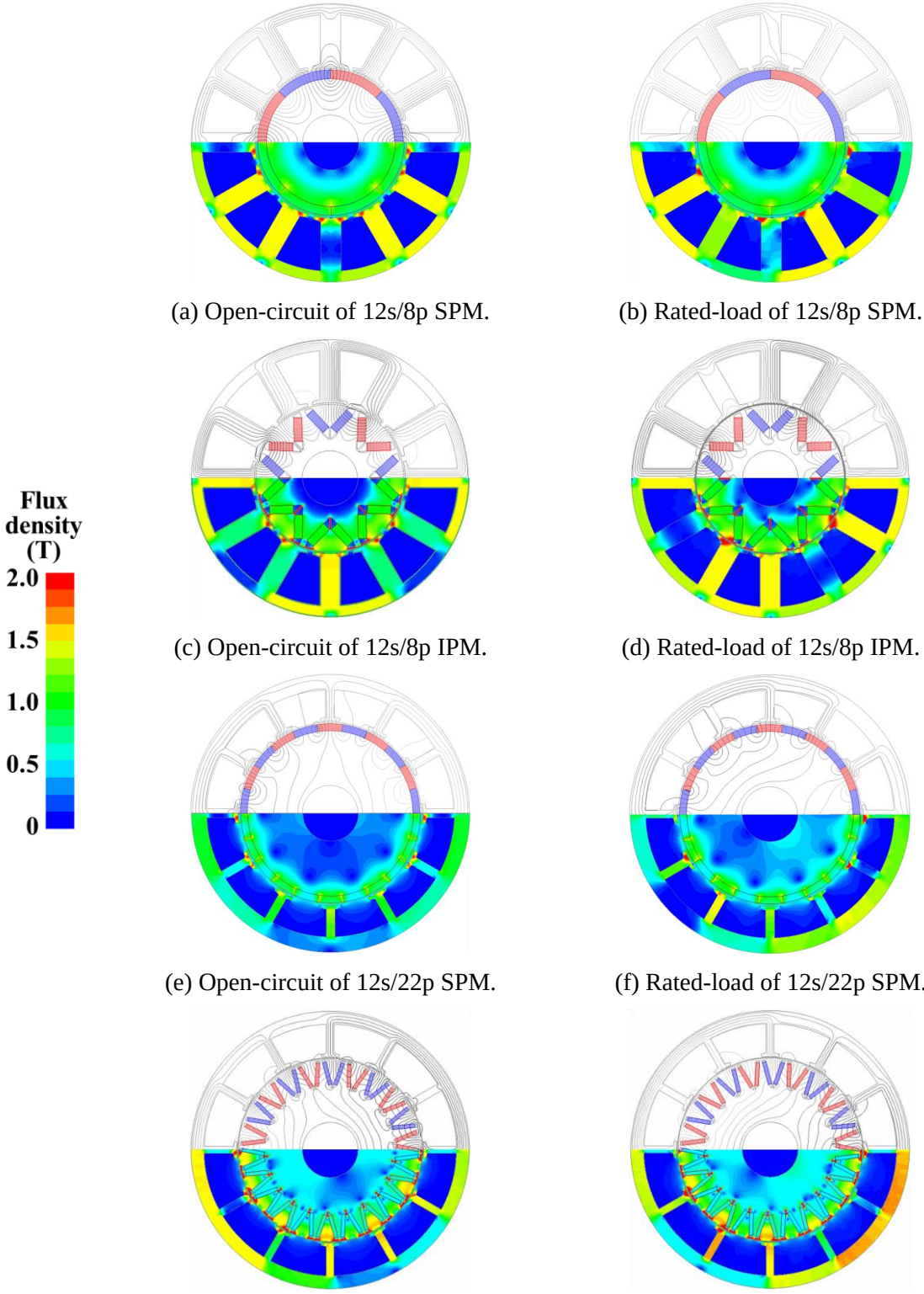

(a) Open-circuit of 12s/8p SPM.

(b) Rated-load of 12s/8p SPM.

(c) Open-circuit of 12s/8p IPM.

(d) Rated-load of 12s/8p IPM.

(e) Open-circuit of 12s/22p SPM.

(f) Rated-load of 12s/22p SPM.

(g) Open-circuit of 12s/22p IPM.

(h) Rated-load of 12s/22p IPM.

Fig. 6.26. Comparison of magnetic field distributions of SPMSMs and IPMSMs under open-circuit and rated-load condition with 40 W copper loss.

6.6.2. PM loss distribution

The PM loss distributions under corresponding rated-load conditions with 40 W copper loss at 5000 r/min are compared in Fig. 6.27. The i_d=0 control with a 0° current advancing angle is applied to SPMSMs, while the MTPA control (with 16° and 28° current advancing angles for 8-pole and 22-pole, respectively) is applied to IPMSMs to generate maximum average torque. The PMs in SPMSMs are directly exposed to the airgap and armature reaction fields, leading to higher PM eddy current loss compared with IPMSMs. In SPMSMs, the PM loss density tends to accumulate on the left-side edge of the PMs due to armature reactions. The PM loss density distributions are more complicated for IPMSM because the PMs are buried in the iron core, and both the magnetic reluctance of the rotor and armature reactions affect the loss distribution as previously analyzed. The PM loss density in IPMSM also shows asymmetric distribution due to armature reactions, but it is not as pronounced as in SPMSMs.

6.6.3. PM temperature distribution

The PM temperature distributions of SPMSMs and IPMSMs are compared using 3-D FEA thermal models, which are aligned with the models described in Chapter 5. Table 6.5 shows the corresponding average losses. The steady-state temperature distributions of the entire machines and PMs are compared in Fig. 6.28.

Table 6.5 Comparison of Average Losses between SPMSMs and IPMSMs

	8-pole		22-pole	
	SPM	IPM	SPM	IPM
Copper loss (W)	40	40	40	40
Stator iron loss (W)	36	40	766	118
Rotor iron loss (W)	0.01	2	10	36
PM loss (W)	2	1	65	14

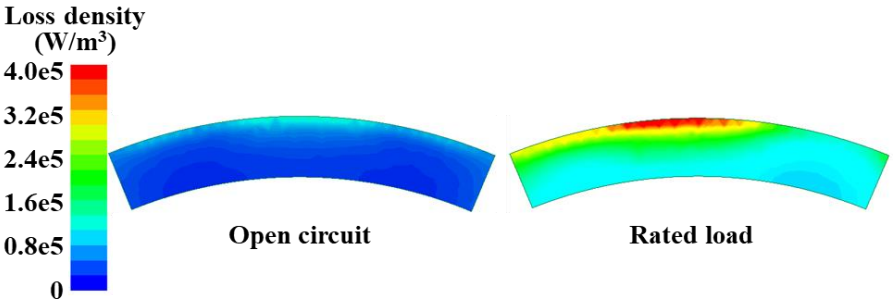

(a) 12s/8p SPM.

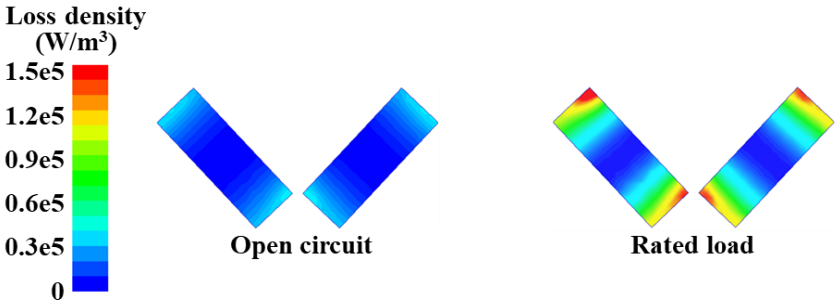

(b) 12s/8p IPM.

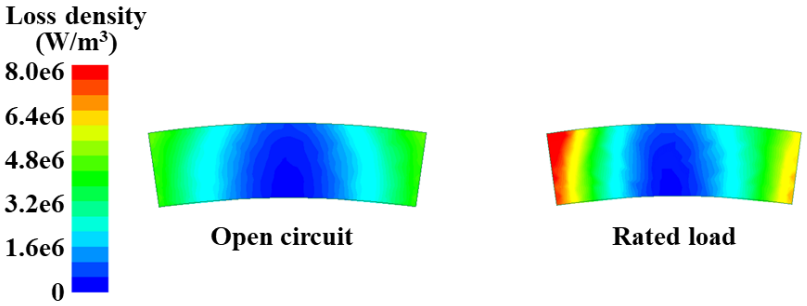

(c) 12s/22p SPM.

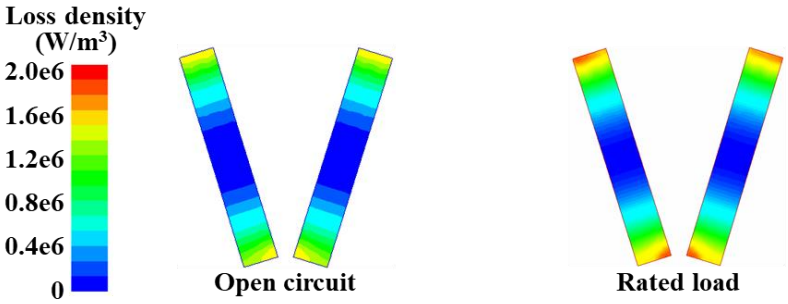

(d) 12s/22p IPM.

Fig. 6.27. PM loss distributions comparison of SPMSMs and IPMSMs under open-circuit and rated-load condition at 5000 r/min.

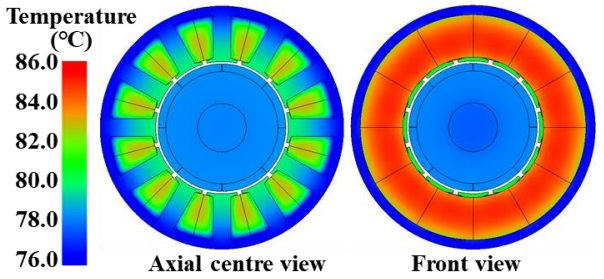

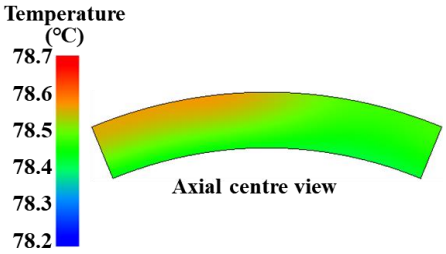

(a) 12s/8p SPM.

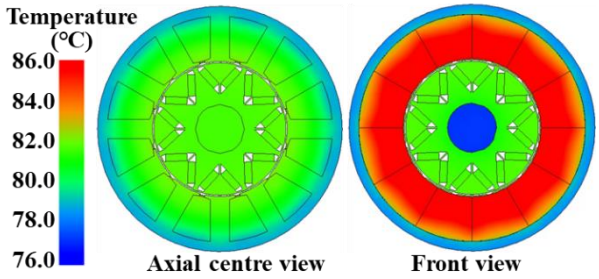

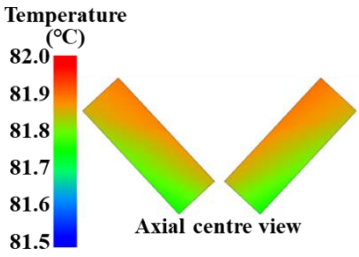

(b) 12s/8p IPM.

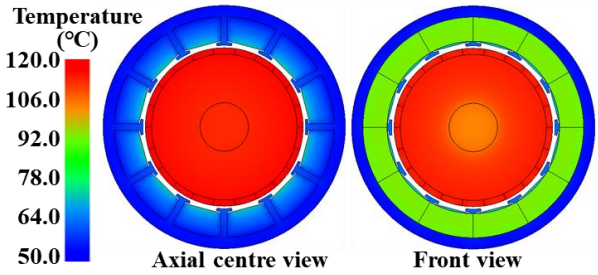

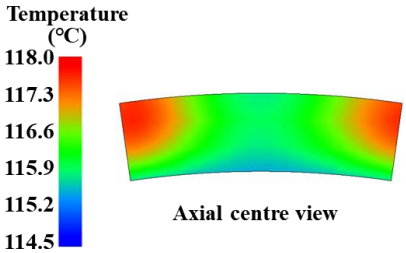

(c) 12s/22p SPM.

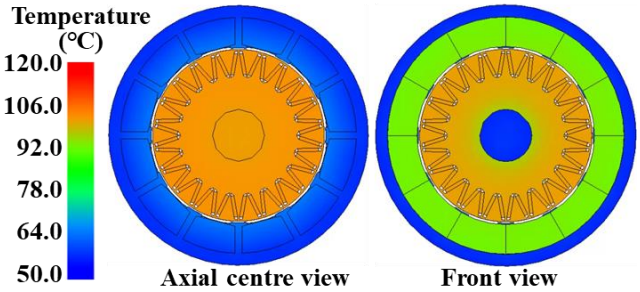

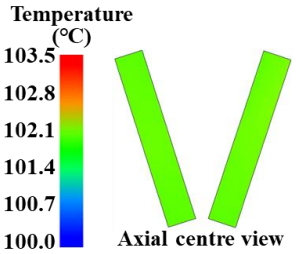

(d) 12s/22p IPM.

(i) Entire machine. (ii) PM only.

Fig. 6.28. Steady-state temperature distributions comparison of SPMSMs and IPMSMs under rated-load condition at 5000 r/min.

Several phenomena can be observed:

1. For SPMSMs, the PM temperature distributions show similar asymmetric distributions along the central line as the corresponding PM loss density distributions. In contrast, the PM temperature distributions in IPMSMs are relatively even due to their low PM loss density.
2. The PMs in SPMSMs are distributed adjacently, with each magnet directly next to another. Consequently, the temperature of each PM is influenced by the adjacent PM. Therefore, the hotspots shift further to the edge compared with their positions of maximum PM loss density. Conversely, the PMs in each pole of IPMSMs are separated by the iron core, resulting in minimal temperature influence between PMs.
3. The symmetrical PM loss and temperature distributions along the central line are not pronounced in small-size IPMSMs with weaker armature reactions.

6.7. Summary

In this chapter, the effect of armature reaction on the asymmetric PM eddy current loss and temperature distributions in a double-layer V-shape IPMSM is investigated. Due to armature reaction, PM eddy current loss densities between left- and right-side PMs of one pole are different, leading to asymmetric temperature distributions. The maximum temperature difference is about 9°C at 15000 r/min with sinusoidal current supply and around 30° current advancing angle. The asymmetric PM loss and temperature distributions between small-size SPMSMs and IPMSMs are compared. The asymmetric PM loss density distribution in IPMSMs is not as pronounced as in SPMSMs since the PMs are buried in the iron core. Meanwhile, the PM temperature distribution in IPMSMs is relatively even due to their low PM loss density and the isolation provided by the iron core.

CHAPTER 7
GENERAL CONCLUSION AND FUTURE WORK

7.1. General Conclusion

7.1.1. Research scope and contributions

This thesis focuses on the investigation of rotor-PM FS PMSMs and VPMSMs with different winding configurations (ISDW and FSCW), rotor PM topologies (NSP and CP), and stator structures (single-tooth and multi-tooth), including torque and torque density enhancement, unipolar end leakage suppression, asymmetric PM eddy current loss distribution calculation, and PM local hotspot investigation. The arrangements, scope, and features of all chapters are illustrated in Fig. 7.1.

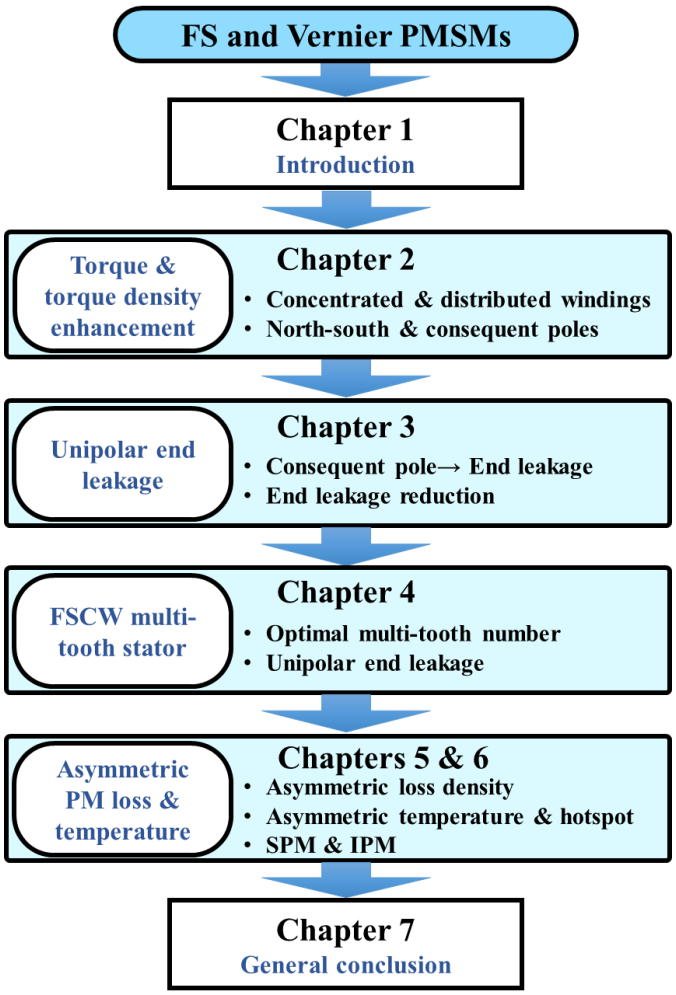

Fig. 7.1. Scope and features of thesis.

Fig. 7.2 shows the relationships among different Chapters. The major contributions of each chapter are summarized in Table 7.1.

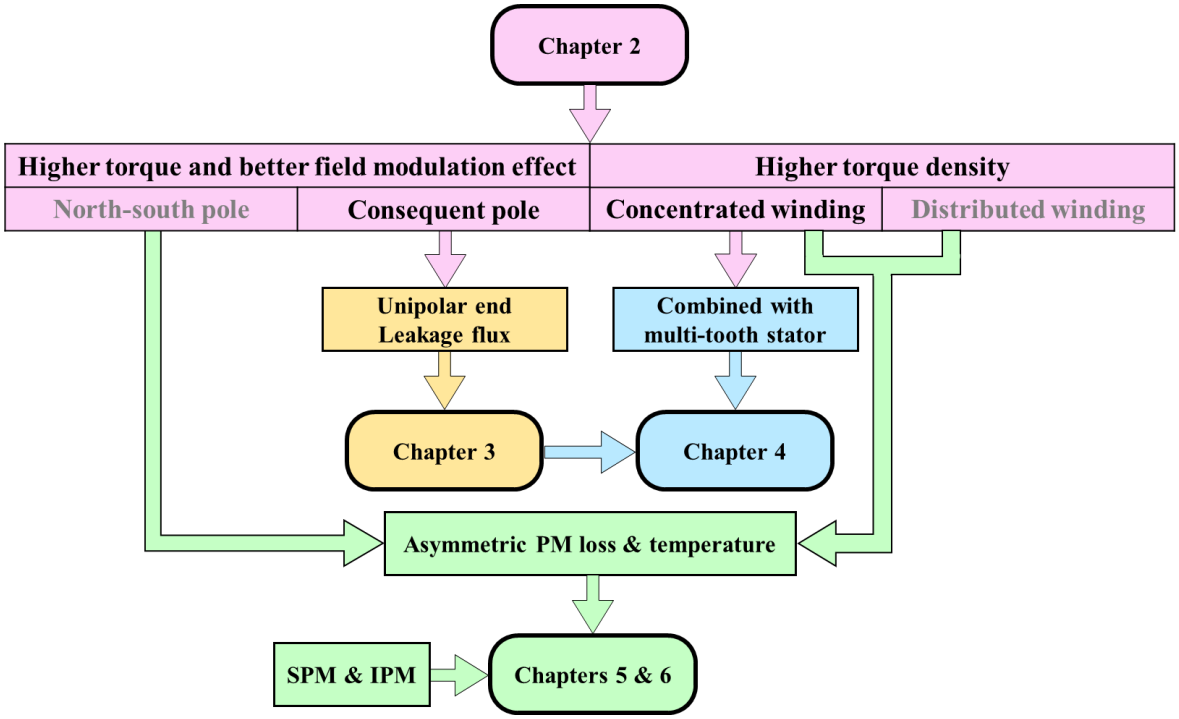

Fig. 7.2. Relationships among different Chapters.

Table 7.1 Major Contributions of Chapters

Chapter	Methodology	Major contributions
2	2-D electromagnetic FEA	• Effect of end windings in FS PMSMs & VPMSMs investigated for the first time. • Effect of slot/pole number combinations considered. • Effect of lamination stack length considered. • Effect of iron loss under different speeds considered. • ISDW & FSCW compared. • NSP & CP rotors compared. • CW → higher torque density. • CP → Better field modulation effect → Potential to generate higher torque.

3	2-D & 3-D electromagnetic FEA	• End leakage systematically investigated. • CP rotor structure → Unipolar end leakage flux. • Effects of slot/pole number combinations & armature reaction investigated. • End leakage found sensitive to shaft diameter & PM pole arc. • Simple composite rotor proposed → Reduce unipolar end leakage flux without sacrificing torque capability. • Non-magnetic ring → 40% reduction in end leakage. • Combining non-magnetic ring with non-magnetic shaft → 95% reduction in end leakage.
4	2-D & 3-D electromagnetic FEA	• NSP & CP rotors compared. • CP rotor combined with single & multi-tooth stator → Better field modulation effect. • Multi-tooth stator → PM utilization significantly improved. • Field modulation effect & torque output capability found sensitive to dimensions of multi-tooth & PMs. • Multi-tooth stator → unipolar end leakage flux suppressed.
5 & 6	2-D electromagnetic FEA 3-D thermal FEA	• No asymmetry for PM (open-circuit) & amature reaction field alone. • Interaction between armature reaction field & PM field → Asymmetric PM loss distribution. • Dominant armature reaction field harmonic → Majority of PM loss • Lower order armature reaction field harmonics → PM loss concentrates on edge of PMs. • Consistent asymmetric temperature distributions & PM hotspot locations with PM loss in SPM. • Almost uniform PM temperature in small-size IPM. Noticeable asymmetric PM loss & temperature in relatively large-size IPM used in electric vehicles • More significant asymmetric PM loss & temperature distributions in SPM than IPM.

7.1.2. Effects of end winding and rotor PM topologies

The effects of end winding and rotor PM topologies on 12-slot SPMSMs with different slot/pole number combinations are investigated.

The results show that CW offers higher torque density. The torques of optimized SPMSMs considering end winding increase with the rotor pole numbers. However, the torque densities of DW VMs with high rotor pole numbers (20-pole and 22-pole) are lower than those of FSCW SPMSMs with lower rotor pole numbers due to the long axial end winding length. However, vernier machines with long lamination stack lengths can maintain both high average torque and torque density simultaneously.

The CP structure has a better field modulation effect, especially for SPMSMs with high rotor pole numbers (14-pole, 20-pole, and 22-pole), which can also generate higher rated torque compared with NSP counterparts. However, higher rotor pole number and CP rotor structure will deteriorate overload capability and power factor, despite having higher rated torque.

7.1.3. Unipolar end leakage flux reduction in CP rotor

Even though the CP rotor structure has the advantages of better field modulation effect, high torque output capability, and high PM utilization, unbalanced magnetic circuits in the CP structure result in unipolar end leakage flux, which may magnetize components in the end region, posing threats to system safety and necessitating reduction.

A simple composite rotor structure, i.e., a combination of the non-magnetic shaft with a non-magnetic ring between the rotor and the shaft, has been proposed and can effectively reduce unipolar end leakage flux without sacrificing torque capability. This design offers several advantages: it maintains a simple structure, reduces unipolar end leakage flux, preserves torque capability, and avoids increasing iron loss and torque ripple compared to alternative methods. Compared with the conventional rotor with magnetic shaft for all the analyzed consequent pole PM machines, the non-magnetic shaft alone can reduce approximately 90% of end leakage flux, while the non-magnetic ring alone can reduce approximately 40%. Additionally, 95% of end leakage flux can be reduced when combining a non-magnetic ring with a non-magnetic shaft (which could be integrated into a single shaft) compared with the conventional rotor with a magnetic shaft. Considering the manufacturing complexity, a non-magnetic shaft alone is highly recommended.

7.1.4. FSCW combined with multi-tooth stator

As previously analyzed, the CW offers higher torque density. Combined FSCW with a multi-tooth stator can further improve the torque and power densities. The effect of multi-tooth numbers on the electromagnetic performances of NSP and CP VPMSMs is investigated. The optimal multi-tooth number, in terms of torque characteristics, PM utilization, efficiency, power factor, and end leakage is determined.

The results reveal that the CP rotor combined with the multi-tooth stator structure has a better field modulation effect and helps increase torque output capability and improve PM utilization. However, the efficiency at higher speeds, power factor, and overload capability are sacrificed when using the CP rotor and multi-tooth stator.

The multi-tooth stator structure helps suppress the unipolar end leakage flux, achieving approximately 60% reduction for the CP VPMSM with 5 multi-teeth compared to the single-tooth stator.

7.1.5. Asymmetric PM loss and temperature distributions

The PM eddy current loss in SPMSMs may be significant since PMs are directly exposed to the armature reaction field. Moreover, the rotor in SPMSMs usually has limited heat dissipation capability, making the induced PM loss more likely to cause the risk of over-temperature.

The mechanisms of asymmetric PM eddy current loss and resultant temperature distributions are investigated. By utilizing the harmonic restoration method, the contributions of individual armature reaction field harmonics, with and without PM fields, to the on-load PM eddy current loss are evaluated and quantified. It has been demonstrated that each 12-slot SPMSM with different pole numbers exhibits a dominant armature reaction field harmonic contributing to the majority of PM loss. Additionally, the on-load PM loss exhibits asymmetric distribution, primarily due to the interaction between the dominant armature reaction field harmonic and the PM field. As pole numbers increase, the maximum PM loss densities for 12-slot SPMSMs shift from circumferential centers toward PM edges. Furthermore, hotspot locations of PMs vary with slot/pole number combinations and consistently follow trends in PM loss density distributions.

The effect of armature reaction on asymmetric PM eddy current loss and temperature distributions in IPMSMs is also investigated. Compared with SPMSMs, the asymmetric PM

loss density distribution in small-size IPMSMs is less pronounced because the PMs are embedded within the iron core. Additionally, the PM temperature distribution in small-size IPMSMs tends to be more uniform due to lower PM loss density and insulation provided by the iron core. However, noticeable differences in PM eddy current loss density between left- and right-side PMs of a single pole are evident in relatively large-size IPMSMs used in electric vehicles. The asymmetric PM eddy current loss results in asymmetric temperature distributions, with a maximum temperature difference of approximately 9℃ observed at 15000 r/min with sinusoidal current supply and a current advancing angle of around 30 degrees for the prototype machine.

7.1.6. Comparison between ISDW and FSCW PMSMs and VPMSMs

ISDW can achieve high winding factors and the largest fundamental harmonic winding factor, resulting in high average output torque. Additionally, ISDW can utilize reluctance torque to achieve high torque per PM volume. However, the longer axial end winding length reduces the torque density. Moreover, modular assembly is difficult to implement.

FSCW has shorter end windings and lower copper usage, offering the advantages of high power and torque densities, high efficiency, lower torque ripple, and enhanced flux weakening capability. Additionally, FSCW has a compact structure and facilitates easy modular assembly. However, FSCW PMSMs result in significantly reduced reluctance torque and abundant sub-harmonic field contents, leading to higher iron and PM losses.

VPMSM offers higher rated torque compared with PMSM. However, the overload capability, power factor, and efficiency are deteriorated.

Fig. 7.3 shows the comparison of torque and torque density among 12-slot NSP SPMSMs with different winding configurations (CW and DW). It demonstrates that DW VMs exhibit higher average torque neglecting end winding but lower torque density considering end winding due to long axial end winding lengths. Fig. 7.4 shows the comparison of torque and torque density among 12-slot CP SPMSMs with different winding configurations (CW and DW) considering end windings. Compared with NSP rotor topologies, CP rotor topologies have slightly higher average torque and torque density for PMSMs with high rotor pole numbers.

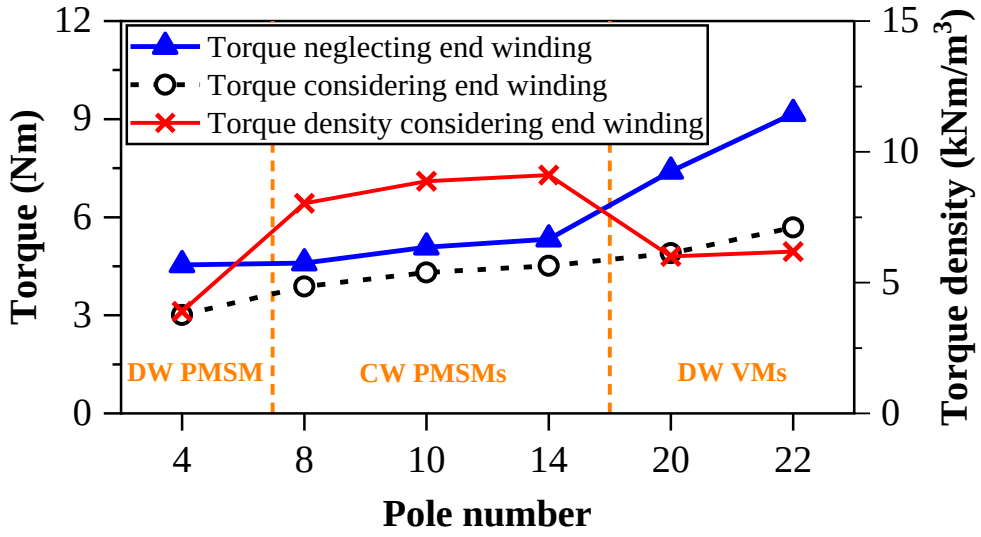

Fig. 7.3. Comparison of torque and torque density among 12-slot NSP SPMSMs with different winding configurations.

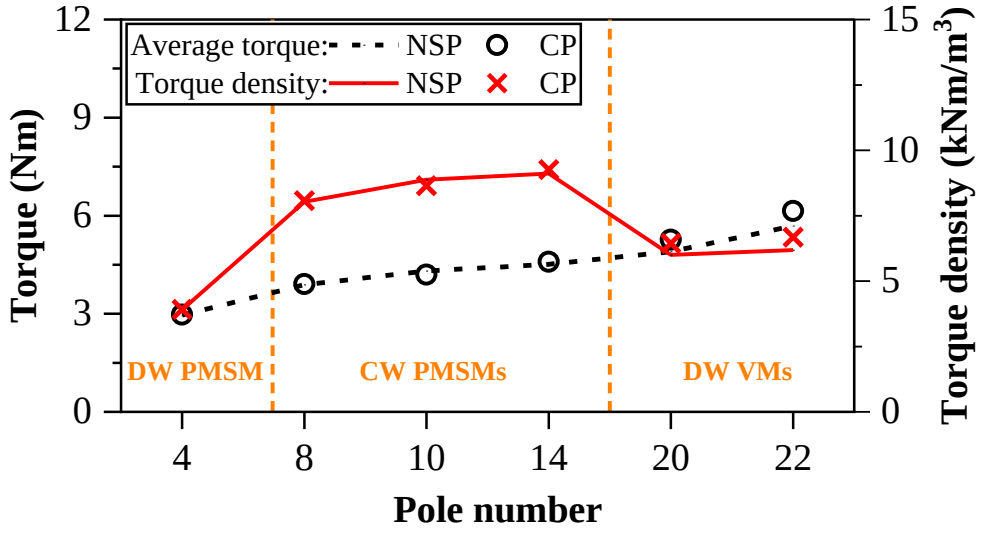

Fig. 7.4. Comparison of torque and torque density among 12-slot CP SPMSMs with different winding configurations considering end windings.

7.1.7. Comparison between single-tooth and multi-tooth VPMSMs

The multi-tooth stator offers a better field modulation effect and generates higher rated torque. Additionally, FSCW is often combined with the multi-tooth stator to achieve higher torque and power densities. Furthermore, the multi-tooth stator helps suppress the unipolar end leakage flux in CP VPMSMs. However, the overload capability, power factor, and efficiency at high speeds are deteriorated.

7.1.8. Comparison between NSP and CP rotor VPMSMs

The CP rotor structure offers a better field modulation effect, particularly beneficial for VMs with high rotor pole numbers, which can also generate higher rated torque compared with NSP counterparts. Additionally, the CP rotor structure can save PM volume and increase PM utilization, especially when combined with the multi-tooth stator. However, the CP structure causes unipolar end leakage flux, deteriorates overload capability and power factor, increases losses, and increases cogging torque and torque ripple compared with the NSP counterpart.

Fig. 7.5 and Table 7.2 show the comparison of torque and torque density among 12-slot single-tooth and 6-slot multi-tooth PMSMs with different winding configurations (CW and DW) and rotor topologies (NSP and CP) considering end winding. It shows that:

1. DW VMs have the highest average torque but lower torque density compared with CW PMSMs and VMs.
2. 6-slot CW VMs with multi-tooth stators have the highest torque density, slightly surpassing that of 12-slot single-tooth CW PMSMs.
3. Compared with NSP rotor topologies, CP rotor topologies have higher average torque for PMSMs with high rotor pole numbers and multi-tooth stator structures.

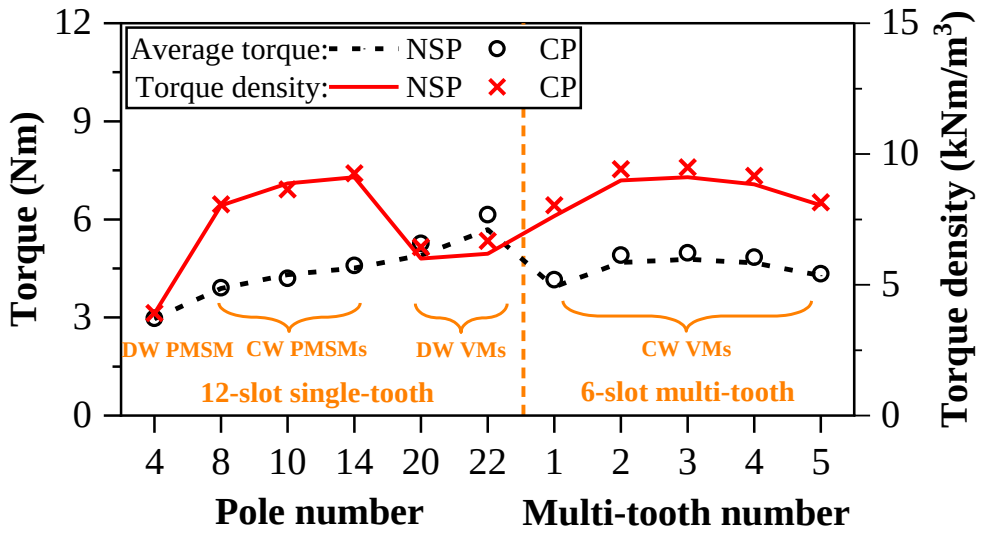

Fig. 7.5. Comparison of torque and torque density among 12-slot single-tooth and 6-slot multi-tooth PMSMs with different winding configurations and rotor topologies considering end windings.

Table 7.2 Comparison of torque and torque density among 12-slot single-tooth PMSMs and 6-slot multi-tooth PMSMs with different winding configurations and rotor topologies

		Torque (Nm)		**Torque density (kNm/m^3)**	
12-slot single-tooth stator	Pole number	NSP	CP	NSP	CP
	4 (DW)	2.96	2.97	3.90	3.92
	8 (CW)	3.89	3.91	8.03	8.07
	10 (CW)	4.31	4.19	8.87	8.64
	14 (CW)	4.51	4.59	**9.11**	**9.26**
	20 (DW)	4.90	5.26	6.00	6.44
	22 (DW)	**5.68**	**6.14**	6.18	6.68
CW 6-slot multi-tooth stator	Multi-tooth number				
	1	3.94	4.15	7.63	8.04
	2	4.68	4.90	8.99	9.42
	3	4.78	4.98	**9.12**	**9.49**
	4	4.67	4.84	8.84	9.16
	5	4.28	4.34	8.04	8.15

7.1.9. Summary of comparisons between different winding configurations, stator structures, and rotor topologies

Table 7.3 summarizes comparisons between PMSMs and VPMSMs with different winding configurations, stator structures, and rotor topologies.

Table 7.3 Summary of Comparisons between PMSMs and VPMSMs with Different Winding Configurations, Stator Structures, and Rotor Topologies

		Features
Winding configurations	ISDW	Advantages: • High winding factor and reduced harmonics. • Utilization reluctance torque. Disadvantages: • Longer axial end winding. • Complex manufacturing. • Hard to achieve modular assembly.
	FSCW	Advantages: • Shorter end windings and lower copper usage. • High torque/power density. • Simple and compact structure. • Easy to achieve modular assembly. Disadvantages: • Reduced reluctance torque. • Abundant sub-harmonic field contents.
Stator structures	Single-tooth	Advantages: • Easy to manufacture. • Lower leakage flux for main magnetic circuit. Disadvantages: • Generally lower torque density compared to multi-tooth since combined with DW. • Higher cogging torque.
	Multi-tooth	Advantages: • Better field modulation effect. • Higher rated torque and torque density. • Suppressed unipolar end leakage flux. Disadvantages: • Complex design and potential for higher costs. • Deteriorated overload capability, power factor, and efficiency at high speeds.

Rotor topologies	NSP	Advantages: • Uniform magnetic field. • Lower cogging torque and torque ripple. • Better overload capability and higher power factor. Disadvantages: • More PM volume. • Potential for higher PM loss.
	CP	Advantages: • Better field modulation effect. • Higher rated torque and torque density. • Saved PM volume and increased PM utilization. Disadvantages: • Unipolar end leakage flux. • Higher cogging torque and torque ripple. • Magnetic saturation. • Deteriorated overload capability, power factor, and efficiency at high speeds.

7.2. Future Work

Based on the analysis and conclusions, the future work can be summarized as follows:

1. Investigating PM loss density and temperature distributions, as well as hotspots, in CP rotor and multi-tooth stator VMs.
2. Investigating the influence of current harmonics caused by PWM effects on asymmetric PM eddy current loss density.
3. Exploring methods to eliminate asymmetric PM eddy current loss density, resultant temperature distribution, and PM hotspots.
4. Investigating the ventilation effect of slot openings in multi-tooth stators under forced air cooling.
5. Investigating the effect of cooling techniques on the performance of various machines in this thesis.

APPENDICES

A. Modelling of End Winding

FSCW and ISDW have different end winding structures. In general, the length of end winding of FSCW is much shorter than that of ISDW. Since end winding structure is quite complicated and difficult to model accurately, there are several simplified models to calculate the length of end winding [HE21] [REF08] [GAR46] [COX08] [BAN05] [HSI07] [ZHA14b] [POT14]. The model in [BAN05], [ZHA14b] uses several serially connected straight lines to model the end winding in Fig. A.1 (a), which is often used for large AC machines. In most cases, the end winding is assumed to be circular or semi-circular in Fig. A.1 (b) [REF08], [HSI07], especially in FSCW machines. In [COX08], [POT14], quarter-circles and straight lines are used to model the end winding in Fig. A.1, whose shape is much closer to the stack.

For double-layer FSCW, the coil center is located in the quadrant of the slot as shown in Fig. A.2, while for single layer ISDW, the coil center is located in the center of the slot.

In this chapter, two quadrants, two end winding extensions, and an arc are used to model the half turn of the end winding, which is shown in Fig. A.1 (c). The corresponding lengths of winding per turn can be calculated by

$$l_w = 2\tau_c - 4r_{end} + 2\pi r_{end} + 4l_{ex} + 2l_{fe} \tag{A.1}$$

where τ_c is the average coil pitch. The end winding extension can be 0 in this model.

The radius of the center of the coils r_{coil} is calculated by:

$$r_{\text{coil}} = \frac{d_{so}}{2} - h_y - 0.5h_s \tag{A.2}$$

The end winding length per turn, l_{end}, is calculated as

$$l_{end} = 2\tau_c - 4r_{\text{end}} + 2\pi r_{\text{end}} + 4l_{\text{ex}} \tag{A.3}$$

For double-layer FSCW, τ_c is calculated as

$$\tau_c = \frac{2\pi r_{coil}}{N_s} - 0.5w_s \tag{A.4}$$

For single-layer ISDW, τ_c is calculated as

$$\tau_c = \frac{2\pi y_c r_{coil}}{N_s} \tag{A.5}$$

where y_c is the coil pitch of slot pitch.

The total winding length per turn l_w is

$$l_w = 2l_{fe} + l_{end} \tag{A.6}$$

Then, the phase resistance r_a can be calculated by

$$r_a = \frac{\rho l_w N_{ph}}{a_1 S_1} \tag{A.7}$$

where a_1 is the number of parallel branches while S_1 is the surface area of the coil.

To investigate the torque density, the axial length of end winding l_{ea} also needs to be calculated. For FSCW, the axial length is easy to calculate by (A.8), where t_w is the thickness of winding in Fig. A.3.

$$l_{ea} = 2l_{ex} + 2r_{end} + t_w \tag{A.8}$$

For ISDW, the calculation of axial length is different from the FSCW as there are overlapping parts. As Fig. A.3 shows, the overlapping part of 12s/22p is more than 12s/20p. Therefore, the axial length of ISDW end winding can be calculated by:

$$l_{ea} = 2l_{ex} + 2r_{end} + (2n+1)t_w \tag{A.9}$$

where n is the number of the overlapping parts, 1 for 12s/20p and 2 for 12s/22p.

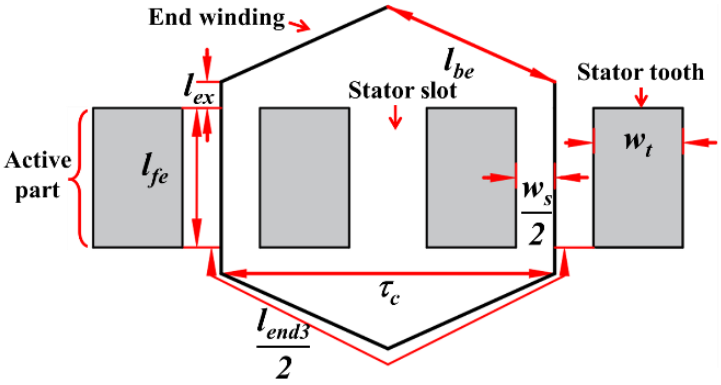

(a) Model 1.

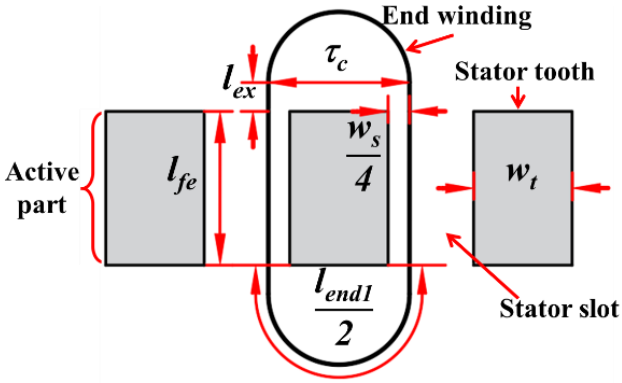

(b) Model 2.

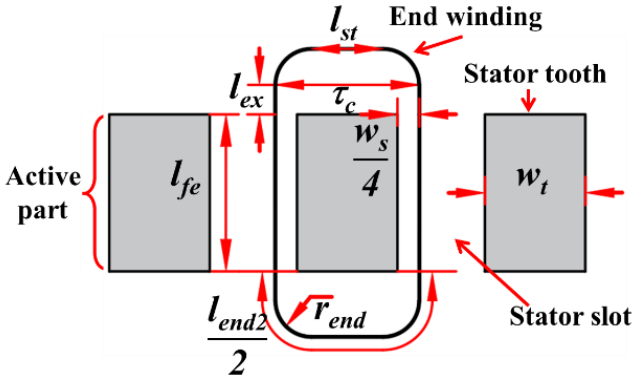

(c) Model 3.

Fig. A.1. Simplified end winding models.

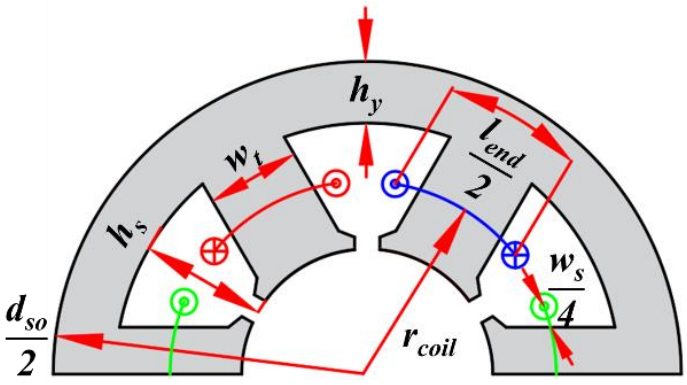

Fig. A.2. End winding structure for double-layer FSCW end winding models.

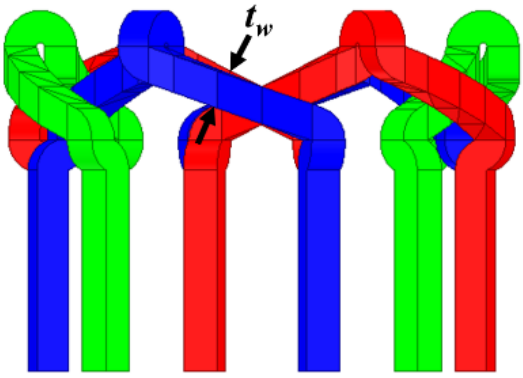

(a) 12s/20p.

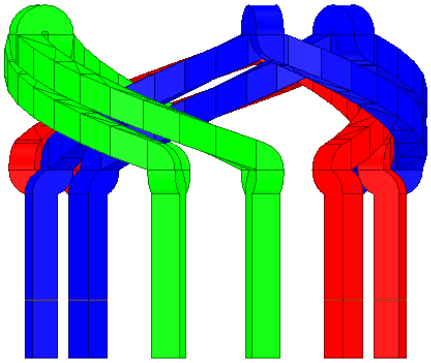

(b) 12s/22p.

Fig. A.3. End winding structure for double-layer FSCW end winding models.

REFERENCES

[ALB13] L. Alberti and N. Bianchi, “Theory and design of fractional-slot multilayer windings,” *IEEE Trans. Ind. Appl*., vol. 49, no. 2, pp. 841-849, Mar./Apr. 2013.

[ALL20] A. Allahyari and H. Torkaman, “A novel high-performance consequent pole dual rotor permanent magnet Vernier machine,” *IEEE Trans. Energy Convers.*, vol. 35, no. 3, pp. 1238–1246, Sep. 2020.

[AME05] J. Amemiya, A. Chiba, D. G. Dorrell, and T. Fukao, “Basic characteristics of a consequent-pole-type bearingless motor,” *IEEE Trans. Magn.*, vol. 41, no. 1, pp. 82-89, Jan. 2005.

[ANS16] ANSI/NEMA MG 1-2016 Motors and Generators. Rosslyn, VA: National Electrical Manufacturers Association, 2016.

[ANS18] *ANSYS*. (2018). Ansys, inc. Accessed: 2018 [online]. Available: https://www.ansys.com.

[ARU13] P. Arumugam, T. Hamiti, and C. Gerada, “Estimation of eddy current loss in semi-closed slot vertical conductor permanent magnet synchronous machines considering eddy current reaction effect,” *IEEE Trans. Magn.*, vol. 49, no. 10, pp. 5326-5335, Oct. 2013.

[ATA00] K. Atallah, D. Howe, P. H. Mellor, and D. A. Stone, “Rotor loss in permanent-magnet brushless AC machines,” *IEEE Trans. Ind. Appl.*, vol. 36, no. 6, pp. 1612-1618, Nov./Dec. 2000.

[BAB20] A. Babl, G. Dajaku, and D. Gerling, “Two new rotor designs with reduced amount of rare-earth magnet material for a permanent magnet wind generator for a 4MW application,” in *Proc. Int. Conf. Electr. Mach.* (ICEM), vol. 1, Aug. 2020, pp. 1944–1949.

[BAN05] D. Ban, D. Zarko, and I. Mandic, “Turbogenerator end-winding leakage inductance calculation using a 3-D analytical approach based on the solution of Neumann Integrals,” *IEEE Trans. Energy Convers*., vol. 20, no. 1, pp. 98-105, Mar. 2005.

[BEC62] K. M. Becker and J. Kaye, “Measurements of diabetic flow in an annulus with an inner rotating cylinder,” *Journ. Heat Transfer,* vol. 84, no. 2, pp. 97-104, 1962.

[BER88] G. Bertotti, “General properties of power losses in soft ferromagnetic materials,” *IEEE Trans. Magn.,* vol. MAG-24, no. 1, pp. 621–630, Jan. 1988.

[BIA04] N. Bianchi, S. Bolognani, and F. Luise, “Potentials and limits of high-speed PM motors,” *IEEE Trans. Ind. Appl.,* vol. 40, no. 6, pp. 1570-1578, Nov./Dec. 2004.

[BIA09a] N. Bianchi, S. Bolognani, D. Bon, and M. Dai Pre, “Rotor flux-barrier design for torque ripple reduction in synchronous reluctance and PM-Assisted synchronous reluctance motors,” *IEEE Trans. Ind. Appl.,* vol. 45, no. 3, pp. 921-928, May/Jun. 2009.

[BIA09b] N. Bianchi and E Fornasiero, “Impact of MMF space harmonic on rotor losses in fractional-slot permanent-magnet machines,” *IEEE Trans. Energy Convers*., Vol. 24, No. 2, pp. 323-328, June 2009.

[BIN75] K. J. Binns, M. A. Jabbar, and W. R. Barnard, “Computation of the magnet field of permanent magnets in iron cores,” Proc. IEE, 1975, 122, (12), pp. 1337-1381.

[BIN78] K. J. Binns, W. R. Barnard, and M. A. Jabbar, “Hybrid permanent-magnet synchronous motors,” Proc, IEE, Vol.125, No.3, 1978, pp. 203-208.

[BOG08] A. Boglietti and A. Cavagnino, “Determination of critical parameters in electrical machine thermal models,” *IEEE Trans. Ind. Appl.*, vol. 44, no. 4, pp. 1150–1159, July/Aug. 2008.

[BRA52] M. W. Brainard, “Synchronous machines with rotating permanent-magnet fields Part I, characteristics and mechanical construction,” AIEE Trans., vol. 71, no. 1, pp. 670–676, Jan. 1952.

[BRO71] A. R. W. Broadway, “Cageless induction machine,” *Proc. IEEE,* vol. 118, no. 11, pp. 1593–1600, Nov. 1971.

[CAI21] S. Cai, Z. Q. Zhu, S. Mallampalli, J.-C. Mipo, and S. Personnaz, “Investigation of novel fractional slot nonoverlapping winding hybrid

excited machines with different rotor topologies," *IEEE Trans. Ind. Appl.*, vol. 57, no. 1, pp. 468–480, Jan. 2021.

[CHA08] K. T. Chau, C. C. Chan, and C. Liu, "Overview of permanent-magnet brushless drives for electric and hybrid electric vehicles," *IEEE Trans. Ind. Electron.*, vol. 55, no. 6, pp. 2246-2257, Jun. 2008.

[CHE11] M. Cheng, K. T. Chau, and C. C. Chan, "Static characteristics of a new doubly salient permanent magnet motor," *IEEE Trans. Energy Convers.*, vol. 16, no. 1, pp. 20-25, Mar. 2001.

[CHE17] M. Cheng and S. Zhu, "Calculation of PM eddy current loss in IPM machine under PWM VSI supply with combined 2-D FE and analytical method," *IEEE Trans. Magn.*, vol. 53, no. 1, pp. 1-12, 2017.

[CHI16] T.W. Ching, K.T. Chau, and W. Li, "Power factor improvement of a linear vernier permanent-magnet machine using auxiliary DC field excitation," *IEEE Trans. Magn.*, vol. 52, no. 7, 2016.

[CHU11] S. U. Chung, J. W. Kim, B. C. Woo, D. K. Hong, J. Y. Lee, and D. H. Koo, "A novel design of modular three-phase permanent magnet Vernier machine with consequent pole rotor," *IEEE Trans. Magn.*, vol. 47, no. 10, pp. 4215–4218, Oct. 2011.

[CHU12] S. Chung, J. Kim, D. Koo, B. Woo, D. Hong, and J. Lee, "Fractional slot concentrated winding permanent magnet synchronous machine with consequent pole rotor for low speed direct drive," *IEEE Trans. Magn.*, vol. 48, no. 11, pp. 2965-2968, Nov. 2012.

[CHU15] S. Chung, J. Kim, Y. Chun, B. Woo, and D. Hong, "Fractional slot concentrated winding PMSM with consequent pole rotor for a low-speed direct drive: Reduction of rare earth permanent magnet," *IEEE Trans. Energy Convers.*, vol. 30, no. 1, pp. 103-109, Mar. 2015.

[COX08] T. Cox, F. Eastham, and J. Proverbs, "End turn leakage reactance of concentrated modular winding stators," *IEEE Trans. Magn.*, vol. 44, no. 11, pp. 4057-4061, Nov. 2008.

[DAJ20] G. Dajaku, "Open-circuit air-gap field calculation of a new PM machine having a combined SPM and spoke-type magnets," *IEEE Trans. Magn.*, vol. 56, no. 6, pp. 1–9, Jun. 2020.

[DEP88] M. Depenbrock, “Direct self-control (DSC) of inverter-fed induction machine,” *IEEE Trans. Power Electron.*, vol. 3, no. 4, pp. 420-429, Oct. 1988.

[DU22] K. Du, L. Xu, W. Zhao, and G. Liu, “Analysis and design of a fault-tolerant permanent magnet Vernier machine with improved power factor,” *IEEE Trans. Ind. Electron.*, vol. 69, no. 5, pp. 4353–4363, May 2022.

[DUB14] F. Dubas and A. Rahideh, “Two-dimensional analytical permanent-magnet eddy-current loss calculations in slotless PMSM equipped with surface-inset magnets,” *IEEE Trans. Magn.*, vol. 50, no. 3, pp. 54-73, Mar. 2014.

[EMAonline] Bunting E-magnets. “Temperature effects on neodymium iron boron magnets.” [Online]. https://e-magnetsuk.com/introduction-toneodymium-magnets/temperature-ratings.

[EVA15] D. Evans, and Z.Q. Zhu, “Novel partitioned stator switched flux permanent magnet machines,” *IEEE Trans. Magn.*, vol. 51, no. 1, pp. 8100114, Jan. 2015.

[FAN22] L. Fang, D. Li, X. Ren, and R. Qu, “A novel permanent magnet Vernier machine with coding-shaped tooth,” *IEEE Trans. Ind. Electron.*, vol. 69, no. 6, pp. 6058–6068, Jun. 2022.

[FAN23] L. Fang, D. Li, and R. Qu, “Torque improvement of Vernier permanent magnet machine with larger rotor pole pairs than stator teeth number,” *IEEE Trans. Ind. Electron.*, vol. 70, no. 12, pp. 12648–12659, Dec. 2023.

[GAI18] Y. Gai, M. Kimiabeigi, Y. C. Chong, J. D. Widmer, J. Goss, U. SanAndres, A. Steven1, and D. A. Staton, “On the measurement and modeling of the heat transfer coefficient of a hollow-shaft rotary cooling system for a traction motor,” *IEEE Trans. Ind. Appl.*, vol. 54, no. 6, pp. 5978-5987, Nov. 2018.

[GAO16] Y. Gao, R. Qu, D. Li, J. Li, and G. Zhou, “Consequent-pole flux-reversal permanent-magnet machine for electric vehicle propulsion,” *IEEE Trans. Appl. Supercond.*, vol. 26, no. 4, Jun. 2016.

[GAR46] M. L. Garik and C. C. Whipple, *Electric Machinery*. New York, USA, D. Van Nostrand Company, 1946.

[GE16] X. Ge, Z. Q. Zhu, J. Li, and J. Chen, “A spoke-type IPM machine with novel alternate airspace barriers and reduction of unipolar leakage flux by step-staggered rotor,” *IEEE Trans. Ind. Appl.*, vol. 52, no. 6, pp. 4789–4797, Nov. 2016.

[GRO15] A. J. Grobler, S. R. Holm, and G. V. Schoor, “A two-dimensional analytic thermal model for a high-speed PMSM magnet,” *IEEE Trans. Ind. Electron.*, vol. 62, no. 11, pp. 6756-6764, 2015.

[HAL80] K. Halbach, “Design of permanent multipole magnets with oriented rare earth cobalt material,” Nucl. Instrum. Methods, vol. 169, pp. 1-10, 1980.

[HAS62] Z. Hashin and S. Shtrikman, “A variational approach to the theory of the effective magnetic permeability of multiphase materials,” *Journ. Appl. Phys.*, vol. 33, no. 10, pp. 3125–3131, Oct. 1962.

[HE21] T. R. He, Z. Q. Zhu, F. X, H. Bin， D. Wu, L. M. Gong, and J. T. Chen, “Comparative study of 6-slot/2-pole high-speed permanent magnet motors with different winding configurations,” *IEEE Tran. Ind. Appl*., vol. 57, no. 6, pp. 5864-5875, Nov./Dec. 2021.

[HE22] T.R. He, Z.Q. Zhu, F. Eastham, Y. Wang, H. Bin, D. Wu, L. Gong, and J. Chen, “Permanent magnet machines for high-speed applications,” *World Electr. Veh. J.*, vol. 13, no. 1, pp. 1-38, 2022.

[HEN94] J. R. Hendershot and T. J. E. Miller, Design of Brushless Permanent Magnet Motors., New York: Oxford Univ. Press, 1994.

[HO11] S. L. Ho, S. Niu, and W. N. Fu, “Design and comparison of Vernier permanent magnet machines,” *IEEE Trans. Magn.*, vol. 47, no. 10, pp. 3280-3283, Oct. 2011.

[HOA97] E. Hoang, A. H. Ben Ahmed, and J. Lucidarme, “Switching flux permanent magnet polyphased synchronous machines,” in *Proc. Eur. Power Electron. Conf.*, vol. 3, pp. 903-908, 1997.

[HON97] Y. Honda, T. Nakamura, T. Higaki, and Y. Takeda, “Motor design considerations and test results of an interior permanent magnet synchronous motor for electric vehicles,” in Proc. 32nd Ind. Appl. Soc. Annu. Meeting, Oct. 1997, pp. 75–82.

[HON19] Q. Hongbo, W. Yanqi, and Y. Ran, “The Influence of unbalance load on the electromagnetic and temperature field of high-speed permanent magnet generator,” *IEEE Trans. Magn.*, vol. 55, no. 6, pp. 1-4, June 2019.

[HSI07] M. F. Hsieh, Y. C. Hsu, D. G. Dorrell, and K. H. Hu, “Investigation on end winding inductance in motor stator windings,” *IEEE Trans. Magn.*, vol. 43, no. 6, pp. 2513-2515, Jun. 2007.

[HUA18] W. Hua, X. Zhu, and Z. Wu, “Influence of coil pitch and stator-slot/rotor-pole combination on back-EMF harmonics in flux-reversal permanent magnet machines,” *IEEE Trans. Energy Convers*., vol. 33, no. 3, pp. 1330-1341, Sep. 2018.

[HUA24] J. Huang, W. Fu, S. Niu, and X. Zhao, “Analysis of a complementary dual-stator vernier machine with reduced non-working harmonics for low-speed direct-drive applications,” *IEEE Trans. Energy Convers.*, vol. 39, no. 1, pp. 711-721, Mar. 2024.

[ISH95] A. Ishizaki, T. Tanaka, K. Takasaki, and S. Nishikata, “Theory and optimum design of PM vernier motor,” in *Proc. Seventh Int. Conf. Elect. Mach. Drives*, 1995, pp. 208–212.

[ISH05] D. Ishak, Z. Q. Zhu, and D. Howe, “Eddy-current loss in the rotor magnets of permanent-magnet brushless machines having a fractional number of slots per pole,” *IEEE Trans. Magn.*, vol. 41, no. 9, pp. 2462-2469, 2005.

[JAN14] D.-K. Jang and J.-H. Chang, “Design of a vernier machine with PM on both sides of rotor and stator,” *IEEE Trans. Magn.*, vol. 50, no. 2, 2014.

[JAN19] D. Jang and J. Chang, “Investigation of doubly salient structure for permanent magnet Vernier machines using field modulation effects,” *IEEE Trans. Energy Convers.*, vol. 34, no. 4, pp. 2019-2028, Dec. 2019.

[JIA17] S. Jia, R. Qu, J. Li, D. Li, and W. Kong, “A stator-PM consequent-pole vernier machine with hybrid excitation and DC-biased sinusoidal current,” *IEEE Trans. Magn.*, vol. 53, no. 6, 2017.

[JIA18] S. Jia, R. Qu, W. Kong, D. Li, J. Li, Z. Yu, and H. Fang, ‘‘Hybrid excitation stator PM Vernier machines with novel DC-biased sinusoidal armature current,’’ *IEEE Trans. Ind. Appl.*, vol. 54, no. 2, pp. 1339–1348, Mar. 2018.

[JIN22] L. Jing, W. Tang, T. Wang, T. Ben, and R. Qu, “Performance analysis of magnetically geared permanent magnet brushless motor for hybrid electric vehicles,” *IEEE Trans. Transp. Electrific.*, vol. 8, no. 2, pp. 2874–2883, Jun. 2022.

[KAM07] M. Kamiya, Y. Kawase, T. Kosaka, and N. Matsui, “Temperature distribution analysis of permanent magnet in interior permanent magnet synchronous motor considering PWM carrier harmonics,” *Proc. Int. Conf. Elect. Mach. Syst.*, 2007, pp. 2023-2027.

[KAW00] Y. Kawase, T. Ota, and H. Fukunaga, “3-D eddy current analysis in permanent magnet of interior permanent magnet motors,” *IEEE Trans. Magn.*, vol. 36, no. 4, pp. 1863-1866, July 2000.

[KIM14] B. Kim and T. A. Lipo, “Operation and design principles of a PM Vernier motor,” *IEEE Trans. Ind. Appl.*, vol. 50, no. 6, pp. 3656–3663, Nov./Dec. 2014.

[KIM16] B. Kim and T. A. Lipo, “Analysis of a PM Vernier motor with spoke structure,” *IEEE Trans. Ind. Appl.*, vol. 52, no. 1, pp. 217–225, Jan. 2016.

[KRA14] C. Kral, A. Haumer, and S. B. Lee, “A practical thermal model for the estimation of permanent magnet and stator winding temperatures,” *IEEE Trans. Power Electron.*, vol. 29, no. 1, pp. 455-464, 2014.

[KYL95] G. Kylander, “Thermal modelling of small cage induction motors,” Ph.D. dissertation, Chalmers Univ. Technology, Göteborg, Sweden, 1995.

[LEE63] C. H. Lee, “Vernier motor and its design,” *IEEE Trans. Power App. Syst.*, vol. 82, no. 66, pp. 343–349, Jun. 1963.

[LI10] J. Li, K. T. Chau, J. Z. Jiang, C. Liu, and W. Li, “A new efficient permanent magnet Vernier machine for wind generation,” *IEEE Trans. Magn.*, vol. 46, no. 6, pp. 1475–1478, Jun. 2010.

[LI14a] D. Li, R. Qu, and T. A. Lipo, “High power factor vernier permanent magnet machines,” *IEEE Trans. Ind. Appl.*, vol. 50, no. 6, pp. 3664-3674, Nov./Dec. 2014.

[LI14b] D. Li, R. Qu and Z. Zhu, “Comparison of Halbach and dual-side vernier permanent magnet machines,” *IEEE Trans. Magn.*, vol. 50, no. 2, 2014.

[LI15a] D. Li, R. Qu, J. Li, and W. Xu, “Consequent-pole toroidal-winding outer-rotor vernier permanent-magnet machines,” *IEEE Trans. Ind. Appl.*, vol. 51, no. 6, pp. 4470-4481, 2015.

[LI15b] D. Li, R. Qu, W. Xu, J. Li, and T. A. Lipo, “Design procedure of dual-stator spoke-array vernier permanent-magnet machines,” *IEEE Trans. Ind. Appl.*, vol. 51, no. 4, pp. 2972-2983, 2015.

[LI16] D. Li, R. Qu, J. Li, L. Wu, and W. Xu, “Analysis of torque capability and quality in vernier permanent magnet machines,” *IEEE Trans. Ind. Appl*., vol. 52, no. 1, pp. 125-135, Jan./Feb. 2016.

[LI17] W. Li, T.W. Ching, and K.T. Chau, “A hybrid-excited vernier permanent magnet machine using homopolar topology,” *IEEE Trans. Magn.*, vol. 53, no. 11, 2017.

[LI18a] J. Li and K. Wang, “Analytical determination of optimal PM-arc ratio of consequent-pole permanent magnet machines,” *IEEE/ASME Trans. Mechatronics*, vol. 23, no. 5, pp. 2168–2177, Oct. 2018.

[LI18b] D. Li, T. Zou, R. Qu, and D. Jiang, “Analysis of fractional-slot concentrated winding PM vernier machines with regular open-slot stators,” *IEEE Trans. Ind. Appl*., vol. 54, no. 2, pp. 1320-1330, Mar./Apr. 2018.

[LI18c] H. Y. Li and Z. Q. Zhu, “Analysis of flux-reversal permanent-magnet machines with different consequent-pole PM topologies,” *IEEE Trans. Magn.*, vol. 54, no. 11, Nov. 2018.

[LI19a] J. Li, K. Wang, and C. Liu, “Comparative study of consequent-pole and hybrid-pole permanent magnet machines,” *IEEE Trans. Energy Convers.*, vol. 34, no. 2, pp. 701–711, Jun. 2019.

[LI19b] J. Li and K. Wang, “A novel spoke-type PM machine employing asymmetric modular consequent-pole rotor,” *IEEE/ASME Trans. Mechatronics*, vol. 24, no. 5, pp. 2182–2192, Oct. 2019.

[LI19c] H. Li, Z. Q. Zhu, and Y. Liu, “Optimal number of field modulation pole in vernier permanent magnet synchronous machines,” *IEEE Trans. Ind. Appl.*, vol. 55, no. 6, pp. 5747-5757, Nov. /Dec. 2019.

[LI19d] J. Li, K. Wang, F. Li, S. S. Zhu, and C. Liu, “Elimination of even-order harmonics and unipolar leakage flux in consequent-pole PM machines by

employing N-S-Iron–S-N-iron rotor," *IEEE Trans. Ind. Electron*., vol. 66, no. 3, pp. 1736-1747, Mar. 2019.

[LI19e] F. Li, K. Wang, J. Li, and H. Y. Sun, "Electromagnetic performance analysis of consequent-pole PM machine with asymmetric magnetic pole," *IEEE Trans. Magn.*, vol. 55, no. 6, Jun. 2019.

[LI20] J. Li, K. Wang, and H. Zhang, "Flux-focusing permanent magnet machines with modular consequent-pole rotor," *IEEE Trans. Ind. Electron.*, vol. 67, no. 5, pp. 3374–3385, May 2020.

[LI21] Y. Li, H. Yang, H. Lin, L. Qin, and S. Lyu, "Investigation of double-side field modulation mechanism in consequent-pole PM machines with concentrated windings," *IEEE Trans. Energy Convers.*, vol. 36, no. 3, pp. 1635–1648, Sep. 2021.

[LI22] Y. Li, Q. Zhou, J. Hang, W. Li, and S. Ding, "Investigation of torque contributions of main-order working harmonics in consequent-pole PM vernier machines," in *Proc. IEEE 5th Int. Elect. Energy Conf.*, 2022, pp. 4853-4858.

[LI23a] Y. Li, H. Yang, H. Lin, and Z. Zhao, "Comparative study of field modulation effects in consequent-pole PM machines with different stator slot configurations," *IEEE Trans. on Magn.*, vol. 59, no. 11, pp. 1-6, Nov. 2023.

[LI23b] Y. Li, H. Yang, H. Lin, S. Ding, J. Hang, and W. Li, "Influences of Magnet Arrangements on Air-Gap Field Modulation Effects in Interior Consequent-Pole PM Machines," *IEEE Trans. Transp. Electrific.*, vol. 9, no. 1, pp. 819-832, Mar. 2023.

[LIA19] D. Liang, Z. Q. Zhu, J.H. Feng, S.Y. Guo, Y.F. Li, J.Q. Wu, and A.F. Zhao, "Influence of critical parameters in lumped-parameter thermal models for electrical machines," in *Conf. Electr. Machines and Syst.* (ICEMS), Harbin, China, 2019, pp. 1-6.

[LIA21] D. Liang, Z. Q. Zhu, Y. Zhang, J. Feng, S. Guo, Y. Li, Y.F. Li, J.Q. Wu, and A.F. Zhao, "A hybrid lumped-parameter and two-dimensional analytical thermal model for electrical machines," *IEEE Trans. Ind. Appl.*, vol. 57, no. 1, pp. 246-258, 2021.

[LIA22a] D. Liang, Z. Q. Zhu, J. Feng, S. Guo; Y. Li, A. Zhao, and J. Hou, "Estimation of 3-D magnet temperature distribution based on lumped-parameter and analytical hybrid thermal model for SPMSM," *IEEE Trans. Energy Convers.*, vol. 37, no. 1, pp. 515-525, 2022.

[LIA22b] D. Liang, Z. Q. Zhu, B. Saho, J. Feng, S. Guo; Y. Li, and A. Zhao, "Estimation of two- and three-dimensional spatial magnet temperature distributions for interior PMSMs based on hybrid analytical and lumped-parameter thermal model," *IEEE Trans. Energy Convers.*, vol. 37, no. 3, pp. 2175-2189, Sept. 2022.

[LIA22c] D. Liang, Z. Q. Zhu, B. Saho, J. Feng, S. Guo; Y. Li, and A. Zhao, "Tracking of winding and magnet hotspots in SPMSMs based on synergized lumped-parameter and sub-domain thermal models," *IEEE Trans. Energy Convers.*, vol. 37, no. 3, pp. 2147-2161, Sept. 2022.

[LIB06] F. Libert and J. Soulard, ''Manufacturing methods of stator cores with concentrated windings,'' in *Proc. 3rd IET Int. Conf. Power Electron., Mach. Drives*, Apr. 2006, pp. 676-680.

[LIU14] C. Liu, K. T. Chau, and Q. Chun, "Design and analysis of a new magnetic geared memory machine," *IEEE Trans. Appl. Supercond.*, vol. 24, no. 3, p. 0503005, Jun. 2014.

[LIU16] X. D. Liu, H. Z. Hu, J. Zhao, A. Belahcen, and L. Tang, "Armature reaction field and inductance calculation of ironless BLDC motor," *IEEE Trans. Magn.*, vol. 52, no. 2, Feb. 2016.

[LIU17] Y. Liu and Z. Q. Zhu, "Comparative study of magnetic gearing effect in integral slot, fractional slot winding and Vernier PM machines," in *Proc. 20th Int. Conf. Electr. Mach. Syst.* (ICEMS), Aug. 2017, pp. 1–6.

[LIU18a] W. Liu and T.A. Lipo, "Analysis of consequent pole spoke type vernier permanent magnet machine with alternative flux barrier design," *IEEE Trans. Ind. Appl.*, vol. 54, no. 6, pp. 5918-5929, 2018.

[LIU18b] Y. Liu, H. Y. Li, and Z. Q. Zhu, "A high-power factor vernier machine with coil pitch of two slot pitches," *IEEE Trans. Magn.*, vol. 54, no. 11, Nov. 2018.

[LIU18c] W. Liu and T. A. Lipo, “Analysis of consequent pole spoke type Vernier permanent magnet machine with alternating flux barrier design,” *IEEE Trans. Ind. Appl.*, vol. 54, no. 6, pp. 5918–5929, Nov. 2018.

[LIU19] Y. Liu and Z. Q. Zhu, “Influence of gear ratio on the performance of fractional slot concentrated winding permanent magnet machines,” *IEEE Trans. Ind. Electron.*, vol. 66, no. 10, pp. 7593–7602, Oct. 2019.

[LIU23] C. Liu, Z. Chao, S. Wang, and Y. Wang, “Design and Performance Analysis of Permanent Magnet Claw Pole Machine with Hybrid Cores,” *CES Trans. Electr. Mach. Syst.*, vol. 7, no. 3, pp. 275-283, Sept. 2023.

[LU20] Q. Lu, R. Muthukumar, H. Ge, and S. Parameswaran, “Numerical study of a rotating liquid jet impingement cooling system,” *Heat and Mass Transfer*. Dec. 2020.

[MA19] J. Ma and Z.Q. Zhu, “Magnet eddy current loss reduction in permanent magnet machines,” *IEEE Trans. Ind. Appl.*, vol. 55, no. 2, pp. 1309-1320, Mar./April 2019.

[MAR08] M. Markovic and Y. Perriard, “Analytical solution for rotor eddy-current losses in a slotless permanent-magnet motor: the case of current sheet excitation,” *IEEE Trans. Magn.*, vol. 44, no. 3, pp. 386-393, March 2008.

[MEL91] P. H. Mellor, D. Roberts, and D. R. Turner, “Lumped parameter thermal model for electrical machines of TEFC design,” *IEE Proc. B, Electr. Power Appl.*, vol. 138, no. 5, pp. 205–218, Sept. 1991.

[NAI16] S. S. Nair, J. Wang, L. Chen, R. Chin, I. Manolas, and D. Svechkarenko, “Computationally efficient 3-D eddy current loss prediction in magnets of interior permanent magnet machines,” *IEEE Trans. Magn.*, vol. 52, no. 10, pp. 1-10, Oct. 2016.

[NAT13] S. Nategh, Z. Huang, A. Krings, O. Wallmark and M. Leksell, “Thermal modeling of directly cooled electric machines using lumped parameter and limited CFD analysis,” *IEEE Trans. Energy Convers.*, vol. 28, no. 4, pp. 979-990, Dec. 2013.

[NIU10] S. Niu, S. L. Ho, W. N. Fu, and L. L. Wang, “Quantitative comparison of novel Vernier permanent magnet machines,” *IEEE Trans. Magn.*, vol. 46, no. 6, pp. 2032–2035, Jun. 2010.

[NIU14] S. Niu, S. L. Ho, and W. N. Fu, “A novel stator and rotor dual PM vernier motor with space vector pulse width modulation,” *IEEE Trans. Magn.*, vol. 50, no. 2, pp. 805-808, 2014.

[OKA13] K. Okada, N. Niguchi, and K. Hirata, “Analysis of a Vernier motor with concentrated windings,” *IEEE Trans. Magn.*, vol. 49, no. 5, pp. 2241–2244, May 2013.

[ONS17] M. Onsal, Y. Demir, and M. Aydin, “A new nine-phase permanent magnet synchronous motor with consequent pole rotor for high-power traction applications,” *IEEE Trans. Magn.*, vol. 53, no. 11, Nov. 2017.

[ONS18] M. Onsal, B. Cumhur, Y. Demir, E. Yolacan, and M. Aydin, “Rotor design optimization of a new flux-assisted consequent pole spoke type permanent magnet torque motor for low-speed applications,” *IEEE Trans. Magn.*, vol. 54, no. 11, pp. 1–5, Nov. 2018.

[OU19] J. Ou, Y. Liu, D. Liang, and M. Doppelbauer, “Investigation of PM eddy current losses in surface-mounted PM motors caused by PWM,” *IEEE Trans. Power Electron.*, vol. 34, no. 11, pp. 11253-11263, Nov. 2019.

[OU21] J. Ou, Y. Liu, and M. Doppelbauer, “Comparison study of a surface-mounted PM rotor and an interior PM rotor made from amorphous metal of high-speed motors,” *IEEE Trans. Ind. Electron.*, vol. 68, no. 10, pp. 9148-9159, Oct. 2021.

[PEL12] G. Pellegrino, A. Vagati, P. Guglielmi, and B. Boazzo, “Performance comparison between surface-mounted and interior PM motor drives for electric vehicle application,” *IEEE Trans. Ind. Electron.*, vol. 59, no. 2, pp. 803-811, 2012.

[PIL91] P. Pillay, and R. Krishnan, “Application characteristics of permanent magnet synchronous and brushless dc motors for servo drives,” *IEEE Trans. Ind. Appl.*, vol. 27, no. 5, pp. 986-996, September/October 1991.

[POL13] H. Polinder, J. A. Ferreira, B. B. Jensen, A. B. Abrahamsen, K. Atallah, and R. A. McMahon, “Trends in wind turbine generator systems,” *IEEE J. Emerg. Sel. Top. Power Electron.*, vol. 1, no. 3, pp. 174-185, Sept. 2013.

[POT14] H. J. Potgieter and M. J. Kamper, “Calculation methods and effects of end-winding inductance and permanent-magnet end flux on performance

prediction of nonoverlap winding permanent-magnet machines," *IEEE Trans. Ind. Appl.*, vol. 50, no. 4, pp. 2458-2466, Jul./Aug. 2014.

[QI22a] J. Qi., Z. Q. Zhu, L. C. Yan, G. W. Jewell, C. Gan, Y. Ren, S. Brockway, and C. Hilton, "Effect of pole shaping on torque characteristics of consequent pole PM machines," *IEEE Trans. Ind. Appl.*, vol. 58, no. 3, pp. 3511-3521, May-Jun. 2022.

[QI22b] J. Qi., Z. Q. Zhu, L. C. Yan, G. W. Jewell, C. Gan, Y, Ren, S. Brockway, and C. Hilton, "Suppression of torque ripple for consequent pole PM machine by asymmetric pole shaping method," *IEEE Trans. Ind. Appl.*, vol. 58, no.3, 3545–3557, March 2022.

[RED12] P. B. Reddy, A. M. El-Refaie, K. Huh, J. K. Tangudu, and T. M. Jahns, "Comparison of interior and surface PM machines equipped with fractional-slot concentrated windings for hybrid traction applications," *IEEE Trans. Energy Convers.*, vol. 27, no. 3, pp. 593-602, Sept. 2012.

[REF04] A. M. EL-Refaie, N. C. Harris, T. M. Jahns, and K. M. Rahman, "Thermal analysis of multibarrier interior PM synchronous machine using lumped parameter model," *IEEE Trans. Energy Convers.*, vol. 19, no. 2, pp. 303-309, 2004.

[REF05] A. M. El-Refaie and T. M. Jahns, "Optimal flux weakening in surface PM machines using fractional slot concentrated windings," *IEEE Trans. Ind. Appl.*, vol. 41, no. 3, pp. 790–800, May/Jun. 2005.

[REF06] A. M. El-Refaie and T. M. Jahns, "Analysis of surface permanent magnet machines equipped with concentrated windings," *IEEE Trans. Energy Convers.*, vol. 21, no. 1, pp. 34–43, Mar. 2006.

[REF08] A. M. El-Refaie, Z. Q. Zhu, T. M. Jahns, and D. Howe, "Winding inductances of fractional slot surface-mounted permanent magnet brushless machines," in *Proc. IEEE IAS Annu. Meet.*, pp. 1-8, 2008.

[REF10] A. M. EL-Refaie, "Fractional-slot concentrated-windings synchronous permanent magnet machines: opportunities and challenges," *IEEE Trans. Ind. Electron.*, vol. 57, no. 1, pp. 107–121, Jan. 2010.

[REN18] X. Ren, D. Li, R. Qu, Z. Yu, and Y. Gao, “Investigation of spoke array permanent magnet Vernier machine with alternate flux bridges,” *IEEE Trans. Energy Convers.*, vol. 33, no. 4, pp. 2112–2121, Dec. 2018.

[SIM13] N. Simpson, R. Wrobel, and P.H. Mellor, “Estimation of equivalent thermal parameters of impregnated electrical windings,” *IEEE Trans. Ind. Appl.*, vol. 49, no. 6, pp. 2505–2515, Nov./Dec. 2013.

[SIM14] N. Simpson, R. Wrobel, and P. H. Mellor, “A general arc-segment element for three-dimensional thermal modeling,” *IEEE Trans. Magn.*, vol. 50, no. 2, pp. 265-268, Feb. 2014.

[STR52] F. Strauss, “Synchronous machines with rotating permanent-magnet fields, part II, magnetic and electrical design considerations,” AIEE Trans., vol. 71, pp. 887–893, Oct. 1952.

[SUN19] H. Y. Sun and K. Wang, “Space harmonics elimination for fractional-slot windings with two-slot coil pitch,” *IEEE Access*, vol. 7, pp. 106961-106972, 2019.

[TAN20] H.Tang, M.Zhang, Y.Dong, W.Li, and, L. Li, “Influence of the opening width of stator semi-closed slot and the dimension of the closed slot on the magnetic field distribution and temperature field of the permanent magnet synchronous motor,” *IET Electr.Power Appl.*, 2020,14, 1642–1652.

[TAP03] J. A. Tapia, F. Leonardi, and T. A. Lipo, “Consequent-pole permanent magnet machine with extended field-weakening capability,” *IEEE Trans. Ind. Appl.*, vol. 39, no. 6, pp. 1704–1709, Nov./Dec. 2003.

[TOB00] A. Toba and T. A. Lipo, ‘‘Generic torque-maximizing design methodology of surface permanent-magnet Vernier machine,’’ *IEEE Trans. Ind. Appl.*, vol. 36, no. 6, pp. 1539–1546, Nov./Dec. 2000.

[TOB99] A. Toba and T. Lipo, “Novel dual-excitation permanent magnet vernier machine,” in *Proc. Conf. Rec. 34th IEEE IAS Annu. Meeting*, vol. 4, Oct. 1999, pp. 2539–2544.

[TON21] W. Tong, R. Sun, S. Li, and R. Tang, “Loss and thermal analysis for high-speed amorphous metal PMSMs using 3-D electromagnetic-thermal bi-directional coupling,” *IEEE Trans. Energy Convers.*, vol. 36, no. 4, pp. 2839-2849, Dec. 2021.

[TON22] W. Tong, L. Sun, S. Wu, M. Hou, and R. Tang, “Analytical model and experimental verification of permanent magnet eddy current loss in permanent magnet machines with nonconcentric magnetic poles,” *IEEE Trans. Ind. Electron.*, vol.69, no.9, pp.8815-8824, 2022.

[VU13] H. Vu Xuan, D. Lahaye, H. Polinder, and J. A. Ferreira, “Influence of stator slotting on the performance of permanent-magnet machines with concentrated windings,” *IEEE Trans. Magn.*, vol. 49, no. 2, pp. 929–938, Feb. 2013.

[WAN01] C. X. Wang, I. Boldea, and S. A. Nasar, “Characterization of three phase flux reversal machine as an automotive generator,” *IEEE Trans. Energy Convers.*, vol. 16, no. 1, pp. 74-80, Mar. 2001.

[WAN14a] J. Wang, V. I. Patel, and W. Wang, “Fractional-slot permanent magnet brushless machines with low space harmonic contents,” *IEEE Trans. Magn.*, vol. 50, no. 1, Jan. 2014.

[WAN14b] K. Wang, Z. Q. Zhu and G. Ombach, “Synthesis of high performance fractional-slot permanent-magnet machines with coil-pitch of two slot-pitches,” *IEEE Trans. Energy Convers.*, vol. 29, no. 3, pp. 758-770, Sep. 2014.

[WAN17a] Q. Wang, S. Niu, and L. Yang, “Design optimization and comparative study of novel dual-PM excited machines,” *IEEE Trans. Ind. Electron.*, vol. 64, no. 12, pp. 9924–9933, Dec. 2017.

[WAN17b] H. Wang, S. H. Fang, H. yang, H. Y. Lin, D. Wang, Y. B. Li, and C. X. Jiu, ‘‘A novel consequent-pole hybrid excited Vernier machine,’’ *IEEE Trans. Magn.*, vol. 53, no. 11, pp. 1–4, Nov. 2017.

[WAN19] K. Wang, J. Li, S. S. Zhu, and C. Liu, “Novel hybrid-pole rotors for consequent-pole PM machines without unipolar leakage flux,” *IEEE Trans. Ind. Electron.*, vol. 66, no. 9, pp. 6811–6823, Sep. 2019.

[WRO10] R. Wrobel and P. H. Mellor, “A general cuboidal element for three-dimensional thermal modelling,” *IEEE Trans. Magn.*, vol. 46, no. 8, pp. 3197-3200, Aug. 2010.

[WU12] L. J. Wu, Z. Q. Zhu, D. Staton, M. Popescu, and D. Hawkins, “Analytical model for predicting magnet loss of surface-mounted permanent magnet

machines accounting for slotting effect and load," *IEEE Trans. Magn.*, vol. 48, no. 1, pp. 107–117, Jan. 2012.

[WU14a] L. L. Wu, R. H. Qu, and D. W. Li, "Reduction of rotor eddy-current losses for surface PM machines with fractional slot concentrated windings and retaining sleeve," *IEEE Trans. Magn*., vol. 50, no. 11, Nov. 2014.

[WU14b] L. Wu and R. Qu, "Comparison of conventional and consequent pole interior permanent magnet machines for electric vehicle application," in *Proc. 17th. Int. Conf. Electr. Mach. Syst.*, Oct. 2014, pp. 70–74.

[WU15a] Z. Z. Wu, Z. Q. Zhu, "Analysis of Air-gap field modulation and magnetic gearing effects in switched flux permanent magnet machines," *IEEE Trans. Magn.*, vol.51, no.5, pp.1-12, 2015.

[WU15b] Z. Z. Wu and Z. Q. Zhu, "Partitioned stator flux reversal machine with consequent-pole PM stator," *IEEE Trans. Energy Convers.*, vol. 30, no. 4, pp. 1472-1482, Dec. 2015.

[WU15c] L. Wu, R. Qu, D. Li, and Y. Gao, ''Influence of pole ratio and winding pole numbers on performance and optimal design parameters of surface permanent-magnet Vernier machines,'' *IEEE Trans. Ind. Appl.*, vol. 51, no. 5, pp. 3707–3715, Sep. 2015.

[WU16] Z. Z. Wu and Z. Q. Zhu, "Comparative analysis of end effect in partitioned stator flux reversal machines having surface-mounted and consequent pole permanent magnets," *IEEE Trans. Magn.*, vol. 52, no. 7, Jul. 2016.

[WU17] L. Wu, R. Qu, and D. Li, "Analysis of eddy current losses in surface-mounted permanent magnet vernier machines," in *Proc. IEEE Int. Conf. Elect. Mach. Drives*, pp. 1-6, 2017.

[XIA22] Z. Xiang, W. Pu, X. Zhu, and L. Quan, "Design and analysis of a V-shaped permanent magnet Vernier motor for high torque density," *CES Trans. Elect. Mach. Syst.*, vol. 6, no. 1, pp. 20–28, Mar. 2022.

[XIE17] K. Xie, D. Li, R. Qu, and Y. Gao, "A novel permanent magnet vernier machine with Halbach array magnets in stator slot opening," *IEEE Trans. Magn.*, vol. 53, no. 6, 2017.

[XIE19] K. Xie, D. Li, R. Qu, X. Ren, M. R. Shah, and Y. Pan, “A new perspective on the PM Vernier machine mechanism,” *IEEE Trans. Ind. Appl.*, vol. 55, no. 2, pp. 1420-1429, Mar. 2019.

[XU15] L. Xu, G. H. Liu, W. X. Zhao, J. H. Ji, H. W. Zhou, W. X. Zhao, and T. T. Jiang, “Quantitative comparison of integral and fractional slot permanent magnet vernier motors,” *IEEE Trans. Energy Convers*., vol. 30, no. 4, pp. 1483-1495, Dec 2015.

[XU16] L. Xu, G. Liu, W. Zhao, J. Ji, and X. Fan, “High-performance fault tolerant Halbach permanent magnet vernier machines for safety-critical applications,” *IEEE Trans. Magn.*, vol. 52, no. 7, 2016.

[XU17] G. Xu, G. Liu, M. Chen, X. Du, and M. Xu, “Cost-effective Vernier permanent-magnet machine with high torque performance,” *IEEE Trans. Magn.*, vol. 53, no. 11, pp. 1-4, Nov. 2017.

[XU21] G. Xu, W. Zhao, G. Liu, F. Zhai, and Q. Chen, “Torque performance improvement of consequent-pole PM motors with hybrid rotor configuration,” *IEEE Trans. Trans. Electrific.*, vol. 7, no. 3, pp. 1561–1572, Sep. 2021.

[XU22] B. Xu, Q. Wu, J. Ma, L. Wu, L. Qiu, X. Liu, and Y. Fang, “Research on the influence of end turn length on consequent-pole Vernier permanent-magnet machines,” *IEEE Trans. Magn.*, vol. 58, no. 2, pp. 1-9, 2022.

[XU23] L. Xu, Y. Li, W. Zhao, and G. Liu, “Reduction of unipolar leakage flux and torque ripple in consequent-pole PM vernier machine,” *CES Trans. Elect. Mach. Syst.*, vol. 7, no. 1, pp. 35-44, 2023.

[XUE17] S. Xue, “Investigation of iron losses in permanent magnet machines accounting for temperature effect,” Ph.D. dissertation, Dept. Electron. Elec. Eng., Univ. Sheffield, Sheffield, U.K., 2017.

[YAM09] K. Yamazaki and A. Abe, “Loss investigation of interior permanent magnet motors considering carrier harmonics and magnet eddy currents,” *IEEE Trans. Ind. Appl.*, vol. 45, no. 2, pp. 659–665, Mar./Apr. 2009.

[YAN13] J. Yang et al., “Quantitative comparison for fractional-slot concentrated-winding configurations of permanent-magnet Vernier machines,” *IEEE Trans. Magn.*, vol. 49, no. 7, pp. 3826–3829, Jul. 2013.

[YAN14] H. Yang, H. Lin, Z. Q. Zhu, S. Fang, and Y. Huang, “Novel flux-regulatable dual-magnet vernier memory machines for electric vehicle propulsion,” *IEEE Trans. Appl. Supercond.*, vol. 24, no. 5, 2014.

[YAN20a] H. Yang, Z. Q. Zhu, H. Lin, H. Li, and S. Lyu, “Analysis of consequent-pole flux reversal permanent magnet machine with biased flux modulation theory,” *IEEE Trans. Ind. Electron.*, vol. 67, no. 3, pp. 2107–2121, Mar. 2020.

[YAN20b] H. Yang, H. Lin, Z. Q. Zhu, S. Lyu, and Y. Liu, “Design and analysis of novel asymmetric-stator-pole flux reversal PM machine,” *IEEE Trans. Ind. Electron.*, vol. 67, no. 1, pp. 101–114, Jan. 2020.

[YAN21] K. Yang, F. Zhao, Y. Wang, and Z. Bao, “Consequent-pole flux reversal permanent magnet machine with Halbach array magnets in rotor slot,” *IEEE Trans. Magn.*, vol. 57, no. 2, Feb. 2021.

[YU19] Y. Yu, F. Chai, Y. Pei, and L. Chen, “Comparisons of torque performance in surface-mounted PM vernier machines with different stator tooth topologies,” *IEEE Trans. Ind. Appl.*, vol. 55, no. 4, pp. 3671-3684, Jul.-Aug. 2019.

[ZHA14a] F. Zhao, T. A. Lipo, and B.-I. Kwon, “A novel dual-stator axial-flux spoke-type permanent magnet Vernier machine for direct-drive applications,” *IEEE Trans. Magn.*, vol. 50, no. 11, pp. 1–4, Nov. 2014.

[ZHA14b] Y. Zhao, B. Yan, C. Chen, J. Deng, and Q. Zhou, “Parametric study on dynamic characteristics of turbogenerator stator end winding,” *IEEE Trans. Energy Convers.*, vol. 29, no. 1, pp. 129-137, Mar. 2014.

[ZHA16] W. Zhao, X. Sun, J. Ji, and G. Liu “Design and analysis of new vernier permanent-magnet machine with improved torque capability,” *IEEE Trans. Appl. Supercond.*, vol. 26, no. 4, 2016.

[ZHA18] Y. Zhang, S. McLoone, and W. Cao, “Electromagnetic loss modeling and demagnetization analysis for high speed permanent magnet machine,” *IEEE Trans. Magn.*, vol. 54, no. 3, pp. 1-5, 2018.

[ZHA19] L. Zhang, K. Wang, J. Li, and F. Li, “Comparison study of interior permanent magnet synchronous machine with conventional and consequent pole rotor,” in *Proc. 22nd Int. Conf. Elect. Mach. Syst.*, Aug. 2019, pp. 1–5.

[ZHA20] H. Zhao, C. Liu, and Z. Song, "Design of an effective double-rotor machine with robust mechanical structure," *IEEE Trans. Magn.*, vol. 56, no. 1, pp. 1-7, Jan. 2020.

[ZHA22] Y. Zhang, D. Li, P. Yan, X. Ren, R. Qu, and J. Ma, "A High torque density claw-pole permanent-magnets Vernier machine," *IEEE Trans. Emerg. Sel. Topics Power Electron.*, vol. 10, no. 2, pp. 1756–1765, Apr. 2022.

[ZHE22] Y. Zheng, D. Liang, Z. Q. Zhu, H. Liu, and Y. Zhou, "Effect of armature reaction on asymmetric PM loss and temperature distributions in V-shape interior permanent magnet synchronous machines," in *2nd Int. Conf. Sustain. Mobility Appl., Renew. Tech. (SMART)*, 2022, pp. 1-10.

[ZHE23] Y. Zheng, Z. Q. Zhu, D. Liang, Y. Zhou, H. Liu, and L. Chen, "Analysis and reduction of unipolar end leakage flux in consequent-pole Vernier and fractional slot PM machines," *Proc. IEEE Int. Electric Mach. Drives Conf.*, San Francisco, USA, 15-18 May 2023, pp. 1-7.

[ZHO19a] H. Zhou, W. Tao, C. Zhou, Y. Mao, G. Li, and G. Liu, "Consequent pole permanent magnet vernier machine with asymmetric air-gap field distribution," *IEEE Access*, vol. 7, pp. 109340-109348, 2019.

[ZHO19b] R. Zhou, G. J. Li, Z. Q. Zhu, Y. X. Li, M. P. Foster, and D. A. Stone, "Investigation of integer/fractional slot consequent pole PM machines with different rotor structures," in *Proc. IEEE Int. Electr. Mach. Drives Conf.* (IEMDC), May 2019, pp. 119–126.

[ZHO22] H. Zhou, W. Tao, G. Jiang, G. Li, and G. Liu, "Reduction of saturation and unipolar leakage flux in consequent-pole PMV machine," *IEEE J. Emerg. Sel. Topics Power Electron.*, vol. 10, no. 2, pp. 1870–1880, Apr. 2022.

[ZHU94] Z. Q. Zhu, D. Howe, and T. S. Birch, "Calculation of winding inductances of brushless motors with surface-mounted permanent magnets," in *Proc. Int. Conf. of Elect. Mach. (ICEM)*, pp. 327-332, Paris, 1994.

[ZHU01] Z. Q. Zhu, and D. Howe, "Halbach permanent magnet machines and applications: a review," *IEE Proc. Elect. Power Appl.*, vol. 148, no. 4, pp. 299-308, 2001.

[ZHU04] Z. Q. Zhu, K. Ng, and N. Schofield, "Improved analytical modelling of rotor eddy current loss in brushless machines equipped with surface mounted

permanent magnets," *IEE P-Elect. Power Appl.,* vol. 151, no. 6, pp. 641–650, Jul. 2004.

[ZHU07] Z. Q. Zhu and D. Howe, "Electrical machines and drives for electric, hybrid, and fuel cell vehicles" *Proc. IEEE,* vol. 95, no. 4, pp. 746-765, April 2007.

[ZHU09] Z. Q. Zhu, "A simple method for measuring cogging torque in permanent magnet machines," *IEEE Power Energy Soc. Gen. Meet*., pp. 3–6, Oct. 2009.

[ZHU17] Z. Q. Zhu, H. Hua, A. Pride, R. Deodhar, and T. Sasaki, "Analysis and reduction of unipolar leakage flux in series hybrid permanent-magnet variable flux memory machines," *IEEE Trans. Magn.*, vol. 53, no. 11, Nov. 2017.

[ZHU18a] Z. Q. Zhu and Y. Liu, "Analysis of air-gap field modulation and magnetic gearing effect in fractional-slot concentrated-winding permanent-magnet synchronous machines," *IEEE Trans. Ind. Electron*., vol. 65, no. 5, pp. 3688-3698, May 2018.

[ZHU18b] S. Zhu, W. Chen, M. Xie, C. Liu, and K. Wang, "Electromagnetic performance comparison of multi-layered interior permanent magnet machines for EV traction applications," *IEEE Trans. Magn.*, vol. 54, no. 11, pp. 1-5, Nov. 2018.

[ZIV13] V. Zivotic-Kukolj and W. L. Soong, "Effect of open stator slots on the performance of an interior permanent magnet automotive alternator," *IET Electr. Power Appl.*, vol. 7, no. 4, pp. 295–302, Apr. 2013.

[ZOU16] T. Zou, R. Qu, D. Li, and D. Jiang, "Synthesis of fractional-slot vernier permanent magnet machines," in *Proc. Int. Conf. Elect. Mach Syst.*, pp. 911-917, Sep. 2016.

[ZOU17a] T. Zou, D. Li, R. Qu, D. Jiang, and J. Li, "Advanced high torque density PM Vernier machine with multiple working harmonics," *IEEE Trans. Ind. Appl.*, vol. 53, no. 6, pp. 5295-5304, Nov./Dec. 2017.

[ZOU17b] T. Zou, D. Li, R. Qu, J. Li, and D. Jiang, "Analysis of a dual-rotor, toroidal-winding, axial-flux vernier permanent magnet machine," *IEEE Trans. Ind. Appl.*, vol. 53, no. 3, pp. 1920–1930, May/Jun. 2017.